2D-Modelling of Earthquake-Induced Rockfall from Basaltic Ignimbrite Cliffs at Redcliffs, Christchurch, New Zealand

Volume 1 of 2

A thesis submitted in partial fulfilment of the requirements for the degree of

Master of Science in Engineering Geology

at the

University of Canterbury

by

Janet C. Brehaut

UNIVERSITY OF CANTERBURY

Te Whare Wānanga o Waitaha

CHRISTCHURCH NEW ZEALAND

University of Canterbury

2012

Abstract

This thesis is concerned with modelling rockfall parameters associated with cliff collapse debris and the resultant "ramp" that formed following the high peak ground acceleration (PGA) events of 22 February 2011 and 13 June 2011. The Christchurch suburb of Redcliffs, located at the base of the Port Hills on the northern side of Banks Peninsula, New Zealand, is comprised of Miocene-age volcanics with valley-floor infilling marine sediments. The area is dominated by basaltic lava flows of the Mt Pleasant Formation, which is a suite of rocks forming part of the Lyttelton Volcanic Group that were erupted 11.0-10.0Ma. Fresh exposure enabled the identification of a basaltic ignimbrite unit at the study site overlying an orange tuff unit that forms a marker horizon spanning the length of the field area.

Prior to this thesis, basaltic ignimbrite on Banks Peninsula has not been recorded, so descriptions and interpretations of this unit are the first presented. Mapping of the cliff face by remote observation, and analysis of hand samples collected from the base of the debris slopes, has identified a very strong (>200MPa), columnar-jointed, welded unit, and a very weak (<5MPa), massive, so-called brecciated unit that together represent the end-member components of the basaltic ignimbrite. Geochemical analysis shows the welded unit is picrite basalt, and the brecciated unit is hawaiite, making both clearly distinguishable from the underlying trachyandesite tuff.

RocFall™ 4.0 was used to model future rockfalls at Redcliffs. RocFall™ is a two-dimensional (2D), hybrid, probabilistic modelling programme for which topographical profile data is used to generate slope profiles. GNS Science collected the data used for slope profile input in March 2011. An initial sensitivity analysis proved the Terrestrial Laser Scan (TLS)-derived slope to be too detailed to show any results when the slope roughness parameter was tested. A simplified slope profile enabled slope roughness to be varied, however the resulting model did not correlate with field observations as well. By using slope profile data from March 2011, modelled rockfall behaviour has been calibrated with observed rockfall runout at Redcliffs in the 13 June 2011 event to create a more accurate rockfall model.

The rockfall model was developed on a single slope profile (Section E), with the chosen model then applied to four other section lines (A-D) to test the accuracy of the model, and to assess future rockfall runout across a wider area. Results from Section Lines A, B, and E correlate very well with field observations, with ≤5% runout exceeding the modelled slope, and maximum bounce height at the toe of the slope ≤1m. This is considered to lie within observed limits given the expectation that talus slopes will act as a ramp on which modelled rocks travel further downslope. Section Lines C and D produced higher runout percentage values than the other three section lines (23% and 85% exceeding the base of the slope, respectively). Section D also has a much higher maximum bounce height at the toe of the slope (~8.0m above the slope compared to ≤1.0m for the other four sections).

Results from modelling of all sections shows the significance of the ratio between total cliff height (H) and horizontal slope distance (x), and of maximum drop height to the top of the talus (H*) and horizontal slope distance (x). H/x can be applied to the horizontal to vertical ratio (H:V) as used commonly to identify potential slope instability. Using the maximum value from modelling at Redcliffs, the future runout limit can be identified by applying a 1.4H:1V ratio to the remainder of the cliff face. Additionally, the H*/x parameter shows that when H*/x ≥0.6, the percentage of rock runout passing the toe of the slope will exceed 5%. When H*/x ≥0.75, the maximum bounce height at the toe of the slope can be far greater than when H*/x is below this threshold. Both of these parameters can be easily obtained, and can contribute valuable guideline data to inform future land-use planning decisions.

This thesis project has demonstrated the applicability of a 2D probabilistic-based model (RocFall™ 4.0) to evaluate rockfall runout on the talus slope (or ramp) at the base of ~35-70m high cliff with a basaltic ignimbrite source. Limitations of the modelling programme have been identified, in particular difficulties with adjusting modelled roughness of the slope profile and the inability to consider fragmentation. The runout profile using RocFall™ has been successfully calibrated against actual profiles and some anomalous results have been identified.

• Table of Contents

VOLUME 2 - APPENDICES

LIST OF FIGURES

LIST OF TABLES

Acknowledgements

Firstly I would like to thank Mr David Bell for his contribution to this thesis. Throughout this process the advice, revision of drafts, support and constant encouragement has been an integral part of my project. The considerable amount of time that you have given me over the past 18 months is greatly appreciated.

Thanks also to Dr Sam Hampton for helping me to understand the ignimbrite and general volcanology in fieldwork and in the lab, and Dr Marlène Villeneuve for discussion of various topics throughout this thesis. Thank you also to the staff in the Department of Geological Sciences for your help and expertise in a range of areas. In particular, thanks to Cathy Higgins and Vanessa Tappenden for help with rock mechanics testing, to Anekant Wandres and Matt Cockcroft for help with the processing of survey data, and Mark Eggers for discussions surrounding my field work and accessing data.

I wish to thank Mr Steven Young for generous access to his property for fieldwork and sampling.

Thank you to Blair, Liz, James and James for assistance with fieldwork, and to Rachel and Erin for help with endless modelling and providing comic relief.

Finally, thanks to my friends and to my family for the support and encouragement, in particular, thanks to my parents for the constant encouragement and patient listening, and to Rich for help with the technical side of things.

1 Introduction

1.1 Project Background

The suburb of Redcliffs lies at the base of the Port Hills, on the northern side of Banks Peninsula, Canterbury, New Zealand (Figures 1.1 and 1.2). The field area for this thesis includes the cliff situated to the southwest of Redcliffs School, from Raekura Place to the south, and Main Road to the northeast (Figure 1.3). The section of the cliff parallel to Main Road including Moa Bone Cave is not within the field area, nor is the area beyond the top of the cliff face.

Figure 1.1: Location map showing field area (yellow square).

The area adjacent to Redcliffs School is a former wave-cut embayment that developed during the postglacial period of marine transgression that was followed by shoreline progradation and alluvial sedimentation sourced from the Waimakariri River. Today Redcliffs is a residential area with single to double storey housing, a primary school, and public roads set close to the

cliff area. The flat land at the base of the cliff comprises marine sands and silts, and lies ~5-10m above sea level (asl; Figure 1.2).

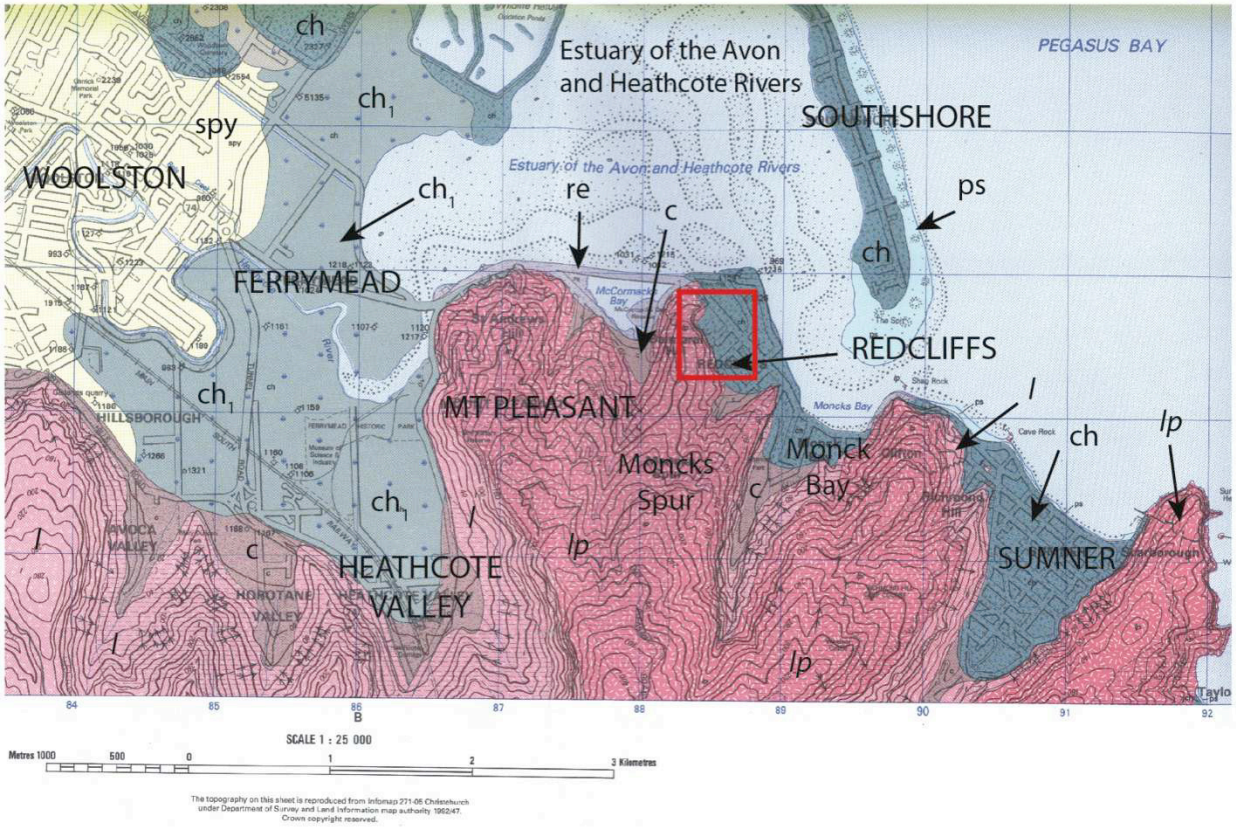

Geological Legend

re	= Reclamation deposits. Dominantly volcanic rip-rap and demolition rubble.
ps	= Sand of active dunes and present day beaches.
spy	= Dominantly alluvial sand and silt overbank deposits
ch	= Sand, silt, and peat of drained lagoons and estuaries.
ch_1	= Undifferentiated subsurface gravel, sand, shelly sand, silt, clay, peat, and wood (marine, estuarine, swamp, dune).
c	= Valley fill and slope wash of loess-volcanic derived colluvium.
lp	= Dark grey, plagioclase-pyroxene-amphibole, phyric hawaiite through to grey-green trachyte with interbedded red-brown pyroclastic deposits - **Mt Pleasant Fm.**
l	= Dark grey to black, plagioclase-pyroxene-olivine phyric basalt through to grey-green trachyte interbedded with pyroclastic deposits - **Lyttelton Volcanic Grp.**

Figure 1.2: Geological map of the Redcliffs area and surrounding suburbs. Field area highlighted by red square. Note Mt Pleasant Formation rocks forming the cliff area, with marine sands and silts forming the flat land unit. Map scale 1:25,000 (Brown & Weeber 1992).

Figure 1.3: Location of the field area at Redcliffs, divided into five sectors. Areas beyond Sector 1 to the north, and Sector 5 to the south, and all land beyond the top of the cliff, is not included in this study.

The 4 September 2010 M_w7.1 Darfield Earthquake represents the start of a period of heightened seismicity in the Canterbury region that is expected to continue for several decades (Massey, McSaveney, & Heron 2012). Damage to buildings and infrastructure from this earthquake was concentrated in the Darfield area (near the epicentre of the earthquake), and liquefaction occurred in the Eastern Suburbs of Christchurch, and at Kaiapoi. Minor damage occurred in Christchurch, generally in the form of collapsed chimney stacks and older unsupported walls. Rockfall associated with the Darfield Earthquake was generally limited, with only two boulders observed to be released onto a driveway (Bell 2010).

The M_w6.3 22 February 2011 Christchurch Earthquake caused widespread damage throughout Christchurch, in the form of shaking and liquefaction damage, as well as rockfall and cliff collapses on Banks Peninsula. There were 181 fatalities, the majority of whom were killed in building failures; two fatalities were caused by rockfall, and three from cliff collapse. Cliff collapse occurred at the Redcliffs site during the 22 February 2011 earthquake, forming a large debris slope at the base of the cliff.

Cliff collapse at Redcliffs occurred again during the M_w6.3 13 June 2011 aftershock, causing further retreat of the top of the cliff. Rock runout exceeded the pre-existing talus slopes in places, however this has been difficult to quantify due to poor quality aerial data. Cumulative cliff retreat of the order of 10-15m has occurred in both earthquake events (February and June 2011).

The consequences of the cliff collapse that has occurred during the Canterbury Earthquake sequence has affected residents both at the top and the base of the cliff. Due to cliff retreat, a number of houses at the top of the cliff have been damaged and subsequently abandoned, although, discussion of cliff top issues (i.e. future cliff collapse) is not within the scope of this thesis. Within the field area at Redcliffs, six buildings have been impacted by rockfall, of which four have been removed or abandoned due to irreparable damage. The School Hall suffered minor damage to the rear wall, however due to the closure of the school site for safety reasons this building is not currently occupied. One of the landowners within the field area

owns multiple buildings on the site. One of these structures has been partially destroyed by debris inundation, however the other buildings on the site are unaffected.

This thesis is concerned with using the cliff profile measured at Redcliffs in March 2011 to model how future rockfall debris will runout on the "ramp" structure formed by the talus slopes. Using slope profile data from March 2011 (from between the two major cliff collapse events of 22 February and 13 June 2011) allows rockfall models to be calibrated against observations in the field such as changes in the runout profile following the June cliff collapse, in order to better constrain the model parameters. This allows a robust model to be developed that could form the basis of future investigations for the purpose of making land-use decisions regarding the occupation or abandonment of the site, or appropriate protection measures against rockfall.

Due to safety restrictions at the study site, interpretations and physical measurements of features on the cliff face have been made remotely using high-resolution photographs and field observations. Where possible, representative samples have been collected from the base of talus slopes for observation and testing. Therefore, small scale features observed in hand samples are assumed to occur consistently throughout the study site, unless observations have suggested otherwise.

1.2 Thesis Objectives

The objectives of this thesis are:

- To develop an engineering geology model of the Redcliffs field area in relation to future rockfall utilising field observations, mapping, geochemical and thin section analysis, and geotechnical tests
- To analyse the influence of talus slope roughness on rockfall runout, and to evaluate the application of RocFall™ for use in accurately modelling rockfall by comparing model results with field observations

- To investigate the key controls on modelled rock runout and bounce height at the toe of the slope by comparing a tested model against other section lines within the field area, and to identify key relationships.

This thesis is not concerned with possible future cliff collapse, but with boulders and blocks released from the damaged cliff faces by future earthquakes, and their likely runout behaviour.

1.3 Banks Peninsula Geological and Geotechnical Setting

1.3.1 South Island Tectonic Setting

The tectonic setting in the South Island of New Zealand is dominated by the Alpine Fault, a dextral strike-slip fault that can be traced some 900km as a linear feature along the West Coast (Figure 1.4; Norris & Cooper 2001; Sutherland et al. 2006). The Alpine Fault separates the Australian Plate on the west from the Pacific Plate to the east, creating oblique continental collision along the margin (Eberhart-Phillips & Bannister 2002). In the central section (~along the South Island), this collision is expressed as mountain building compression, forming the Southern Alps. Subduction zones have created the Hikurangi Trough to the northeast of the South Island, and the Puysegur Trough to the southwest. Slip rates along the central part of the fault range from 35-40mm/year parallel to the fault trace, and 10-22mm/year perpendicular to it (Norris & Cooper 1995, 2001; Sutherland et al. 2006).

1.3.2 Canterbury Tectonic Setting

Brown & Weeber (1992) quote the Officers of the New Zealand Geological Survey (1979) who stated that "an active fault is one along which there is evidence of either surface displacement during the last 50 000 years, or of repeated surface displacement during the last 500 000 years and can be expected to move again in the future". In keeping with that definition, Brown & Weeber (1992) suggest that "the nearest onshore active fault to Christchurch is the Ashley Fault 20km to the north, [and] the nearest offshore fault is the Pegasus Bay Fault about 20km

to the northeast". Since the Canterbury earthquake sequence commenced in September 2010, the knowledge of active faults within the Canterbury Region has increased significantly through the accumulation of an abundance of data collected during the long aftershock sequence, and the installation of a greater number of recording devices. Discussion of seismicity relating to the Canterbury Earthquake sequence is found in Chapter 2. Faulting specific to Banks Peninsula, particularly as it relates to the formation of volcanic structures, is summarised in Figure 1.5.

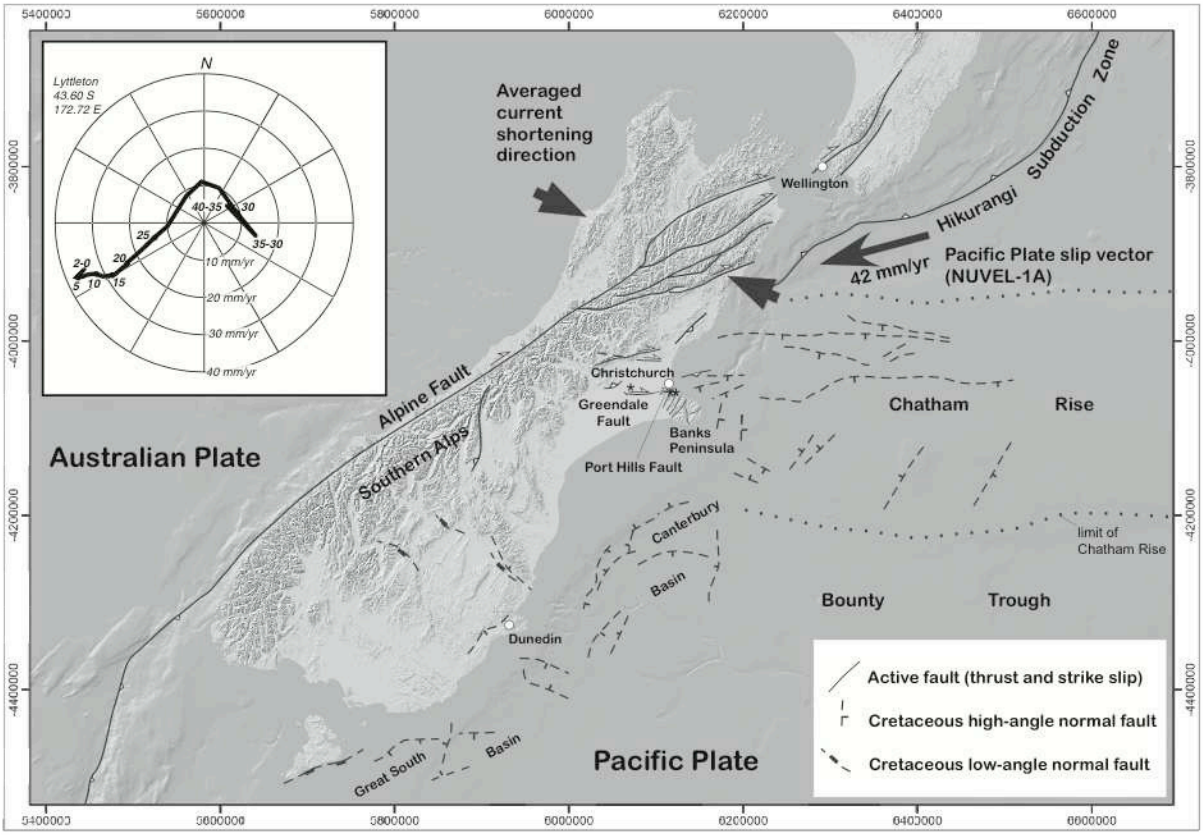

Figure 1.4: Plate tectonic setting of the South Island of New Zealand. Banks Peninsula faulting, the Canterbury Earthquake sequence since 2010, and mid- to late Cretaceous extensional faults in the South Island are also included (Ring & Hampton 2012).

1.3.3 Geologic History/ Stratigraphy of Banks Peninsula

Banks Peninsula, a 1200km^2 area on the East Coast of New Zealand's South Island, comprises three main, deeply dissected basaltic volcanoes active between 11.0 and 5.8Ma (Hampton & Cole 2009). The Banks Peninsula area is a complex volcanic area, with its geomorphology

strongly controlled by volcanic process, faulting, and erosion (Figure 1.5). Lyttelton Volcano, the older of the two main volcanic constructs, is currently considered to have been comprised of two discrete eruptive centres (Figure 1.6), Lyttelton 1 at the Head of the Bay, and Lyttelton 2 at Charteris Bay (Hampton 2010). The younger Akaroa Volcano was located in the southeast of the Peninsula.

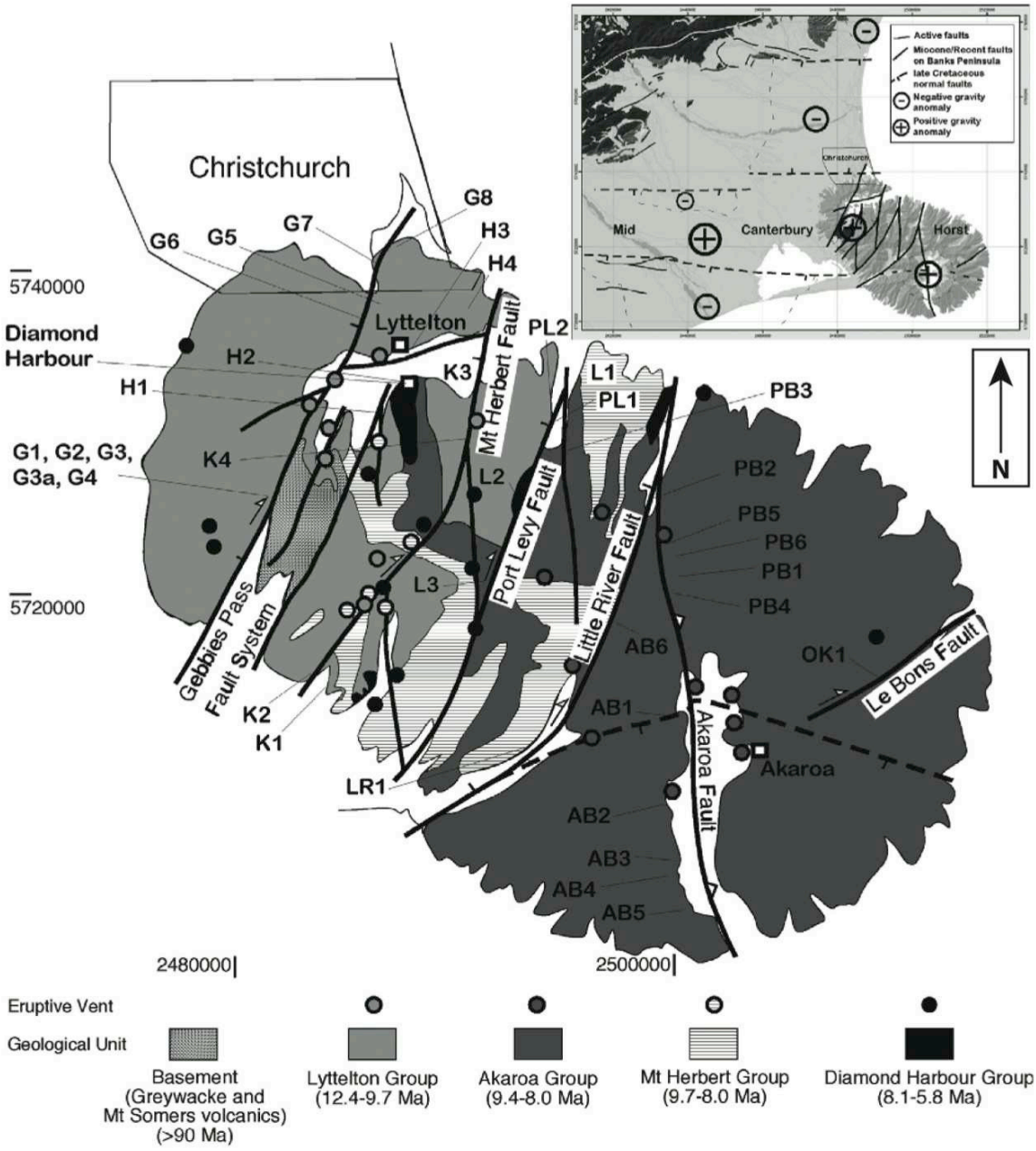

Figure 1.5: Simplified volcanic geology of Banks Peninsula after Weaver & Sewell (1986) and Sewell et al. (1992) with inferred faults and volcanic vents. Field of view is ~45km (horizontal direction; Hampton 2010; Ring & Hampton 2012).

The stratigraphy of the area has been well documented (Sewell 1985; Weaver & Sewell 1986; Sewell 1988; Sewell et al. 1992). Hampton (2010) provides detailed unit descriptions. For brevity, main stratigraphic formations from Banks Peninsula are presented in Table 1-1, and a short description of the Lyttelton Volcanics is presented below. Detailed discussion of the wider Banks Peninsula stratigraphy is not within the scope of this thesis.

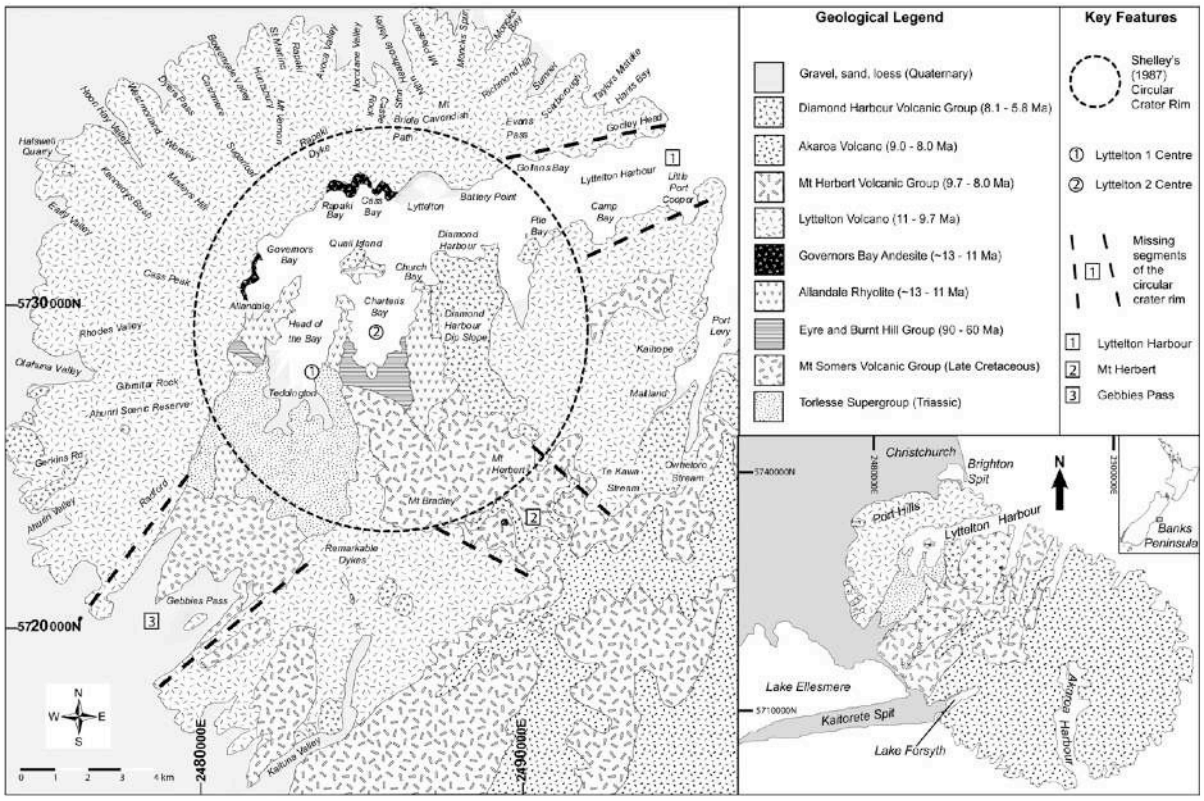

Figure 1.6: Simplified geological map of Banks Peninsula showing features of previous evolutionary models of Lyttelton Volcano (Hampton 2010, based on Sewell (1985) and Shelley (1987). Note location of Lyttelton Volcano centres in Head of the Bay and Charteris Bay.

Lyttelton Volcanics – Mt Pleasant Formation (10.4-9.7Ma)

The Lyttelton Volcanic Group consists of hawaiite lava flows, minor basaltic flows, mugearite lava flows, trachyte, and interbedded clastic sediments of varying thickness (Sewell et al. 1988; Sewell et al. 1992; and Sewell & Weaver 1990; in Brown & Weeber 1992; Hampton 2010).

Table 1-1: Summary of Banks Peninsula stratigraphy.

Group Name	Rock Type	Approximate Age (Ma)	Reference
Post-Volcanic Geology			
Port Hills Loess	Loess	2.0 -	eg. Sewell 1985; Weaver et al. 1985; McDowell 1989
Miocene Geology			
Stoddart Volcanics	Olivine Basalts – Olivine Hawaiites	7.0 - 5.8	Weaver & Sewell 1986
Church Volcanics	Olivine Basalts – Basanitoids	8.1 - 7.3	
Akaroa Volcanics	Basaltic to Trachytic lavas; pyroclastics	9.0 - 8.0	
Mt Herbert Volcanics	Olivine Hawaiites	9.7 – 8.0	
Lyttelton Volcanics	Hawaiites, Trachytes, Basalts	11.0 – 10.0	
Governors Bay Volcanics	Andesites and Rhyolites	?12.0 – 11.0	
Pre-Miocene Geology			
Charteris Bay Sandstone	Quartz-arenite sandstone	65	Sewell 1985; Weaver et al. 1985; Altaye 1989
McQueens Volcanics	Pyroxene Andesite and peraluminous high silica Rhyolites	90	Weaver et al. 1985; Weaver & Sewell 1986; Altaye 1989
Torlesse Terrane	Basement rocks – sandstones, mudstones, minor cherts, and their schistose equivalents	?250 - 200	Weaver & Sewell 1986

During late-phase Lyttelton volcanism, the Mount Pleasant Formation was formed, primarily from flank eruptions on Lyttleton Volcano (Brown & Weeber 1992; Hampton 2010). The lavas range in composition from hawaiite to trachyte, and dip north and east from Mt Pleasant, reaching sea level at Ferrymead, Redcliffs, and Moncks Bay (Brown & Weeber 1992; Figure 1.2). This is the unit forming the Redcliffs cliff line, including the study area for this thesis.

1.4 Review of Rockfall Modelling Literature

1.4.1 Introduction

Modelling rockfall trajectories down a slope is a useful tool in understanding the rockfall hazard at a site, and to enable design of effective mitigation systems. Azzoni et al. (1995) suggest that the main targets of a rockfall model are:

- The assessment of velocities, heights of bounces and energies achieved during the fall;
- The assessment of maximum runout distances, in order to determine the areas at risk.

In order to do this, an understanding of the factors influencing the behaviour of rockfall is important. Ritchie (1963) suggests that slope geometry, slope material properties, rock geometry and rock material properties all influence the behavior of rockfalls. These factors have been subdivided into respective parameters in Table 1-2. Pfeiffer & Bowen (1989) suggest that of these parameters, slope inclination and the interaction of surface irregularities with the rock are the most critical factors in determining the behaviour of rockfall.

Of the rockfall analysis literature available, Azzoni et al. (1995) suggest a simple division can be made by separating experimental methods from computer models. Experimental methods involve empirical studies and physical modelling usually by way of performing tests on scale models (Azzoni et al. 1995), or in some cases at full scale (Dorren et al. 2006). This type of analysis is expensive, time consuming, often impossible in field locations (such as near built structures or in urban areas), and is “unsuitable for statistical analysis” according to (Azzoni et al. 1995). Those authors recognise however, the benefit that experimental data, particularly scaled or full scale tests can have on calibration of mathematical models. Since the Azzoni et

al. (1995) paper was published, the advancement in technology has no doubt increased the validity of experimental studies further, through the use of high-speed digital video to create a more complete data set, which can then complement computer modelling, as done by Peng (2000), Richards et al. (2001), and Dorren et al. (2006).

Table 1-2: Parameters determining behaviour of rockfall (Pfeiffer & Bowen 1989).

Factor	Parameter
Slope Geometry	Slope Inclination
	Slope Length
	Surface Roughness
	Lateral Variability
Slope Material Properties	Slope Coefficients
	Rock Coefficients
Rock Geometry	Rock Size
	Rock Shape
Rock Material Properties	Rock Durability
	Rock Mass

1.4.2 Rockfall Models in the Literature

Since the 1970s, many authors have created computer programs to model rockfall trajectories. With the advancement of computers, this field has grown considerably, with both two-dimensional (2D) and three-dimensional (3D) models commercially available today. Table 1-3 presents the main characteristics of a selection of software that has been developed. This list is not exhaustive, rather it provides a brief account of programmes as collated by Guzzetti et al. (2002), with additional references to more recent software available also included.

Table 1-3: Main characteristics of some of the software created to model fall of a boulder along a slope and to compute rockfall trajectories. (After Guzzetti et al. 2002**; other sources specified in footnotes). RocFall™ (the model used in this thesis) is highlighted.**

Year	Author(s)	Programme Name	Dimensions	Approach	Probabilistic
1976	Piteau & Clayton	Computer Rockfall Model	2-D	Lumped mass	Partly
1982-86	Bozzolo & Pamini	SASS-MASSI	2-D	Hybrid	Yes
1985	Bassato et al.	Rotolamento Salto Massi	2-D	Lumped mass	No
1987	Descouedres & Zimmerman	Eboul	3-D	Rigid body	No
1989-91	Pfeiffer & Bowen; Pfeiffer et al.	CRSP	2-D	Hybrid	Yes
1990	Kobayashi et al.	-	2-D	Rigid body	No
1991-95	Azzoni et al.	CADMA	2-D	Hybrid	Yes
1991	Scioldo	Rotomap	3-D	Lumped mass	No
1998-12	Dorren	Rockyfor3D[1]	3-D	Hybrid	Yes
1998	Stevens	RocFall	2-D	Hybrid	Yes
1999	Paronuzzi & Artini	Mobyrock	2-D	Lumped mass	Yes
2000	Jones et al.	CRSP 4.0	2-D	Hybrid	Yes
2002	Guzzetti et al.	STONE	3-D	Lumped mass	Yes
2007	Lan et al	RockFall analyst[2]	3-D	Lumped mass	
2012	"Geociel" (company)	RocPro3D[3]	3-D	Hybrid	Yes

[1]Dorren (2012); [2] Lan et al. (2007); [3]Geociel (2012)

A key difference between the models, both 2D and 3D, is in the representation of the rock mass fragment moving downslope. As shown in Table 1-3, the "Approach" column presents three options: lumped mass, rigid body, and hybrid. A brief summary of these approaches is presented here, however further detail is not within the scope of this thesis.

In simple lumped mass models, the rock fragment travelling downslope is represented by a single, dimensionless point of defined mass (Bourrier & Hungr 2011; Peng 2000; Stevens 1998). A type of model not mentioned in Table 1.3 that is similar to lumped mass is a kinematic method, whereby the rock is modelled with no consideration for mass at all (Azzoni et al. 1995), however this type of model is generally uncommon. In contrast to lumped mass models, rigid body modelling considers the rock as a body with its own shape and volume (Azzoni et al. 1995). These authors suggest that rigid body models are generally more accurate than lumped mass models because they are "more capable of accurately reproducing the different phases of the fall phenomena". Finally, as the name suggests, a hybrid modelling approach uses a combination of lumped mass and rigid body considerations in calculations, as used in RocFall™ which is the subject of this thesis.

1.4.3 2D versus 3D Rockfall Modelling

As indicated by Table 1-3, there is a large range of rockfall modelling software available. The key division within available programmes is whether the model is based on 2D or 3D data. 2D modelling requires only topographical profile data to create a model, however this model is then limited to the vertical plane, with no capability to model lateral motion during rockfall. In contrast, 3D models require a more detailed Digital Elevation Model (DEM) or similar to input the slope topography. This allows rocks to have lateral variation in their modelled trajectories, rather than being constrained to a single plane, and is more realistic. In some cases, such as for the modelling of Redcliffs in this thesis, a simple 2D model is sufficient because the key output parameter is the runout distance.

Table 1-4 illustrates the differences between two contrasting rockfall analysis models, used here as an example of the different input requirements and output results for currently used 2D and 3D models. RocFall™ is a commercially available, 2D rockfall simulation programme that uses a hybrid, probabilistic approach, and has been used for rockfall modelling in this

thesis. In contrast, STONE is a research code developed by Guzzetti et al. (2002) for 3D simulation of rock falls (Tagliavini et al. 2008), based on a probabilistic, lumped mass model.

Table 1-4: Data required as input and output results prepared by STONE and RocFall™ (Tagliavini et al. 2008).

	STONE (3D)	**RocFall™ (2D)**
Input	Source area of the rock fall	Source area of the rock fall
	Number of boulders for each simulation	Number of boulders for each simulation
	Horizontal starting velocity	Horizontal and vertical starting velocity
	Horizontal starting angle	Horizontal starting angle
	Digital Elevation Model	Topographic profile
	Coefficients for dynamic rolling friction	Coefficients for dynamic rolling friction
	Coefficients for normal and tangential energy restitution	Coefficients for normal and tangential energy restitution
		Mass of the boulder
Output	Cumulative count of rock fall trajectories	Horizontal location of rock endpoint
	Statistics of rock fall velocity	Velocity envelope
	Statistics of rock fall distance to the ground	Height envelope
		Kinetic energy envelope

Advantages of 2D Models

Using RocFall™ as an example, the advantages of a 2D model over a 3D version include being simpler and faster to use, both in preparing the modelled slope profile and running simulations. As shown in Table 1-4, only topographical profile data is required to create a slope model in RocFall™, and the modelled output consists of simple distribution and

maximum envelope graphs and their statistics. In RocFall™, the particle model used also plays a large part in simplifying the modelling process because the effects of size, shape, and angular momentum of the particle are neglected (Stevens, 1998). This allows multiple simulations to be run in a short space of time, which is an important factor in completing sensitivity analyses.

Limitations of 2D Models

The simplicity of 2D modelling also contributes to the limitations of the model. In selecting the topographical profile to be modelled, the user must take care to choose the most likely fall-line of rock, so that the model can obtain realistic analysis results (Lan et al. 2007). By excluding the third spatial dimension, there is also no consideration of lateral motion of rock trajectories, or related energy considerations.

Advantages of 3D Models

Theoretically, 3D rockfall models are more accurate than the 2D programmes (Azzoni et al. 1995). This is due to the capability to analyse the spatial distribution of rock motion laterally, as well as longitudinally down a slope. This is particularly important in areas where the lateral spread of rockfall runout is critical, not just the runout distance. The integration of rockfall modelling with geographic information systems (GIS) databases, such as RockFall Analyst (Lan et al. 2007) provide the opportunity to access an ever-growing data resource, which could be of particular use in modelling large field areas, particularly where manual survey methods are not available.

Limitations of 3D Models

The current major limitation of 3D rockfall modelling relates to the format and amount of data used in creating the model. While it varies between models, a digital elevation model (DEM) or similar is generally required in order to model rockfall trajectories in 3D. This level of data is not always available, and data conversion for GIS-type information can be time

consuming and tedious (Lan et al. 2007). 3D models are inherently more complex, and are frequently more expensive to purchase than 2D programmes.

1.5 RocFall™

As discussed in Section 1.4, RocFall™ is a commercially available, 2D, hybrid, probabilistic rockfall trajectory model. RocFall™ was selected for use in modelling rockfall at Redcliffs for this thesis on the basis of simplicity, speed of running simulations, and availability of the programme. It was also considered appropriate for the geology and geometry of the site, but a primary aim of this study has been to evaluate its applicability as a runout modelling technique.

1.5.1 Model Assumptions

In order to make the model simple, the following assumptions were made (Stevens, 1998):

- Each rock is modelled as an infinitely small particle, so there is no interaction between particles.
- Rocks are not considered to have size, however their mass is considered in calculating their kinetic energy. Mass is not used in any of the equations for calculating the motion of the rocks.
- The mass of rocks is constant throughout each simulation, and rocks cannot break or split into multiple pieces during the simulation.
- Frictional resistance of the air is not considered.

These assumptions are required to limit the number of variables in the model, however some of them contribute to shortcomings in the model, particularly the lack of consideration of a rock's mass, the inability to consider interaction between particles, and the lack of fragmentation consideration. Pfeiffer & Bowen (1989) suggest that the assumption that fragmentation will not occur represents the worst-case scenario presented by the largest rock that remains intact while travelling down a slope. Conversely, by excluding fragmentation,

the model does not include any consideration of flyrock resulting from fragmentation, particularly at the base of the slope, where fragments can be propelled beyond the main toe of the talus slope. This was an issue at Redcliffs where indentations in buildings suggest flyrock passing 2-4m above the toe of the slope. In this case, consideration of fragmentation is necessary in interpreting results, as it is not included in modelled results.

1.5.2 Input Parameters used in RocFall™

Coefficients of Restitution

Pfeiffer & Bowen (1989) state that "slope material properties influence the behavior of a rock rebounding from the slope". These rebounding rocks are represented by normal (R_n) and tangential (R_t) coefficients of restitution, where the "normal direction is perpendicular to the impacted surface, and the tangential direction is parallel to the impacted surface, at the point of contact" (Piteau and Associates Limited, 1980; Wu 1984; in Pfeiffer & Bowen 1989). These authors further define these parameters, saying "R_n is a measure of the degree of elasticity in a collision normal to the slope, while R_t is a measure of the resistance to movement parallel to the slope". Richards et al. (2001) provide a further review using RocFall™ as the analysis method, from which values for R_n and R_t were considered in selecting initial values for these parameters in modelling.

Friction Angle (Phi)

The friction angle as used in RocFall ™ is a specific input parameter that controls the mode of movement downslope, rather than an internal friction angle of a rock material. The following description explains the use of the parameter as defined by the RocFall™ software:

> *"The friction angle is chosen based on the particle shape and the mode of movement. [It] is the critical angle of the slope segments for the purpose of rocks moving downslope. If the slope segment is inclined more than this angle, the rocks will move downslope, if it inclined less than this, they will come to rest on the segment" (RocScience 2003).*

Because the friction angle controls the mode of movement, this parameter represents a significant approximation of block shape, in the crude form of ranging from long flat slabs to spherical rocks (Figure 1.7). Long flat slabs are most likely going to topple and slide, so a higher friction angle is used. In contrast, a spherical rock will tend to roll, so a low friction angle (close to zero) is used (Figure 1.7).

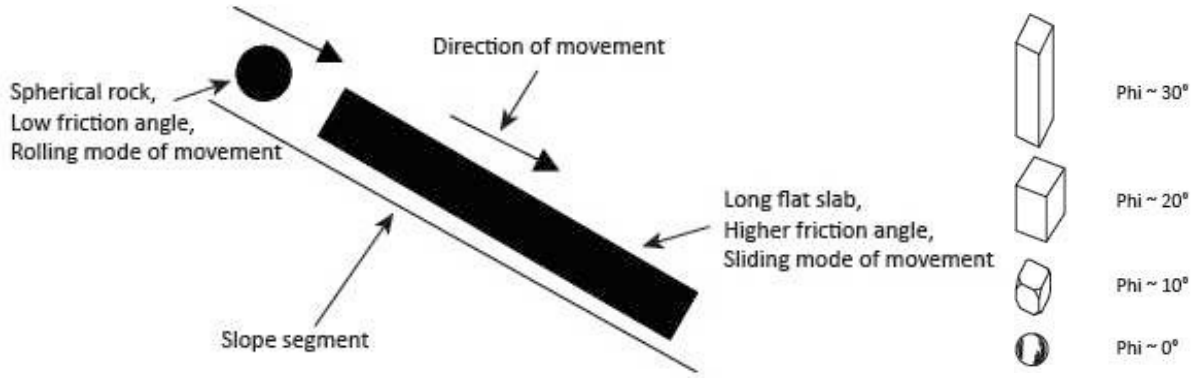

Figure 1.7 (Left) Illustration of the friction angle as used in RocFall (TM) (after RocScience 2003). (Right) Interpretation of representative block shapes as represented by friction angles.

Slope Roughness

Within RocFall™ slope geometries are input as vertices, with a line segment joining adjacent vertex points. Slope roughness is used to model local variations in geometry, on a scale that is measured between the vertices entered as the slope geometry (RocScience, 2003). Figure 1.8 shows this variability graphically, where the dashed line represents the line segment joining two adjacent vertices, and the solid line represents the adjusted profile after roughness has been calculated.

Slope roughness is represented by a normal distribution, where the mean value is calculated directly from the slope geometry, and the user controls the roughness by adjusting the standard deviation. As the standard deviation is increased, variability of the generated slope compared to the measured slope will get more pronounced, the rocks are more likely to bounce in directions increasingly different from the angle of the slope segment, and the rock paths will look more “unpredictable” or “unusual” (RocScience 2003).

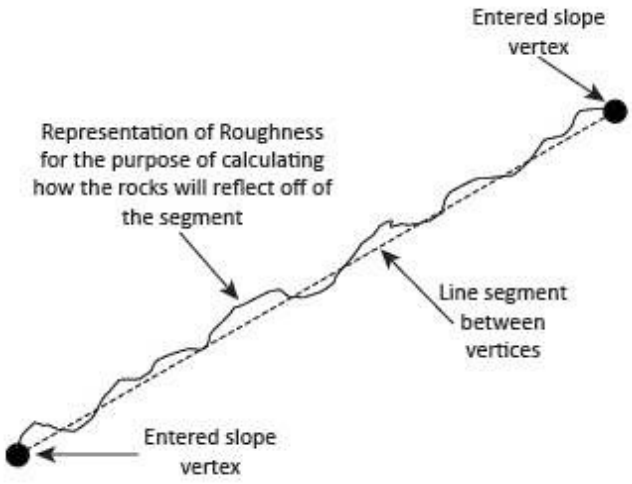

Figure 1.8: Illustration of Roughness as used in RocFall™ (after RocScience 2003).

Angular Velocity

Angular velocity refers to the "time rate at which an object rotates, or revolves, about an axis" ("Angular Velocity" 2012). In RocFall™, consideration of this parameter in calculations can affect the downslope transportation of rocks as discussed in Section 5.5.3. According to material published by RocScience (2003), the initial value of angular velocity is not as influential in the calculations that produce runout paths as the consideration of the concept itself. The article also states that as a general rule, the initial angular velocity value is very small and often zero, due to most rocks starting with very little movement but rocks begin to rotate quite quickly as they travel downslope. Because of this, consideration of angular velocity is the only aspect of this parameter that has been varied during modelling.

Rockfall Source Areas

RocFall™ defines the rockfall source areas on a slope as point- or line- seeders. A point seeder releases simulated rocks from a single point on the slope profile, whereas a line seeder allows the user to select a continuous area from which simulated rocks can originate.

1.6 Thesis Methodology

1.6.1 Data Collection

Field data has been collected during the period April to September 2012, involving capture of high-resolution photographs that have been used in constructing engineering geology face logs, as well as for general reference; collection of representative rock samples from the base of talus slopes; and mapping of existing rockfall runout onto aerial photographs. Photographs have been taken from a range of locations including the school field, Main Road, and from private properties. Photographs were taken in different light conditions also, as it was found that bright exposures obscured some cliff face features that were more clearly visible under low light conditions. Detailed notes were also recorded during each site visit.

Aerial photographs were accessed from Google Earth and www.koordinates.com. These photographs are freely available online, and have been used in creating rockfall runout maps. Aerial photographs from after the June 2011 cliff collapse event were not available, so runout maps were supplemented with field observations.

Terrestrial Laser Scan (TLS) data captured by GNS Science in March 2011 has been processed using Golden™ Surfer® 9 software to obtain the topographical profile data to input into the RocFall™ model to create the modelled slope profiles. Some of the lower reaches of the slopes were obscured from the TLS, so the lower ~10m of two of the modelled profiles have been estimated from aerial photographs and field observations.

Representative samples have been collected from the base of talus slopes for bulk geochemical analysis, thin section analysis, and geotechnical testing.

1.6.2 Analysis

Sensitivity testing has been undertaken to identify key variables in the RocFall™ model. This involves repeatedly running a single section line simulation using constant variables, while changing a single parameter to observe the influence on the overall model. Having identified

the input variables and calibrated them with field observations, the selected model has been tested on the other four section lines. From this site-wide model, runout data have been collected by the software. The key parameters analysed at this stage of the process are the influence that total cliff height, maximum drop height to the talus slope, and the horizontal runout distance of the modelled profile. These control the number of rocks exceeding the measured toe of the slope, and the maximum modelled bounce height at the base of the slope.

1.7 Thesis Format

Chapter 2 provides a summary of the Canterbury Earthquake Sequence from 4 September 2010 to the present. Within this chapter, a key focus is on the extraordinarily high Peak Ground Acceleration (PGA) values recorded, particularly during the 22 February and 13 June 2011 earthquakes, because these are thought to be a major contributing factor in the widespread rockfall and large scale cliff collapse failures that occurred on Banks Peninsula.

Chapter 3 presents the stratigraphy of the Redcliffs field area, with a primary focus on the identification and description of a basaltic ignimbrite unit that has not been previously recorded in the Banks Peninsula volcanic geology literature. The ignimbrite and the other rock units at Redcliffs are discussed in terms of the way that particular features affect the behavior of the rock during a rockfall, as this understanding is critical to the accuracy of the engineering geology model, and the subsequent rockfall model of the area.

Chapter 4 presents and discusses the engineering geology site model for Redcliffs, with particular emphasis on the engineering geology face logs that have been constructed. The face logs map lithological units and broad-scale discontinuity sets for the units exposed above the talus aprons. Discontinuity mapping, while at broad scale, show distinctive areas where more closely jointed rock is concentrated, which is important for rockfall source area considerations. Chapter 4 also summarises the results of geotechnical testing, and the implications that these results have on the rockfall model.

Chapter 5 summarises the results of the rockfall model for Redcliffs by using the School Hall Section as a case study. The model is shown to be sensitive to source area elevation as is expected; however roughness of the talus apron did not have the influence on rockfall runout that was expected. This is due to the high level of detail in the section profile, but results from the detailed profile were more comparable to field observations than a simplified slope version that had to be used.

In Chapter 6, the rockfall model has been tested for the other four section lines at Redcliffs, and the results from these models are used to identify the key parameters controlling future rockfall runout. This is particularly useful for applying the data from the modelled section lines to other areas of the cliff to estimate the percentage of rocks that could exceed the existing talus slope, and the maximum bounce height expected at the toe of the slope. This is useful for future land use planning at Redcliffs.

Chapter 7 summarises the conclusions presented in this thesis, and makes recommendations for future work.

2 Canterbury Earthquake Sequence 2010-2011

2.1 Introduction

The cliffs at Redcliffs are a dominant feature of the landscape, standing over 70m high in places, and extending approximately 900m from Moa Bone Point to Raekura Place, Redcliffs (Figure 1.3). The cliffs are composed of material erupted from Lyttelton Volcano during the latter stages of the eruption phase, and were modified by marine action when sea level reached its present elevation at about 6,500 year BP (= before present) following Postglacial sea-level rise (Brown & Weeber 1992). According to recent work (Hampton 2010; Hampton & Cole 2009), Lyttelton Volcano was a complex containing 15 eruptive centres rather than two large ones (Shelley 1987, in Forsyth et al. 2008). A summary of Banks Peninsula geology was presented in Chapter 1.

This chapter deals with the Christchurch Earthquake sequence, and its impact on the Redcliffs study area. It considers Peak Ground Accelerations (PGA) in the various earthquake events and also also briefly reviews the history of rockfall on Banks Peninsula. These include seismically induced falls, gravitational failures and anthropogenic causes.

2.2 Rockfall Pre-September 2010

Prior to 2011, rockfall occurrences in the Port Hills have been generally infrequent and minor in terms of fallen volumes and effect on people and infrastructure. Figure 2.1 shows a photograph of a historic rockfall at Clifton, Sumner that blocked both the road and the tram line on 9 October 1912 (Brown & Weeber 1992). Those authors reported significant historical rockfalls to have occurred in 1968, 1970, and 1986, however in at the time of writing (1992) rockfalls "have only caused damage to property and public works, and inconvenience to residents".

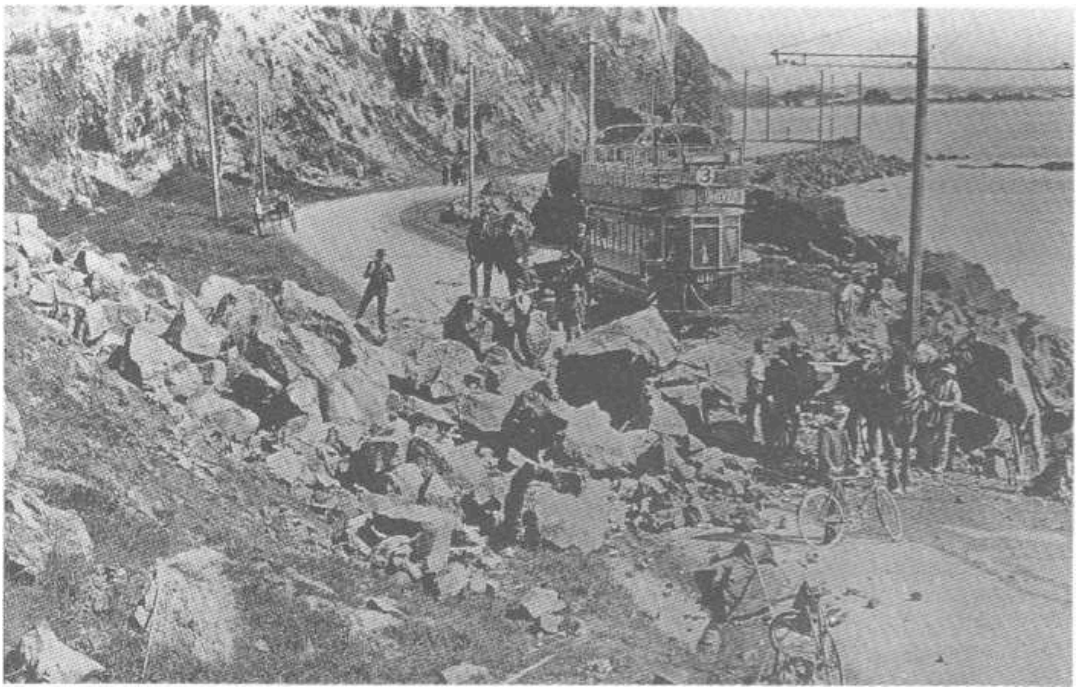

Figure 2.1: Rockfall blocking road and tramline, Clifton, Sumner on 9th October 1912 ***(Photo: Canterbury Times, Canterbury Museum collection;*** **Brown and Weeber 1992).**

According to data collated by Lundy (1995), naturally occurring rockfalls prior to the 4 September 2010 Darfield Earthquake appear to be rare and localised. Appendix 2 provides an account of mass movement events on Banks Peninsula recorded between 1886 and 1992. This provides a chronological summary of all mass movement events recorded primarily in public documents such as local newspapers, which have been collated by the Sumner Museum. Where significant time gaps occurred in this collection, information regarding these periods was compiled by records held by the Canterbury Public Library (Lundy 1995).

Although there are breaks in data during this period, the majority of rockfalls occurred as a result of human activity, generally associated with the construction of roads and the general urbanization of hillside areas, chiefly due to blasting (Lundy 1995). Heavy rain and snow were the other predominant causes of rockfall and other mass movement events. Given the nature of the data, being largely obtained from newspaper records, little distinction is made between failure types or mechanisms, such as loess failure, debris slides and rockfalls (Lundy 1995).

According to this data set, seismicity was a contributing factor in only two rockfall events. At Sumner Cliffs on 13 September 1929, heavy rain and a recent earthquake are suggested as likely causes. Similarly on 7 June 1992 at Raekura Place, Redcliffs, rockfall was thought to be triggered by "progressive weakening and fretting of a thick ash unit immediately underlying lava blocks", as well as a recent storm event and a Marlborough earthquake acting as contributing factors (Bell referenced in (Lundy 1995)). In both cases, seismicity was only a contributing factor, as opposed to the primary trigger.

2.3 Christchurch Earthquake Sequence

2.3.1 Introduction

The Christchurch Earthquake sequence is a continuing period of heightened seismicity in the Christchurch area, following the 4 September 2010 Darfield Earthquake. Seismic activity has been considerably higher than the long-term average, and is expected to remain higher for several decades (Massey, McSaveney, & Heron 2012). Major earthquakes (classified here as those of Magnitude, $M_w \geq 6.0$) from this sequence to the end of 2011 are discussed in this thesis. Table 2-1 summarises the four earthquakes included in this discussion. All dates and times are in New Zealand Time (NZT).

2.3.2 Seismological Data

Seismological data, particularly magnitude and depth of large earthquakes were collected from GeoNet (www.geonet.org.nz) and GNS Science from late 2011 to mid 2012. These data are frequently being reviewed and adjusted by these agencies as more data becomes available. Adjustments are generally minor, thus data collected during this period was used, rather than renewing data each time a revision was made. Where applicable, the date data were accessed has been indicated.

Figure 2.2 presents the earthquake sequence plotted based on the epicentre locations of all recorded earthquakes of $M_w \geq 3.0$ since the 4 September 2010 Darfield Earthquake. As can be observed in the figure, seismic activity has generally moved in an east-northeasterly direction over the course of the aftershock sequence, with the latest of the large aftershocks (23 December 2011) being centred offshore. Figure 2.2 also demonstrates the close proximity of the epicentre of the 22 February 2011 Christchurch Earthquake to central Christchurch. This is considered to be one of the significant factors in the severe damage that was sustained in the city.

Table 2-1: Summary table of earthquakes of Mw ≥ 6.0 or larger in the Canterbury region from the period September 2010 to December 2011 (www.geonet.org.nz).

Date (NZT)	Time (NZT)	Magnitude, M_w	Depth (km)
4 September 2010	4.35am	7.1	11.0
22 February 2011	12.51pm	6.3	5.4
13 June 2011	2.20pm	6.3	6.9
23 December 2011	3.18pm	6.0	7.5

2.3.3 4 September 2010 Darfield Earthquake

On September 4 2010, at 4:35am local time, a magnitude M_W7.1 earthquake struck the Canterbury region. The epicentre of this quake was located 9km southeast of Darfield, a small rural town approximately 43km from central Christchurch. Rupture occurred along a previously unrecognised fault, now known as the Greendale Fault. This earthquake resulted in approximately 29km of ground surface rupture, and a total of around 40km subsurface rupture (Cubrinovski 2010). Surface displacement of the fault rupture produced predominantly dextral strike-slip movement, with average horizontal displacement around 2.5m and maximum displacements of ~5m horizontally and ~2.5m vertically (Quigley et al. 2010). Key seismological features of the Darfield Earthquake are summarised in Table 2-2.

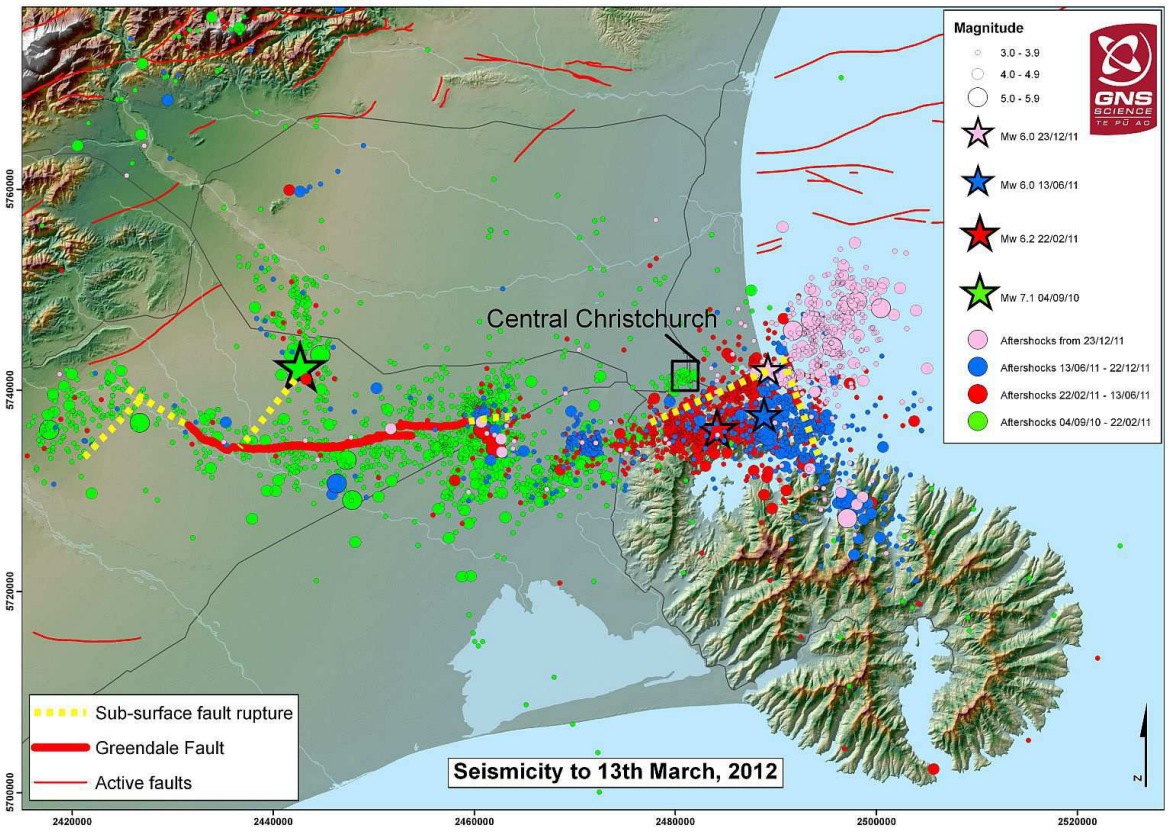

Figure 2.2: Aftershock sequence from the 4th September 2010 Darfield Earthquake to 13th March 2012 (www.geonet.org.nz).

Table 2-2: Key seismological features of the Darfield Earthquake (Gledhill et al 2011; www.geonet.org.nz).

Origin Time	September 4, 2010 at 04:35 NZT
Epicentre	43.52° South, 172.17° East
Depth	11.0km
Magnitude	M_W 7.1
Location	9km south-east of Darfield
	37km west of Christchurch
Approximate Redcliffs PGA	63(%g)

Damage to buildings and infrastructure

While the Darfield earthquake had a long duration and recorded a Modified Mercalli Shaking Intensity of 9 (Gledhill et al. 2011), damage to buildings and infrastructure was relatively localised, and no deaths occurred.

Where the fault rupture passed directly beneath structures, or where structures were within or partially within the fault rupture deformation zone, damage occurred to structures, however none collapsed (Quigley et al. 2010). The fault rupture deformation zone was oriented perpendicular to the strike of the fault ~30-300m wide (Van Dissen et al., 2011). On the whole, buildings in Christchurch and Darfield performed well, with little structural damage due to ground shaking (Buchanan and Newcombe 2010 (in Gledhill et al. 2011)). Damage occurred in unreinforced masonry buildings, particularly in older buildings (more than 20 years old) where chimneys fell, causing damage as they collapsed (Cubrinovski 2010; Gledhill et al. 2011).

Significant damage occurred in the Eastern Suburbs of Christchurch, in Kaiapoi, and in areas near major streams, rivers and wetlands. This was primarily a result of differential settlement of foundations caused by liquefaction of soils and lateral spreading (Gledhill et al. 2011).

Rockfall Occurrences

Rockfall during the Darfield earthquake was generally localised and caused minimal damage to buildings and infrastucture. There were no casualties from rockfall. A section of Evans Pass was blocked by rockfall, causing closure of one of the critical access routes into the Port of Lyttelton. This rockfall was relatively isolated, and fallen rock, once past the roadway, fell into open water. In this regard, the rockfall did not pose significant hazard to life or property after the road was closed.

Another example of rockfall triggered by the Darfield Earthquake comes from a report by Bell (2010) regarding the performance of a section of the current field area at Redcliffs. Rockfall was noted to have occurred at this site during the main shock (M_W 7.1 event). Rockfall was

minimal, however, with runout exceeding the historic toe of the slope only where two boulders <10kg each impacted the access driveway. The Peak Ground Accelerations (PGA) at Redcliffs during this event have been estimated to be ~0.49g (www.geonet.org.nz) based on nearby strong motion stations.s

2.3.4 22 February 2011 Christchurch Earthquake

The largest and most devastating aftershock from the Darfield Earthquake occurred on 22 February 2011, at 12:51pm local time. The shallow M_W6.3 event was centred 6km deep beneath the Port Hills, 10km southeast of Christchurch (www.geonet.org.nz; Figure 2.2). There were 181 fatalities in total, and several thousand injured (eg Webb et al. 2011; Wood et al. 2011). 176 of these fatalities resulted from building failures, largely in the inner city area, a further two from rockfall and three from cliff collapses in the Port Hills (e.g. Kaiser et al. 2012; Massey, McSaveney, Heron, & Lukovic 2012).

Faulting occurred on the Port Hills Fault, a structure that was only recognised on 22 February 2011, as a result of concentrated aftershock activity in the months leading up to the Christchurch Earthquake (Massey, McSaveney, Heron, & Lukovic 2012). The Port Hills Fault did not rupture the surface, however slip is thought to have reached within approximately 1km of it (Massey, McSaveney, Heron, & Lukovic 2012). The movement of the fault was oblique-reverse (a combination of right-lateral strike-slip and thrust faulting) (Webb et al. 2011). Key seismological features are summarised in Table 2-3.

A key feature of the Christchurch Earthquake was the very high peak ground accelerations that occurred during the event. PGA were recorded as high as 2.2g at Heathcote Valley School. These peak ground accelerations were a major contributor to the extensive damage caused both on the Port Hills and on the flat areas, including the central business district (CBD) and the eastern suburbs. Damage included shaking and foundation damage to buildings; widespread liquefaction on the flat areas; damage to roading and infrastructure; and damage

caused by rockfall and cliff collapse on the Port Hills. Causes and implications of high PGA values are discussed in Section 2.4.

Table 2-3: Key seismological features of the 22 February 2011 Christchurch Earthquake (www.geonet.org.nz).

Origin Time	February 22, 2011 at 12:51 NZT
Epicentre	43.58° South, 172.68° East
Depth	6.0km
Magnitude	M_W6.3
Location	Within 5km of Lyttelton Within 5km of Diamond Harbour 10km south-east of Christchurch
Approximate Redcliffs PGA	220(%g)

Rockfall Occurrences

Rockfall and cliff collapses were widespread and numerous on the Port Hills during the Christchurch Earthquake. Massey, McSaveney, Heron, & Lukovic (2012) noted that the main earthquake on 22 February 2011 was closely followed by a large aftershock that also triggered rockfall on the Port Hills. Rockfall from these two events could not be distinguished in the debris. As such, in both the literature and in this thesis, both rockfall events were treated as if they occurred in the mainshock at 12.51pm.

As mentioned earlier in this section, five fatalities resulted from rockfall and cliff collapses in the Christchurch Earthquake main shock. Damage to property from rockfall and cliff collapses was also severe, with large numbers of houses damaged or destroyed, with others condemned due to future rockfall risk.

2.3.5 13 June 2011 Earthquake

The 13 June 2011 aftershock was a M_w6.3 event that occurred at 2.20pm local time. The earthquake caused further damage to buildings and infrastructure around the city through shaking damage, as well as liquefaction and lateral spreading. The aftershock also triggered further widespread rockfalls and cliff collapses on the Port Hills. According to Webb et al. (2011), one fatality resulted from this aftershock, although this statistic has not been widely reported in other literature.

The epicentre of the earthquake was centred 10km east of Christchurch, near the suburb of Sumner, at a depth of 6.9km (Figure 2.2; www.geonet.org.nz). The fault movement was strike-slip – a contrast to the 22 February 2011 earthquake (oblique-reverse), the effects of which are discussed in Section 2.4. Key seismological features of the 13 June 2011 earthquake are summarised in Table 2-4.

Table 2-4: Key seismological features of the 13 June 2011 earthquake (www.geonet.org.nz).

Origin Time	June 13, 2011 at 14:20 NZT
Epicentre	43.57° South, 172.74° East
Depth	6.9km
Magnitude	M_W6.3
Location	10km north-east of Lyttelton 10km north-east of Diamond Harbour 10km east of Christchurch
Approximate Redcliffs PGA	119(%g)

Rockfall Occurrences

Further rockfall and cliff collapses occurred during the 13 June 2011 earthquake. According to (Massey, McSaveney, Heron, & Lukovic 2012), 190 rockfalls were mapped following this event, similar to the number triggered by the Christchurch earthquake in the same area. Associated with the cliff collapses, recession of the cliff top was appreciable in places, including at the

study site at Redcliffs, however exact recession measurements were unavailable at the time of writing.

Whitewash Head, near Sumner, collapsed catastrophically during this event where an estimated 100,000m^3 of rock failed from this site (Massey 2012). Cliff top recession at this site resulting from the 2010/11 Canterbury earthquake sequence was 17m (Massey, McSaveney, & Heron 2012), of which a large proportion occurred during this single event.

2.3.6 23 December 2011 Earthquake

The last of the large magnitude earthquakes included in this thesis occurred on 23 December 2011 at 2.18pm local time. The M_w6.0 aftershock was centred 10km east of Christchurch, at a depth of 6.9km (www.geonet.org.nz; Figure 2.2; Table 2-5). As shown in Figure 2.2, the 23 December aftershock continued the trend of seismic activity moving in an easterly direction from the Darfield main shock, with aftershocks since this date generally concentrated offshore. As with previous large magnitude earthquakes, high PGA values were recorded, however ground movement was generally similar to shaking that occurred in Christchurch city during to the Darfield Earthquake.

Table 2-5: Key seismological features of the 23 December 2011 earthquake (www.geonet.org.nz).

Origin Time	December 23, 2011 at 14:18 NZT
Epicentre	43.53° South, 172.74° East
Depth	6.9km
Magnitude	M_W 6.0
Location	10km east of Christchurch 10km north of Lyttelton
Approximate Redcliffs PGA	33(%g)

Rockfall Occurrences

Rockfall associated with the 23 December 2011 earthquake is not well documented in the literature. Anecdotal evidence suggests small, localised rockfall occurrences, however these are not considered significant in this research. There is no evidence for large-scale failures.

2.4 Peak Ground Acceleration Data

2.4.1 Strong Motion Network

A network of strong-motion accelerographs recorded peak ground acceleration (PGA) data during the earthquake sequence that struck Canterbury from 2010. Prior to the Darfield Earthquake, a network of 36 of a planned 60 strong-motion stations (SMS) were installed as part of the Canterbury Accelerograph Network (CanNet), a regional network to collect data from future large earthquakes, such as those expected from the Alpine and Hope Faults (Berrill et al. 2011). The low-cost, low-sensitivity nature of CanNet was designed to permit the addition of tens of stations, to supplement the existing National Strong Motion Network (NSMN) that consisted of seven, generally 18-bit accelerographs (Berrill et al. 2011). This combined network would provide greater detail for analysis of earthquake strong-motion data. Both networks are now operated under the GeoNet organsation.

At the time of the Darfield Earthquake, 30 of the 36 installed accelerographs were located within 40km of the epicentre of the quake, providing a rich database from which to reconstruct the source mechanism of the earthquake in detail (Berrill et al. 2011). Following the Darfield event, another strong-motion station was installed in Halswell to boost the network coverage in the area. After the 22 February 2011 earthquake, further accelerographs were also installed on the Port Hills to further increase the density of the network. Figure 2.4 shows the location of strong-motion stations in the Christchurch area. From this map, the spread of the network over the wider Canterbury area can be seen, as well as the dense array of stations the Christchurch City.

Throughout this thesis and other studies conducted on the Canterbury earthquake sequence, PGA data has been used to characterise ground shaking during an earthquake. It is an index value that provides a measure of ground acceleration at a particular strong-motion station, so nearby values may differ from the recorded value dependent on factors such as site specific geology, and topography. The latter can influence peak ground acceleration through topographic amplification (Kanari 2008; Massey, McSaveney, Heron & Lukovic 2012), where shaking is enhanced at a topographic high point such as a break in slope at the top of a cliff or ridge. Because of this, PGA data is best used as an indicator of maximum values at the recording station, not necessarily an absolute maximum over the wider area.

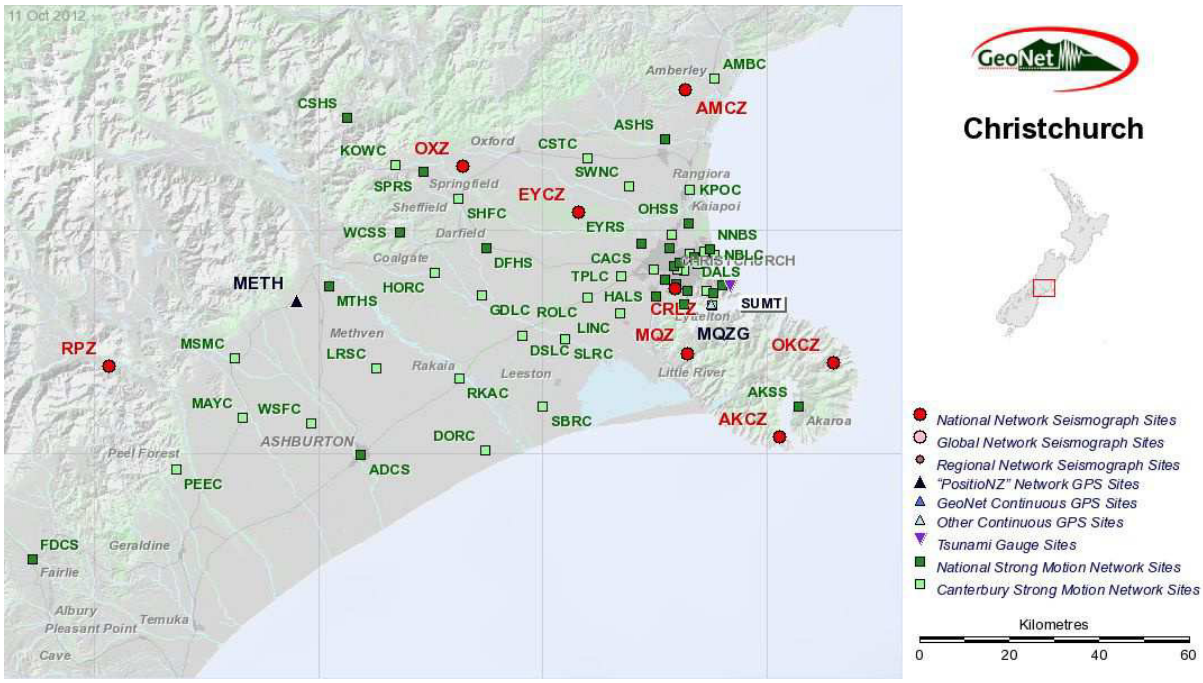

Figure 2.3: Strong-motion sites around Christchurch as of October 2012 (www.geonet.org.nz).

2.4.2 Analysis of Data

PGA data from local strong-motion sites on Banks Peninsula are summarised in Table 2-6. The sites have been selected for analysis primarily due to their proximity to the Redcliffs field area (Figure 2.4). Three additional stations were established near the field area prior to the 13 June 2011 aftershock, however data from these were only available for the June and December aftershocks in this sequence, so they are not included in this summary table. Figure 2.3

presents an example of PGA data reflected graphically, showing the data following the 22 February 2011 Earthquake. Graphic representations of PGA data from strong-motion stations around Christchurch city for the major earthquake events discussed in this section are presented in Appendix 3.

Table 2-6: Summary of Peak Ground Acceleration values from nearby strong-motion sites following major earthquakes (www.geonet.org.nz). Note: LPCC station used in calculating average PGA value for Redcliffs for Darfield and Christchurch earthquakes, however stations closer to Redcliffs were established after the 22 February event so these were used preferentially.

Station Name	PGA (%g)			
	4 September 2010 (M7.1)	22 February 2011 (M6.3)	13 June 2011 (M6.0)	23 December 2011 (M6.0)
Heathcote Valley School (HVSC)	63	220	115	66
"Station A"			71	24
"Station B"			77	25
Whitewash Head			213	19
Average[1]	63	220	119	33

[1]LPCC not included in calculation of average PGA for Redcliffs for 13 June and 23 December earthquake events.

PGA data presented in this section refers to the peak ground acceleration (either vertical or horizontal) recorded at a strong-motion station during the four large magnitude ($M_w \geq 6.0$) earthquakes from 4 September 2010 to 23 December 2011. Of these four earthquakes, PGA data were recorded to have exceeded 1g on two occasions at the Heathcote Valley School (HVSC). These occurred on 22 February and 13 June 2011, which correlates with the two major rockfall and cliff collapse events at Redcliffs, and around Banks Peninsula.

Comparing the values from Heathcote Valley School with those of nearby Lyttelton Port (LPCC), it can be seen that the HVSC site has had consistently higher PGA values recorded during each of the four large earthquakes. While values were higher at Heathcote Valley

School, PGA values recorded during the 22 February 2011 event reached almost 0.96g at Lyttelton Port, triggering widespread rockfall in the Lyttelton Area. Rockfall also occurred during the 13 June 2011 M_w 6.3 event, when PGA of 0.65g was recorded. This suggests that even though LPCC sustained less vigorous ground shaking than HVSC, it was still sufficient to trigger rockfall.

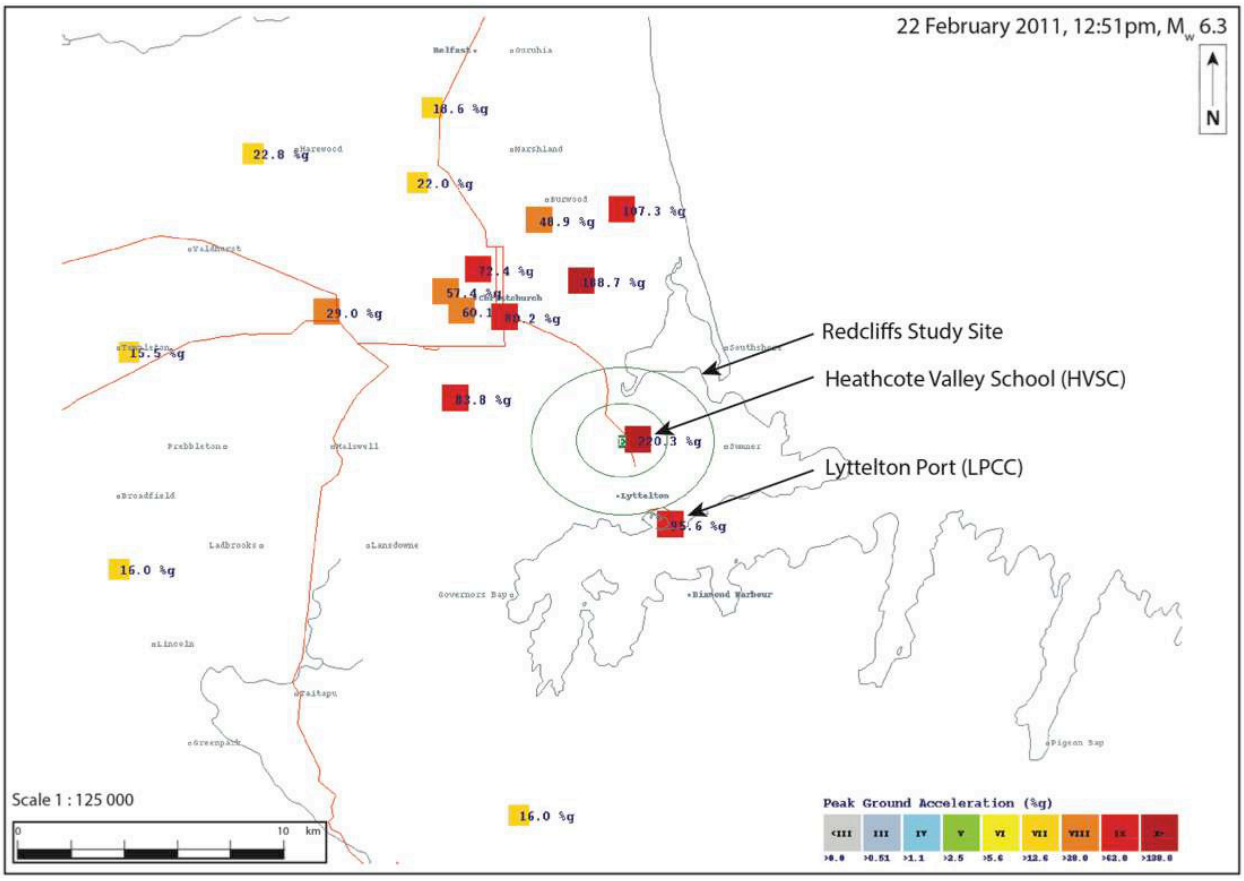

Figure 2.4: Example of PGA data from the 22 February 2011 Christchurch Earthquake (www.geonet.org.nz). PGA data maps for other large earthquakes are included in Appendix 3.

Similarly, to the east of Sumner, PGA of 2.13g was recorded during the 13 June 2011 M_w 6.3 earthquake. During this event, major cliff collapse occurred at Whitewash Head, a site that had previously been under observation because of tension cracks forming along the cliff top following the 22 February 2011 earthquake. As seen at Redcliffs, steep cliff faces such as those at Whitewash Head could not withstand the forceful ground shaking that occurred during this event, and failed catastrophically as a result. Data from this strong-motion site was not

available for the previous two large earthquakes, so comparisons with earlier earthquakes were not possible.

The 2.2g PGA value recorded at Heathcote Valley School on 22 February 2011 represents hugely significant ground motion, on a scale that has not been recorded in New Zealand prior to this event. According to Bradley (2010, in Bradley & Cubrinovski 2011), prior to the Darfield earthquake, the maximum recorded PGA in New Zealand was 0.39g. This shows that ground shaking of this intensity was unprecedented in this country, let alone in Canterbury, which was a significant factor in why damage, particularly to buildings and infrastructure was so widespread following this earthquake.

While the magnitude of the 23 December 2011 earthquake (M_W 6.0) is considered large from a New Zealand seismicity perspective, the ground shaking recorded was similar to the 4 September 2010 Darfield earthquake. PGA for the 23 December event were consistently lower than the February and June 2011 earthquakes that caused widespread rockfall and substantial areas of cliff collapse on Banks Peninsula. As a result, rockfall and cliff collapse was comparable in both, with generally only minor rockfalls recorded in the Darfield Earthquake, and no significant rockfalls recorded in the 23 December 2011 event.

2.4.3 PGA threshold value for triggering failure

Based on these observations, it is clear that a so-called "threshold value" is required to be overcome for rockfall and cliff collapse to occur. Massey, McSaveney, Heron & Lukovic (2012) have identified a value based on a number of sites across the Port Hills. This threshold therefore represents the "minimum peak ground acceleration required to trigger one rockfall", and have found it to be about 0.3 to 0.4g. As seen during each of the four large magnitude earthquakes presented in this section, this threshold was exceeded at Heathcote Valley School in each event.

The threshold value cannot be the sole factor in determining if and how failure could occur in a rock mass. Kanari (2008) found that not all large earthquakes trigger rockfalls, rather the rock mass needs to be weakened in order to facilitate this type of failure. This relates to both the geological composition of the rock mass, as well as joints and fractures within it. Massey , McSaveney, Heron & Lukovic (2012) presented a theory whereby rock most susceptible to failure is preferentially removed by earthquake shaking, but this shaking in turn may weaken other rocks, making them less stable. This process then provides weakened rock to be preferentially removed by subsequent earthquake shaking. The analogy for this process has been described as a conveyor belt, whereby the rock most easily dislodged is removed first, and then is essentially "replaced" by the next mass of loose rock (Massey 2012 – GNS Talk). Massey, McSaveney, Heron & Lukovic (2012) cite the repeated failures of some 190 mapped rockfalls from the February and June earthquakes as evidence of this process occurring in the Port Hills.

2.4.4 Horizontal versus vertical peak ground acceleration

Figures 2.5- 2.7 compare the PGA values recorded from the 4 September 2010, 22 February 2011, and 13 June 2011 earthquakes respectively. The figures are not representing vectors, but rather the vertical and horizontal shaking components recorded by temporary, low-cost accelerographs (Webb et al. 2011). From these figures, the level of shaking, and the dominant shaking direction are clearly shown to vary markedly between earthquakes. Key observations from these figures are:

- Ground movement in the Darfield Earthquake was generally small, however strong horizontal shaking was recorded at one location on the Port Hills (Figure 2.5)
- Ground movement in the 22 February 2011 aftershock was dominated by strong vertical shaking (Figure 2.6)
- High levels of ground shaking was widespread throughout the CBD, Eastern Suburbs, and the Port Hills during the Christchurch Earthquake
- In the 13 June 2011 aftershock, strongest shaking was more predominant in the horizontal direction than the vertical (Figure 2.7)

A reason for the difference between the contrasting shaking directions noted above was offered by Massey, McSaveney, Heron & Lukovic (2012) using the 22 February and 13 June 2011 events as examples. Those authors noted the contrasting fault movements: 22 February was an oblique-reverse fault, whereas the 13 June aftershock was strike-slip; as reason to account for the contrasting shaking direction recorded.

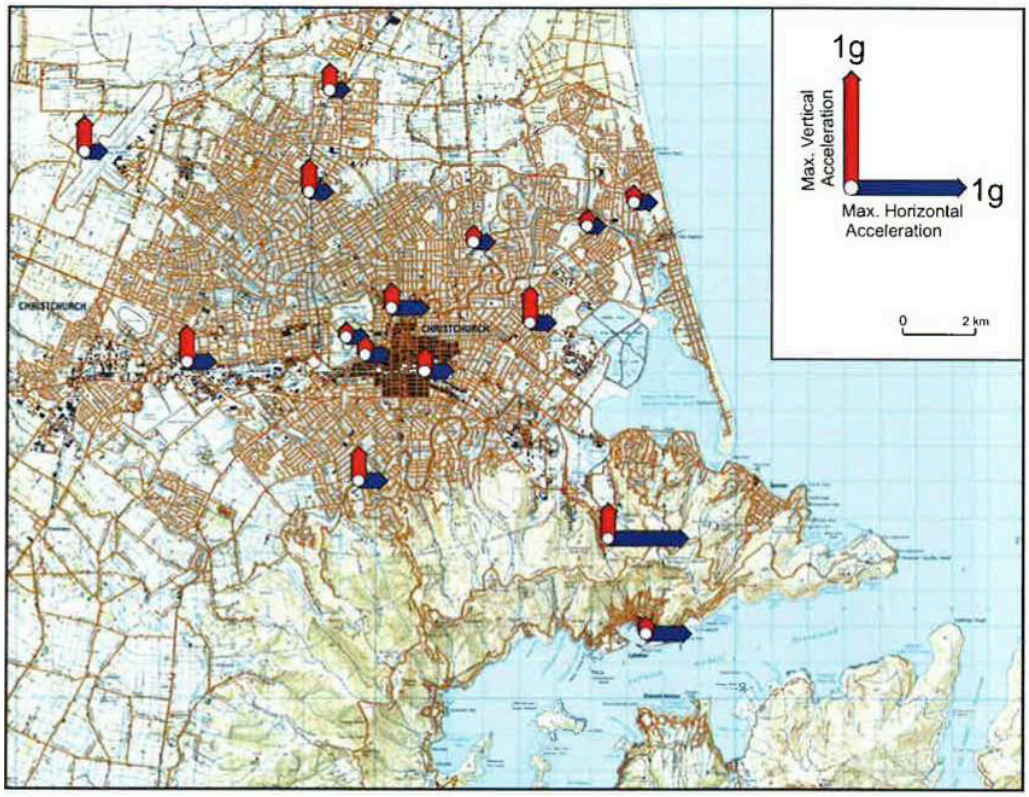

Figure 2.5: Maximum horizontal and vertical PGAs recorded during the 4 September 2010 Darfield Earthquake (Quake-Catcher Network, in Webb et al. 2011

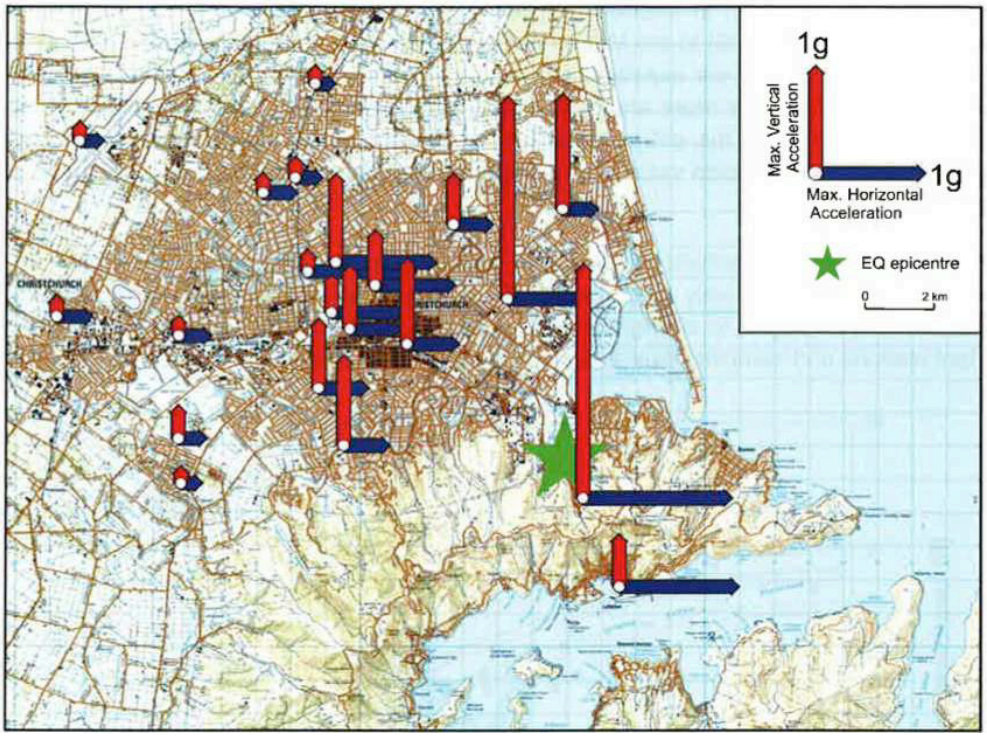

Figure 2.6: Maximum horizontal and vertical PGAs recorded during the 22 February 2011 Christchurch Earthquake (Quake-Catcher Network, in Webb et al. 2011).

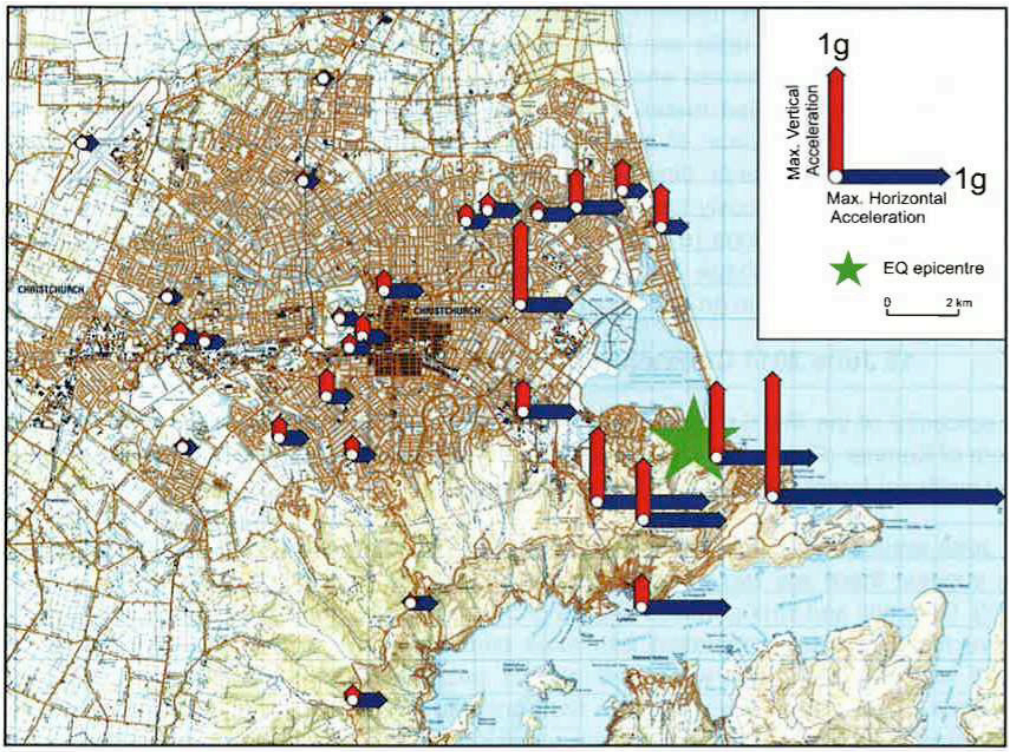

Figure 2.7: Maximum horizontal and vertical PGAs recorded during the 13 June 2011 Christchurch Earthquake (Quake-Catcher Network, in Webb et al. 2011).

2.5 Synthesis

- Naturally occurring rockfall events on Banks Peninsula prior to the Canterbury Earthquake sequence have been generally rare and localised.
- Rockfall occurences during the 4 September 2010 M_w7.1 Darfield Earthquake were few in number, and caused little damage.
- Widespread rockfall and cliff collapse was triggered by the high peak ground accelerations that occurred during the M_w6.3 22 February 2011 Christchurch Earthquake. These events caused five fatalities on Banks Peninsula, and were responsible for considerable damage to buildings and infrastructure in the area, with many residential dwellings destroyed or abandoned as a result of rockfall or cliff collapse damage. Cliff collapse occurred at Redcliffs, generating large amounts of debris at the base of the cliff.
- High PGA values during the M_w6.3 earthquake on 13 June 2011 caused additional devastating rockfall and cliff collapse on Banks Peninsula, including further cliff collapse at Redcliffs.
- PGA values during the M_w6.0 23 December 2011 aftershock were of similar magnitude to those recorded on Banks Peninsula during the Darfield Earthquake, and subsequently there is no evidence for large-scale failures.
- The critical PGA value above which rockfall and cliff collapse-type failures are likely to occur on Banks Peninsula is ~0.3-0.4g (Massey, McSaveney, Heron, & Lukovic 2012), although PGA is not the sole factor in determining if and how failure could occur.

3 Site Stratigraphy and Ignimbrite Recognition

3.1 Introduction

Basaltic ignimbrite observed at Redcliffs represents the first recorded example of this rock type on Banks Peninsula. The newly discovered ignimbrite unit was originally mapped in this study as a number of lava flows, however its correct nature was established through analysis of samples collected from the base of talus aprons formed by cliff collapse during the earthquakes on 22 February and 13 June 2011. Geological characteristics of this unit are presented in Section 3.5, with engineering geology properties and mapping presented in Chapter 4. This chapter describes site stratigraphy and ignimbrite recognition.

3.2 Site Stratigraphy

The site stratigraphy is relatively straightforward, in that a prominent orange tuff is exposed mid-height (~35m above ground level) and the volcanic units above and below are clearly layered and dip generally to the northeast at ~10° (Figure 3.1).

Figure 3.1: General view of the northeast facing cliff face at Redcliffs, photographed from Main Road on 4 April 2012. Note the orange tuff horizon exposed at mid-height, the channel-shaped structure in the centre-left, and the top of the large talus apron reaching the orange tuff near the centre of the photograph. Orange roof at left of centre is the now abandoned School Hall building.

Vertical elevation referred to within this thesis represents the height, in metres above ground level (AGL). This datum was set by the Terrestrial Laser Scanner (TLS) during data collection by GNS Science, and is regarded as the flat surface of the Redcliffs School Field. This location is approximately 10m above sea level (Google Earth 2012). TLS data and data collection methods are discussed in Chapter 5.

A simplified stratigraphic column (Figure 3.2) shows the relationships of the four main units found at Redcliffs. This includes a loess capping layer ≤3m thick that is not included in cross-sectional diagrams or face logs, as it was difficult to map on vertical photographs and is not a source of rockfall. The three bedrock units recognised in the simplified stratigraphy (Figure 3.2) are discussed below, starting from the largely unexposed base of the sequence at Redcliffs. Figure 3.3 shows a representative example of site stratigraphy at Redcliffs from an area of the cliff face behind the School Hall building, in particular focusing on the basaltic ignimbrite that overlies the orange tuff.

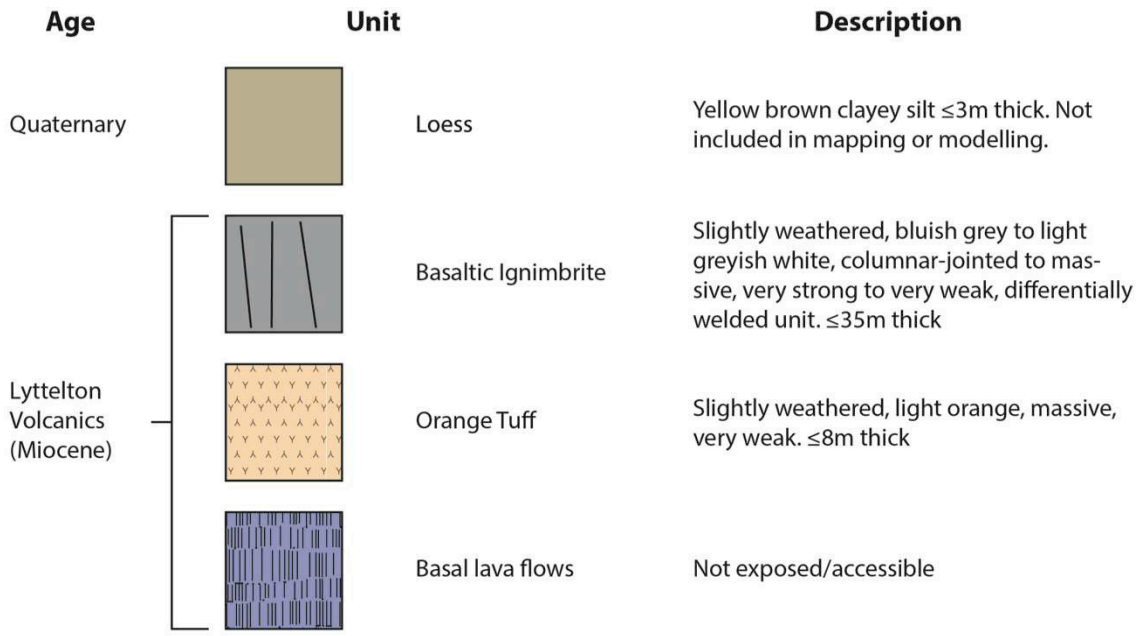

Figure 3.2: Simplified Redcliffs stratigraphy.

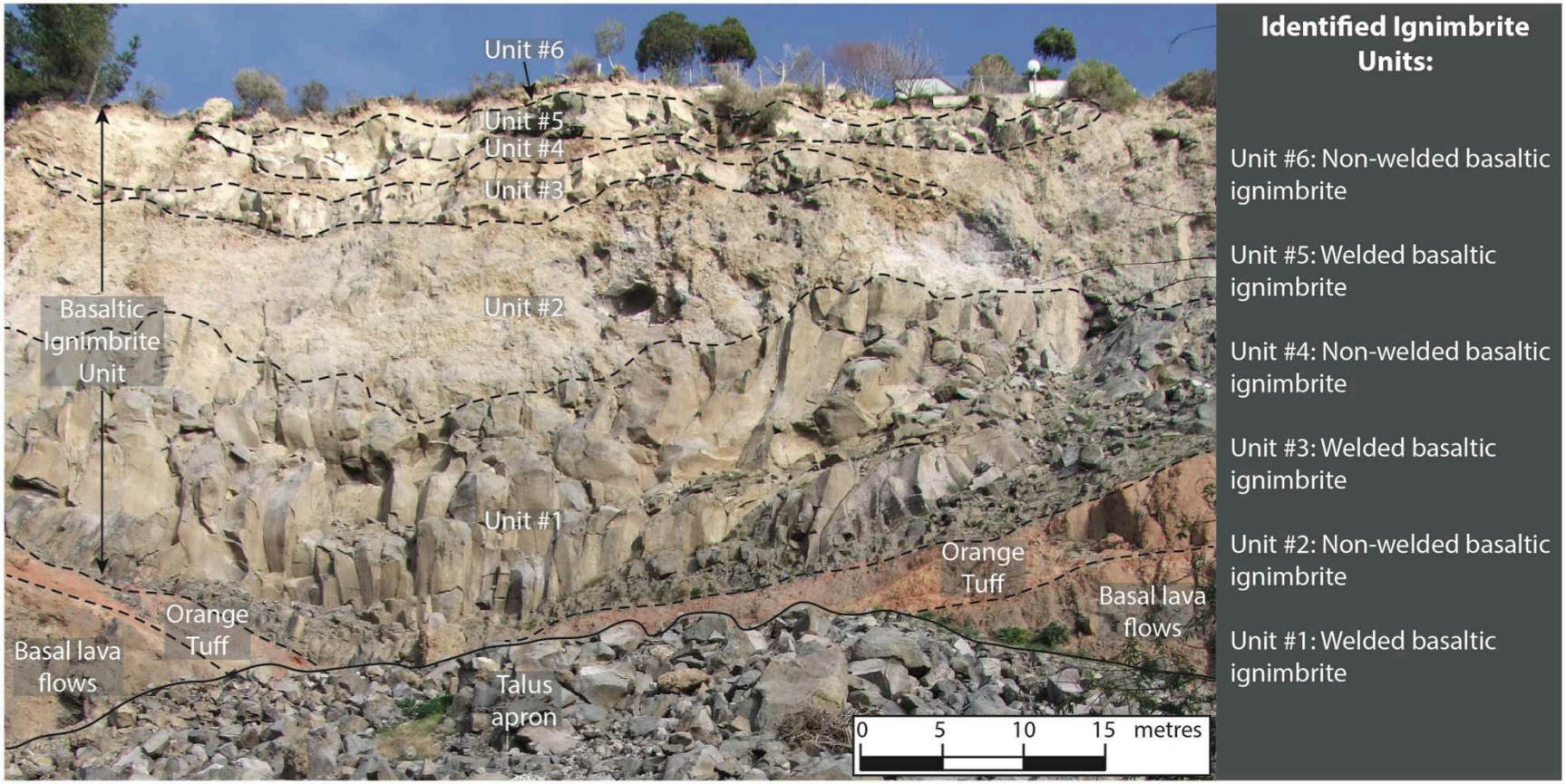

Figure 3.3: Photograph of the upper section of a representative outcrop at Redcliffs showing stratigraphic relationships in the cliff face behind the School Hall building. Individual ignimbrite units are identified within the basaltic ignimbrite unit.

As mentioned in Section 3.2, loess forms a capping layer that is widespread across Banks Peninsula and the wider Canterbury Plains. Work conducted by D. Bell (pers. comm. 2012) found the loess in the Redcliffs area to be ≤3m thick. An engineering geology description of the typical Port Hills Loess is:

> Yellow-brown CLAYEY-silt with some fine sand; firm; moist, low plasticity, dark brown mottled in top metre (D. Bell pers. comm. 2012)

The Port Hills Loess is not discussed further in this thesis as it not considered a rockfall source.

The three bedrock units are discussed in the following sections (3.3-3.5). The Redcliffs field area was divided into five sectors for mapping purposes (Figure 3.4). These sectors were based on separating major changes in cliff face orientation (ie. cliff geometry), as well as the location of unobstructed photographs, with geological relationships playing a lesser role. Engineering geology face logs of these sectors are discussed in Chapter 4.

3.3 Basal lava flows

Geological units below the orange tuff horizon have not been investigated in this research for two main reasons that are outlined below. According to Hampton (2010), an eruptive package of lavas from Lyttelton Volcano is well exposed in the former wave-cut sea cliffs of the Redcliffs area. These lavas are termed "Eruptive Package IX" in Hampton's work, and were formerly called the Mt Pleasant Formation by Sewell et al. (1992). This package of basaltic lavas is currently thought to form the lower unit(s) of the Redcliffs site, however this has not been confirmed due to safety-imposed access restrictions.

While it was possible to collect samples from the base of the talus at Redcliffs, it was not possible to collect samples from the cliff face itself. This posed the difficulty of clearly identifying the source area of a sample, based on broad physical characteristics and the end location at the base of a talus slope. Where units appeared distinctly different from those stratigraphically above and below, source areas were interpreted, as with collection of the

Figure 3.4: Sector location map.

basaltic ignimbrite samples. This was not so simple in the case of the lava flow units, as the units themselves do not appear very thick or laterally continuous. The presence of welded ignimbrite in close vertical proximity added to the complexity of accurately identifying the source area of fallen rock. This could lead to confusion around origins of rock samples within the chaotic sorting of the talus apron. Therefore, the only way to clearly constrain a block of this nature to its source area would be to collect it directly from the source.

From work by Bell & Crampton (1986) and Crampton (1985), these basal lava flows have been characterised as massive or rubbly basaltic lavas, or a combination of both, belonging to the Lyttelton Group. Engineering geology descriptions of both types are:

> **Massive basaltic lavas:** Slightly to moderately weathered; hard; grey to black; massive BASALTIC LAVA; slightly to highly vesicular, and porphyritic. At least 3 joint sets closely spaced; slightly to very rough; infilling ≤ 5mm thick of oxidised or highly weathered material; typical block size 100-300mm.
>
> **Rubbly basaltic lavas:** Slightly to moderately weathered clasts (up to boulder size) of massive BASALTIC lava (qv) in a matrix of slightly to highly weathered, soft to hard, greyish black and reddish mixture of silt, sand and gravel-sized fragments of BASALTIC lava. Not jointed, but may display rare random defects ≤ 2m in persistence.

The second and principal reason for not focusing on the units below the tuff horizon is due to their low elevation and subsequent proximity to the top of the talus. As a rockfall source area, this was considered to pose a much less important source compared to source areas above the tuff horizon. Based on the low source elevation, most of the blocks were not expected to travel far beyond the upper few metres of the talus or be prevented from releasing by the apron of debris that covers the rock faces.

3.4 Orange Tuff

The orange tuff unit is a crystal-rich, trachyandesite tuff that forms a distinctive horizon which can be traced continuously along the cliff face at Redcliffs (Figure 3.1). In the southeast corner of the field area, the orange tuff ramps up over an existing topographical high point created by existing volcanic units below. Beyond this, the orange tuff is difficult to trace continuously. In the northwest of the field area the tuff is obscured by the talus slope, however beyond the field area the horizon can be partially traced along the cliff face near Moa Bone Cave at approximately the same elevation and thickness.

At outcrop scale, based on high-resolution photographs taken from the base of the cliff, this tuff unit is comprised of a number of thin deposits that have been laid down in quick succession. This was observed through variation in colour and contact relationships between the different deposits. From the photographs, there was no evidence of soil deposition or other paleo-horizons indicative of a time break sufficient to form soils or deposit fluvial sediment between eruptive events.

Some deposits appeared to mantle topography, while others were more topographically constrained within channel structures or natural low points. The upper contact is variable and appears to be generally topographically controlled. This is further discussed in Section 4.4.3.

Clasts are angular to sub-rounded, consisting of lithic fragments, altered pyroxene minerals, scoria clasts, and small crystals (Figure 3.5). The matrix is fine to coarse grained. There are no visible structures in hand-specimen.

The orange tuff may be described geologically as follows:

> Massive to bedded, porphyritic rock containing altered and unaltered pyroclastic fragments including scoriaceous clasts and wall-rock lithics. Altered and unaltered crystals include pyroxene and plagioclase feldspar.

An engineering geology description of the orange tuff unit is presented in Section 4.4.

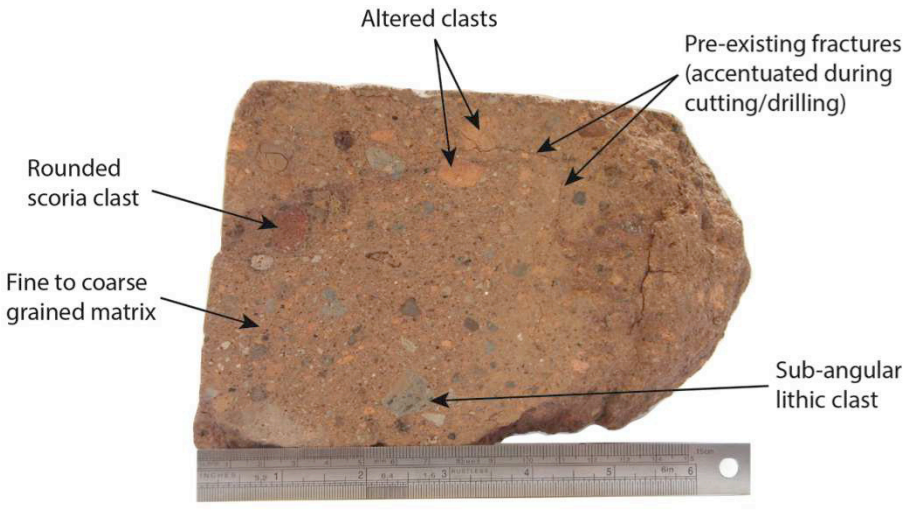

Figure 3.5: Example of orange tuff sample collected from Redcliffs 24 June 2012. Ruler for scale (150mm).

3.5 Basaltic Ignimbrite

3.5.1 Introduction

The unit overlying the orange tuff was originally mapped as a series of basaltic flows. However, on examining the debris shed from the upper cliff face, it was recognised that the unit was in fact a basaltic ignimbrite. Observations of this unit are presented in this section, with interpretation of features and their relevance to distinguishing this ignimbrite unit from a basaltic lava flow discussed in Section 3.7.

The basaltic ignimbrite unit directly overlies the orange tuff along the entire cliff exposure in Sectors 1, 2 and 3 (Figure 3.4). Engineering geology mapping of each of these three sectors is presented in Chapter 4. The basaltic ignimbrite dominates the cliff geology above the tuff horizon and is the main rockfall source material. As seen in Figure 3.1, the ignimbrite unit has a sharp, undulating basal contact with the orange tuff. Above this, the ignimbrite unit consists of a blue-grey, jointed basal section, grading into a whitish-grey, massive section above. In

places, thin bands of blue-grey, jointed material lie within the whitish-grey rock, such as the two bands in the centre-left in Figure 3.1. These thin bands of blue-grey rock are visible throughout the cliff face, and are discussed in detail in Section 3.7.4, and 4.4.1-4.4.3.

Using colour and jointing variation, as well as hand sample and thin section analysis, the two units described above have been interpreted to represent two end-member units within the basaltic ignimbrite: the blue-grey, jointed type is identified as a welded type, and the whitish-grey unit as a brecciated (non-welded) type. In this thesis, the terms welded and brecciated are used to mean the following:

- Welding refers to a rock showing distinctive cooling joints, with a smooth surface texture. Cooling joints may be variably spaced, and the orientation may also vary, however the primary orientation is sub-vertical. Blocks are commonly columnar or tabular shaped, and are typically up to $2m^3$ in volume.
- Brecciated refers to a non-welded unit that does not show distinct cooling joints, and as such commonly produces sub-angular to sub-rounded blocks of up to $25m^3$ in volume, however typically ~$2m^3$.

Rock comprising the ignimbrite unit at Redcliffs is considered as a continuum between the two units (welded and brecciated) as end members, with highly variable lithofacies in between. Examples of end member units are described in this section, with distinguishing characteristics and geological models discussed in Section 3.7.

3.5.2 Welded Basaltic Ignimbrite

The welded basaltic ignimbrite generally forms the lowest unit within the ignimbrite sequence, directly overlying a sharp, undulating orange tuff contact. The unit is generally blue-grey with a porphyritic texture. It consists of a fine, variably welded ash matrix, with small (<8mm), angular to sub-angular crystals, sub-angular to sub-rounded lithics (up to 40mm), and some small vesicles (<2mm) that are more common in less welded examples (Figure 3.6). There are no visible structures in blocks from hand-specimen size to >$10m^3$.

Where larger lithic clasts are visible (eg >20mm), their surface boundaries range from clear and well defined to indistinct. Causes of this clast boundary variation are discussed in Sections 3.7.3 and 3.6.

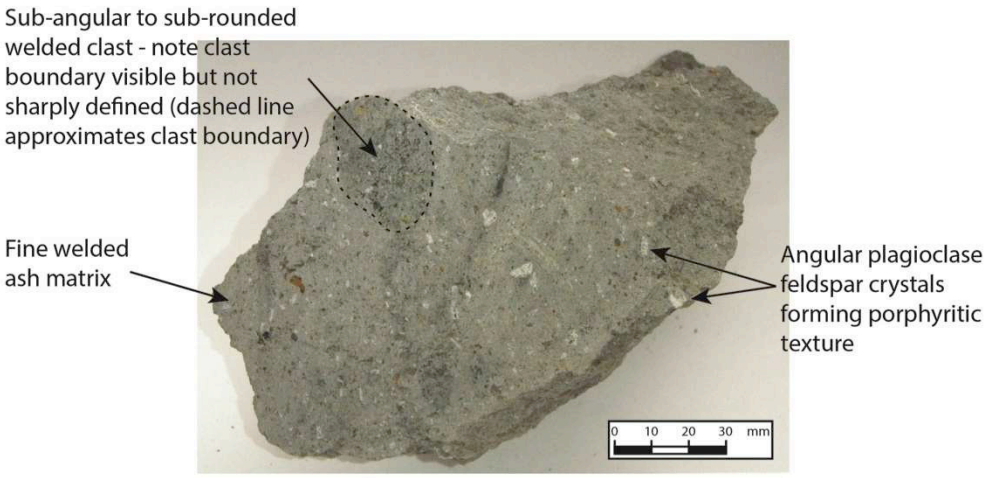

Figure 3.6: Welded basaltic ignimbrite sample (RCP2) collected from Redcliffs on 1 June 2012.

The welded basaltic ignimbrite may be described geologically as follows:

> Massive, porphyritic rock containing pyroclastic fragments including vesicular and non-vesicular clasts. The matrix consists of fine welded ash and contains plagioclase feldspar, olivine, and iddingsite phenocrysts.

An engineering geology description of the welded basaltic ignimbrite unit is presented in Section 4.4.1.

3.5.3 Brecciated (or non-welded) Basaltic Ignimbrite

The term brecciated is used here to describe the non-welded end member ignimbrite unit. The brecciated basaltic ignimbrite unit generally forms the upper portion of each ignimbrite unit at Redcliffs, with a variable thickness up to ~25m. Crude vertical joints are visible towards the northern end of the field area, and these are discussed in Section 3.7.4.

The unit is whitish-grey in hand specimen, with some brown-grey colouring visible at outcrop scale, and comprises a porphyritic texture consisting of fine-grained ash with angular to sub-rounded, crystals. Lithic clasts and fragments are abundant, ranging from fine lithic fragments <1mm in diameter, up to 120mm. Generally larger lithic clasts are ~50mm in diameter, angular to sub-rounded, scoriaceous or vesicular to welded (Figure 3.7). There are no visible structures in hand-specimen.

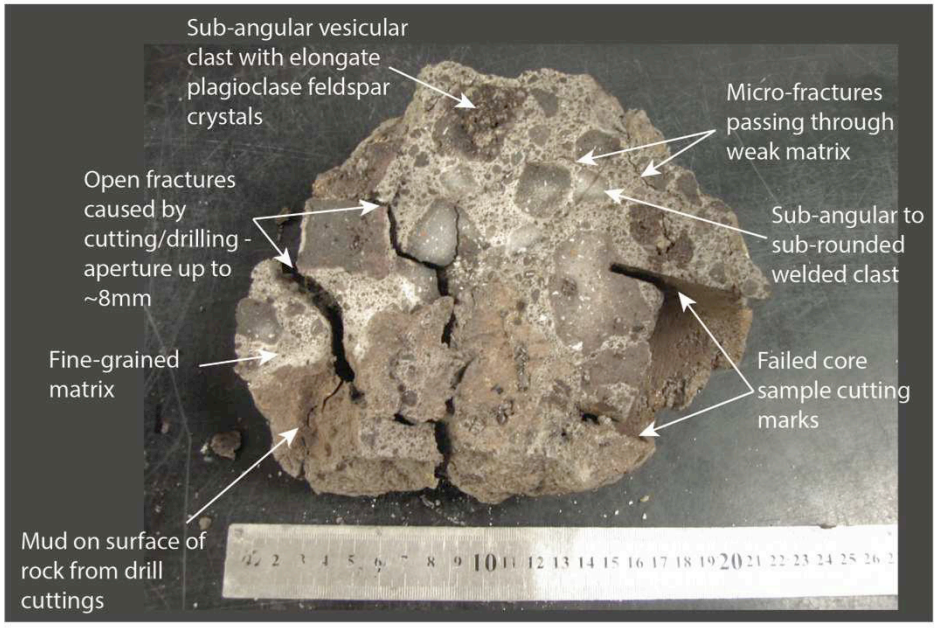

Figure 3.7: Brecciated basaltic ignimbrite sample collected from Redcliffs 1 June 2012. Ruler for scale (in centimetres).

The brecciated (non-welded) basaltic ignimbrite may be described geologically as follows:

> Massive, porphyritic rock containing pyroclastic fragments including vesicular/scoriaceous and non-vesicular clasts. The matrix consists of fine ash and contains plagioclase feldspar, olivine, and some iddingsite phenocrysts.

An engineering geology description of the welded basaltic ignimbrite unit is presented in Section 4.4.1.

3.6 Thin Section and Geochemical Analysis

3.6.1 Methodology

Samples used in thin section and geochemical analysis were from the same larger samples as used throughout the rest of this thesis. Collection of representative samples was undertaken on 1 and 22 June 2012. These samples were sourced from the toe of various talus aprons at Redcliffs. Thin section samples were cut from the larger samples, while X-Ray Diffraction (XRD) and X-Ray Fluorescence (XRF) geochemical testing was conducted on crushed bulk samples of the orange tuff (RC-T), brecciated basaltic ignimbrite (RCB1) and a welded basaltic ignimbrite example (RCP2). Lava flows stratigraphically below the orange tuff unit were not considered in this analysis as the lavas are not considered rockfall sources and were inaccessible in the field.

3.6.2 Thin Section Analysis

Samples of the orange tuff and the brecciated ignimbrite, and two samples of the welded ignimbrite were collected and thin sections produced (Figure 3.8). Analysis is presented at the scale of the slides as shown in Figure 3.8, rather than as viewed down a microscope. This is because alteration textures were more clearly visible at this scale, and therefore the variation between rock units is more obvious. Brief descriptions of composition and textures visible in thin section slides are presented in this section

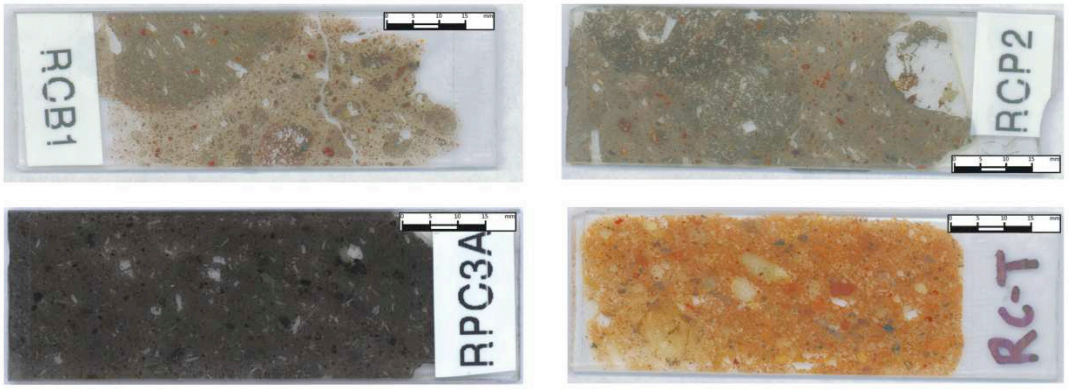

Figure 3.8: Example of thin section slides from Redcliffs. RCB1: Brecciated basaltic ignimbrite; RCP2 & RPC3A: welded basaltic ignimbrite; RC-T: Orange tuff. Scale bar on each slide is ~15mm long.

Of particular interest was the comparison between the brecciated and welded ignimbrites, as the increase in degree of welding was clearly evident in the thin section textures. The transition along the welding continuum was of interest to the modelling of rockfall at this site, because rock strength plays an important role in determining how a rock will behave during movement downslope.

Orange Tuff

The orange tuff thin section (RC-T) presented a crystal-rich texture amongst an orange groundmass that ranged from fine to moderately coarse. The characteristic orange colour dominated the groundmass, with larger crystals, clasts, and fragments of various colours within. Larger crystals were dominantly plagioclase feldspar, while the darker red clasts were commonly scoriaceous in nature. The large, bright orange clasts were altered feldspar minerals that weathered to clay. There was also a significant portion of light- to mid-grey clasts, and there was no visible alteration texture or dominant crystal alignment.

Light- to mid-grey clasts were most likely sourced from the conduit walls upon eruption [ref]. Given the lack of crystal alteration in either individual crystal shape or alignment as a whole rock texture, the texture of the orange tuff is consistent with a pyroclastic airfall deposit

Basaltic Ignimbrite

As mentioned, the transition from brecciated basaltic ignimbrite through to the most highly welded basaltic ignimbrite was clearly visible in thin section. This transition was gradational so thin sections presented in this analysis represented steps along the welding continuum. These examples were not presented as the complete spectrum of welding present at Redcliffs, merely to show the variation available during limited site reconnaissance. Further to this, there may be examples in the field that show greater variation than those presented, however this section presents what was found during this thesis study.

The brecciated basaltic ignimbrite (RCB1) showed large, clearly defined clasts within a coarse porphyritic groundmass containing large fragments and crystals. Plagioclase feldspar and olivine dominated the groundmass, with dark red, vesicular scoria clasts also common. A fracture was visible cutting through the groundmass within the thin section.

Welded basaltic ignimbrite examples were presented in order of increasing welding grade in slides RCP2 and RPC3A. RCP2 contained large clasts within a finer porphyritic groundmass, with the same minerals dominating. Clast boundaries were visible, but less well defined than RCB1.

RPC3A presents a porphyritic texture with large plagioclase feldspar and altered olivine crystals in a fine groundmass. In contrast to previous samples however, individual clasts and/or clast boundaries were not visible. This is indicative of a greater degree of welding, resulting in secondary alteration of components to form a more homogenous material (when compared to non-welded examples). Initial observation suggests the presence of iddingsite crystals, a product of olivine alteration, which could also be the result of a low temperature environment (Haggerty & Baker 1967) during and post emplacement.

3.6.3 Geochemical Analysis

Geochemical analysis was conducted on crushed bulk samples which meant that the analysis reflected the sample as a whole, rather than defining individual crystal constituents. Results of these compositional analyses are summarised in Table 3-1. This analysis clearly distinguished the orange tuff from the overlying ignimbrite units, suggesting an evolved magma chamber source. Geochemical plots showing all Redcliffs samples, as well as Lyttelton suite rocks are shown in Appendices 4.1 and 4.2.

Table 3-1: Summary of geochemical analysis.

Sample	Geochemical rock classification
Orange Tuff (RC-T)	Trachyandesite
Welded Ignimbrite	Picrite basalt
Brecciated Ignimbrite	Hawaiite

3.7 Ignimbrite Recognition

3.7.1 Background

Prior to the large-scale cliff collapse events that occurred in both February and June 2011, cliff exposures at the Redcliffs field area were generally limited to weathered bedrock covered in places by overhanging vegetation. Following these events, a far more unobstructed exposure is available at Redcliffs due to the removal of much of the established vegetation, as well as the removal of surficial weathered rock. This has allowed a more detailed investigation of the relationships between geological units, and recognition of the basaltic ignimbrite unit, which had not been previously recognised in the Banks Peninsula volcanic complex. The ignimbrite unit is considered to be the product of late stage volcanic activity from Lyttelton Volcano around 10Ma.

3.7.2 Geological Characteristics

Stratigraphic descriptions of the two end-member ignimbrite units (the columnar-jointed blue-grey welded material, and the massive light whitish grey brecciated material) have been presented in Section 3.5. The ignimbrite unit as a whole ranges from bluish-grey to light whitish grey in colour. It is massive, very strong to very weak, with very widely spaced (≤5m spacing) columnar-jointing, to extremely closely spaced (≤20mm), very narrow fractures (≤2mm estimated aperture).

Because the ignimbrite unit is interpreted to have been erupted as a series of small pulses from the same eruptive episode, the variability in characteristics is considered the result of different rates of cooling, visible in the rock units as differing degrees of welding. Welding of the ignimbrite refers to the "cohesion, deformation, and eventual coalescence of pyroclasts at high temperatures under loading stress" (Freundt et al. 2000). This interpretation is based on the units sharing similar geochemical composition (Section 3.6.3) as well as the variability in welding distribution throughout the cliff. Because welding is a product of the cooling rate of a pyroclastic flow, variation in welding creates variability in the rock mass, which is observed as both colour and joint spacing variation. These characteristics have been used to distinguish welded from non–welded ignimbrite units in the field.

3.7.3 Differential Welding

Differential welding describes the highly variable degree of welding present within the ignimbrite unit at Redcliffs. This variation formed the two end-member units, and the variably welded rock types between these members. The contrast between different levels of welding is presented both in this section at outcrop scale in the form of variable unit thicknesses and morphology, as well as in thin section (Section 3.6.2).

Welding of the basaltic ignimbrite was variable throughout the cliff exposure, with some rocks showing very low-grade, high-temperature-induced crystal alteration in a moderately coarse groundmass, while others show a very high degree of welding producing a very fine groundmass. This could represent variation in any of: magma composition, load stresses, and/or temperature (Freundt et al. 2000). Samples collected from the debris apron at the base of the talus show this variation, with degree of welding best exposed in thin section (Section 3.6.2).

Where thin bands or lenses of welded ignimbrite are surrounded by brecciated rock (Figure 3.1), this most likely represents smaller eruption pulses that followed shortly after the previous flows. The same cooling process occurs within these units, however on a smaller

scale due to less material having been erupted. Smaller eruptive pulses are visible in the engineering geology logs by their thin welded portions. Individual eruption pulses have not been identified within collected samples, as the chaotic nature of the talus makes this impossible.

Prismatic or columnar jointing is typical of welded ignimbrites (Freundt et al. 2000), with examples particularly similar to Redcliffs shown in basaltic ignimbrites at Tofua volcano, Tonga (Caulfield et al. 2011). The spacing of joints reflects the cooling rate, while the orientation is perpendicular to isotherms in the rock mass during cooling (Freundt et al. 2000). The Hokula ignimbrite from Tofua volcano presents a similar ignimbrite succession to that seen at Redcliffs, in that the jointing becomes more distinct as the welding grade increases. Figure 3.9 shows the similarity between the welded ignimbrites at these two localities. Other examples of characteristics that distinguish the welded ignimbrite from basaltic lava flows are presented in Section 3.7.4.

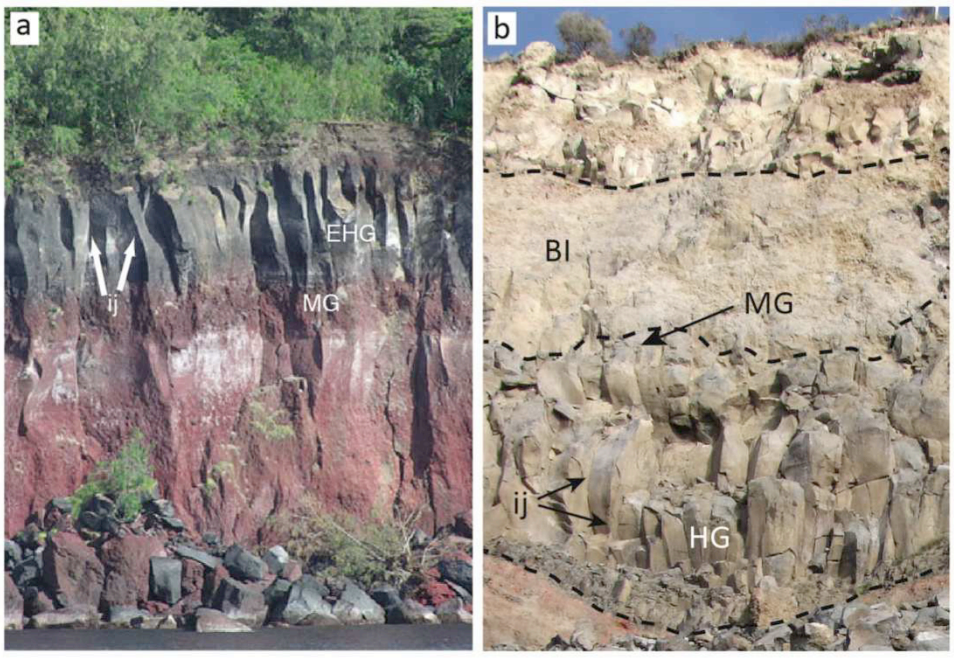

Figure 3.9: a) Hokula welded ignimbrite (Tonga) showing variation in welding from moderate grade (MG) to extremely high grade (EHG), Irregularly spaced joints (ij). Scarp is approximately 18m in height (Caulfield et al. 2011). b) Variation in welding at Redcliffs: Brecciated ignimbrite (BI), high grade (HG) and moderate grade (MG) welding; Irregularly-spaced jointing (ij). Field of view is approximately 35m in height.

3.7.4 Ignimbrite Characteristics

Prior to this thesis no other records of pyroclastic density currents, and therefore recognition of ignimbrite emplacement on Banks Peninsula, have been found. In support of this new discovery, a number of ignimbrite characteristics have been identified at Redcliffs which differentiate the deposits from lava flows (Figure 3.10). Some of the key defining features identified, which are discussed in the following sections, are as follows;

- Irregularly spaced jointing (cooling joints)
- Highly variable structures within lithofacies units that cannot be explained by topographically controlled lava flow deposits
- Lack of a basal breccia and the presence of a sharp basal contact
- Observation of a possible example of lithic lag breccia
- Fragmented scoria clasts
- Crude vertical cooling joints in an area of brecciated basaltic ignimbrite.

Irregularly spaced jointing (Location (a), Figure 3.10)

Irregularly spaced jointing is a key factor in distinguishing a welded pyroclastic deposit from a lava flow (Caulfield et al. 2011). This is of particular importance given the abundance of basaltic lava flows on Banks Peninsula. Figure 3.9 provides examples of irregularly spaced jointing in the Hokula welded ignimbrite (Tofua volcano, Tonga), and at Redcliffs. While jointing within the welded ignimbrite is highly variable in orientation and persistence, in geotechnical terms the spacing is considered quite regular. While this is more of a terminology issue, the comparison with evidence from Tofua in Tonga (Figure 3.8; Caulfield et al. 2011) shows clear similarities, suggesting an ignimbrite unit at Redcliffs above the orange tuff rather than lava flow units.

Highly variable structures (Location (b), Figure 3.10)

Because of the irregular jointing, it is clear that the welded lithofacies units are variable in both the vertical and horizontal direction, creating structures within the rock mass

that cannot be explained by a topographically controlled lava flow. An example is discussed in a later section (Section 4.4.3; Figure 4.7)

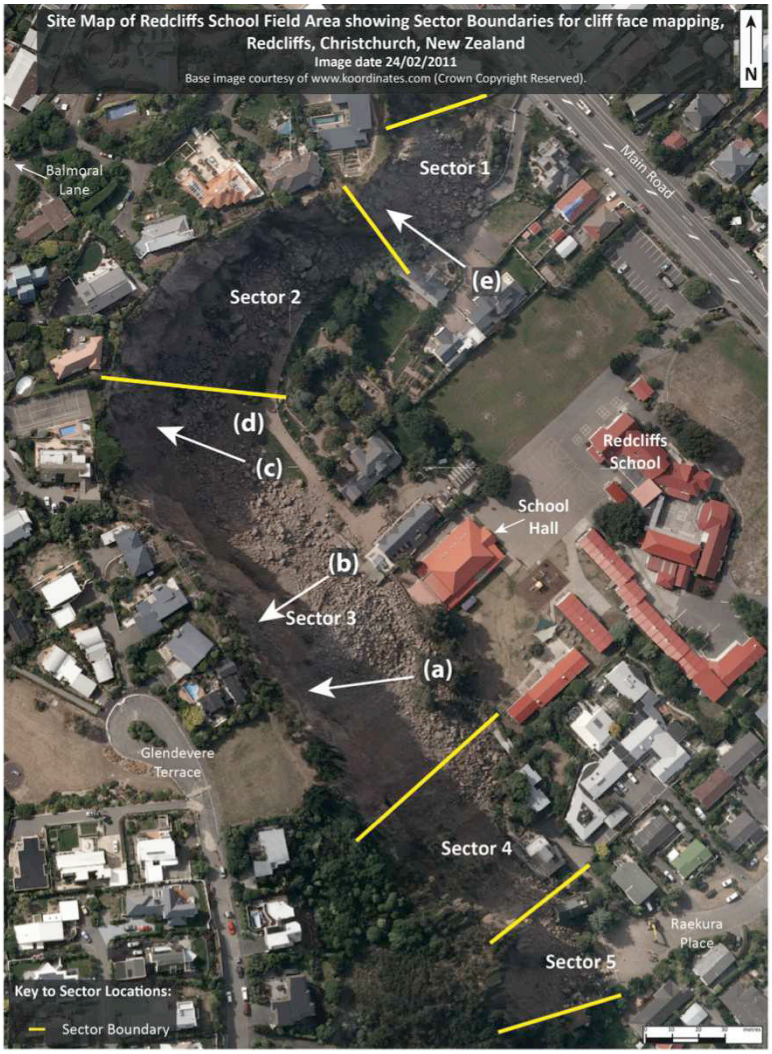

Figure 3.10: Approximate location of observed ignimbrite identification features. (a) Irregularly spaced jointing; (b) welded ignimbrite bands within brecciated ignimbrite; (c) sharp basal contact; (d) possible example of lithic lag in boulder at the base of the talus slope; (e) crude vertical cooling joints in brecciated ignimbrite (Sector 1).

Welded bands of ignimbrite in the upper section of the cliff face were observed, and these are discussed in greater detail in Section 4.4.1-4.4.3. The welded bands are fully surrounded by what appears to be brecciated basaltic ignimbrite, and the irregularity of the welded structures, both vertically and laterally, appear very complex. Given the brecciated ignimbrite

that surrounds both welded structures, the likelihood of eruption pulses alternating between explosive basaltic pyroclastic flows and basaltic lava flows was considered unrealistic to deposit the contrasting units. From this example, it was considered that individual pulses of pyroclastic eruptions cooling at different rates was more likely.

Welded ignimbrite grading into brecciated ignimbrite was also observed on a smaller scale, where individual brecciated basaltic ignimbrite boulders (up to ~25m^3) at the base of the talus slope contained thin (<0.3m thick), isolated "lenses" of welded material showing parallel joint sets. An example from a boulder at the base of the talus slope in Sector 1 is shown in Figure 3.11, where the lenses and jointing are indicated. The indistinct boundaries between welded lenses and brecciated material are further evidence of cooling-related variation on a larger scale to the welding textures observed in thin section (Section 3.6.2).

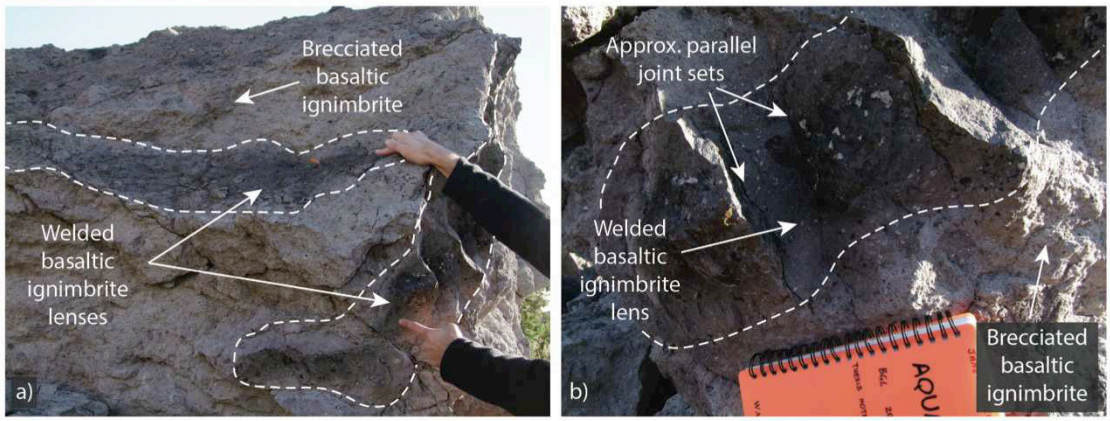

Figure 3.11: Welded basaltic ignimbrite lenses within brecciated basaltic ignimbrite, Sector 1, Redcliffs. Note dashed lines show approximate limit of welded rock.

a) Two lenses within brecciated basaltic ignimbrite boulder. Hands for scale.

b) Close-up photograph of lower lens (Figure a) from different angle showing jointing. Notebook for scale.

Lack of basal breccia (Location (c), Figure 3.10)

Where the ignimbrite unit directly overlies the orange tuff unit, the lack of a basal breccia (and instead the presence of a sharp basal contact) is also characteristic of a pyroclastic flow base. Evidence of the sharp basal contact can be seen in Figures 3.1 and 3.3. A basal breccia would be expected in an a'a flow, based on the basaltic lava found elsewhere in this area.

Lithic lag breccia (Location (d), Figure 3.10)

Based on large blocks at the base of the talus slope near the Sector 2-3 boundary (Figure 3.10), an example of a possible lithic lag breccia was identified from the base of the ignimbrite unit. A lithic breccia in a more distal zone is generally controlled by specific topographic conditions (Freundt et al. 2000), and therefore could be expected to be quite localised (compared to a proximal zone where a breccia rich in vent-derived rock would be expected). This could account for the isolated example found at Redcliffs. Further investigation of this phenomenon is an area of research that would benefit from being able to access the cliff face, as this could help to trace the source of this rock, and establish if there is in fact a lithic breccia exposed in situ.

Fragmented scoria clasts

The presence of fragmented scoria clasts within the ignimbrite suggests the explosive origins of a pyroclastic unit, with further fragmentation occurring during emplacement due to the high-speed nature of the downslope transport. Given the contrasting emplacement methods of a basaltic lava flow, these fragmented clasts would not be present.

Crude vertical cooling joints in brecciated unit (Location (e), Figure 3.10)

While the brecciated basaltic ignimbrite does not share many similarities with a lava flow unit, the association of the brecciated unit with the welded ignimbrite provides context to explain the presence of crude vertical cooling joints. These cooling structures were visible within the brecciated ignimbrite towards the northern end of the field area in Sector 1. The crude joints presented an interesting feature that was of significance to the behavior of the rockmass. This is interpreted to represent very low grade welding of the upper portion of an emplaced pyroclastic flow unit. These structures were generally constrained to the lower ~13m of the breccia, below the thin welded band near the top of the cliff, with the latter representing a later eruptive pulse. The later eruption pulse was likely emplaced shortly after the first, which could explain these cooling structures. The renewed heat source from above would slow the

cooling that propagates from the exposed surface of the deposit. Once again, this is an area that would benefit from more detailed investigation.

3.7.5 Ignimbrite Emplacement Mechanism

The current hypothesis for the emplacement of the Redcliffs basaltic ignimbrite units is based on the model proposed for emplacement of the mafic Villa Senni Eruption Unit (VSEU) ignimbrite succession from Colli Albani volcano, Italy (Watkins et al. 2002). As the emplacement mechanism does not directly affect future rockfall runout at this site, it has not been a major focus of this research. It is hoped that future research on the emplacement mechanism at Redcliffs could provide wider application of the current research on other areas, namely the nearby suburb of Sumner in Canterbury.

According to the model presented in Figure 3.12, strong similarities can be observed between the morphology of the flow base at Colli Albani and at Redcliffs. This is interpreted to suggest the pyroclastic density current that formed the ignimbrite succession at Redcliffs did so by initially filling a preexisting valley structure in the landscape, thus being constrained by the valley sides. The flow base is controlled by the morphology of the eroded valley system as can be interpreted from the variable ignimbrite base shown in Figure 3.1, and in mapping of Sector 3 (Section 4.3.3).

3.8 Synthesis

The geology of the exposed cliff sections at Redcliffs is relatively simple, with an upper ignimbrite separated from the lower volcanics by an orange tuff unit. The units dip at ~10° to the northeast, and the following have been identified:

1. The basal lava flows could not be accessed, and samples could not be collected. These have been described from earlier studies (e.g. Hampton 2010) as a sequence of basaltic lava flows.

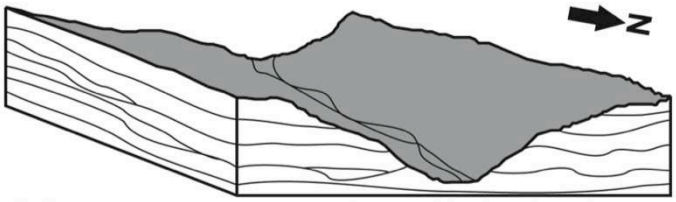

A) Eroded valley system on the flanks of the Lyttelton Volcanic Complex. Incision of stratified lava flows, accompanied by deposition of volcanogenic sediments. Later explosive eruptions forming airfall ash horizons, mantling topography.

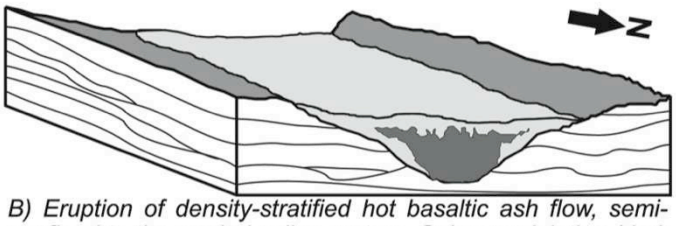

B) Eruption of density-stratified hot basaltic ash flow, semi-confined to the eroded valley system. Columnar jointing (dark grey) more welded than surrounding breccia (light grey), variation in welding due to thickness relationships and topographic control

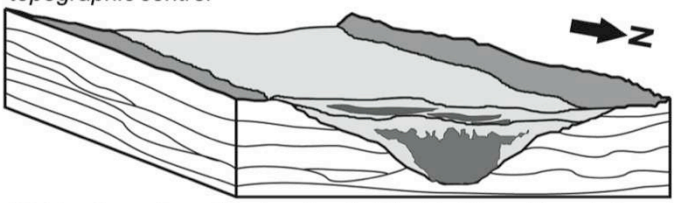

C) Eruption of smaller density stratified hot basaltic ash flows. Flows are confined to the upper surface of the infilling eroded valley system, lenses of more welded basaltic ignimbrite formed in small scour channels of previous ignimbrite.

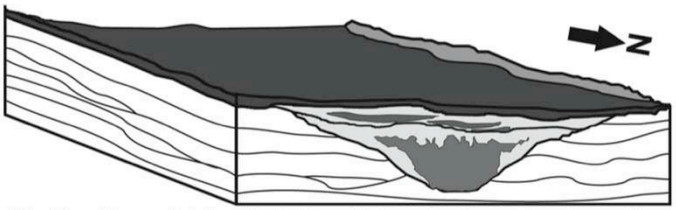

D) Eruption of later Lyttelton Volcanic Complex lava flow sequence.

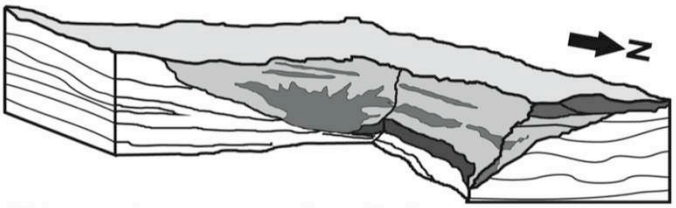

E) Present day exposure at Redcliffs. Subsequent erosion, due to sea level fluctuations, resulted in preferential erosion to the brecciated and columnar units on the eastern side of the exposure, forming the 'L-shaped' cliff aspect.

Figure 3.12: Current model of basaltic ignimbrite emplacement mechanism at Redcliffs, showing valley filling and later erosion forming "L-shaped" cliff aspect of the present day (Sam Hampton, unpublshed).

2. The orange tuff unit is exposed in the central part of the face, with a bench ≤3m wide on the northeast-facing slope (Sector 3). It consists of weak to very weak (≤4MPa) trachyandesite airfall deposits, and has widely spaced jointing, some of which is probably earthquake induced.
3. The upper unit is interpreted as a basaltic ignimbrite that is variably welded and brecciated. The total thickness of the ignimbrite unit is ~35m, and this is the primary source area for rockfall.
4. The overlying loess is ≤3m thick and is described as clayey silt. It has not been investigated because of access difficulties, and it is not considered relevant to the rockfall analysis project.

4 Engineering Geology Model & Geotechnical Testing

4.1 Introduction

This chapter builds on information regarding the stratigraphy and key geological properties, as outlined in Chapter 3, and develops an engineering geology model for the Redcliffs field area. The critical component of this chapter is the engineering geology face logs, and the associated discussion of geological controls in the principal rockfall source area. These face logs clearly illustrate the broad-scale engineering geology properties present at Redcliffs, which form the basis of the rockfall model used in Chapters 5 and 6. Results of geotechnical testing of the orange tuff and the two basaltic ignimbrite units (welded and non-welded) are also discussed, as they relate to rockfall runout behaviour.

4.2 Methodology

Due to the significant rockfall hazards present at the field site, engineering geology mapping relied on high-resolution vertical photographs taken from a distance of 50-150m from the cliff face. These photographs, used in conjunction with field observations, formed the basis of studying lithological relationships within the cliff faces. Where possible representative samples were collected for laboratory testing, and results are presented in Section 4.5.

The majority of the detailed face photographs were taken over the period April to June 2012, although reference was made to photographs taken before this period, including those taken during limited reconnaissance from as early as May 2011. Selected photographs have been joined together using free panorama stitching software available online. From these panoramic images and field observations, lithological relationships were mapped using Adobe® Illustrator® CS 5.1 (vector graphics editing software). Due to the residential setting of the field area, clear line-of-sight photography was not always available. Where exposure of

the face was obscured, photographs from different viewpoints were used to complete the maps. This is indicated with a dashed line and is specified on the map legend.

Due to the maps often comprising a combination of a number of wide-angle photographs spanning a considerable lateral distance, some distortion has occurred. The panorama stitching software has built in corrections to reduce "bending" of images along the length of the panorama, however perspective may still be somewhat misleading in places. As such, map scales are approximate, as geo-referenced survey points were not available within the failed areas.

Geotechnical testing was conducted on representative samples of the orange tuff unit, and three basaltic ignimbrite samples that were collected from the base of the talus slope. The uniaxial compressive strength of the orange tuff and two welded basaltic ignimbrite samples were tested for from core, however the very weak basaltic ignimbrite unit relied upon estimates from point load testing. This testing is further discussed in Section 4.5

4.3 Engineering Geology Face Mapping

4.3.1 Base Photographs

The high-resolution photographs used as the basis of engineering geology mapping were taken from a variety of distances and angles from the face, as well as under different lighting conditions. The variable angles and lighting were important to observe initially less obvious features, where bright exposure conditions and a viewpoint perpendicular to the face made some features difficult to see. For interpretation and mapping, photographs were used individually or stitched together to create large panoramic images. The panoramic images provided the best method for documenting the lateral extent of different geological units, and provided an overall perspective of the cliff face, even allowing for scale distortion .

4.3.2 Engineering Geology Maps

As discussed in Section 3.3, the Redcliffs field area was divided into five sectors for mapping purposes (reproduced in Figure 4.1 as for Figure 3.4). Engineering geology face maps of Sectors 1-3 are presented in Figure 4.2, Figure 4.4 and Figure 4.3 respectively.

Engineering geology face maps were produced using high-resolution photographs captured in the field. Mapping consisted of documenting two main components:

- Lithological relationships
- Dominant fracture patterns/joint sets

This was achieved by mapping both interpreted lithological boundaries and visible fractures onto vertical cliff face photographs ("base photographs"). These features were then converted into engineering geology face logs that could be viewed independently of the base photograph. No attempt has been made to generate stereonet plots from the remote data, as that was not considered necessary to estimate block sizes in future rockfall events.

The focus area for mapping and subsequent rockfall modelling was constrained to Sectors 1-3 (Figure 4.1). Sectors 4-5 were included in initial field reconnaissance mapping, but due to different and more complex geology as well as time constraints, these two Sectors were excluded from future detailed analysis and RocFall™ modelling. Sector 4 was largely unaffected by cliff collapse, with only localised rockfall in places. Because of the lack of disturbance, the cliff face and lower slope area was vegetated, obscuring view in some areas, and the geology appeared to be becoming more complex towards the south-east. Sector 5 was more complex again, with units at this site lying stratigraphically above the main Redcliffs succession.

Figure 4.1: Sector boundaries as used for mapping.

4.4 Engineering Geology Face Logs

4.4.1 Sector 1

Introduction

Sector 1 is the most northerly sector within the field area (Figure 4.1). As shown in the engineering geology face log (Figure 4.2), the area consists of a thick basal unit of orange tuff (up to 8m exposed thickness), overlain by up to 7m of variably welded basaltic ignimbrite,

and grading upwards into ~16m thick brecciated basaltic ignimbrite. Both the orange tuff and the welded basal portion of the basaltic ignimbrite were obscured by ignimbrite talus for much of the exposed length. Where exposures were not obscured, access to the basal section was limited due to safety, and therefore the basal contact of the tuff could not observed for the full length of Sector 1.

Orange Tuff

Due to the orange tuff generally being obscured by talus in this sector, engineering geological observations are limited. Orange tuff was not observed in the talus slope in Sector 1, rather this was generally comprised of basaltic ignimbrite material. Based on field observation of the unit in this sector, combined with observations of the other two sectors, an engineering geology description of this unit is:

> Slightly to moderately weathered, light reddish orange, massive to thickly bedded TUFF; very weak; sub-vertical, widely to very widely spaced fractures.

Geological features, including thin section and geochemical analysis have been presented in Chapter 3, and are not considered further in the context of rockfall sources.

Basaltic Ignimbrite

The basaltic ignimbrite unit can be divided into two distinct units based on field observation, and due to colour and joint intensity variation. An engineering geology description of the type example for the welded basaltic ignimbrite lithofacies unit is:

> Slightly weathered, blue-grey, massive IGNIMBRITE; very strong; sub-vertical, widely to very spaced, smooth planar, narrow cooling joints.

An engineering geology description of the brecciated basaltic ignimrbite is:

> Slightly weathered, light whitish-grey, massive IGNIMBRITE; very weak, with extremely closely spaced, very narrow earthquake-induced fractures.

The prominent feature of this sector is the crudely columnar features within the brecciated basaltic ignimbrite (Figure 4.2; Section 3.3.4). These formed distinctive features on the cliff face where columns of rock were exposed in situ, with toppled blocks visible near the top of the talus. Columns appeared to have formed where sub-vertical fractures propagated to the free face. The aperture of these fractures could not be physically measured, however from photographs of the site, widths of the order of hundreds of millimetres were common.

As shown on the engineering geology face log (Figure 4.2), a thin zone of welded ignimbrite was interpreted near the top of the brecciated basaltic ignimbrite. The band was approximately 1m thick and represented an example of the highly variable welding conditions present during formation of this unit.

Strongly prismoidal blocks of welded basaltic ignimbrite were visible below the brecciated ignimbrite and in the talus, although the blocks were considerably smaller than the large brecciated boulders (<0.3-3m^3 compared to up to non-welded blocks up to ~25m^3). Variability of welding was evident in the field by colour, texture, and joint spacing. Prismoidal blocks were more commonly visible in the upper ~3m of the welded part, in contrast to the more massive lower ~4m where the unit overlay the orange tuff. Welding variability has been discussed in Section 3.7.3 and 3.7.4.

Sector 1 Face Log, Redcliffs

Image date April 2012

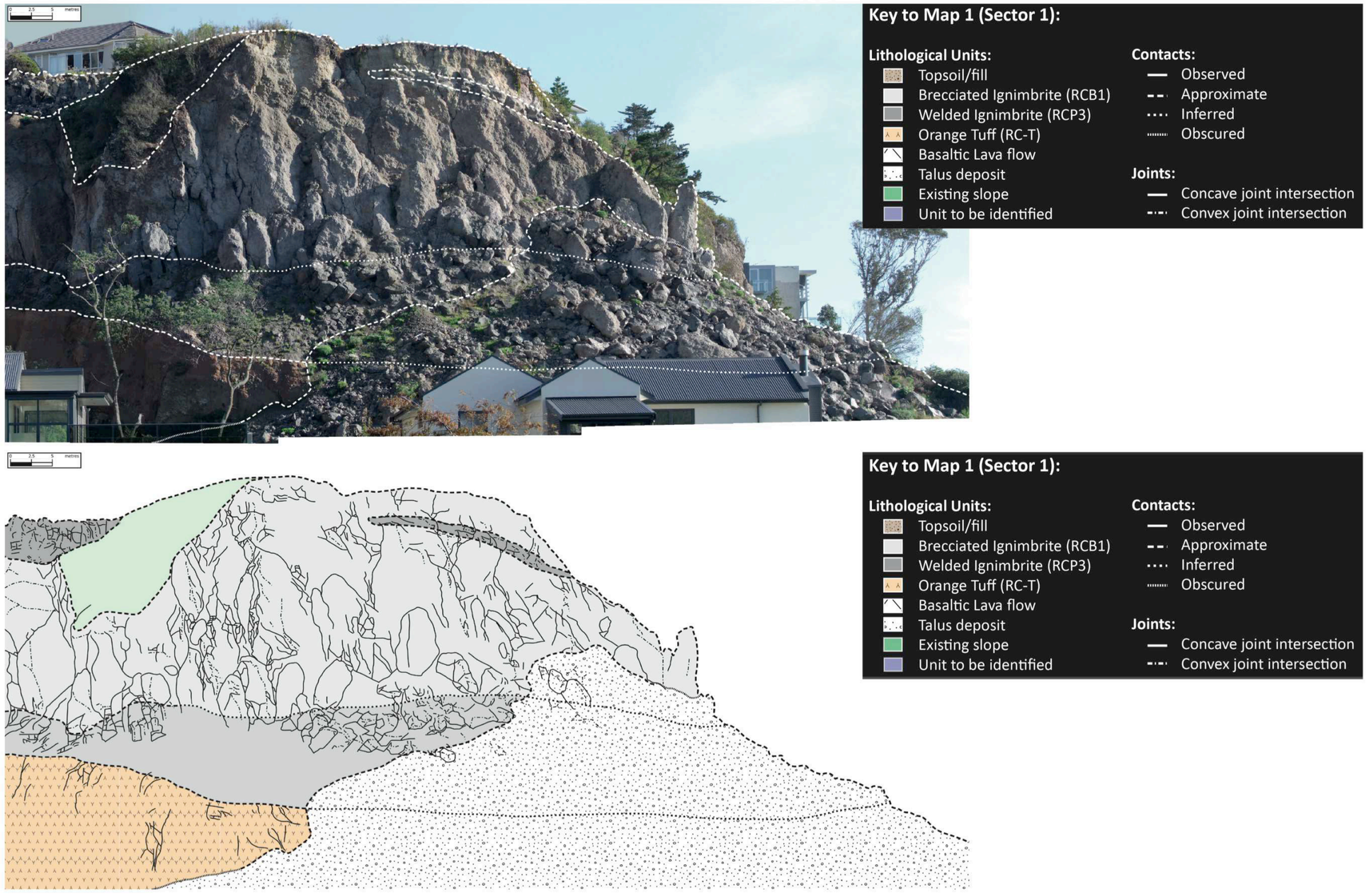

Figure 4.2: Sector 1 vertical base photograph showing interpreted lithological boundaries (upper image); and engineering geology face log (lower image). Map scales are approximate.

4.4.2 Sector 2

Introduction

Sector 2 presented a more geologically complex area than Sector 1 due to the increased variability and interlayering of welded ignimbrite within brecciated ignimbrite material (Figure 4.3), as well as a ~45° change in cliff orientation. A steep talus apron obscured most of the units below the orange tuff. A unit was visible outcropping below the orange tuff towards the southwestern end of the sector with <5m exposed thickness, as indicated by blue shading in Figure 4.3. This unit appeared to be strongly fractured, with an irregular upper contact surface. However, more detailed investigation was not possible because of its positioning on the cliff.

Orange Tuff

The orange tuff was observed to be approximately 10m thick near the boundary with Sector 1, and the lower contact is largely obscured by talus throughout the rest of Sector 2. A number of sub-vertical fractures were observed in the orange tuff unit, with some forming wedge- to cubic-shaped blocks up to ~120m^3 (Figure 4.4). This could create the potential for larger scale wedge-failures in the future depending on defect orientation and geotechnical characteristics, discussion of which is not within the scope of this thesis. As in other areas, measurements of fracture aperture was not possible due to safety restrictions, however from the engineering geology face log, aperture range was estimated to be up to 200mm. Fractures also appeared to cut across lithlogical contacts in places, and could be traced from the orange tuff into the base of the welded basaltic ignimbrite that overlay it.

Sector 2 Face Log, Redcliffs

Image date April 2012

Key to Map 2 (Sector 2): **Engineering Geology Face Log**

Lithological Units:
- Loess/Topsoil
- Brecciated Ignimbrite (RCB1)
- Welded Ignimbrite
- Orange Tuff (RC-T)
- Basaltic Lava flow
- Talus deposit
- Pre-existing slope
- Unit not identified (obscured)

Contacts:
- Observed
- Approximate
- Inferred
- Obscured

Joints:
- Concave joint intersection
- Convex joint intersection

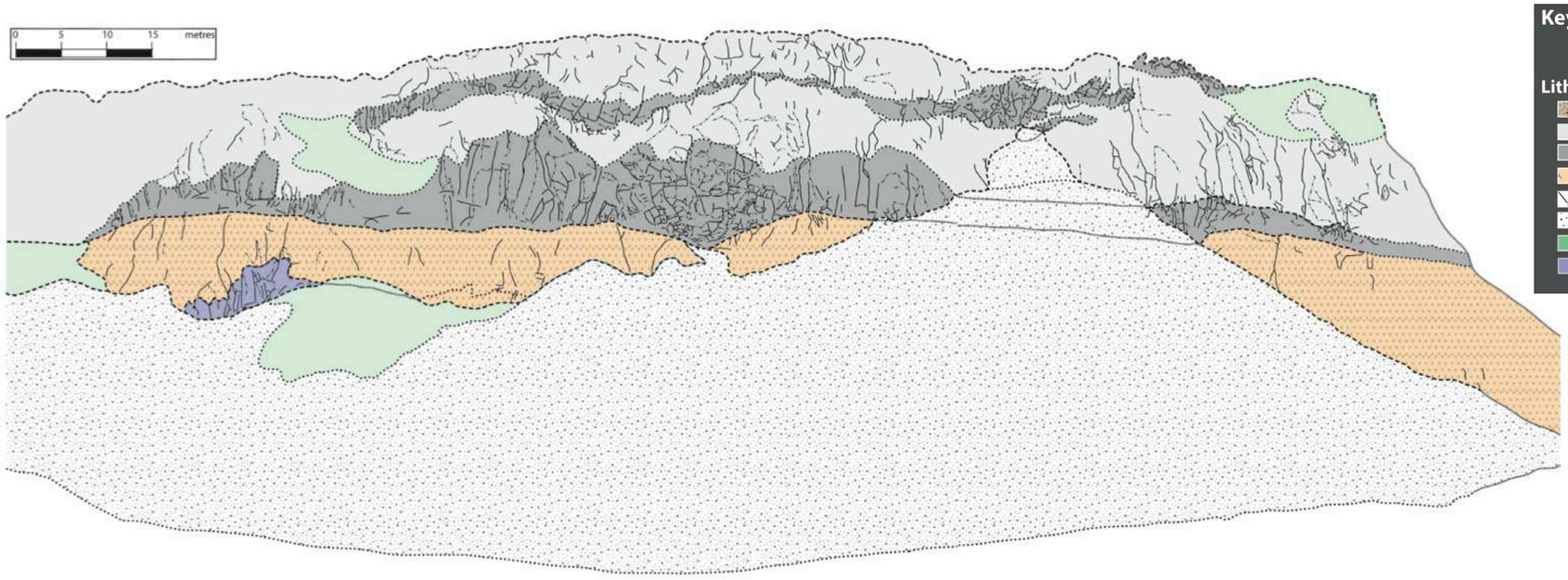

Key to Map 2 (Sector 2): **Engineering Geology Face Log**

Lithological Units:
- Loess/Topsoil
- Brecciated Ignimbrite (RCB1)
- Welded Ignimbrite
- Orange Tuff (RC-T)
- Basaltic Lava flow
- Talus deposit
- Pre-existing slope
- Unit not identified (obscured)

Contacts:
- Observed
- Approximate
- Inferred
- Obscured

Joints:
- Concave joint intersection
- Convex joint intersection

Figure 4.3: Sector 2 vertical base photograph showing interpreted lithological boundaries (upper image); and engineering geology face log (lower image). Map scales are approximate.

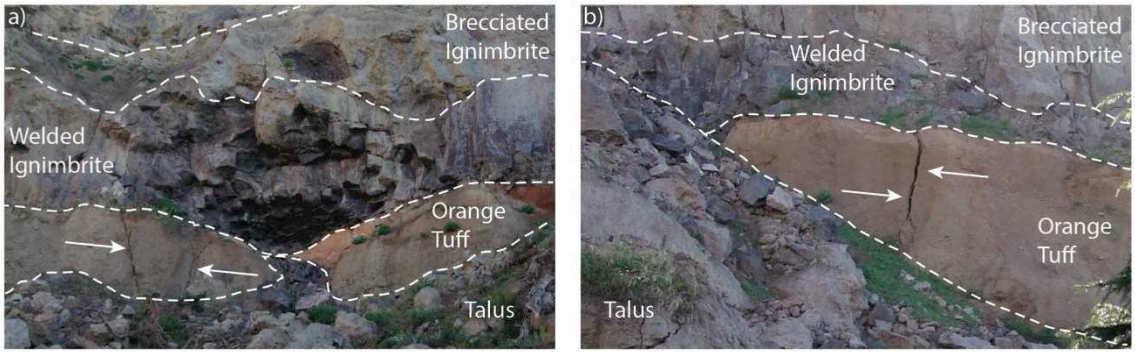

Figure 4.4: Earthquake-shaking induced fractures (indicated by white arrows) within orange tuff unit in Sector 2.

(a) Wedge-shaped block overlain by closely jointed overhanging section of welded ignimbrite. Note lateral variation within welded unit with closely columnar jointed rock (centre) adjacent to very widely spaced joints. Centre of orange tuff unit is obscured by a the top of the talus slope. Field of view ~35m (horizontal).

b) Cubic-shaped block in orange tuff. Note also sharp basal contact of welded ignimbrite. Field of view ~25m (horizontal).

Basaltic Ignimbrite

Overlying the orange tuff, the welded basaltic ignimbrite displays joint spacing in the range of ~0.5-5m, which is interpreted to represent variation in welding because of variable cooling rates (Section 3.7.2). An example of this variability is visible near the centre of the mapped sector, where joint spacing is predominantly ~0.5-1m, however adjacent to this joint spacing is up to 5m wide (Figure 4.3; Figure 4.4). The closely jointed area is approximately 30m wide and 10m high, featuring an overhanging section caused by undercutting of more closely spaced curved joints giving columnar-shaped blocks.

As mentioned, the upper surface of the welded ignimbrite was highly variable, creating a unit that ranged in thickness from ~2 to 12m. Given the remote investigation methods used to interpret the geological relationships, the accuracy of lithological boundaries particularly in this Sector, must be considered approximate.

Above the main welded ignimbrite section, brecciated basaltic ignimbrite was interpreted to comprise the remaining thickness of the cliff, together with a lense of welded ignimbrite. As with the main welded portion, this lense was highly variable in thickness and elevation, ranging from <0.5 to 5m thick. Near the centre of the sector, the lense appeared to almost pinch-out (Figure 4.3), however further to the east the lense was approximately 5m thick. Still further east no welded ignimbrite was observed in Sector 2.

Vegetated Slopes

A feature of Sector 2 was the presence of vegetated slope surfaces that pre-date the February 2011 cliff collapse sequence, and these do not appear to have been disturbed or buried by fallen material. Given the fresh, unweathered surfaces above these vegetated areas, it appears some failure has occurred, however fallen material was most likely of a smaller block size than in adjacent areas of the cliff. The slope surfaces that pre-date the cliff collapse sequence also appeared quite steep, so any material that landed on them most likely continued downslope without coming to rest there.

4.4.3 Sector 3

Introduction

Sector 3 covered the largest segment of the cliff in the field area (Figure 4.1), and was dominated by extensive talus slopes, with thick ignimbrite deposits and variable jointing in the welded unit above the orange tuff (Figure 4.5). The lowest units visible were the probable lava flows. Although not accessed, these were well exposed in places, but samples from these units were not able to be identified in the talus deposits due to the chaotic sorting. Up to three individual lava flows were identified,

but these had low lateral persistence and could not be traced continuously across the cliff face.

Orange Tuff

Above the basal lava flow units, the orange tuff provided a distinct marker-horizon that could be traced for the full length of Sector 3. As described in Section 3.2.2 this unit consisted of a series of thin, on-lapping deposits creating a topographically-controlled unit. In particular, this was seen above the main talus slope behind the School Hall, where the orange tuff was deposited into a pre-existing channel structure ~60m wide incised in the underlying unit(s) (Figure 4.6).

Fracturing within the tuff was generally randomly oriented and very widely spaced in Sector 3, and represented a less well jointed unit than in Sector 2. This could be due the ~90° change in cliff orientation, which would have reduced the impact of the earthquake shaking direction by having the shaking directed perpendicular to, rather than in the direction of the free face.

A feature of the tuff that was particularly prominent in parts of Sector 3 was a sloping bench structure formed by the orange tuff. In places this bench was estimated to be up to ~3m wide, although it was less prominent in other areas, particularly behind the School Hall where it was largely concealed by the top of the talus slope.

Sector 3 Face Log, Redcliffs

Image date April 2012

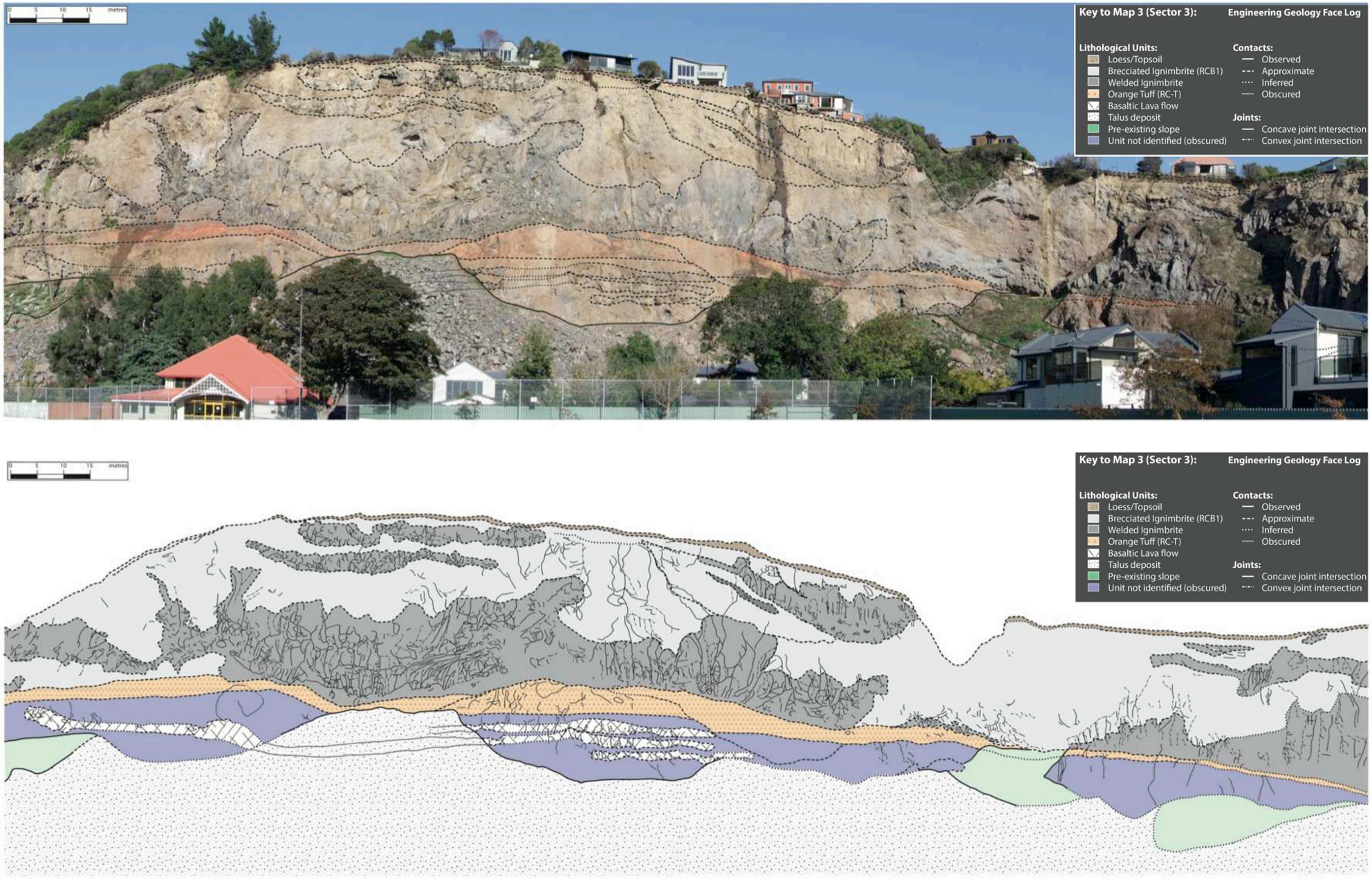

Figure 4.5: Sector 3 vertical base photograph showing interpreted lithological boundaries (upper image); and engineering geology face log (lower image). Map scales are approximate.

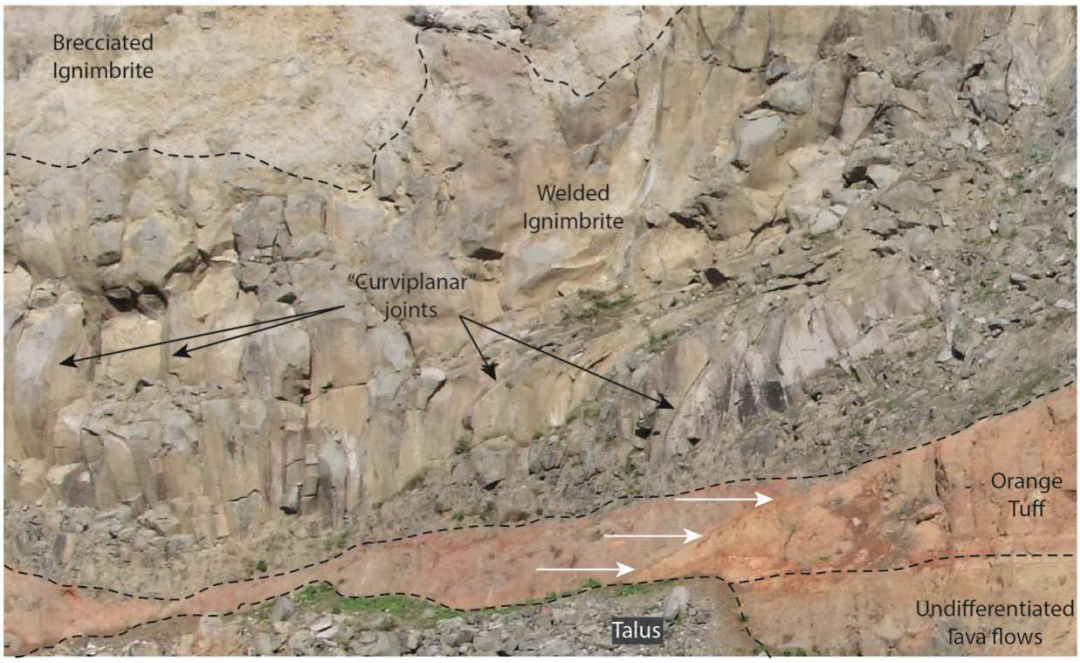

Figure 4.6: Structures visible in Sector 3. Onlap structure within orange tuff unit indicated by white arrows (centre-bottom). Examples of curviplanar joints in welded unit indicated by black arrows. Note sharp basal contact of welded ignimbrite. Field of view ~38m (horizontal).

Basaltic Ignimbrite

From ~35m AGL to the top of the cliff (~70m AGL), basaltic ignimbrite dominated the cliff profile. On average the blue-grey welded part was ~14m thick, above which the brecciated basaltic ignimbrite averaged ~14m thick. Above this, two welded bands of basaltic ignimbrite were interlayered with the brecciated material creating a total thickness of around 7m. The welded lower portion of the ignimbrite unit showed closely spaced, columnar jointing, particularly in the thickest section behind the School Hall. Jointing frequently curved upwards, while joints curved towards horizontal in some places. (Figure 4.6) The overlying brecciated material appeared generally massive, with isolated fractures visible in places.

The variability in welding created an unusual appearance to this part of the cliff face due to the highly changeable boundary between welded and brecciated ignimbrite (refer to Chapter 3 for terminology). This is one of the features that is indicative of a welded ignimbrite as opposed to this succession being part of a lava flow deposit, and has been discussed in Section 3.7.4.

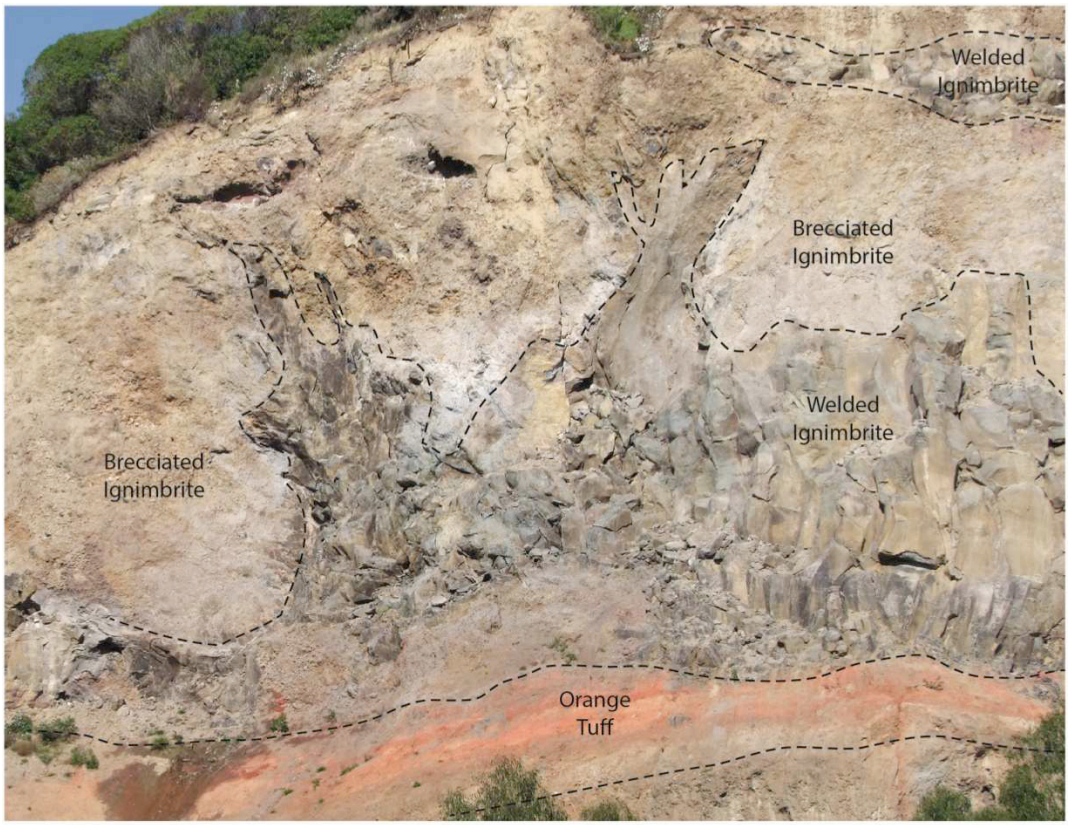

Figure 4.7: Irregular structures created by welding variation, Sector 3, Redcliffs. Field of view ~38m (horizontal).

4.5 Geotechnical Testing

4.5.1 Uniaxial Compressive Strength

Uniaxial Compressive Strength (UCS) was the primary strength testing method used to establish intact rock properties of the orange tuff and the welded basaltic ignimbrite in this research. Testing of the non-welded basaltic ignimbrite unit by uniaxial compression was not possible due to core specimens being unable to be prepared because of the very weak rock strength. Testing of the other two rock types was conducted in accordance with ISRM (1979a). Every effort was made to meet the conditions of the standard for the preparation of rock core specimens (ASTM 2004).

Core of diameter 50mm was cut using a diamond tipped drill bit, with core length of 100mm (2:1 length to diameter ratio). This was selected to provide the optimum number

of core samples from the block samples collected in the field although it does not strictly meet ISRM recommendations. It was also considered the best method for producing core samples of the more difficult rocks, where fractures were visible through the block samples following transport from the field area and longer core was difficult to prepare.

Where core samples could not be produced, point load testing (PLT) was used, as discussed in Section 4.5.2.

Sample Preparation

Given the weak nature of the orange tuff (RC-T), perfect cylinders could not be produced consistently. The main issue with the tuff was the tendency for corner sections to break off whereby clasts were removed whole from the groundmass rather than being cut. Because of this, length of cylinders was also difficult to control as grinding the ends resulted in further loss of material from the corners. Cylinders were considered to be adequate for testing to provide an approximate strength value. An example of a prepared core sample and the failed core following testing is shown in Figure 4.8.

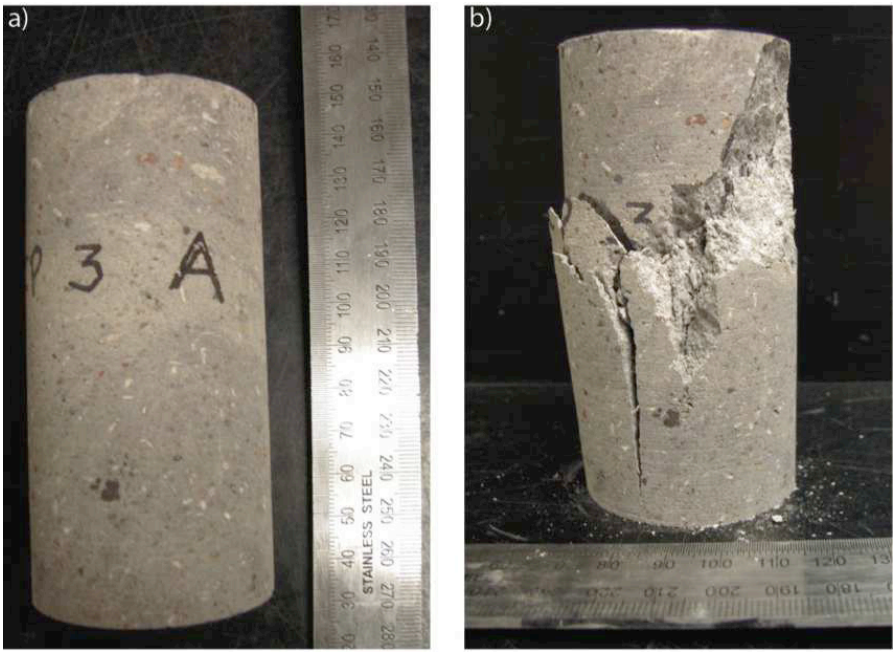

Figure 4.8: a) Example of prepared welded ignimbrite core; b) same failed core after UCS test.

Samples of the more highly welded basaltic ignimbrite (RCB4 – not shown in thin section) were prepared to produce six core samples. Unlike the orange tuff, this sample could be machined to produce high quality core specimens to the required standard. One of these core specimens contained a visible defect in the form of a void approximately 200mm^3 at the surface. This was documented and noted during testing. The other five core specimens were homogenous and free of any visible defects.

Similarly, the less welded basaltic ignimbrite sample (RCP3) could be cut to the required dimensions and machined with minimal damage to the corners of the specimen. Unfortunately, the collected sample was not large enough to extract more than one core sample of the dimensions required for testing.

Results

As expected, the welded basaltic ignimbrite samples had a significantly higher compressive strength than the crystal tuff samples tested, as indicated in Table 4-1.

Table 4-1: Summary UCS data for 50mm diameter core samples.

Sample	Average core length (mm)	Mean Failure Stress (MPa)	Failure Stress Range (MPa)	Number of Samples
Crystal tuff (RC-T)	99.4	4	4-5	4
Welded basaltic ignimbrite (RCP3)	100.4	29	-	1
Highly welded basaltic ignimbrite (RCB4)	100.3	216	155-311	5

4.5.2 Point Load Strength Testing

Where cylindrical rock core specimens were not able to be prepared, point load testing was used to obtain Point Load Strength (PLS) Index (Is_{50}) values. These values were then

converted to MPa by multiplying by 24 to estimate a relative strength for comparison with UCS values obtained from other samples, acknowledging the limitations involved. PLS testing was required to test the Brecciated Basaltic Ignimbrite (RCB1) unit as cylindrical core could not be cut from collected samples, nor was it possible to cut cubic blocks for modified UCS testing. Modified UCS testing included methods for testing cubic coal specimens developed by Bieniawski (1968) and used by Harris (2002). Cube UCS testing was not able to be used with the brecciated ignimbrite material due to the very low strength of the rock, primarily a result of the abundance of micro-fractures throughout the samples collected. These micro-fractures propagated and widened significantly in aperture during the drilling and cutting processes. As a result, cubic blocks could not be cut from collected samples.

Due to the composition of the basaltic ignimbrite unit, it was important to test the strength of the groundmass rather than the scoriaceous clasts as the former is significantly weaker. This is most likely the result of existing micro-fractures that can be observed to pass preferentially through the matrix, while tending to divert around the edges of stronger scoriaceous clasts (Figure 3.7). As such, it was assumed that the groundmass material will fail preferentially, thus the strength of the groundmass will ultimately control the overall strength of the unit in terms of block release.

Results

Point load testing showed the brecciated basaltic ignimbrite material to be very weak according to NZGS (2005) rock strength terms based on ~1.8MPa equivalent unconfined compressive strength of the groundmass. The unit was tested as groundmass and scoria clast components separately due to the contrast in component strength. A summary of testing results is presented in Table 4-2.

As expected, the scoria clasts were considerably stronger than the groundmass, in the order of ten times stronger. Using rock strength terms according to NZGS field description guidelines (2005) the groundmass is considered “very weak”, and the scoria clasts “weak” (see Appendix 5 for Rock Strength Terms table). It is noted by Hoek & Brown (1997) and Bieniawski (1989), that rock with UCS strength less than 25MPa should be tested with UCS

rather than point load, as rocks in this low range may "yield ambiguous results" (Hoek & Brown 1997). For classification purposes PLS is considered sufficient, and results were consistent.

Table 4-2: Summary Point Load strength data of brecciated basaltic ignimbrite (RCB1).

Sample description	Point Load Strength Is_{50} (MPa)	Approximate Compressive Strength (MPa)[1]
Groundmass	0.073	1.8
Scoria clasts	0.76	18

[1] Assuming UCS ≈ 24x$Is_{(50)}$

Comparison of data from Table 4-1 and Table 4-2 show the variation of rock strength at Redcliffs. The marked contrast between the strength of the welded basaltic ignimbrite and the brecciated ignimbrite is a significant factor to consider when modelling these units for future rockfall events. This is important because a very strong rock such as the welded unit would be expected to move in coherent blocks, in contrast to a very weak rock that would be expected to fragment readily during movement downslope. This concept and the capacity to model it is discussed in Chapter 6.

4.1 Synthesis

- Engineering geology face logs show the broad-scale features of the cliff face, focusing on lithological boundaries and joint discontinuities
- Mapped features are critical to the development of the engineering geology model that is used for modelling 13 June 2011 rockfall, and for modelling future rockfall runout at Redcliffs. The engineering geology face logs are also particularly important in identifying potential rockfall source areas
- Intact rock properties were analysed using UCS testing for the orange tuff unit and welded basaltic ignimbrite samples, and point-load testing to estimate the compressive strength of the very weak non-welded ignimbrite unit. The non-welded basaltic ignimbrite had the lowest approximate mean compressive

strength (1.8MPa), followed by the very weak orange tuff (4MPa). The two welded ignimbrite samples tested gave mean strength estimates of 29MPa and 216MPa, respectively. These properties are important in considering how the rocks may behave during rockfall, particularly in terms of rock fragmentation.

5 School Hall Section: Modelling Analysis Case Study

5.1 Introduction

This chapter presents a rockfall model for the Redcliffs field area that has been developed using the engineering geology model discussed in Chapter 4, and calibrates modelled runout against field observations. The School Hall Section is used as a test-section to assess the sensitivity of the modelling programme to input variables, and to analyse the influence that selected parameters have on modelled output so that an accurate, calibrated model can be created. The modelling has been undertaken on a slope profile that was obtained from data collected by GNS Science in March 2011, which allowed modelled outputs to be calibrated against runout data from the 13 June 2011 cliff collapse event. The calibrated model is then applied to other section lines at Redcliffs, which are discussed in Chapter 6, with the primary aim of assessing runout down the talus "ramp" in future earthquake-triggered rock fall events. Future large-scale cliff collapse is not evaluated in this study.

The location of the School Hall Section (Section E) was chosen as it provides a central study site on the highest part of the cliff section at Redcliffs, where large-scale failure has occurred during both 22 February 2011 and 13 June 2011 earthquake events (Figure 5.1). It is also an area where high-resolution slope survey data has been obtained by GNS Science along the full length of the slope. In addition, it is an area that affords good access for field calibration within the limits of safety that are required. Map coordinates at the base of the section are -43.55972°, 172.73298° (Cubrinovski et al. 2011), and a detailed plan map is shown in Figure 5.2.

From a modelling perspective, the School Hall Section provides a section through one of the "worst cases" present in the Redcliffs field area. This assessment is based on the large volume of fallen material at the base of the cliff (approximately 150m^3/m width), a maximum cliff height of 71m, and an approximate cliff-top recession measurement of 10m (Massey, McSaveney, & Heron 2012). This high cliff height (~70m), blocky and fragmented nature of

existing material on the cliff, and the proximity to a significant building (School Hall) all contribute to this section being an important site to undertake study of future rockfall runout.

Figure 5.1: Section location map, Redcliffs.

5.2 Modelling Approach

Mapping of slope features such as significant geological boundaries, runout extent, and fly-rock zones has been achieved through field reconnaissance mapping and aerial photograph interpretation. Four zones have been mapped using this method, as presented in Figure 5.2. These are:

- February rockfall source area
- February runout zone
- June runout zone (where it extends beyond February limits)

- Fly-rock zone

Detailed geological mapping of the cliff face and interpretations have been presented in Chapter 4.

Two-dimensional (2D) modelling of rockfall runout has been conducted using RocFall™ 4.0 software, the specific features of which were detailed in Chapter 2. The initial slope profile was obtained from Terrestrial Laser Scanner (TLS) data captured by GNS Science. This was collected during March 2011, following the 22 February 2011 Christchurch Earthquake which caused large-scale rockfall and cliff collapse on the Port Hills, and specifically at Redcliffs. This event has been widely documented in the literature, and has been discussed in Chapter 3. Significant rock mass failure also occurred at this site during the 13 June 2011 earthquake. By using slope profile data from March 2011, modelling results were able to be calibrated against June 2011 rockfall evidence from runout down the recently formed talus "ramp" in order to better control the simulated output.

Terrestrial Laser Scanning (TLS) is a form of ground-based LiDAR (Light Detection and Ranging) that is becoming widely used in geological applications for rapid acquisition of three dimensional (3D) point data. LiDAR scanners measure range and intensity of terrain points hit by the laser beam, from which raw data is converted into X,Y,Z coordinates forming a point-cloud (Lemmens 2011). From this, geometric features can be identified, and 2D and 3D models created. A major advantage of this non-contact method lies in the capability to accurately map geological features remotely, allowing dangerous areas such as vertical cliffs to be analysed with safety, while still in great detail (Buckley et al. 2010).

TLS-derived slope profile data has been processed using Golden Software Surfer 9™ to produce the cross section for modelling in RocFall™. This dataset is sufficiently detailed for this scale of mapping, with approximately 280 data points forming the slope profile. Discussion of slope profile generation within RocFall™ has been presented in Chapter 2. Figure 5.3 represents the measured slope profile in vertical section, with the geological units, rockfall source areas, and general slope features identified.

Figure 5.2: Cliff collapse runout comparison, February 2011 vs June 2011, showing Source Area, Runout, and Fly-rock Zones , Section E, School Hall, Redcliffs.

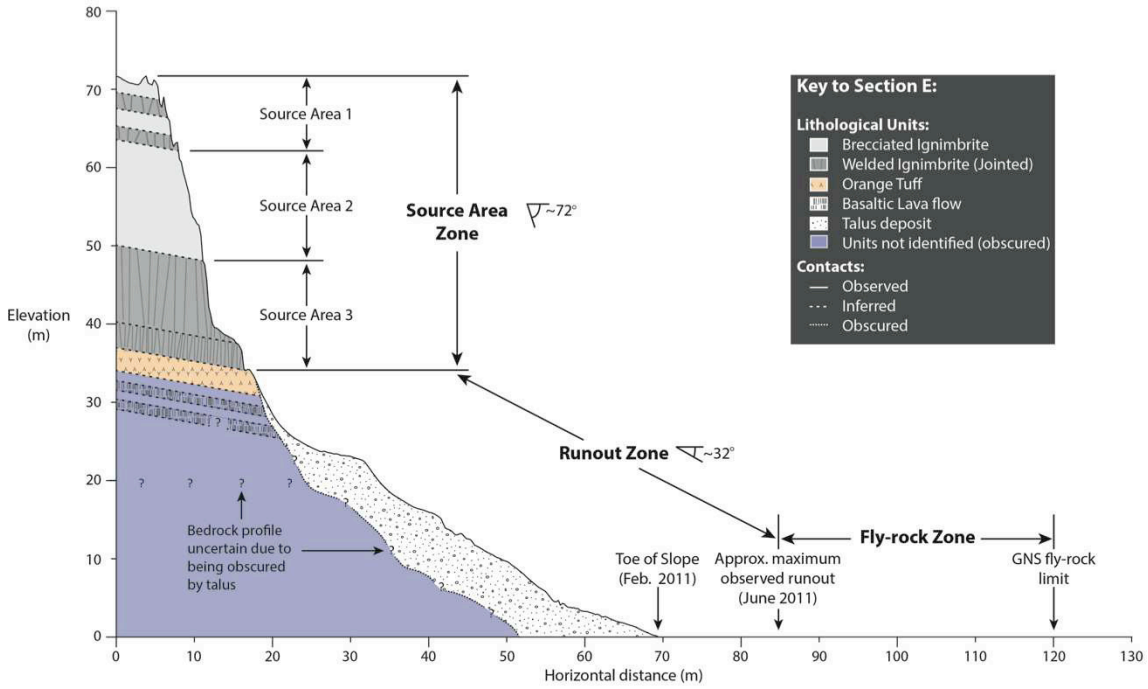

Figure 5.3: Cross-sectional diagram showing interpreted geological boundaries, rockfall source area zone, rockfall runout zone, and fly-rock zone, Section E, School Hall, Redcliffs. Note that geological boundaries are not necessarily representative of actual variability, rather they have been simplified for figure clarity.

The primary drawback of TLS data is the creation of a shadow zone behind objects such as buildings or large trees. This creates areas where data is unobtainable, due largely to the perspective of the scanner. This also occurs on a macro scale, such as where a shadow zone is created behind large boulders, obscuring upslope voids. This has the effect of reducing the roughness of the slope due to the smoothing effect of the vertices between recorded data points. As such, modelled sections may not accurately represent the true roughness of the talus slopes. This influences the runout distance of modelled rockfall events, because in reality boulders that may have been caught or at least be slowed in an upslope void have been modelled as travelling downslope. The issue of slope geometry is discussed later in Section 5.6 as it pertains to slope roughness.

5.3 Methodology

5.3.1 Input variables

In order to create a robust, calibrated, and realistic rockfall model, it is of critical importance to assess the sensitivity of individual, parameters in order to better constrain the output. Stevens (1998) stresses the importance of such analysis, and implies that rockfall modelling is more an art than a science:

> *"Since the input for most rockfall analyses is so poorly defined, it is equally important to determine the sensitivity of the results as it is to determine the results themselves."*

In order to assess the sensitivity of models to particular input parameters, it is necessary to isolate variables and analyse their influence. Systematically changing input parameters and comparing these with a control group for each have achieved this in the present study. The primary role of these variables, and of the approach, has been to allow calibration of the model to actual field runout.

Table 5-1 presents a summary of the input variables evaluated in testing of the School Hall Section slope model, and the range of values tested. This is not a complete list of all variables available to be controlled within RocFall™, however they are considered to be those of greatest influence to the output and design of protection measures, which has been a secondary objective of this thesis.

Variables have been divided into those tested during the primary modelling phase and those tested during the secondary modelling phase. Variables tested in the primary phase are more simplistic in their influence on model output, whereas those in the secondary phase had a more complex influence. Variables tested in the primary phase were calibrated with field observations, and then set as controlled variables during secondary phase modelling. In contrast, default values were used for modelling the complex variables during primary modelling, with these values tested and calibrated during the secondary modelling phase.

Table 5-1: Summary of input variables considered for modelling.

Variable	Brief Description	Values Tested
"PRIMARY MODELLING PHASE"		
Initial Velocity	Controls initial velocity conditions	Static and Dynamic conditions
Angular Velocity	RocFall™ includes the option to consider angular velocity, or to calculate models without considering this variable	Angular velocity either considered or not considered in calculations
Boulder Mass	Physical mass of modelled rock(s)	500, 2 000, 5 000, 10 000, 20 000kg
"SECONDARY MODELLING PHASE"		
Restitution Coefficients (R_n and R_t)	Represents the rate of conversion of energy from falling object to ground surface; Normal (R_n) and Tangential (R_t)	"Bedrock": R_n=0.35-0.45, R_t=0.75-0.85 "Talus": R_n=0.28-0.32, R_t=0.70-0.82
Phi	Block friction angle	10-50°
Slope Roughness	Slope roughness (individual slope segment scale)	0-7.5°

As with the primary phase, modelling throughout the secondary phase has been progressive as the influence of each parameter has been analysed and calibrated with field data. This means that in the order that variables are presented in this section, the calibrated optimal values were carried into the testing of the following variable. The outcome from this testing is a calibrated "best-fit" slope model which is presented in Section 5.10.

Initial Velocity Conditions

Initial velocity conditions were tested to represent outcomes in both dynamic and static conditions. Static conditions include any rockfall caused by a factor other than earthquake shaking such as weathering, extreme weather conditions, or human factors. Alternatively,

during seismically active conditions, source rocks may have an initial velocity that could enhance the trajectory of rocks downslope, resulting in a potentially more dangerous rockfall event. Specific values used in modelling are presented in Table 5-2.

Table 5-2: Initial velocity conditions.

	Static Conditions		Dynamic Conditions	
	Mean	Standard Deviation	Mean	Standard Deviation
Horizontal Velocity (m/s)	0.0	0.0	1.5	0.0
Vertical Velocity (m/s)	0.0	0.0	1.0	0.0

Because of the high ground accelerations generated by large earthquakes, both 22 February and 13 June 2011 are examples of earthquake shaking providing substantial initial velocity conditions. As discussed in Section 2.4, this is the major reason why catastrophic cliff collapse failure occurred during both 22 February and 13 June 2011 earthquakes, but very little rock failure was recorded from either the 4 September 2010 Darfield Earthquake, or the 23 December 2011 aftershock, even though these two events were also both of high magnitude ($M_W \geq 6.0$).

Estimates of dynamic velocity conditions were calculated from Peak Ground Acceleration (PGA) data collected by GeoNet during the Canterbury Earthquake Sequences. PGA data is presented for earthquakes of $M_W \geq 6.0$ in Section 2.4. From these calculations, the values presented in Table 5-2 were considered to be realistic values to represent the velocity conditions experienced during the 13 June 2011 earthquake, which is the event being modelled in this thesis.

Angular Velocity

Angular velocity is the rate at which an object rotates about an axis (Section 1.5.2). RocFall™ includes the option to consider angular velocity, or to calculate models without considering this variable. The influence of this variable was tested to analyse the effect this would have on the three main output components of runout distance, bounce height, and total kinetic energy . Results of this analysis are presented in Section 5.7.

Boulder mass

Boulder mass values were selected to represent a realistic range based on field observations. In the field, block size was seen to increase significantly from the top to the base of the talus (Figure 5.4). In the literature, this pattern is commonly referred to as "gravity" or "fall sorting" (e.g. Evans & Hungr 1993; Luckman 2007). This sorting pattern is considered to be controlled by two mechanisms:

- Large boulders have greater momentum and therefore tend to travel greater distances downslope (Luckman 2007); and
- Frictional resistance offered by a slope is a function of its roughness in proportion to the size of the object moving over it and particles will tend to be stopped when the magnitude of roughness approaches their own dimensions (McSaveney 1971).

Observed block sizes ranged from <0.5m^3 to ~25m^3, and the larger blocks were generally at the base of the talus apron. It was not possible, however, to excavate beneath this surface "veneer" to verify vertical block size distribution.

Another consideration when estimating the mean block size of the talus slope is the "sieve effect" created by smaller rocks and fragments falling into voids between larger blocks (McSaveney 1971; Perez 1989; Luckman 2007). This has the effect of obscuring the smaller rocks from view, as larger blocks will dominate the surface of the talus. Because of this, care was taken to observe the size of smaller rocks between larger ones, in order to limit the sampling bias towards larger rocks. Given the safety restrictions at the Redcliffs site, this was

achieved primarily through aerial and ground photograph interpretation.

As a result of field observations, the estimated mean block size observed at the toe of the talus slope was approximately 1.7m^3 (~5t or 5,000kg assuming a density multiplication factor of 3). Because of this, in all models not specifically testing the influence of boulder mass, modelled rocks were represented by the 5,000kg mean block size and not the maximum block size observed. To consider rocks of significantly larger mass, slope models were also run using 10,000 and 20,000kg rocks. These larger rock block sizes are consistent with some of the larger blocks that were observed locally, and which appeared to have been "rafted" part-way downslope following cliff collapse.

As discussed in Section 1.5.1, the mass of the rock does not influence the runout distance in RocFall™ software, so the larger block sizes were more relevant to protection requirements and kinetic energy considerations. The selection of the estimated mean rock block size is considered appropriate for the purpose of this analysis, but the limitation in any modelling of variable source block size due to joint spacing and persistence is acknowledged.

Restitution Coefficients

Initial restitution coefficients were based on default input settings in RocFall™ Table 5-3). These values were constant throughout the initial modelling phase to analyse the influence of other parameters on the output. These values were adjusted for the secondary modelling phase, by testing the influence of different combinations on model output. The range of values for normal and tangential restitution coefficients tested is presented in Table 5-3.

Figure 5.4: Photo looking southwest towards the main section of the cliff showing gravity sorting of talus slope, School Hall Section (Section E), Recliffs. Approximate location of Section E shown by dashed red line. Note relatively small blocks near the top of the talus slope in contrast to the large blocks at the base. Large block in left fore-ground is approximately 2m high and ~4m wide (~25m^3; left-hand end not shown). Blue object at the base of the slope (centre-right) is the buried car indicated in Figure 4.2. Large, angular blocks in the immediate foreground were released from the face during the 13 June cliff collapse event. Photo credit: Sam Hampton, June 2012.

T able 5-3: Tested material property restitution coefficients. Blue shading indicates RocFall™ default values. Standard deviation for all values = 0.04.

Restitution Coefficient	Slope Material					
	Talus				Bedrock	
Normal (R_n)	0.28	0.30	0.32		0.35	0.45
Tangential (R_t)	0.70	0.75	0.82		0.75	0.85

Block Friction Angle (phi) and Slope Roughness

As with restitution coefficients, default values for both block friction angle and slope roughness have been used in primary phase modelling. To analyse the effect of both parameters on modelling output, a range of variables have been tested in the secondary phase. Tested values for friction angle and roughness are given in Table 5-4.

Table 5-4: Tested friction angle and slope roughness values. Blue shading indicates RocFall™ default values for both slope materials. Standard deviation for phi = 2.0.

Input Variable	Values Tested				
Friction Angle (phi, degrees)	10	20	30	40	50
Slope Roughness (degrees)	0.0	2.5	5.0	7.5	

5.3.2 Output results

Format

Modelling in RocFall™ has been set up to produce four data plots for each simulation conducted. The four plots are:

- Slope profile with runout indicated (axes in true scale)
- Horizontal location of rock end-points (runout)
- Total Kinetic Energy of rocks passing a specified location on the slope
- Bounce Height Envelope

Each individual simulation is recorded with a model code, variables specified, and the four graphical plots on a single page. An example of the graphical component of the simulation output is shown in Figure 5.5. Statistical distribution data obtained from runout plots are included with most of the graphical plots. Full data sets are presented in Appendix 6.

Method of analysis

Throughout this thesis, three critical output components are being considered. They are:

- Horizontal rock end-point (also referred to as rock runout);
- Bounce height (both at a given point on the slope, as well as at the toe of the slope); and
- Total kinetic energy

The three critical output components have been selected because they provide the necessary data to calibrate theoretical models with field observations, and to provide an indication of critical values for future consideration of protections measured. Using graphical plots and statistical distribution data, these three critical output components form the basis for model analysis, with rock end-point being fundamental.

Calibration has been achieved through constantly refining model outputs to replicate field observations. Horizontal rock end-points were the most useful for this purpose, because exising rock runout data is the most easily collected parameter through aerial photograph interpretation and field mapping. Both bounce height and total kinetic energy are of critical importance to the design of rockfall protection systems, however these parameters are more difficult to calibrate with field observations, and design of rockfall protection measures are not within the scope of this study.

Three types of rock runout data have been primarily used for analysis, all of which are obtained from the horizontal rock end-point plots and associated statistical data. These are:

- Mean runout distance
- Maximum runout distance
- Runout distribution across six specified locations in the profile (Figure 5.6)

Section 5.42.9	2/11/12	Area 1 Line Seeder	TLS-derived profile	100 Rocks, Mass 5000kg
Talus: Rn=0.28/ Rt=0.70/ phi=30/ Slope Roughness=2.5		Bedrock: Rn=0.45/ Rt=0.75/ phi=10/ Slope Roughness=0		DYNAMIC INITIAL CONDITIONS

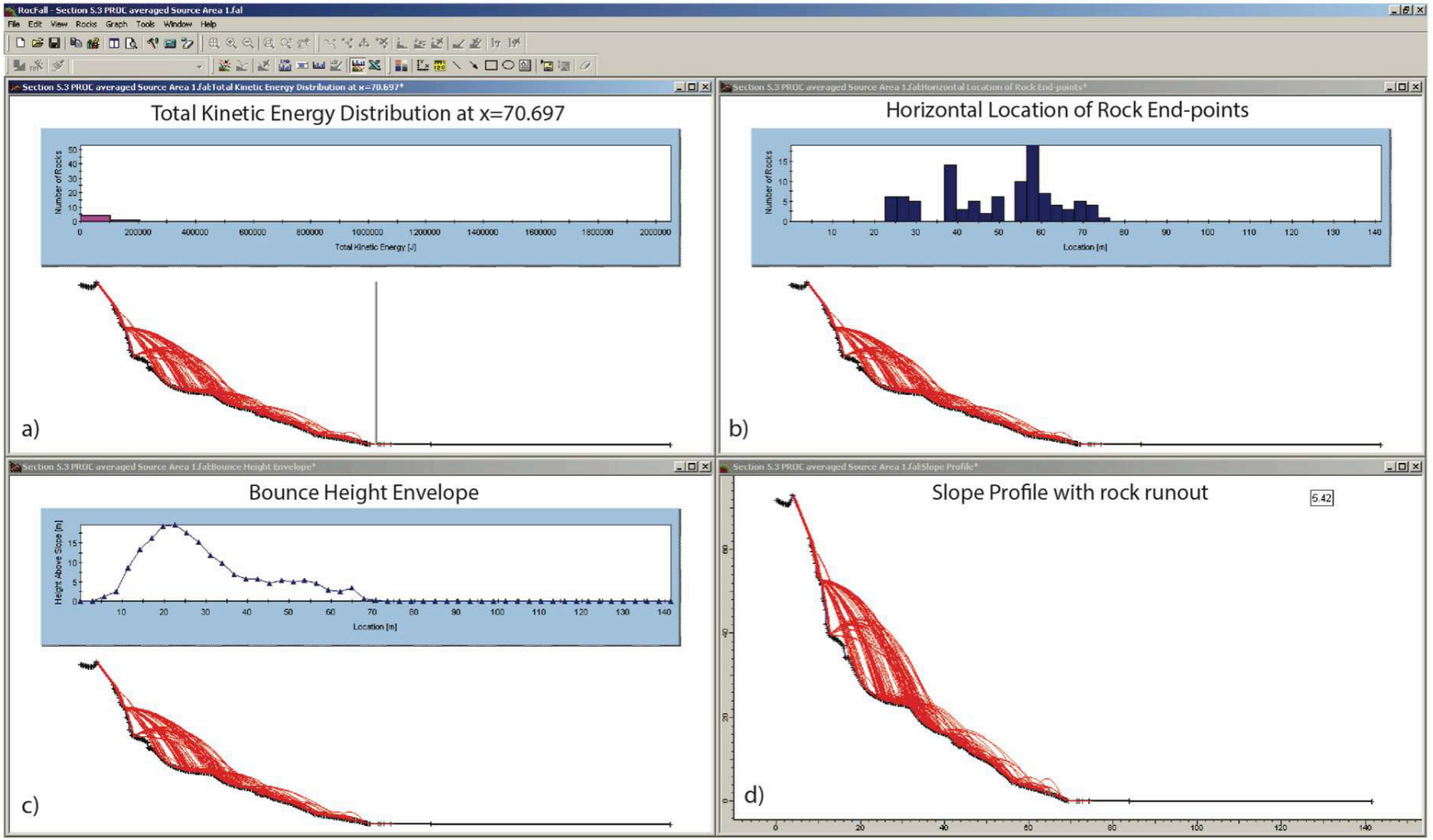

Figure 5.5: Example of combined RocFall™ individual simulation output.

All runout distances are measured in metres with reference to a zero datum (Figure 5.6). The zero datum corresponds to the origin of the slope profile plot on the RocFall™ model, rather than the cliff edge. This datum is constant throughout all models, so it is irrelevant that runout is not measured exactly from the cliff edge. No reference is made to the corresponding slope length as this is not a measurement that is facilitated by the RocFall™ software, as locations are only defined by an x,y coordinate system.

Figure 5.6 presents a TLS-derived cross-sectional profile of Section E showing the six specified locations where runout distribution data has been collected. These locations are generally associated with significant breaks or changes in slope where accumulation of rock debris could occur. Specifications of each location are presented in Table 5-5.

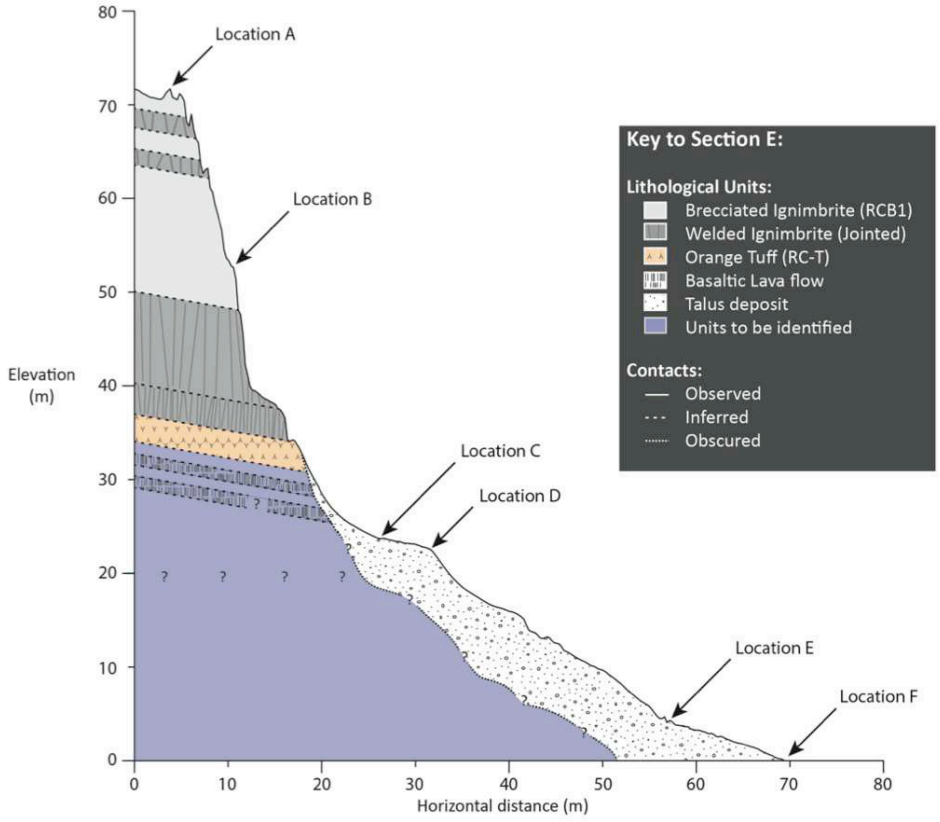

Figure 5.6: TLS-derived cross section showing the measurement locations of cumulative runout percentage statistics, Section E, School Hall, Redcliffs.

Table 5-5: Specifications of Locations where runout distribution has been specifically considered.

Location	Horizontal Distance from zero datum (m)	Height above ground level (m)	Geology and significance of Location point
A	4	73	Brecciated Basaltic Ignimbrite; highest rockfall source
B	10	53	Brecciated Basaltic Ignimbrite; frequently impacted point
C	26	24	Talus slope; mid-point of talus bench - possible accumulation area
D	32	23	Talus slope; lower edge of talus bench - possible accumulation area
E	57	4	Talus slope; break in slope; possible accumulation area
F	69	0	Talus slope endpoint; expect most material to have deposited upslope of this point

Based on the horizontal component of the coordinates of the chosen locations, each significant break in slope can be identified in statistical runout data. These data present each rock by rank with the cumulative percentile of rocks stopped to that point, as well as the horizontal distance each rock reached. For example, a rock that stopped ~60m from the source under specific conditions, may lie in the 52nd percentile. This means that 52% of the rocks in the model, where each model run involves 100 rocks released from source, have come to rest upslope of, or at that point on the slope. This method of data collection is beneficial because a larger number of calibration points are obtained along the slope, rather than a singular point as provided by the mean or maximum values.

Both bounce height and total kinetic energy are critical parameters to consider, however

given the difficulty in calibrating these with observed field data, they are really only of relevance in regards to potential protection measures.

5.4 Source Area Model

The TLS-derived measured slope profile forms the basis of the School Hall Section model. In conjunction with aerial photograph mapping, the model comprises three main components, as outlined in Figure 5.3 These zones mapped onto an aerial photograph are presented in Figure 5.2. The following sections should be read in conjunction with both of these figures.

Within the near-vertical portion of the School Hall Section, three broad areas have been identified as possible rockfall source areas based on field observations and geological interpretations. These are:

- **Area 1:** Brecciated basaltic ignimbrite with two welded bands, each 2.5-3.5m thick and total thickness ~9.5m.
- **Area 2:** Brecciated basalitc ignimbrite with incipient fractures. Total thickness ~14m.
- **Area 3:** Welded basaltic ignimbrite with irregularly spaced (0.5-3m) columnar jointing. Total thickness ~14m.

These areas and their geological units are shown in Figures 5.3 and 5.7. The average gradient of the Source Area Zone is ~72° according to the TLS data. Field observations and subsequent geological interpretations were made from remote observation through high-resolution vertical cliff photographs, and supplemented with samples collected from the base of the talus slope. Engineering geology descriptions were based on these collected samples and geotechnical testing (Chapter 4).

In the same way that horizontal distance was measured from a zero datum, vertical elevation represents the height above ground level (AGL), as set by the TLS during data collection by GNS Science (see Section 5.1.2). The zero datum is acceptable for this study as all elevation

measurements in this thesis are calibrated to the same zero datum.

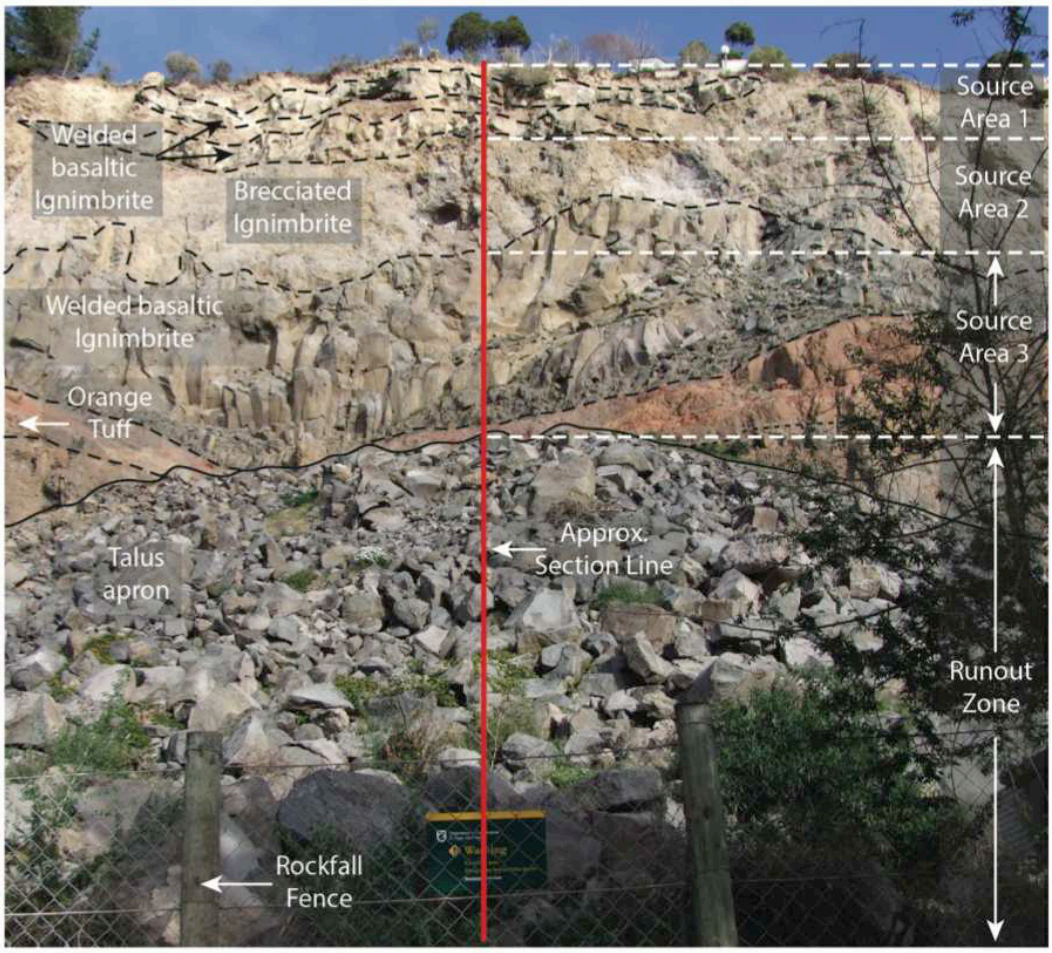

Figure 5.7: Rockfall source areas, Section E, School Hall Section, Redcliffs. Some image distortion due to low angle perspective. Field of view ~70m (vertical). Note variable columnar joint orientation and irregular contact relationships between units.

5.4.1 Area 1

The upper source area, Area 1, consists of the brecciated basaltic ignimbrite material containing two welded bands. This area has a source area height range of ~9m, with the welded bands within the breccia each between 2.5 to 3.5m thick. As a rockfall source area, Area 1 presents the greatest height from which rock could fall, with the top of the cliff approximately 71m above ground level (AGL), and the lower limit of the area being around 62m AGL.

The welded bands display columnar jointing, with sub-parallel joints intersecting sub-horizontal to random oriented joints, producing a blocky and potentially unstable source area. Joint spacing is generally in the range 0.5 to 2m, with joint persistence in the vertical plane up to 1m, but more commonly <0.5m. This gives a likely maximum block dimension of around 4m^3, with a mass of ~12T (assuming a density multiplication factor of 3).

Two bands of brecciated basaltic ignimbrite above the welded units in Area 1 are estimated to each be 1.5 to 2m thick. This greatly decreases the maximum block size from this source area approximately 8m^3, which equates to a tonnage of ~25t, because of the joint-controlled nature of these two thin but more blocky units. As discussed below, it appears that the maximum block size from Source Area 1 will equate to a mass of approximately 25t.

The brecciated basaltic ignimbrite component of Area 1 are interpreted to contain incipient fractures, most likely caused by the extremely high ground accelerations experienced during earthquake shaking of 22 February and 13 June 2011 (refer to Section 2.4) This interpretation is based on remote observations that showed a largely massive unit with few obvious open natural (i.e. iron-stained) fractures in situ, but large blocks of what appears to be the same material up to ~25m^3 (or ~75t) were observed in the talus apron.

Incipient fracturing was not clearly observable in the unit in the remote analysis used in this thesis. However, vibration caused by transportation both in a car and on a laboratory trolley across a concrete surface caused numerous fractures to develop through the samples. In the laboratory, vibrations produced during cutting and drilling caused abundant fractures to propagate through the samples, and was the reason that testable core could not be obtained for this material (as discussed in Section 4.5). Considering the propensity of the material to fracture under uncontrolled shaking conditions, incipient fractures in the rock mass are a geologically plausible explanation for block fragmentation.

It is also possible that the micro-fracturing within hand samples was a result of fragmentation of falling blocks during the cliff collapse process. The blocks that were able to be collected

from the base of the talus slope could therefore contain a greater number of fractures than the in situ unit. This could be the reason why the brecciated basaltic ignimbrite unit stands at such a high angle (~78°) in the cliff face, but is so weak in hand sample. Irrespective of the origin of microfracturing in Source Area 1 material, maximum block sizes between about 10 and 75t seem reasonable for modelling purposes, and the adoption of the mean block size of 5,000kg (~5t) for analysis is considered realistic.

5.4.2 Area 2

Area 2 represents the brecciated basaltic ignimbrite source area, commencing at a height of approximately 62m AGL at the upper contact with Area 1, and continuing to around 48m AGL at the base, making the source area approximately 14m thick. From remote field observation, Area 2 is interpreted to comprise the same brecciated basaltic ignimbrite as is found in Area 1, but is distinguished from this overlying source area by the lack of visible welding. As such, incipient fractures are assumed to occur through this source area as they did through Area 1, although this has not been verified because of lack of access.

As with the brecciated ignimbrite component of Area 1, estimation of likely maximum block size was determined through back-analysis of brecciated basaltic ignimbrite blocks observed in the talus. Given the brecciated basaltic ignimbrite in Area 2 is some 14m thick, it is likely that a block size of ~25m^3 as observed in the talus apron could have come from this source area. This equates to a tonnage of ~75t assuming a density multiplication factor of 3, as determined for the similarly unwelded but brecciated ignimbrite from Source Area 1.

As with Source Area 1, the blocks form Source Area 2 are interpreted to have maximum dimensions of about 25m^3 (or 75t in mass), but these are mostly observed to fragment either due to shaking damage or block impact on the debris apron. Adoption of a mean 5t (5,000kg) block mass for Source Areas 1 and 2 is consistent with field and aerial photograph observations.

5.4.3 Area 3

The lowest of the three source areas consists of approximately regularly spaced (0.5-3m) columnar-jointed, welded, basaltic ignimbrite. This area is approximately 48m AGL at the upper contact, and continues to around 34m AGL at the base, thus presenting ~14m of near-vertical rockfall source area.

Area 3 represents the most visibly fractured rock mass within this section. Columnar jointing is dominant, with some joints curved outwards. Vertical joint persistence of up to 10m was observed, but <7m was more prevalent. Of the blocks controlled by the longer, curved vertical to sub-vertical joints, joint spacing in the horizontal direction was generally of the order of 1-2m, creating long, tabular block shapes with curved sides. More commonly, equidimensional blocks up to 2m^3 (~6t) were observed, an example of which is shown in Figure 5.8.

Figure 5.8: Example of columnar-shaped welded basaltic ignimbrite blocks from Area 3, and brecciated basaltic ignimbrite blocks from Area 3, and brecciated basaltic ignimbrite example from Area 1 or 2. Block size up to maximum of 5t or 5,000kg.

A significant factor in terms of rockfall analysis from Area 3 is the block shape created by the intersecting joint sets. Blocks from this area often showed strongly columnar shapes, with angular faces (Figure 5.8). Intuitively, angular blocks should travel shorter distances from source than more rounded blocks. It was difficult to model this in RocFall™, as block shape was primarily controlled by the friction angle of the rocks. Sensitivity to this parameter, and runout implications are discussed in Section 5.8.

5.4.4 Other source rock

The portion of the cliff face below Area 3 comprises the upper part of the crystal-rich orange tuff unit (RC-T) that is visible immediately above the talus. The tuff is a very weak material that is easily broken apart in hand specimen, particularly along fine fractures, however it stands sub-vertically in situ. In the School Hall Section, no natural fractures have been mapped in the crystal tuff unit for some 20m either side of the section line. This is because no fractures were visible in the high-resolution images in this area. It does not mean that there are no fractures, rather that they are too small to see remotely. Fractures were visible in the orange tuff in other areas of the field site, and these were discussed in Section 4.4.2.

This orange tuff is not considered to be a significant rockfall source area due to the relatively low elevation (with respect to the distance to the top of the talus), and the way the unit has withstood previous earthquake shaking reasonably well. While there is evidence of some material from this unit falling from the cliff, it does not appear to have contributed many rocks to the surface of the talus on the School Hall Section from field observation and photographic interpretation.

5.5 Runout and Fly-rock Zone

5.5.1 Runout Zone

The runout zone within the School Hall Section is dominated by some 50m (horizontal

distance) of talus slope, with the area beyond the end of the talus slope modelled by "Asphalt", which corresponds to the sealed bitumen driveway beside the School Hall. The start of the runout zone is marked by the upper limit of the talus apron which was interpreted from TLS data to commence at ~34m AGL. From this point to the toe of the talus slope (~0m AGL), the average talus slope angle is ~32°.

Figure 5.3 shows the runout zone extending approximately 15m beyond the toe of the talus slope. This is in reference to mapped boulders that have exceeded the toe of the slope ~20-30m northwest of the School Hall. This is clearly shown in Figure 5.2, with boulders from the 22 February 2011 cliff collapse (red) having been differentiated from those derived during the 13 June 2011 event (blue). It is obvious that in the 13 June 2011 series of shaking events the February 2011 talus apron acted as a "ramp", and it is this slope which is primarily being modelled.

The talus slope comprises a mixture of lithologies from the fallen cliff, and is dominated by large, blocky to slabby, welded basaltic ignimbrite (primarily from Area 2, some from welded bands in Area 1), and less angular brecciated ignimbrite blocks (primarily from Area 2, and from the non-welded part of Area 1). For modelling purposes, the entire "runout zone" is represented as a singular talus unit, as it was not realistic geologically to specify explicit lithologies within the talus itself.

The "Talus Cover" material is used as the initial default material for modelling, with adjustments made to these values occurring throughout model testing. This zone is referred to simply as "talus" throughout this thesis where specific parameters are being discussed. On the School Hall Section E there is nothing mapped beyond the talus apron toe because the post-September 2010 bund is intersected by the section line and effectively precludes further runout.

5.5.2 Fly-rock Zone

Beyond the Runout Zone is the Fly-rock Zone. This is a zone constrained by the expected limit of rock fragments (fly-rock) thrown downslope by fragmentation of falling rock during future cliff collapse events. GNS Science define fly rock as "broken rock released as high-velocity projectiles created in impacts between rocks and other hard objects" (Massey et al. 2012). In this case the limit has been derived by GNS Science as part of the life-safety risk from cliff collapse assessments conducted on the Port Hills, and is shown as extending a further 50m (approximately) from the toe of the talus apron (Figure 5.2).

Calculation of the fly rock line is based on application of the fahrboeschung angle, which is the tangent of the slope angle from the top of the cliff face to the tip of the cliff collapse deposit (after Lucchitta 1979). Further discussion around the fly-rock limit is discussed in Section 6.

5.6 Slope Models

5.6.1 TLS-derived Slope Models

RocFall™ joins measured, neighbouring coordinates with a linear vertex to create the slope profile. The slope profile obtained from TLS data was used in the original form for initial modelling. Due to the high level of detail available from the TLS data, two key issues were identified in using this slope profile for modelling:

- rocks were stopped on near-vertical sections of the cliff; and
- increasing modelled slope roughness did not reduce rockfall runout as expected.

To resolve these issues, modifications were made to the original TLS-derived slope profile. These modifications are presented in the following two sections. Detailed analysis of rockfall runout resulting from these changes is discussed in Section 5.7.

5.6.2 Slope Profile Input

The TLS-derived slope profile (Figure 5.3) consisted of some 280 individual data points joined with a linear vertex to make a detailed slope profile. Due to the high level of detail, the profile represented macro-roughness that was additional to the slope roughness parameter within the software. The profile included two surface features in Source Area 1 where notches of ~1m wide and ~0.5-1m deep were represented by the measured slope surface. From comparison with field observations and photographs, these two features were considered anomalous, most likely the result of an artifact of the survey method rather than a true representation of the cliff face. This could be the result of poor reflector surfaces for the TLS created by particularly poorly reflective rock, or shadow from an overhanging rock etc. It is possible that some surface roughness was present in this area, but not in the exaggerated manner presented by the model.

The implications of these anomalies were that rock stopped on these surfaces during initial modelling. This was not acceptable for two reasons:

- these features were considered an artifact of the survey method, rather than a true representation of the face; and
- the modelled rocks were too large to be stopped by a feature of such dimensions (based on rocks of 5,000kg, which equates to boulders of ~1.7m^3)

These anomalies arose due to the style of modelling in the software programme whereby each rock is considered as an infinitely small circle so the size of the rock is not considered in the algorithm. The only consideration in this regard is the mass of the rock, which is used to calculate kinetic energy (Stevens 1998). As a result, the software allows rocks to come to rest on small ledges that in reality are not large enough to permit catching of the rock. This resulted in high concentrations of rocks coming to rest on the near-vertical section of cliff, where this is intuitively and practically not possible.

Even if some surface roughness of the nature represented by the initial slope model did exist, these surfaces would quickly fill up with fallen rock. This is another artifact of the software in

that each rock is modelled independently of the others, so there is no consideration of rock interaction during fall.

To correct this modelling deficiency, the slope profile of Area 1 was adjusted to reflect the same slope gradient without the measured roughness (Figure 5.9). This was achieved by calculating the gradient of the measured Area 1 portion of the cliff profile, and replacing it with a single vertex with the same gradient.

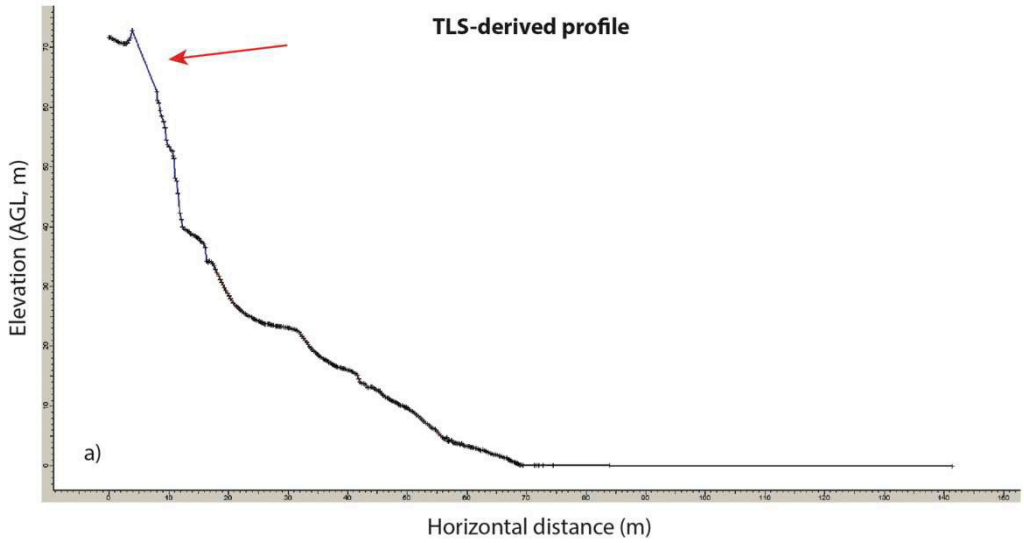

Figure 5.9: TLS-derived slope profile with modified upper Area (arrowed). Note single, straight vertex to remove small ledges where modelled rocks were stopping (compared to Figure 5.3). Vertical and horizontal axes are equal scale: Vertical field of view =~70m, horizontal distance =~150m. Vertex colours are unclear in this diagram due to the high number of vertices - refer to Figure 5.8 for material colour description.

Another issue arising from the TLS-derived slope profile was due to the "macro-roughness" of the slope, resulting from the high level of detail in the measured profile. This detail created vertices that were too small for the slope roughness parameter to have any effect because neighbouring slope vertices offset any changes, making the overall effect negligible. Implications for this on runout distances are discussed in Section 5.8.4 and 5.8.5.

In order to resolve the negligible effects of the slope roughness parameter, the measured slope profile was simplified on the advice of RocScience Inc. engineers, as shown in Figure 5.10. This was achieved by reducing the number of data points between vertices from ~280 to about 20.

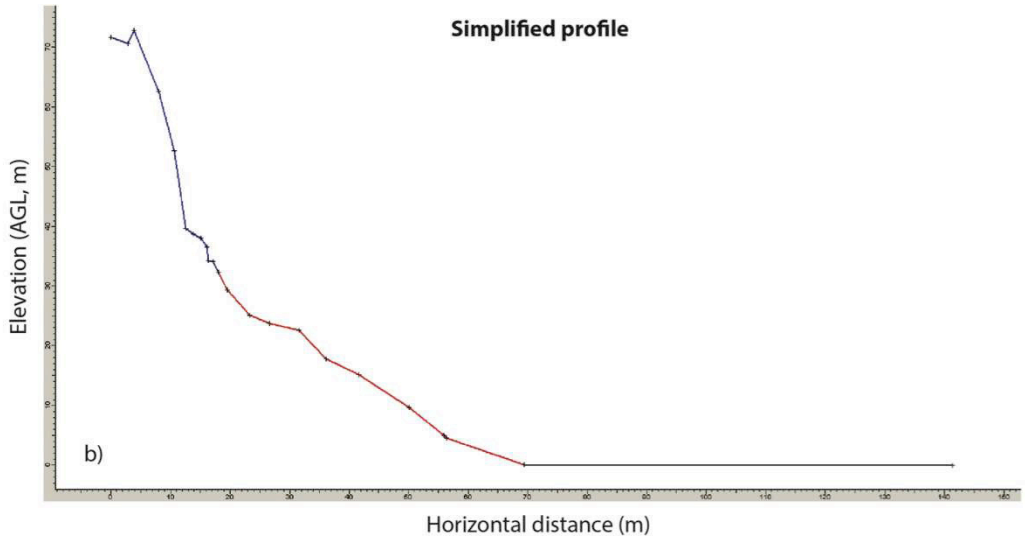

Figure 5.10: Simplified slope profile. Vertical and horizontal axes are equal scale: Vertical field of view =~70m, horizontal distance =~150m. Note vertex colour represents the material used to model each section. Blue = "bedrock", Red = "talus cover", Black = "asphalt". Discussion of these materials is in Section 4.6

5.7 Rockfall Runout Analysis – Primary Modelling Phase Variables

Rockfall runout was the primary output used to calibrate theoretical models with observed field data. This section presents results of model testing where rockfall runout was affected by varying the "primary phase" input parameters. Rockfall bounce height and kinetic energy analyses are presented in Section 5.8.

5.7.1 Slope profile input effect

As discussed in Section 5.6, modifications to the originally measured TLS-derived slope profile were required following initial modelling. This section presents the results of initial modelling,

and the output following modifications. Comparison of the TLS-derived slope profile and the simplified slope profile is covered in the following section.

Modified TLS-derived slope profile

Figure 5.11 presents a comparison of horizontal end-point data from the original TLS-derived profile and the modified TLS-derived slope profile. The distribution of rockfall runout showed significant variation between slope profile input conditions. The red lines in the lower section of both diagrams represent the paths travelled by rocks in the model. Both models represent 100 rocks being released from the source area.

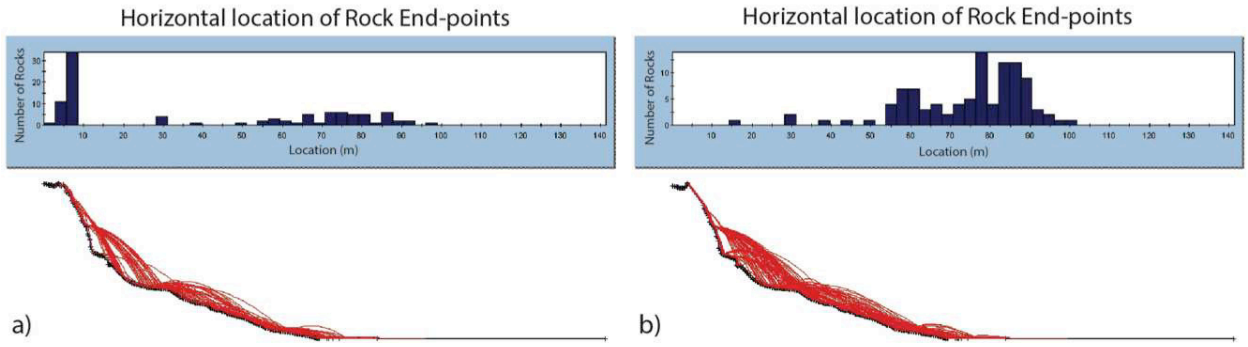

Figure 5.11: Comparison of horizontal end-point location for TLS-derived slope profile (a) and modified TLS-derived slope profile (b; Profile modified by smoothing Source Area 1 slope). Note vertical axes of runout plot compressed post-modelling. Horizontal axes represent the location in metres from the zero datum; vertical axes represent the number of rocks. Note vertical scale has been reduced post-modelling producing a shrunken scale, therefore graphs are not to natural scale. Input Parameters: Talus: R_n=0.32, R_t=0.82, phi=30, Slope Roughness=5, Bedrock: R_n=0.35, R_t=0.85, phi=30, Slope Roughness=0; Dynamic initial conditions.

a) Vertical scale range= 0-30 rocks, b) Vertical scale range= 0-13 rocks.

Altering the slope profile caused marked changes in the modelling results. As seen Figure 5.11a, the original slope profile produced a "spike" where ~45% of rocks came to rest within the first 10m of the slope. Figure 5.11b shows the modified slope profile, where rocks pass over the near-vertical Source Area 1 and continue onto the lower slope region.

Because of slope modification to smooth the upper portion of the slope profile, the distribution of rocks along the length of the slope, particularly in the Runout Zone, are more

consistent with field observations (Figure 5.2). The modified slope has therefore been adopted for analysis, even though it may remove some of the actual roughness. Note that the vertical axes have been shrunk post-modelling, so scales are not at natural scale.

5.7.2 Initial Velocity Conditions

Comparing rockfall runout distances under dynamic and static initial velocity conditions showed a consistently higher runout (both mean and maximum distance) when rocks had initial velocity. Table 5-6 summarises the results of testing from the primary modelling phase, including testing the influence that initial velocity conditions had on modelled rocks.

Figure 5.12 shows modelled rocks that had initial velocity (horizontal velocity=1.5ms^{-1}, vertical velocity=1.0ms^{-1}) generally had greater mean and maximum runout distances than those rocks which started under static initial conditions (horizontal velocity=0.0ms^{-1}, vertical velocity=0.0ms^{-1}). As expected the mean ruonut distance reduces significantly as the height of initial fall reduces (i.e. from about 75m in Source Area 1 to about 30m in Source Area 3), but the reduction in maximum runout distance (while greater than the mean) does not show this change (from 100m in Source Area 1 to about 90m in Source Area 3). There is relatively little difference between the initial static and dynamic profiles, however, which is again most likely an artifact of the computer programme.

5.7.3 Angular Velocity

When the RocFall™ model calculates rockfall paths the default setting is to consider the influence of angular velocity on the path of the falling rock. When this influence was not considered, mean rockfall runout was consistently higher than default conditions from all three source areas (Figure 5.13).

The difference between mean runout values within each source area became smaller as the elevation of the source area reduced. This was interpreted to show the influence that source area elevation had on the time the angular velocity had to affect the modelled rock path. This

Table 5-6: Summary table of primary modelling phase results. Blue shading indicates RocFall™ default settings. Full data sets are provided in Appendix 6

PRIMARY MODELLING PHASE									
Model Code	Seeder Zone	Initial Velocity	Angular Velocity Considered	Boulder Mass (kg)	Max. Runout (m)	Mean Runout (m)	Max. Kinetic Energy at x=71m	Mean Kinetic Energy at x=71m	Bounce Height at x=71m (m, above slope)
5.1	Area 1	Dynamic	Yes	5,000	102	77	9.7E+05	3.9E+05	2.5
5.2	Area 2	Dynamic	Yes	5,000	93	70	5.9E+05	2.9E+05	2.5
5.3	Area 3	Dynamic	Yes	5,000	86	36	4.3E+05	2.1E+05	1.0
5.4	Area 1	Static	Yes	5,000	98	75	8.2E+05	3.8E+05	4.0
5.5	Area 2	Static	Yes	5,000	89	60	5.4E+05	2.5E+05	3.0
5.6	Area 3	Static	Yes	5,000	85	29	2.7E+05	2.0E+05	0.5
5.7	Area 1	Dynamic	Yes	2,000	102	77	3.9E+05	1.5E+05	2.5
5.8	Area 2	Dynamic	Yes	2,000	93	70	2.4E+05	1.2E+05	2.5
5.9	Area 3	Dynamic	Yes	2,000	86	36	1.7E+05	8.5E+04	1.0
5.10	Area 1	Dynamic	Yes	500	102	77	9.7E+04	3.9E+04	2.5
5.11	Area 2	Dynamic	Yes	500	93	70	5.9E+04	2.9E+04	2.5
5.12	Area 3	Dynamic	Yes	500	86	36	4.3E+04	2.1E+04	1.0
5.13	Area 1	Dynamic	Yes	10,000	102	77	2.0E+06	7.7E+05	2.5
5.14	Area 2	Dynamic	Yes	10,000	93	70	1.2E+06	5.9E+05	2.5
5.15	Area 3	Dynamic	Yes	10,000	86	36	8.5E+05	4.2E+05	1.0
5.16	Area 1	Dynamic	Yes	20,000	102	77	3.9E+06	1.5E+06	2.5
5.17	Area 2	Dynamic	Yes	20,000	93	70	2.4E+06	1.2E+06	2.5
5.18	Area 3	Dynamic	Yes	20,000	86	36	1.7E+06	8.5E+05	1.0
5.19	Area 1	Dynamic	No	5,000	122	85	1.5E+06	5.8E+05	7.5
5.20	Area 2	Dynamic	No	5,000	101	76	9.3E+05	3.8E+05	5.0
5.21	Area 3	Dynamic	No	5,000	91	40	6.5E+05	1.8E+05	2.5

suggests that rocks from higher elevation source areas are more affected by angular velocity compared to rocks from lower elevations, but the height of fall is still the dominant influence.

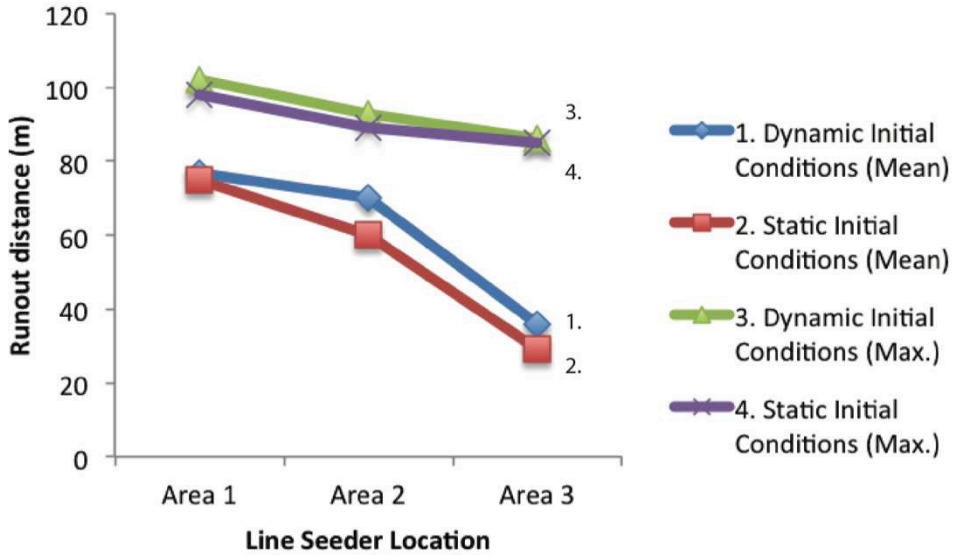

Figure 5.12: Plot of dynamic versus static initial velocity conditions against mean runout distance (from zero datum).

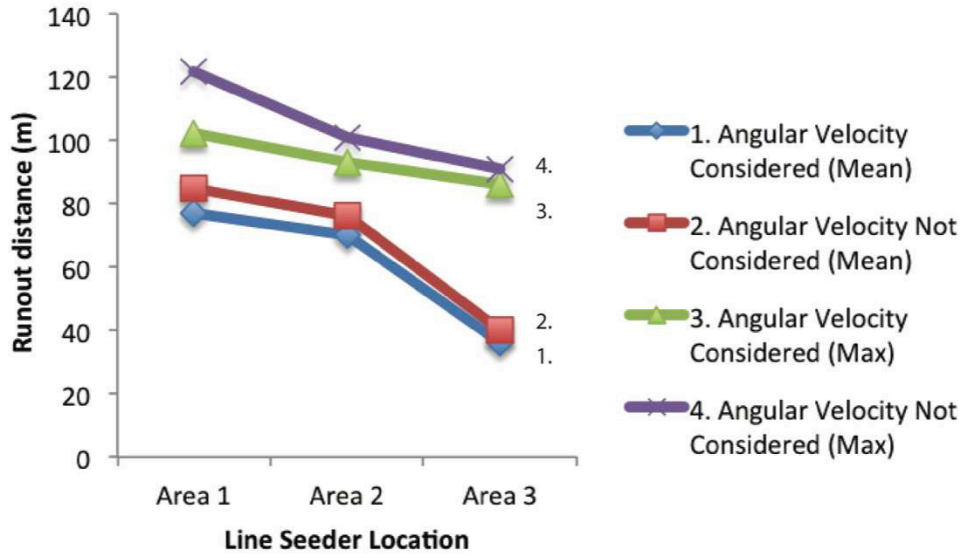

Figure 5.13: Plot of angular velocity consideration against runout distance (from zero datum).

5.7.4 Boulder Mass

Intuitively, the mass of a rock is an important input parameter to investigate due to the potential for larger rocks to cause more damage at the toe of the slope than smaller rocks due to their larger momentum and kinetic energy. This is based on simple physics in that if the rocks can initially gain the momentum required to convert potential energy into kinetic energy, then rocks with greater mass will travel at greater speed. This would create larger bounce heights and allow rocks to travel further, in addition to impacting barriers with greater force. All of these factors contribute to a greater hazard at the toe of the slope.

The mass of the rock does not affect rock runout or bounce height in RocFall™, rather it is only considered in calculating total kinetic energy (Stevens 1998), Results from testing the influence of boulder mass on rock runout proved there to be no relationship between boulder mass and rockfall runout (Table 5-6).

5.8 Rockfall Runout Analysis – Secondary Modelling Phase Variables

5.8.1 Restitution Coefficients – Talus Slope

As discussed in Chapter 1, coefficients of restitution are used in RocFall™ to represent the energy transfer that occurs as falling rocks contact the slope surface during downslope movement. This parameter therefore is expected to have considerable effect on the runout distance achieved by modelled rocks.

As expected, higher R_n and R_t values produced greater rockfall runout distances. This can be clearly seen in Table 5-7, where R_n=0.32, R_t=0.85 produced a mean runout distance of ~77m. In comparison, with the talus R_n=0.28, R_t=0.70, mean runout was ~56m, a reduction of 21m or 27% of the runout distance.

Table 5-7: Mean runout distance (metres from zero datum) under variable talus restitution coefficient conditions. Talus: phi=30°, slope roughness=2.5, Bedrock: R_n=0.35, R_t=0.85, phi=10°, slope roughness=0.

Slope Material	R_n	R_t	Approximate mean runout distance (m)	Approximate max. runout distance (m)
Talus	0.30	0.70	57	85
Talus	0.28	0.70	56	80
Talus	0.30	0.75	63	87
Talus	0.28	0.75	59	89
Talus	0.32	0.82	77	102

Figure 5.14 presents percentile data of horizontal endpoints of rockfall runout at the six previously specified statistical data collection locations (Figure 5.6). From these data, a number of observations can be made regarding the influence that Talus R_n and R_t have on the RocFall™ model:

- R_n(Talus)=0.32, R_t(Talus)=0.82 (the highest combination of restitution coefficients tested) has the lowest percentile of rock stopped at location F;
- R_n(Talus)=0.28, R_t(Talus)=0.70 (the lowest combination of restitution coefficients tested) has the highest percentile of rock stopped at location F
- The percentile stopped at or before Locations E and F increases with decreasing R_n and R_t values; and
- From this data set, it is difficult to judge which parameter (normal or tangential) has the greater influence over rockfall runout distance.

Interpretation of Results

The combination resulting in the lowest percentile of rock stopped at Location F can be interpreted to show that these conditions produce the greatest rock runout distance. In contrast, R_n=0.28 and R_t=0.70 conditions produce the shortest rock runout of the tested talus restitution coefficient conditions, and this is much closer to the observed runout as

determined from aerial photographs.

The effect of R_t is more marked when R_n is higher (such as when comparing plotted line one with line three, and line two with line four). This is most likely a reflection of the influence that the R_n value has on the model overall, and suggests that the overall runout is sensitive to a very small (0.02) data range when considering the talus restitution coefficients.

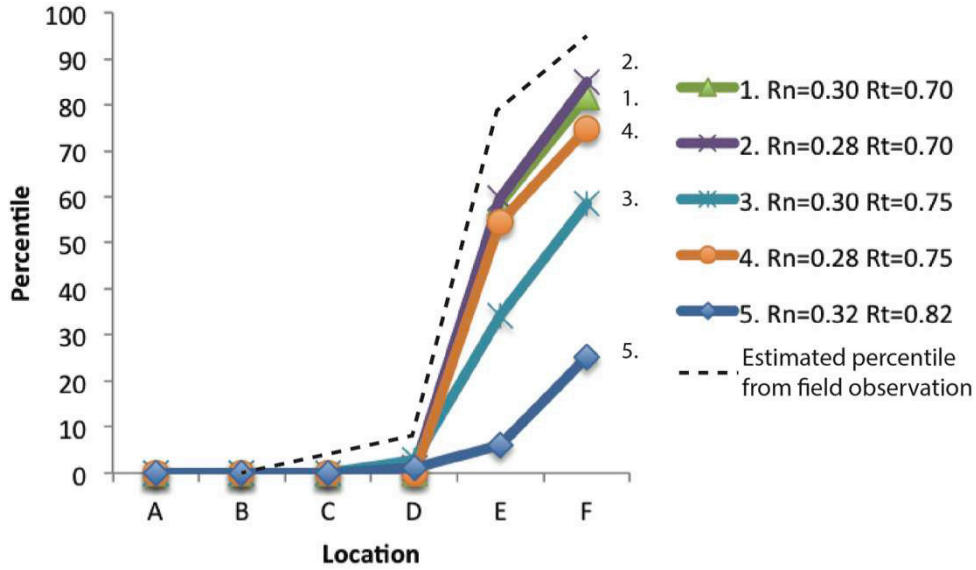

Figure 5.14: Plot showing the effect of varied talus restitution coefficients on rockfall runout as a percentile. Locations according to Figure 5.6.

Conclusions

Overall, it can be observed that the RocFall™ model was sensitive to variation in R_n and R_t values for talus. Considering the angle and length of the talus slope surface, falling rocks came into contact with this surface for a longer time due to the large number of their bounces being within this part of the slope. Therefore, it was expected that changes to the restitution coefficients of the talus slope would strongly affect the overall runout distance of the modelled rocks.

From Figure 5.14 it appears that the model is more sensitive to variation in R_t than R_n, however this is most likely an artifact of the larger range of values tested (ie. data range of 0.05 for R_t compared to 0.02 for R_n), rather than a result of the sensitivity of the software to

one coefficient more than the other.

Based on calibration of these results with rockfall runout observed in the field, talus restitution coefficients of R_n=0.28 and R_t=0.70 were considered the best representation of field data. In testing these with default bedrock restitution values (R_n=0.32, R_t=0.82), the maximum runout distance under these conditions was ~80m, with the mean distance ~56m. While ~80m is considered to be further than generally observed in the field, ~85% of the modelled rocks were stopped at or before Location F, which approximately represents the toe of the modelled slope. As shown in Figure 5.3, runout from the 13 June 2011 cliff collapse event exceeded the runout of the 22 February 2011 event in places. Therefore, a small percentage (e.g. ≤5%) of runout exceeding the toe of the modelled talus slope is accepted as being within field observations. The results of modelling with talus restitution coefficients of Rn=0.28 and Rt=0.70 which found 15% of rocks exceeding the toe of the slope are considered tolerable given that more parameters have still to be adjusted at this point of the calibration exercise.

5.8.2 Restitution Coefficients – Bedrock surface

As expected, the highest Bedrock R_n and R_t values produced the greatest mean runout distance (~60m), however, the lowest mean runout distance was obtained with R_n=0.45, R_t=0.75 (Table 5-8). This is not consistent with the expected outcome, where R_n=0.35, R_t=0.75 would be expected to produce the lowest mean runout distance in this analysis because of lower block rebound.. The interpretation of this result is discussed in the following section.

Figure 5.14 presents percentile data of the horizontal end-points of rocks under variable R_n and R_t (bedrock) conditions at the six locations chosen to measure runout statistics. From these data, it can be observed that:

- Some variation is observed when comparing plotted lines one and two (constant R_n=0.45, variable R_t); suggesting that R_t may be important;
- However, when R_n=0.35, variation in runout under Rt=0.75 and Rt=0.85 is very similar

(comparing plotted lines three and four);

- Under high R_n and lower Rt coefficient conditions, the highest percentile of rocks were stopped at Location F (~95%) as was observed.

Table 5-8: Mean runout distance (metres from zero datum) under variable talus restitution coefficient conditions. Talus: R_n=0.28, R_t=0.70, phi=30°, slope roughness=2.5, Bedrock: phi=10°, slope roughness=0.

Slope Material	R_n	R_t	Approximate mean runout distance (m)	Approximate max. runout distance (m)
Bedrock	0.45	0.85	60	100
Bedrock	0.45	0.75	50	75
Bedrock	0.35	0.75	53	77
Bedrock	0.35	0.85	56	80

As shown by Figure 5.14, the data range of runout distance for the bedrock restitution coefficients tested is relatively small, as shown by the closely spaced plots. This is also evident in the approximate mean runout distance data with the range being about 55 ± 5m.

Interpretation of Results

In contrast to the talus restitution coefficient runout plot (Figure 5.14), significant variation in runout percentile was noticeable only when comparing tangential restitution coefficients, under higher normal coefficient conditions. Runout percentile data was similar under all other tested conditions. This suggests that the model is more sensitive to tangential coefficient variation under higher normal coefficients, and is not greatly affected by bedrock coefficient variability.

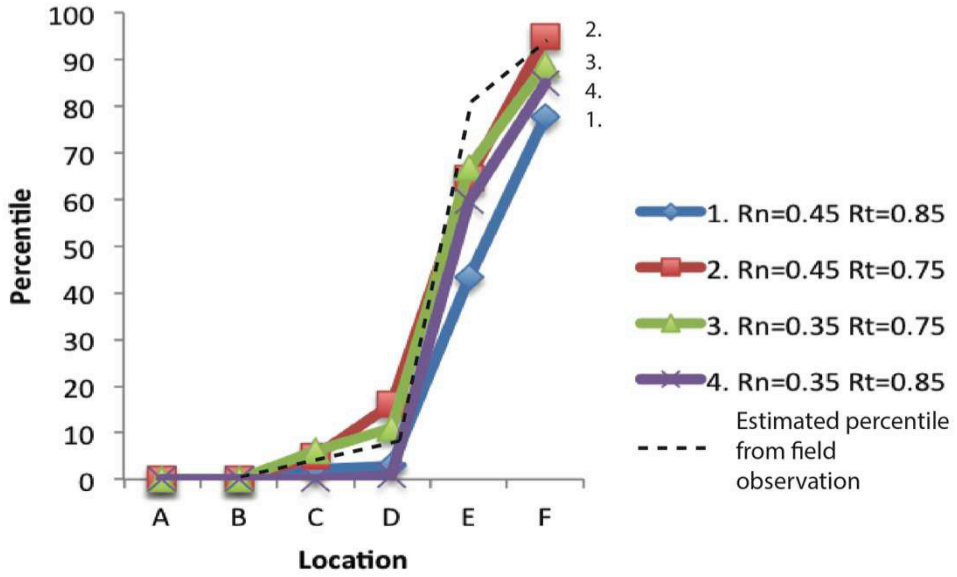

Figure 5.15: Plot showing the effect of varied bedrock restitution coefficients on rockfall runout as a percentile. Locations according to Figure 5.6.

Conclusions

The low sensitivity of the RocFall™ model to variation in bedrock restitution coefficients is most likely due to the morphology of the bedrock cliff section at Redcliffs. Because the area of the cliff modelled by bedrock (Source Area Zone) is very steep (~72°), the frequency and duration of contact between falling rock and the bedrock surface is very low. Therefore, the influence that this material has on the falling rock is minimal, given that most blocks are free falling.

Based on the data presented in this section, the bedrock restitution coefficients that best represent observed rockfall runout are R_n=0.45 and R_t=0.75. Under these conditions with the talus coefficients of R_n=0.28 and R_t=0.70 (as presented in Section 5.7.1), 95% of rockfall is stopped at or before Location F (~70m from the zero datum) which accords with on-site observations.

5.8.3 Restitution coefficient conclusions

Data from RocFall™ models presented in this analysis show observable variation in rockfall runout due to changes to both R_n and R_t conditions for the modelled talus slope (slope angle

~32°). In contrast, variation in restitution coefficients of the bedrock part of the slope (slope angle ~72°) had less effect on overall rock runout distance. The difference in model responses is due to the morphology of the different slopes, and the resulting frequency and duration of contact that a modelled rock will have with each surface.

From these analyses, it appears that both normal and tangential restitution coefficients have generally similar influence on rock runout. Within variable talus conditions, rockfall runout behaved according to expectations where runout was greater under higher restitution coefficients. Sensitivity to bedrock variation was less marked, and some restitution coefficient combinations produced results that were not expected. The significance of bedrock coefficient results is of less significance however, due to the slope profile and the materials present within Section E at Redcliffs.

By calibrating the models with observed field data as they were presented, and then including preceding results, the progressive modelling allowed the final restitution coefficient component of this model to reach a high level of accuracy. Through this method, ~95% of the modelled rocks were stopped at or before the measured toe of the slope.

5.8.4 Friction Angle and Slope Roughness – TLS-derived slope profile

Block friction angle and slope roughness are parameters used in RocFall™ to represent the block shape and the roughness of the slope surface, respectively (Section 1.5.2) Testing of these parameters against the modified TLS-derived slope profile produced unexpected results that led to the development of a simplified slope profile. Results and interpretations of varied friction angle and slope roughness parameters tested on both slope profiles are presented in this section, and Section 5.7.5.

TLS data used in modelling the slope profile behind the School Hall produced a section comprising ~280 individual vertices. Results from testing the influence of both block friction

angle and slope roughness on rockfall runout are presented in Figure 5.16. Table 5-9 provides the test matrix used to track variables in each test.

Results

From Figure 5.16, the following observations were made:

- There is not apparent relationship between slope roughness and rockfall runout distance.
- Friction angle showed a weak correlation with rockfall runout when talus material properties were tested (Figure 5.16a and d) although some friction angles ≥30° caused conflicting results.
- Friction angle did not appear to show a relationship with rockfall runout when the bedrock material was tested (Figure 5.16c and d).

Table 5-9: Test matrix for friction angle and slope roughness testing.

Plot label	Friction angle material tested	Slope roughness material tested
a	Talus	Talus
b	Bedrock	Bedrock
c	Bedrock	Talus
d	Talus	Bedrock

Interpretation of Results

From the TLS-derived slope model, it was concluded that slope roughness did not influence the rockfall runout distance, regardless of which slope surface material was tested. This is contrary to what was intuitively expected. The source of this result was the highly detailed data set used in generating the slope profile (Section 5.5.1). Simplifying the slope profile solved this issue, as noted in Section 5.5.2 and the results are detailed in the following section.

Block friction angle showed a weak visual correlation with rockfall runout distance under variable talus conditions, for most friction angles, but no statistical analysis was attempted. This was generally consistent with expectation, although the higher friction angles causing contradictory trend results were not anticipated. It was also expected that the talus friction angle would have greater effect on rockfall runout than was observed.

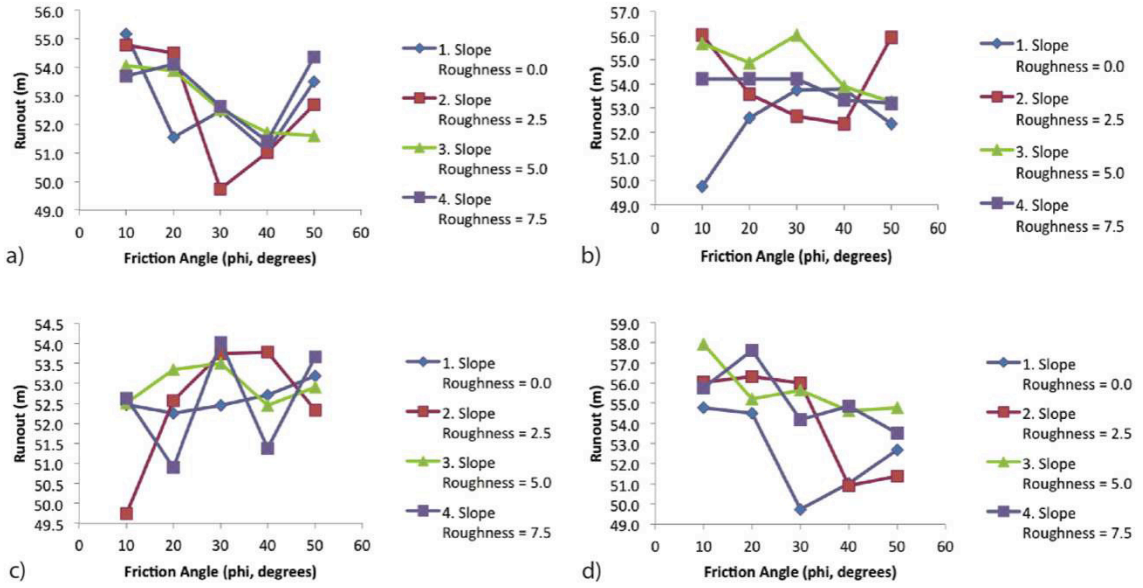

Figure 5.16: Plots showing relationships between runout distance (metres from zero datum) and block friction angle (phi, degrees) under various slope roughness conditions for TLS-derived slope profile, Section E, School Hall, Redcliffs. a) Friction angle (Talus) vs slope roughness (Talus); b) friction angle (Bedrock) vs slope roughness (Bedrock); c) friction angle (bedrock) vs slope roughness (Talus); d) friction angle (Talus) vs slope roughness (Bedrock). Note lack of significant relationships. n=100 rocks thrown per simulation (where one simulation is represented by a single point on a plot.

5.8.5 Friction Angle and Slope Roughness - Simplified Slope Profile

Following the lack of rockfall runout response to variation in slope roughness, the TLS-derived slope profile was simplified as described in Section 5.6.2 (Figure 5.17). The results of friction angle and slope roughness testing are presented in this section, and Table 5-9 summarises the tests conducted.

Results

Figure 5.17 shows the results of friction angle and slope roughness testing of the simplified slope profile. The results from this profile showed considerably clearer relationships between both block friction angle and slope roughness when plotted against rockfall runout. Key observations are:

- Figures 5.17a and d both showed a strongly inverse correlation between rockfall runout distance and talus friction angle
- Figure 5.17c showed a strong correlation between talus slope roughness and rockfall runout distance where rocks under lower talus slope roughness conditions travelled greater distances than those under higher talus slope roughness conditions.
- Slope roughness was also shown to have an effect on rockfall runout distance in Figures 5.17a and d, however this was less obvious due to the influence of the bedrock phi parameter in Figure 5.17c.
- Correlation between either friction angle and rockfall runout or slope roughness and runout was not observed under varied bedrock conditions

Interpretation of Results

The simplified slope profile produced expected results when block friction angle and slope roughness were tested to analyse the influence on rockfall runout. From these results (Figure 5.17), the talus slope was shown to strongly control the rockfall runout distance, whereas the bedrock slope showed very little influence. This is interpreted to represent the relatively long talus slope length that rocks have contact with, in contrast to the very short contact time that rocks have with the bedrock section of the slope, as seen in Section 5.8.1 with restitution coefficients.

Conclusions

These results showed that the RocFall™ software is particularly sensitive to variation in block friction angle and slope roughness when the slope segments are of sufficient length to

facilitate this. The optimal balance between measured slope detail and vertex length is not within the scope of this thesis.

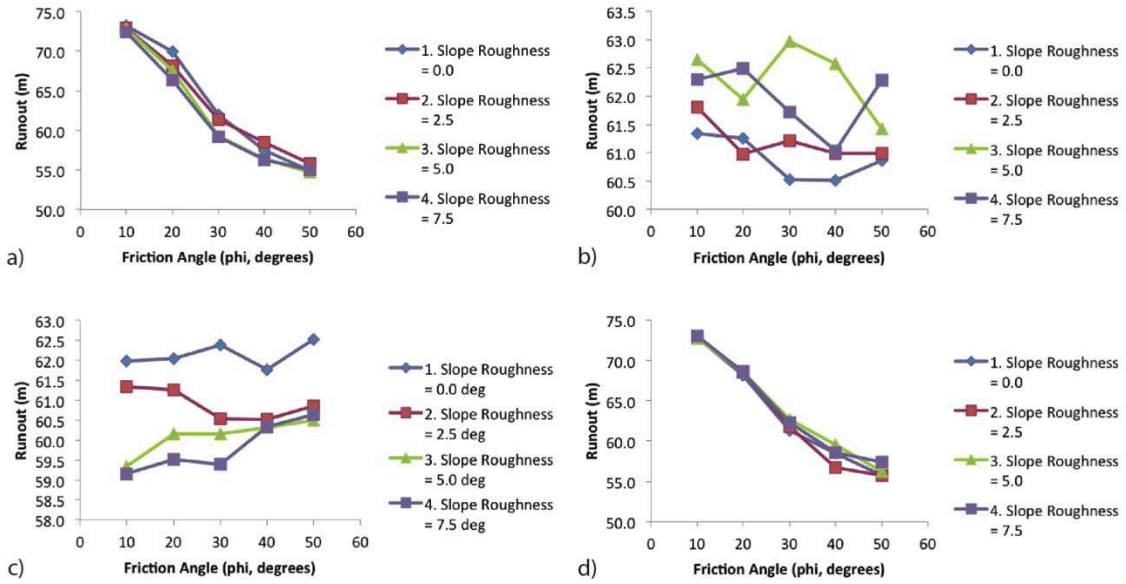

Figure 5.17: Plots showing relationships between runout distance (metres from zero datum) and block friction angle (phi, degrees) under various slope roughness conditions for the simplified slope profile, Section E, School Hall, Redcliffs. a) Friction angle (Talus) vs slope roughness (Talus); b) friction angle (Bedrock) vs slope roughness (Bedrock); c) friction angle (bedrock) vs slope roughness (Talus); d) friction angle (Talus) vs slope roughness (Bedrock). Note lack of significant relationships. n=100 rocks thrown per simulation (where one simulation is represented by a single point on a plot.

5.9 Kinetic Energy and Bounce Height

5.9.1 Initial Velocity

Kinetic Energy

As shown in Figure 5.18 and Table 5-6, the maximum kinetic energy ~71m from the zero datum (roughly the toe of the measured talus slope) was higher under dynamic conditions than static initial velocity conditions. The inverse relationship shown by both dynamic and initial velocity conditions represents decreasing kinetic energy with decreasing source area elevation, as expected.

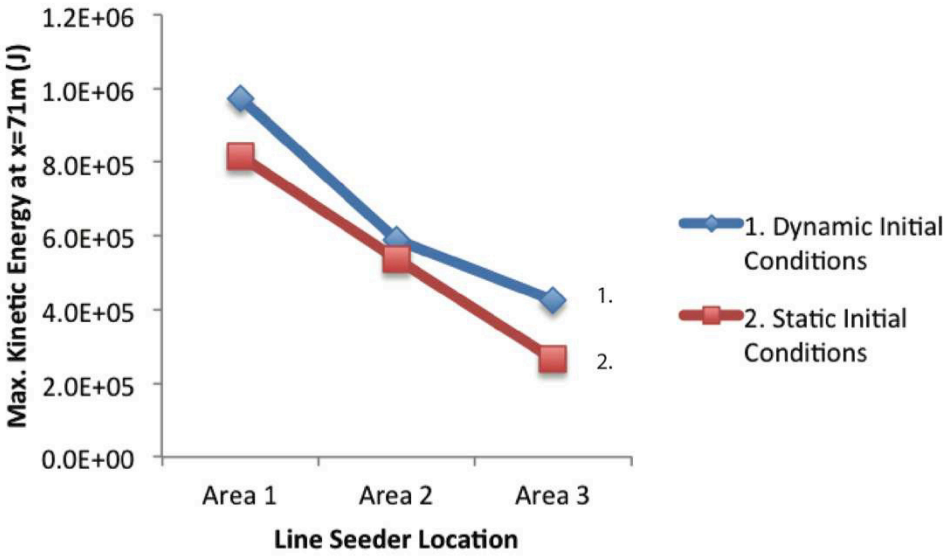

Figure 5.18: Plot of maximum kinetic energy at x=71m (from zero datum) under dynamic and static initial velocity conditions.

Bounce Height

Bounce height was modelled as bounce height envelope data, which represents the upper limit of bounce height above the slope surface at any location along the slope. These data are included in the simulation output in Appendix 6.2. Two observations were made:

- Along the entire length of the slope, dynamic initial conditions generally produced a higher bounce height envelope, however
- At the toe of the slope (~71m from the zero datum) static initial conditions modelled rocks passing higher than in dynamic conditions from both Source Areas 1 and 2 (Table 5-6)

While it was unexpected to observe higher bounce height envelopes under static conditions, modelled rocks, as in the field, are susceptible to being "ramped" up when they come into contact with rough or blocky slope surfaces. This can propel the rocks higher and further than might otherwise be expected. As such, the fact that results under static conditions were higher than under dynamic conditions does not mean the model is flawed, rather that this "ramping" could have significant effect on rock behavior under initial static or dynamic conditions. Protection systems therefore need to take this into consideration.

5.9.2 Angular Velocity

Kinetic Energy

As shown by Figure 5.19, maximum kinetic energy at the toe of the talus slope was strongly controlled by both the consideration of angular velocity in model calculations, and by the elevation of the source area (measured relative to the adopted datum). When angular velocity was not considered in calculations, kinetic energy at the toe of the slope was consistently higher than when angular velocity was considered. The inverse relationship between source area elevation (where Area 1 was highest and Area 3 the lowest) and maximum kinetic energy shows that source area elevation plays the most important role in determining kinetic energy (as expected).

Bounce Height

Bounce heights were also strongly controlled by the higher kinetic energy of rocks passing the toe of the slope under conditions where angular velocity was not considered. Under conditions where angular velocity was not considered, rocks passing the toe of the slope were ~5.0, 2.5, and 1.5m higher than when angular velocity was considered (from Source Areas 1, 2 and 3, respectively).

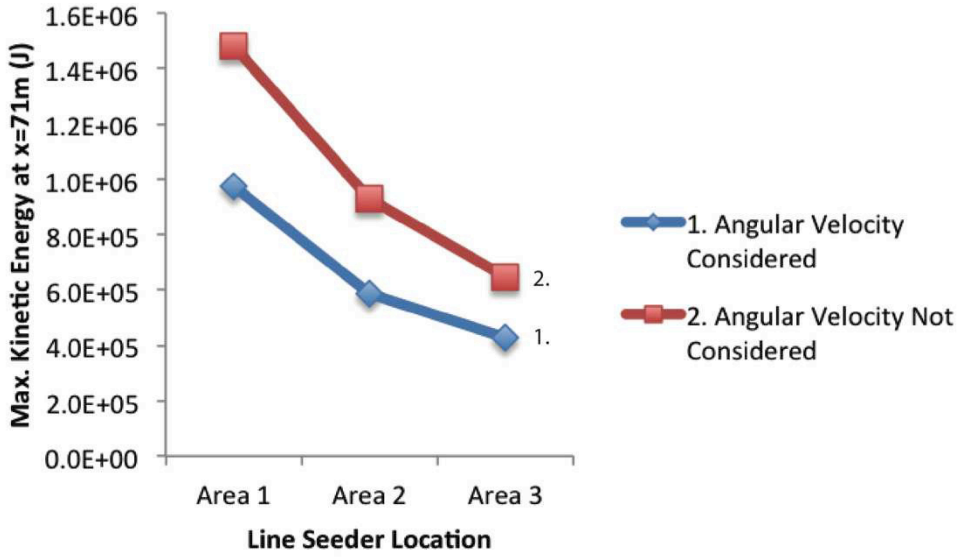

Figure 5.19: Plot of maximum kinetic energy at x=71m (from zero datum) where angular velocity is considered and not considered in calculations.

5.9.3 Boulder Mass

Kinetic Energy

As expected based on basic physics, boulder mass strongly controlled the maximum kinetic energy of modelled rocks passing the toe of the talus slope (Figure 5.20). Of the five boulder masses tested, observations were:

- Kinetic energy was directly related to boulder mass, as shown by the larger boulders (by mass) having the greatest kinetic energy, whereas the smaller rocks had the least;
- Kinetic energy was directly related to source area elevation as shown by the inverse correlation between kinetic energy and Line seeder location (this is more clearly evident for rocks with larger mass because the energy difference between Source Areas is much greater).

Bounce Heights

As shown in Table 5-6, bounce height was not influenced by the mass of modelled rocks. This is a limitation of the software that is discussed in Chapter 7.

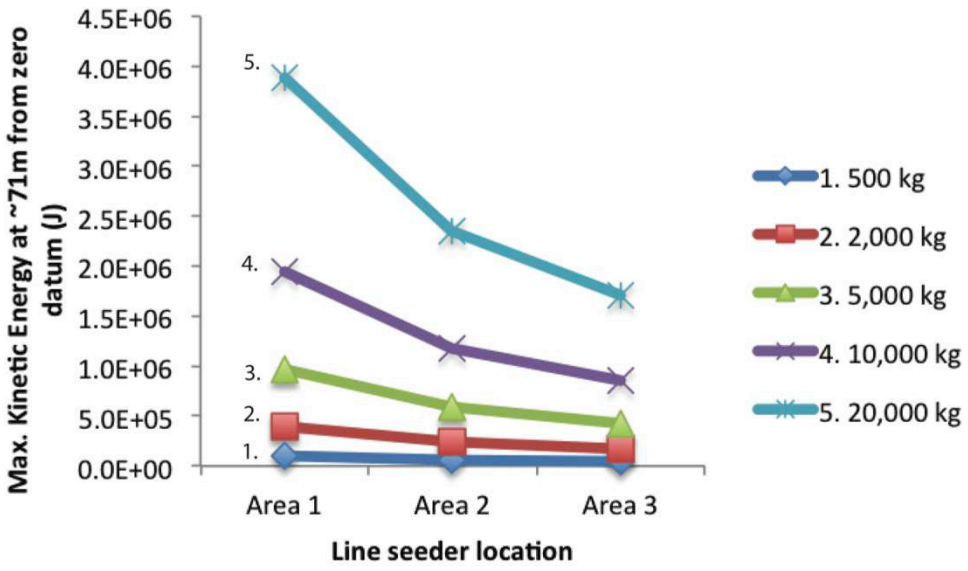

Figure 5.20: Plot of maximum kinetic energy at x=71m (from zero datum) for variable boulder masses.

5.10 "Best-Fit" Model

The "best-fit" model was developed following consideration of all testing and calibration discussed in this chapter. The TLS-derived slope profile was used to model the "best-fit" simulation because this profile produced more satisfactory calibration with field observations than the simplified version.

Selected Input Parameters

Selected input parameters for modelling Section E using the TLS-derived slope profile are summarised in Tables 5-10 and 5-11. As discussed in Section 5.7.4, slope roughness parameters have little influence on the TLS-derived slope profile, however the talus roughness value of 2.5 presented the most accurate rockfall runout results. Block friction and slope roughness values for the upper part of the slope also had little influence on the runout, however the values of phi=10° and slope roughness=0 produced marginally more realistic results (Appendix 6.4).

Table 5-10: Chosen input values for Primary Modelling Phase variables.

Variable	Chosen Input Value
Initial Velocity	Horizontal velocity=1.5ms^{-1}, Vertical velocity=1.0ms^{-1}
Angular Velocity	Considered in calculations
Boulder Mass	20,000kg

Table 5-11: Secondary Modelling Phase input parameters of "best-fit" model of cliff collapse at Redcliffs, based on Section E, School Hall. Standard deviation given in parentheses where applicable.

Material	R_n	R_t	Phi (degrees)	Slope Roughness (degrees)
Bedrock	0.45 (0.04)	0.75 (0.04)	10 (2)	0.0
Talus	0.28 (0.04)	0.70 (0.04)	30 (2)	2.5

Results of "Best-Fit" Model

The selected primary and secondary phase modelling parameters (Tables 5-10 and 5-11) produced rockfall runout results that correlate very well with field observations (Table 5-12). Both maximum runout distance and the distribution of rock end-points along the length of the slope were used in calibration. The distribution of rocks from the "best-fit" model measured as a cumulative percentage at the six specified data collection locations is presented in Figure 5.21, and end-point locations are shown in Figure 5.22. These results show 5% of modelled rockfall exceeding the toe of the slope profile, which is within the acceptable range given the comparison with June 2011 runout

.

Table 5-12: Summary of roclkfall modelling data from "Best-Fit" Model, Section E, Redcliffs. Source Area 1 used for all analysis of this model as this unit represents the "worst-case scenario".

Boulder Mass (kg)	Max. Runout (m)	Mean Runout (m)	Number of rocks passing x=71m	Max. Kinetic Energy at x=71m (J)	Max. Bounce Height at x=71m (m)
5,000	75	50	5	110,000	0.5
10,000	75	50	5	210,000	0.5
20,000	75	50	5	430,000	0.5

The worst-case scenario presented by the chosen rockfall model suggests maximum kinetic energy of modelled rocks reaching the toe of the slope (~70m from the zero datum) to be 430,000J (430 kJ), and maximum bounce heights of ~0.5m above the slope. These results are considered acceptable, although field verification of bounce heights is difficult so these output values require further investigation for better calibration.

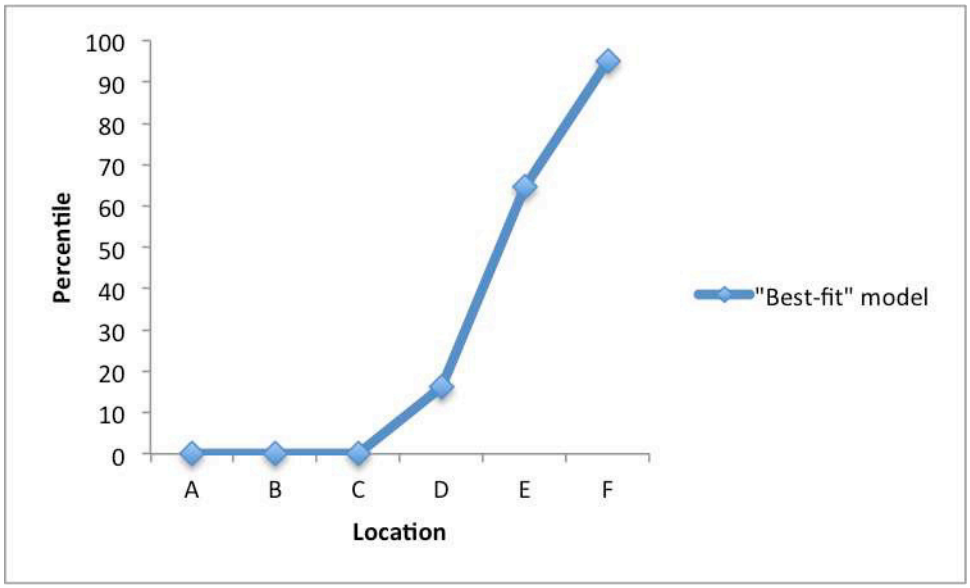

Figure 5.21: Plot of cumulative percentile of rocks stopped at or above specified Locations for the "best-fit" model, Section E, Redcliffs.

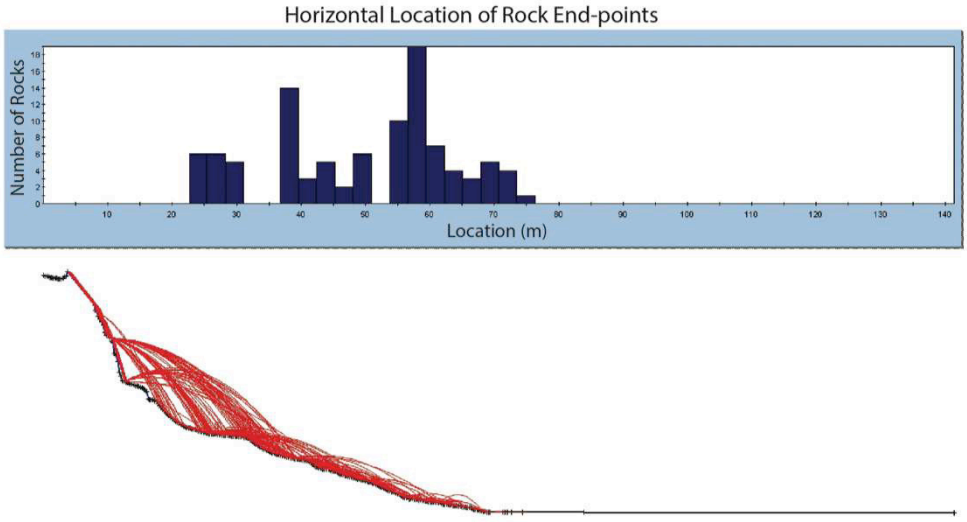

Figure 5.22: Horizontal Location of rock end-points for "best-fit" model, Section E, Redcliffs.

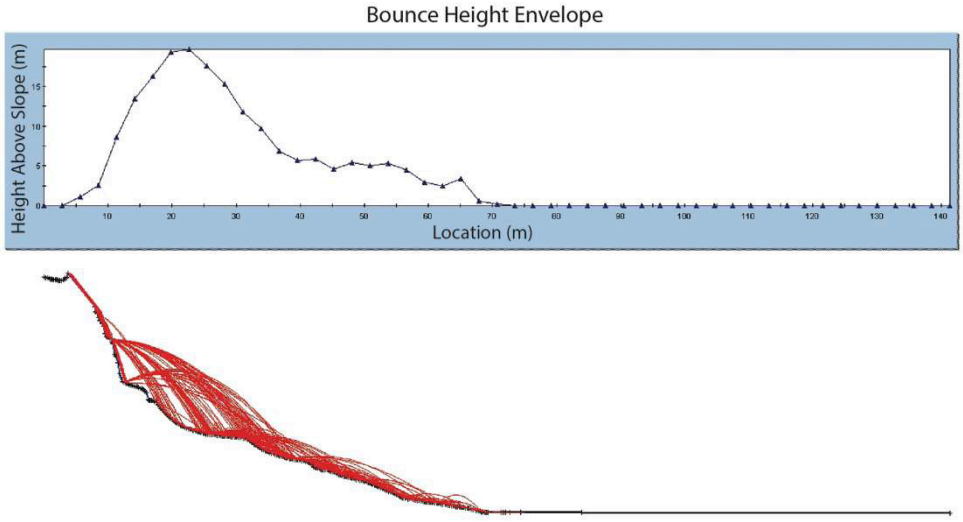

Figure 5.23: Bounce height envelope plot of "best-fit" model, Section E, Redcliffs.

5.11 Synthesis

- Rockfall source area elevation has proven to be a major influence on rockfall runout across all modelled output parameters (runout distance and distribution, bounce height and kinetic energy
- Coefficients of restitution for the lower slope (talus) portion of the slope profile also exhibited significant control on simulating rockfall, more so than the restitution coefficients of the upper (bedrock) slope area. This is consistent with modelled rocks spending less time in contact with the upper slope section during predominantly free-fall phase of trajectory compared to the lower slope area where rocks are more likely to roll and bounce down the talus slope.
- The modelled slope roughness parameter had very little effect on rockfall runout when using the TLS-derived slope profile due to the closely spaced vertices effectively cancelling out roughness variation of neighbouring vertices. By reducing the number of slope vertices from ~280 to 20, the slope roughness parameter had more effect on runout, however the TLS-derived slope profile was adjudged to present a better representation of rockfall runout observed in the field.

- Input parameters calibrated with field observations from this section (School Hall Section) can be applied to other section lines at Redcliffs to model future rockfall runout in other locations.

6 Modelling of Sections A – D and Discussion

6.1 Introduction

This chapter presents the other four section lines analysed at Redcliffs in terms of interpreted engineering geology cross sections, and results from RocFall™ modelling. These four section lines have been used to test the accuracy of the rockfall model developed for Section E – School Hall by applying the model and comparing results to field observations. Discussion of modelling results from these sections, and the implications of these results on rockfall remediation at Redcliffs, is presented in Section 6.7.

6.2 Methodology

The section lines selected for rockfall modelling at Redcliffs are displayed in Figure 6.1. Sections A – D are discussed in this chapter, and Section E is discussed in detail in Chapter 5. As discussed in Section 4.3.2, Sectors 4 and 5 (including Section Lines F and G) were included in initial field reconnaissance mapping, however they have been excluded from further detailed analysis and RocFall™ modelling.

As with the School Hall Section (Chapter 5), slope profile data used in creating engineering geology models, and for defining the slope for rockfall modelling, was obtained from Terrestrial Laser Scan (TLS) surveys conducted by GNS Science during March 2011.

Rockfall modelling was undertaken using RocFall™ 4.0 software using the input variables obtained through development of the model for the School Hall Section. Table 6-1 summarises the critical input parameters developed throughout that process, and as used in modelling Sections A-D. From this data rockfall runout, kinetic energy and bounce height data were analysed. Rockfall runout has been analysed primarily using maximum end-point data and graphical distribution plots. Unlike Section E, specific locations along the length of the slope were not identified to create more detailed distribution analysis, because the aim of this chapter is to assess the accuracy of the model across a greater number of slopes.

Figure 6.1: Sector boundary (left) and modelling section line (right) location maps, Redcliffs.

Table 6-1: Summary of input variables used in modelling Sections A-D at Redcliffs. Values selected following detailed analysis of rockfall model for School Hall Section E. Note values in parenthesis represent standard deviation values.

Variable	Values Selected	
"Primary Modelling Phase"		
Initial Velocity	Horizontal velocity = 1.5ms^{-1} (0.0) Vertical Velocity = 1.0ms^{-1} (0.0)	
Angular Velocity	Considered in calculations	
Boulder Mass	500kg; 5,000kg; 20,000kg	
"Secondary Modelling Phase"		
Restitution Coefficients (R_n and R_t)	"Bedrock" R_n = 0.45 (0.04) R_t = 0.75 (0.04)	"Talus" R_n = 0.28 (0.04) R_t = 0.70 (0.04)
Phi	10° (2)	30° (2)
Slope Roughness	0°	2.5°

Rockfall source areas are defined as the upper 10m of the cliff face, regardless of geological units. This is because input parameters have not been tested for specific geological units (for example to distinguish welded from brecciated ignimbrite units) because of time constraints. Additionally, based on runout, kinetic energy, and bounce height data analysed in the School Hall Section (Chapter 5), the biggest influence on all three of these factors is source area elevation. By selecting the upper 10m of each section, models represent the worst-case situation at each location.

6.3 Section A – Main Road

Section A is the most northerly section line in the field area at Redcliffs (Figure 6.1), approximately parallel with Main Road. This section was selected for modelling as it represents an area of the cliff where debris runout is within 30m of four separate dwelling structures (Figure 6.1), so modelling is useful to assess implications of future rockfall on the long term occupation or abandonment of these properties. Section A also afforded closer

viewing of the upper ignimbrite units than the other sections, due to the units dipping towards the northeast and being exposed essentially in the direction of density current flow.

6.3.1 Engineering Geology Model

Figure 6.2 displays the engineering geology model of the volcanic units observed at Section A at Redcliffs. Following the general stratigraphy discussed in Section 3.2, this model shows the orange tuff unit ~10m thick overlying an unknown thickness of obscured basal lava flows. The basaltic ignimbrite units that overlie the orange tuff total ~20m thickness, with a brecciated ignimbrite unit dominating the majority of the exposed cliff face and having ~10m observed thickness. A thin lens of welded ignimbrite is present in the upper 5m of the cliff face. The talus apron has an overall gradient of ~32°.

6.3.2 Runout Analysis

RocFall™ modelling was conducted using input variables specified in Table 6-1, the rock runout results from which are displayed in Figure 6.3 and Table 6-2. Because rock end-point locations are not affected by the mass of the modelled rocks, horizontal rock end-point data is identical for all three modelled rock mass values (500kg; 5,000kg; and 20,000kg).

From Figure 6.3 and Table 6-2, it can be seen that modelled rock runout is similar to the measured slope profile runout. Some 99% of the modelled rocks stopped upslope of the measured toe of the slope (~43m from the zero datum) at Section A, with a maximum horizontal end-point of ~50m from the zero datum. The toe of the slope is defined, as for the School Hall Section (Chapter 4), by the obvious change in slope at the base of the talus apron. In most areas the material forming the underlying ground is marine sediment, and mostly beach sand (Chapter 1; Brown & Weeber 1992).

From the results presented in this section, the rockfall model provided data that was similar to the runout observed along the measured profile at Section A. The distribution of the rocks down the slope is consistent with the measured profile, and variability is interpreted as those

surfaces where a number of neighbouring slope vertices are of sufficiently low gradient to facilitate the stopping of rocks from passing downslope.

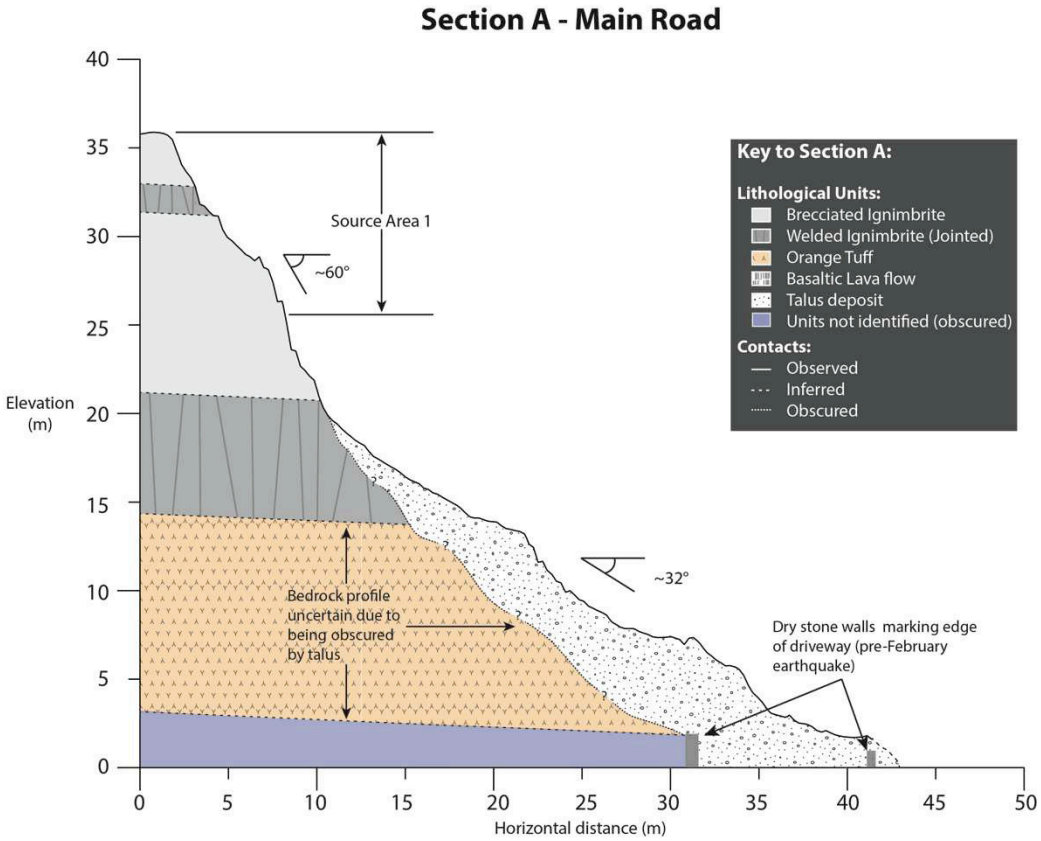

Figure 6.2: Schematic engineering geology model for Section A - Main Road.

Table 6-2: Summary runout results for modelled Section A at Redcliffs.

Mean distance travelled (m)	Maximum distance travelled (m)	% of rocks passing measured toe of slope
30.1	50.3	1.0

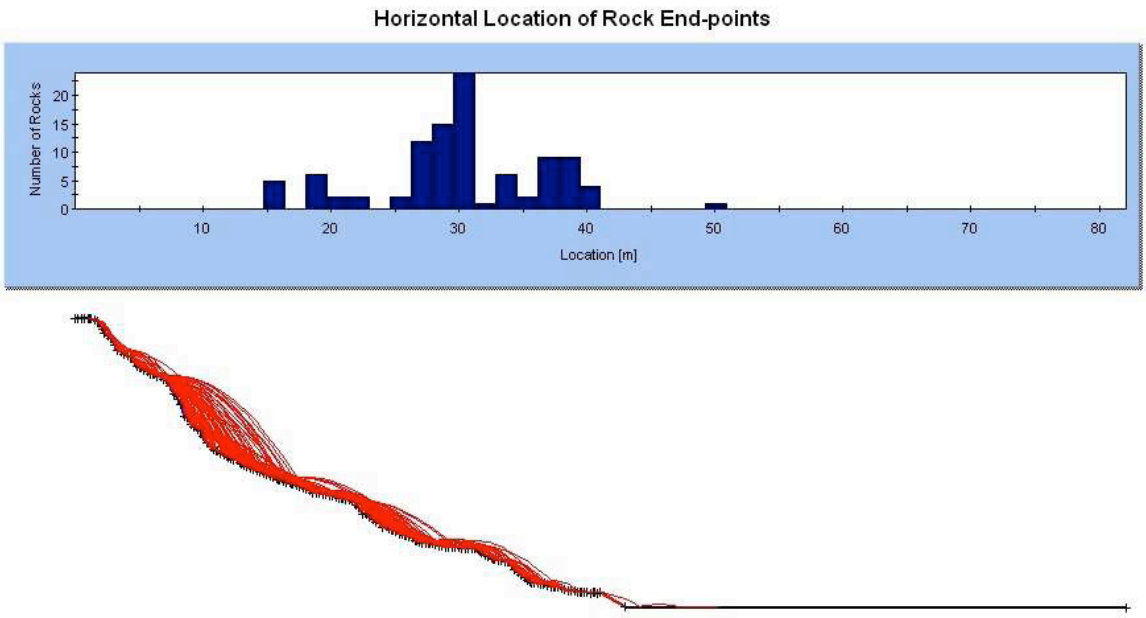

Figure 6.3: RocFall™ modelling output showing Horizontal Location of Rock End-points for Section A at Redcliffs. Upper plot shows rock end-point distribution graphically as a bar graph, while the lower plot represents the paths travelled by each of the 100 rocks sampled. Note that the vertical axis of the lower plot has been reduced post-modelling, so the slope of the profile appears flatter than actually measured.

6.3.3 Kinetic Energy and Bounce Height Analysis

Total kinetic energy of modelled rocks at the toe of the talus slope is presented in Table 6-3. As proven by basic physics and discussed in Section 5.5.4, the kinetic energy of a rock is directly related to its mass. As such, modelled kinetic energy increases with increasing boulder mass so for modelled rocks of 20,000kg, maximum kinetic energy of 690,000J (690kJ) was recorded at the toe of the slope, whereas the maximum kinetic energy of the 500kg rocks was 1,700J (1.7kJ). In this instance, only 1% of the modelled rocks passed the toe of the slope.

Similar to horizontal rock end-points, the bounce height of modelled rocks are not affected by variation in the mass of the rock. Figure 6.4 and Table 6-4 show the results of rockfall modelling with respect to maximum bounce height, referred to as the bounce height envelope, measured in metres from the slope surface. For Section A, the maximum bounce height at any point on the slope was ~7.5m, approximately 10m from the zero datum. This

corresponds to a steep part of the cliff face where rocks have bounced over the top. At the toe of the slope (~43m from the zero datum), the maximum bounce height was ~1m above the slope surface.

Table 6-3: Total kinetic energy summary at the toe of the slope (~43m from the zero datum) for Section A, Redcliffs.

Modelled Boulder Mass (kg)	Mean kinetic energy at x=43m (J)	Maximum kinetic energy at x=43m (J)	% of rocks passing measured toe of slope
500	1,700	1,700	1.0
5,000	17,000	17,000	1.0
20,000	690,000	690,000	1.0

Table 6-4: Summary of bounce height envelope data for all modelled boulder masses for Section A, Redcliffs.

Maximum bounce height above slope (m)	Maximum bounce height at toe of slope (m)
7.5 (11m[1])	1.0 (43m[1])

[1]Values in parenthesis represent approximate horizontal distance from zero datum.

6.4 Section B – Gardens

Section B is located on a southeast-facing section of the cliff in an area where very large blocks (up to 250m^3) of basaltic ignimbrite have come to rest along the talus slope (see Figure 4.3). The section line is ~40m from a building, but is at a different orientation such that the structure is not within the runout zone of the section when modelled in 2D by RocFall™.

6.4.1 Engineering Geology Model

Figure 6.5 shows the schematic engineering geology model for Section B at Redcliffs. The lower 10m of the talus slope was obscured from view of the TLS due to overhanging trees, so

this part of the slope profile was inferred from aerial photographs and field observations, as indicated by the dashed line on Figure 6.5.

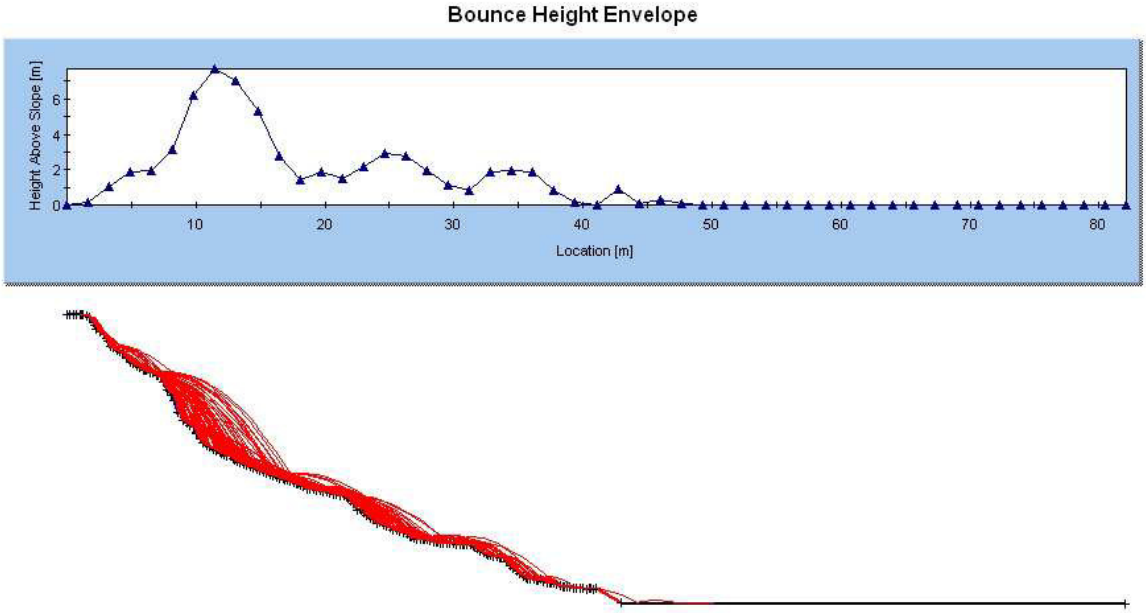

Figure 6.4: RocFall™ modelling output showing the Bounce Height Envelope for Section A, Redcliffs. Upper plot shows the maximum bounce height of all modelled rocks as a line graph, while the lower plot represents the paths travelled by each of the 100 rocks sampled. Note that the vertical axis of the lower plot has been reduced post-modelling, so the slope of the profile appears flatter than actually measured.

The talus slope reaches ~25m above ground level (AGL) in this Section, obscuring the basal lava flows, the orange tuff, and the lower welded basaltic ignimbrite unit. Thicknesses of these units have been interpreted from limited exposures adjacent to the section line. Above the talus, the basaltic ignimbrite unit comprises the ≥15m exposed part of the cliff at Section A, with that showing brecciated ignimbrite apart from a ≤5m thick welded ignimbrite band near the top of the exposure. The overall gradient of the talus slope is ~33°, however the slope is considerably steeper in the upper 8m of the talus slope where a number of very large boulders have been stopped at the top of the talus slope.

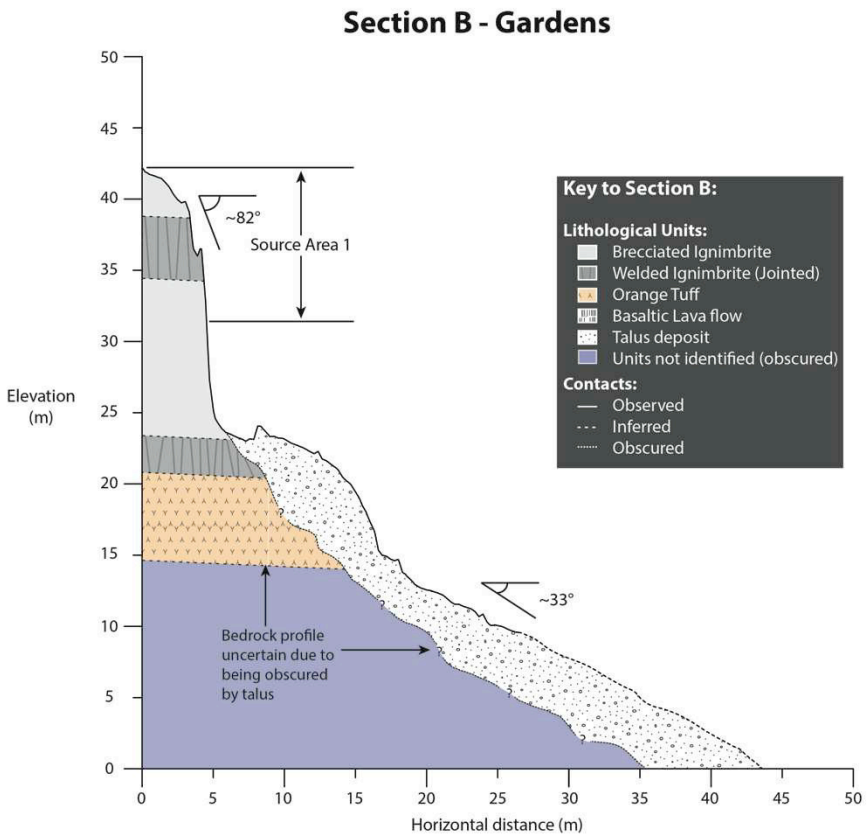

Figure 6.5: Schematic engineering geology model of Section B - Gardens.

6.4.2 Runout Analysis

As shown in Figure 6.6 and Table 6-5, modelled rockfall runout data provided results very similar to runout observed from field observations and aerial photograph interpretation. The maximum distance travelled by a modelled rock was ~44m. Therefore 100% of modelled runout stopped within the limits of the measured profile, consistent with field observations (Figure 6.5).

As shown by Figure 6.6, the distribution of rocks along the length of the modelled slope reflects rocks stopping along areas of the slope where the gradient was lower. Some 73% of modelled rocks came to rest less than 15m (horizontally) from the zero datum, and up to ~93% had stopped before 25m from the zero datum (horizontally). These two zones, particularly the area from 5-15m horizontally from the zero datum, represent lower gradient

areas of the slope, which obviously facilitates the entrapment of rock. This is consistent with field observations, as the area ~5m from the horizontal datum represents the top of the talus slope. The modelled results therefore reflect the distribution observed in the field.

Runout did not exceed the measured toe of the slope during modelling due to the large rock catch area created by the low-gradient upper talus surface. This is caused by the very large blocks that have fallen prior to March 2011, which act to contain a large volume of material near the top of the talus.

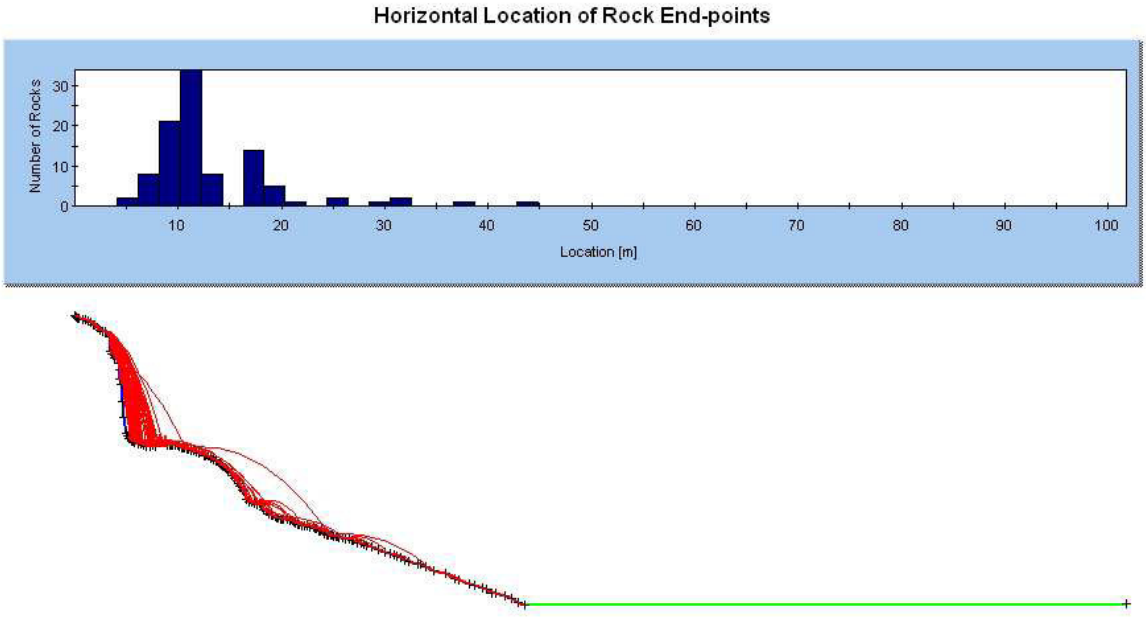

Figure 6.6: RocFall™ modelling output showing Horizontal Location of Rock End-points for Section B at Redcliffs. Upper plot shows rock end-point distribution graphically as a bar graph, while the lower plot represents the paths travelled by each of the 100 rocks sampled. The green slope on lower graph shows the material has been modelled as vegetated soil cover using RocFall™ default parameters. Note that the vertical axis of the lower plot has been reduced post-modelling, so the slope of the profile appears flatter than actually measured.

Table 6-5: Summary runout results for modelled Section B at Redcliffs.

Mean distance travelled (m)	Maximum distance travelled (m)	% of rocks passing measured toe of slope
13.5	43.7	0.0

6.4.3 Kinetic Energy and Bounce Height Analysis

Total kinetic energy at the toe of the slope for Section B ranged from ~1,300 – 50,000J (1.3-50kJ) for the 500, 5 000 and 20 000kg rocks modelled (Table 6-6). As with Section A, the increase in kinetic energy relates to the increase in boulder mass.

Table 6-6: Total kinetic energy summary at the toe of the slope (~43m from the zero datum) for Section B, Redcliffs.

Modelled Boulder Mass (kg)	Mean kinetic energy at x=43m (J)	Maximum kinetic energy at x=43m (J)	% of rocks passing measured toe of slope
500	1,300	1,300	1.0[1]
5,000	12,500	12,500	1.0[1]
20,000	50,200	50,200	1.0[1]

[1]Location of data collector for kinetic energy is ~1m upslope of the measured toe of the slope.

Maximum bounce height data for Section B are presented in Figure 6.7 and Table 6-7. From these data, it can be seen that the maximum bounce height of modelled rocks is ~10.5m above the slope surface, and this occurs at a break in slope where rocks bounce and fall over a near-vertical section of the cliff face. At the toe of the slope the maximum bounce height is zero, suggesting any rocks reaching thins point are rolling at this point on the slope.

Table 6-7: Summary of bounce height envelope data for all modelled boulder masses for Section B, Redcliffs.

Maximum bounce height above slope (m)	Maximum bounce height at toe of slope (m)
10.5 (6m[1])	0.0 (44m[1])

[1]Values in parenthesis represent approximate horizontal distance from zero datum.

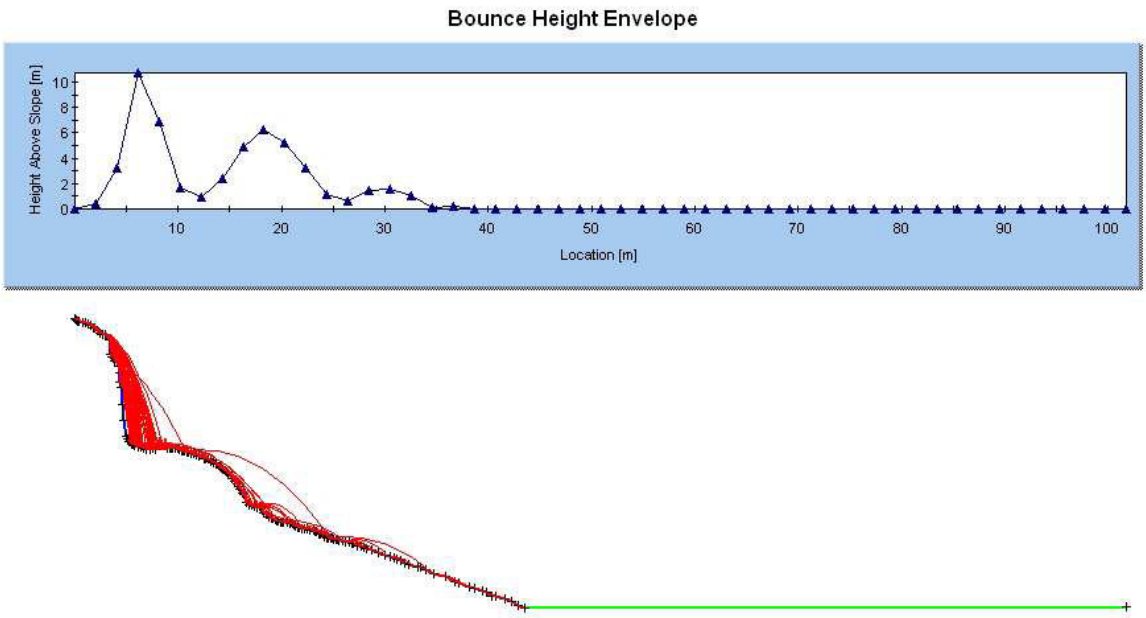

Figure 6.7: RocFall™ modelling output showing the Bounce Height Envelope for Section B, Redcliffs. Upper plot shows the maximum bounce height of all modelled rocks as a line graph, while the lower plot represents the paths travelled by each of the 100 rocks sampled. Note that the vertical axis of the lower plot has been reduced post-modelling, so the slope of the profile appears flatter than actually measured.

6.5 Section C

Section C is located in the northwest corner of the cliff face, near the boundary between Sectors 2 and 3 (Figure 6.1). In the general path of this section is a residential dwelling, located approximately 30m from the toe of the observed rockfall runout.

6.5.1 Engineering Geology Model

Figure 6.8 shows the schematic engineering geology model of Section C for Redcliffs. As with Section B (see section 6.4), the lower ~10m of the talus slope was obscured from view of the TLS during slope profile data collection, so this part of the slope has been inferred from field observations and aerial photograph interpretation. The talus slope in Section C reaches ~15m AGL, providing ~40m of exposed volcanic units in the cliff face. This exposed section consists of ~9m of orange tuff, overlain by almost 30m of basaltic ignimbrite, which is interpreted to be comprised of a lower ~13m of welded ignimbrite with ~16m of brecciated ignimbrite

above. The gradient of the talus slope is the lowest of any of the modelled sections at Redcliffs at~26°, the others all being in the range 28-33°.

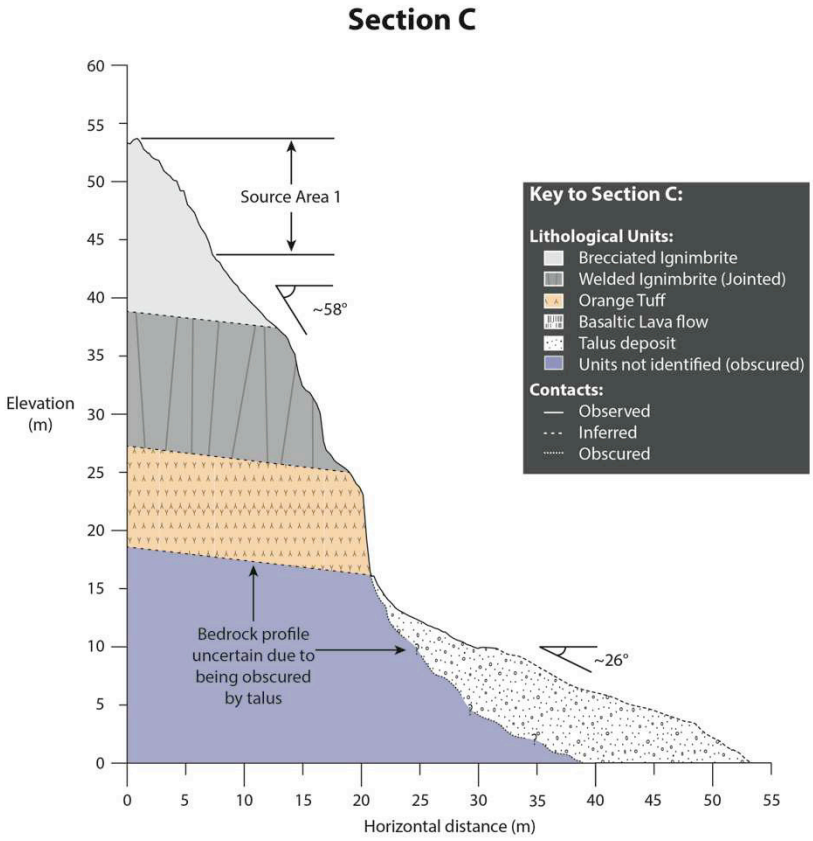

Figure 6.8: Schematic engineering geology model of Section C.

6.5.2 Runout Analysis

Horizontal end-point location data presented in Table 6-8 and Figure 6.9 show the modelled results calibrate with rockfall runout observed in the field and through aerial photograph interpretation. The maximum distance travelled by modelled rocks was 62m, with 23% of rocks passing the existing measured toe of the slope. Rocks stopped moving within the range ~30-65m from the horizontal zero datum. This is consistent with rocks stopping along the length of the talus slope, and with some continuing beyond onto the grassed area.

Table 6-8: Summary runout results for modelled Section C at Redcliffs.

Mean distance travelled (m)	Maximum distance travelled (m)	% of rocks passing measured toe of slope
47.0	62.0	23.0

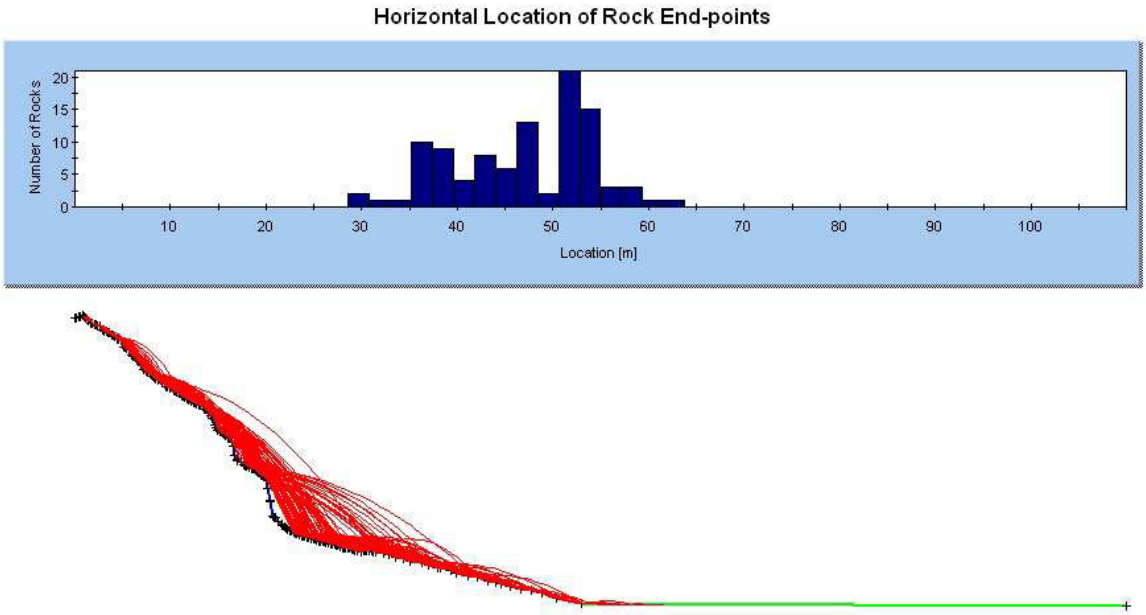

Figure 6.9: RocFall™ modelling output showing Horizontal Location of Rock End-points for Section C at Redcliffs. Upper plot shows rock end-point distribution graphically as a bar graph, while the lower plot represents the paths travelled by each of the 100 rocks sampled. The green slope on lower graph shows the material has been modelled as vegetated soil cover using RocFall™ default parameters. Note that the vertical axis of the lower plot has been reduced post-modelling, so the slope of the profile appears flatter than actually measured.

While almost 25% of runout exceeded the toe of the slope, this is interpreted to be the result of the talus slope acting as a natural ramp for moving rocks. In contrast to Sections A and B where maximum modelled runout was very similar to that observed following the 22 February 2011 cliff collapse event, in the case of modelling for Section C the shape of the talus slope enabled ~23% of modelled rocks to exceed the measured toe in that there were no flat benches or hollows to trap blocks or boulders.

6.5.3 Kinetic Energy and Bounce Height Analysis

Kinetic energy results from Section C show a maximum kinetic energy at the toe of the slope (~53m from the zero horizontal datum) of 2,100,000J (2100kJ), when 20,000kg rocks are modelled (Table 6-9).

The kinetic energy for modelled Section C is considerably larger than the maximum kinetic energy recorded for Sections A or B, and this is interpreted to be the result of the higher source rock elevation and the greater drop height (H*=38m).

Table 6-9: Total kinetic energy summary at the toe of the slope (~43m from the zero datum) for Section C, Redcliffs.

Modelled Boulder Mass (kg)	Mean kinetic energy at x=53m (J)	Maximum kinetic energy at x=53m (J)	% of rocks passing measured toe of slope
500	13,000	52,000	23.0
5,000	132,000	520,000	23.0
20,000	530,000	2,100,000	23.0

Maximum bounce height recorded for modelling of Section C showed rock bouncing 11m above the slope surface 22m from the zero horizontal datum, and rocks bouncing <1m high at the toe of the slope. As with other modelled sections, the maximum value recorded for the whole slope occurred at the steepest part of the slope, where rock was propelled off the slope. This is not strictly a "bounce height", but a fall distance controlled by slope geometry.

Table 6-10: Summary of bounce height envelope data for all modelled boulder masses for Section C, Redcliffs.

Maximum bounce height above slope (m)	Maximum bounce height at toe of slope (m)
11 (22[1])	1.0 (53[1])

[1]Values in parenthesis represent approximate horizontal distance from zero datum.

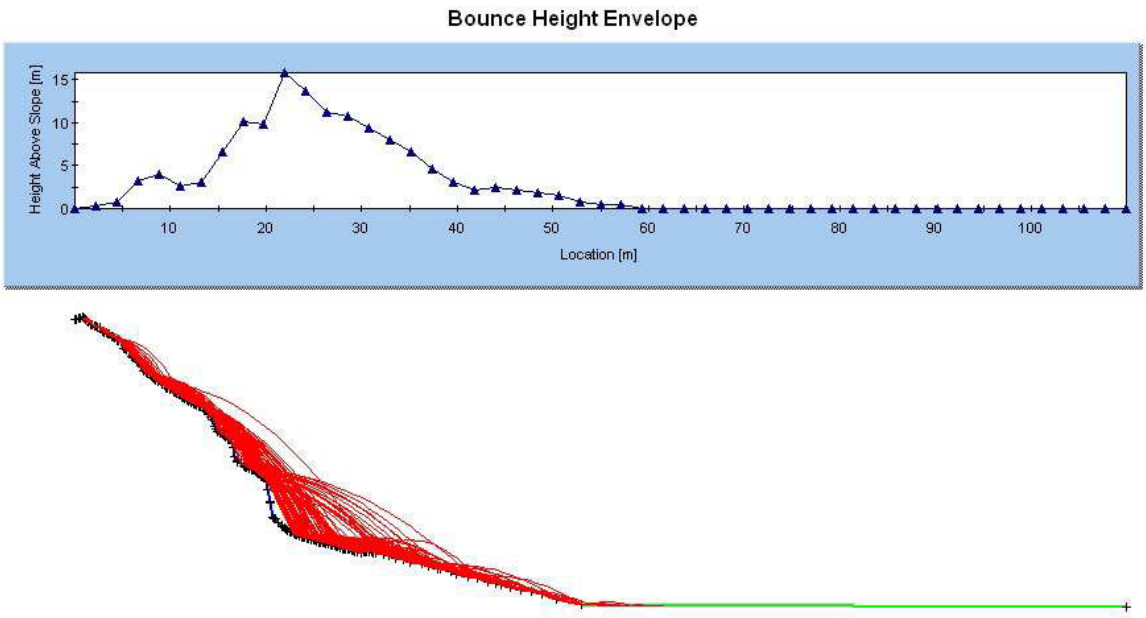

Figure 6.10: RocFall™ modelling output showing the Bounce Height Envelope for Section C, Redcliffs. Upper plot shows the maximum bounce height of all modelled rocks as a line graph, while the lower plot represents the paths travelled by each of the 100 rocks sampled. Note that the vertical axis of the lower plot has been reduced post-modelling, so the slope of the profile appears flatter than actually measured.

6.6 Section D

Section D is located near the centre of the field area at Redcliffs, approximately 25m northwest of, and parallel to, School Hall Section E (Figure 6.1). The location of Section D has been chosen as it provides a section similar to Section E in orientation and proximity to buildings, the base of the section being ~15m from two residential dwellings. It displays a steeper lower cliff face than Section E, caused by a much lower talus apron at the base of the slope and a correspondingly greater maximum drop height (H*=54m). Another significant feature of Section D is that the toe of the slope is unobstructed, in contrast to the rock bund, rockfall fence, and other structures that intercepted the path of rockfall at Section E.

6.6.1 Engineering Geology Model

The schematic engineering geology model of Section D is shown in Figure 6.11. From this figure, the exposed basal lava flows are prominent, comprising the lower ~27m of the cliff face. Overlying the lavas, the orange tuff unit shows the best evidence of the bench feature

that is visible in various places throughout the cliff face. The influence of this feature is discussed in Sections 6.6.2 and 6.6.3. Above the orange tuff, the welded ignimbrite unit is ~10m thick, with brecciated ignimbrite comprising the remaining ~20m above the welded unit. The main part of the talus slope is ~28°, with the key feature being the short horizontal distance this feature covers (<24m from the start of the talus apron), when compared to other sections.

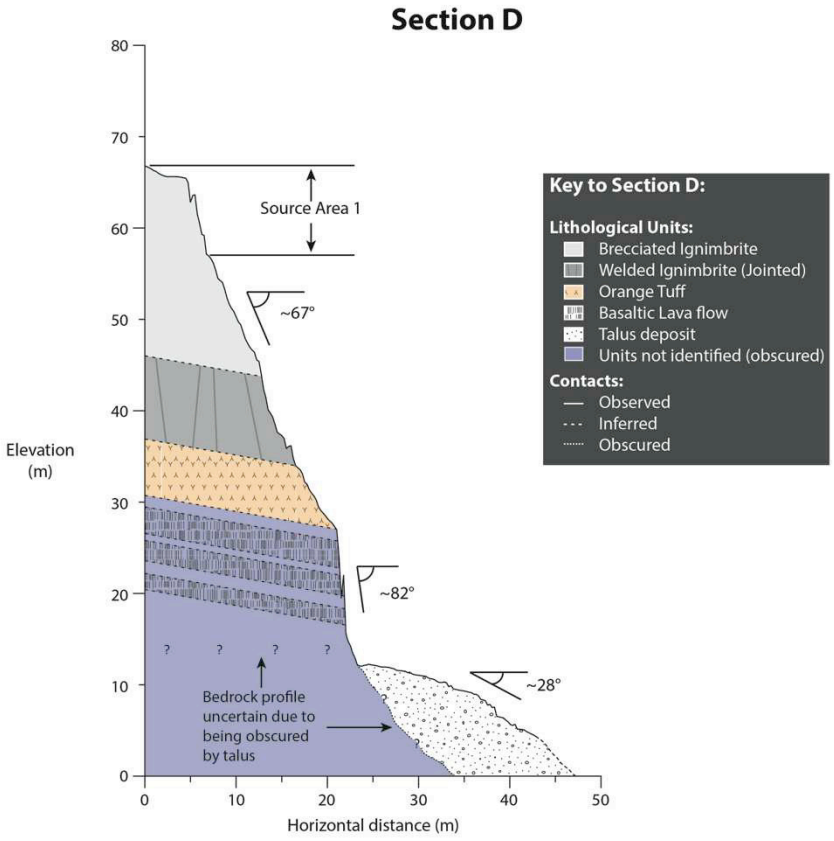

Figure 6.11: Schematic engineering geology model of Section D.

6.6.2 Runout Analysis

From Figure 6.12 and Table 6-11, it can be clearly seen that by volume and distance, rockfall runout for Section D far exceeded the toe of the modelled slope. The maximum distance travelled by modelled rock was ~69m, with ~85% of all modelled rocks exceeding the toe of the slope. The distribution of rockfall runout is dominated by horizontal end-points between ~46 - 69m from the zero horizontal datum. This area represents the flat area at the base of the slope, modelled as grassed soil.

The high volume of rock exceeding the modelled toe of the slope shows the influence that high source area elevation (>57m AGL) and a very steep (~67°) cliff face have on rockfall runout. The results from 2D RocFall™ modelling for this section line do not correlate well with field observations, however as discussed in Section 6.7, this is considered to be the result of a high maximum drop height to talus over horizontal slope distance ratio, and is useful in predicting maximum runout potential at Redcliffs, given the cliff geometry.

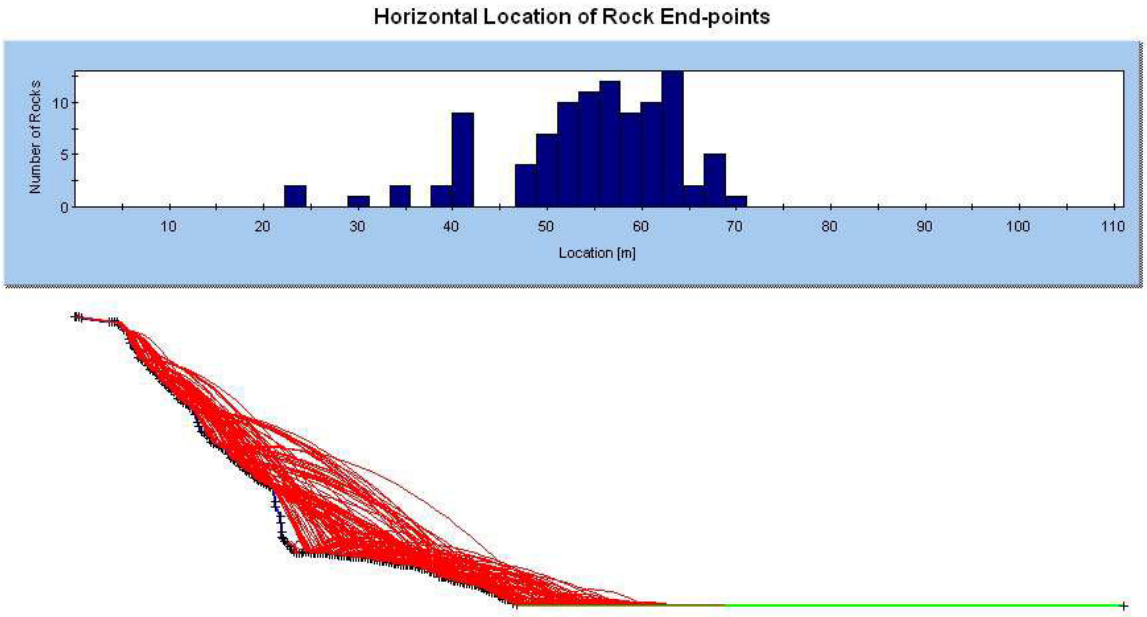

Figure 6.12: RocFall™ modelling output showing Horizontal Location of Rock End-points for Section D at Redcliffs. Upper plot shows rock end-point distribution graphically as a bar graph, while the lower plot represents the paths travelled by each of the 100 rocks sampled. The green slope on lower graph shows the material has been modelled as vegetated soil cover using RocFall™ default parameters. Note that the vertical axis of the lower plot has been reduced post-modelling, so the slope of the profile appears flatter than actually measured.

Table 6-11: Summary runout results for modelled Section D at Redcliffs

Mean distance travelled (m)	Maximum distance travelled (m)	% of rocks passing measured toe of slope
54.0	69.0	85.0

6.6.3 Kinetic Energy and Bounce Height Analysis

The maximum kinetic energy recorded at the toe of the modelled slope for Section D was 8,500,000J (8,500kJ) (Table 6-12). This value represents the largest kinetic energy of any of the modelled sections at Redcliffs (including Section E), the implications of which are discussed in the following section.

Table 6-12: Total kinetic energy summary at the toe of the slope (~43m from the zero datum) for Section D, Redcliffs.

Modelled Boulder Mass (kg)	Mean kinetic energy at x=47m (J)	Maximum kinetic energy at x=47m (J)	% of rocks passing measured toe of slope
500	51,000	210,000	85.0
5,000	510,000	2,100,000	85.0
20,000	2,100,000	8,500,000	85.0

Maximum bounce heights recorded from modelling Section D show an overall maximum height of 26m above the slope surface at ~24m from the horizontal zero datum (Figure 6.13 and Table 6-13). This location corresponds to the near vertical (~82°) lower part of the cliff face where the basal lava flows are exposed, and therefore is not strictly a bounce height. At the toe of the modelled slope, the maximum bounce height was ~8m. This value from the base of the slope is also far higher than from any other modelled section at Redcliffs, and the implications of this are discussed in the following section.

Table 6-13: Summary of bounce height envelope data for all modelled boulder masses for Section C, Redcliffs.

Maximum bounce height above slope (m)	Maximum bounce height at toe of slope (m)
26.0 (24[1])	8.0 (47[1])

[1]Values in parentheses represent approximate horizontal distance from zero datum.

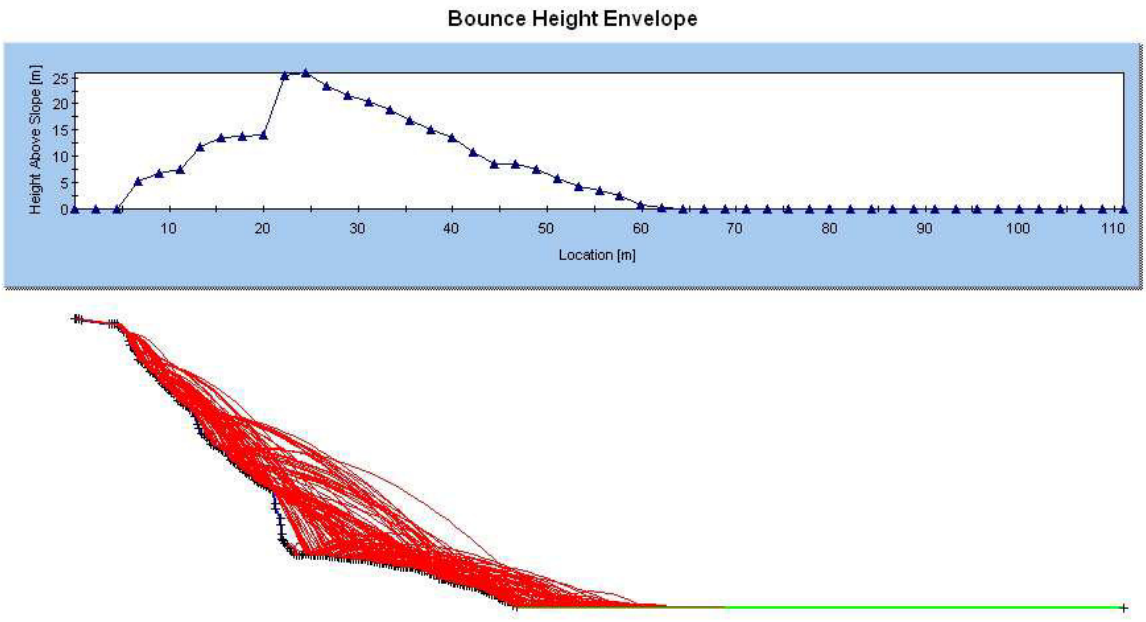

Figure 6.13: RocFall™ modelling output showing the Bounce Height Envelope for Section D, Redcliffs. Upper plot shows the maximum bounce height of all modelled rocks as a line graph, while the lower plot represents the paths travelled by each of the 100 rocks sampled. Note that the vertical axis of the lower plot has been reduced post-modelling, so the slope of the profile appears flatter than actually measured.

6.7 Modelling and Protection Implications

6.7.1 RocFall™ Modelling

The aim of this section is to analyse the data collected in testing of the five section lines at Redcliffs to determine which cliff morphology parameters have the greatest affect on rockfall runout and bounce height. The selected cliff parameters, and results from each section line, are summarised in Table 6-14. Definitions for each of the parameters as they are used in this discussion are provided below. As discussed in Chapter 4 and Sections 6.3-6.6, results from rockfall modelling have been constantly compared to field observations and aerial photographs to assess whether or not the results are realistic at Redcliffs.

Definitions of terms used are as follows (refer also Figure 6.14):

- **Total height (H)** represents the total height of the cliff section, from the top of the profile to the zero datum as measured by TLS (~10m above sea level)
- **Maximum drop height to talus (H*)** is a measure of the maximum vertical distance from the top of the rockfall source area to the top of the talus slope
- **Horizontal slope length (x)** represents the horizontal distance covered by the section line, i.e. from the edge of the cliff face at the top, to the furthest edge of the talus runout at the base of the slope
- **H/x** is the ratio between the total cliff height and the horizontal slope length (dimensionless as it is a ratio)
- **H*/x** is the ratio between the maximum drop height and the horizontal distance parameter "x" (also dimensionless as it is a ratio)
- **% of rocks passing toe of slope**, which measures the percentage of rocks that stop beyond the surveyed base of the talus apron
- **Maximum bounce height at toe of slope,** calculated from bounce height envelope data and relevant to protection options

Values summarised in Table 6-14 show that some parameters influence performance of the rockfall model in terms of rock runout and bounce height at the toe of the slope more than others. This is highlighted by Section Line D (shaded blue in Table 6-14), where values for the percentage of rocks passing the toe of the slope, and the maximum bounce height at the toe of the slope, are considerably higher than for the same parameters from all other modelled sections. This particular section line (D) raises important questions about the extent to which RocFall™ realistically models runout behaviour.

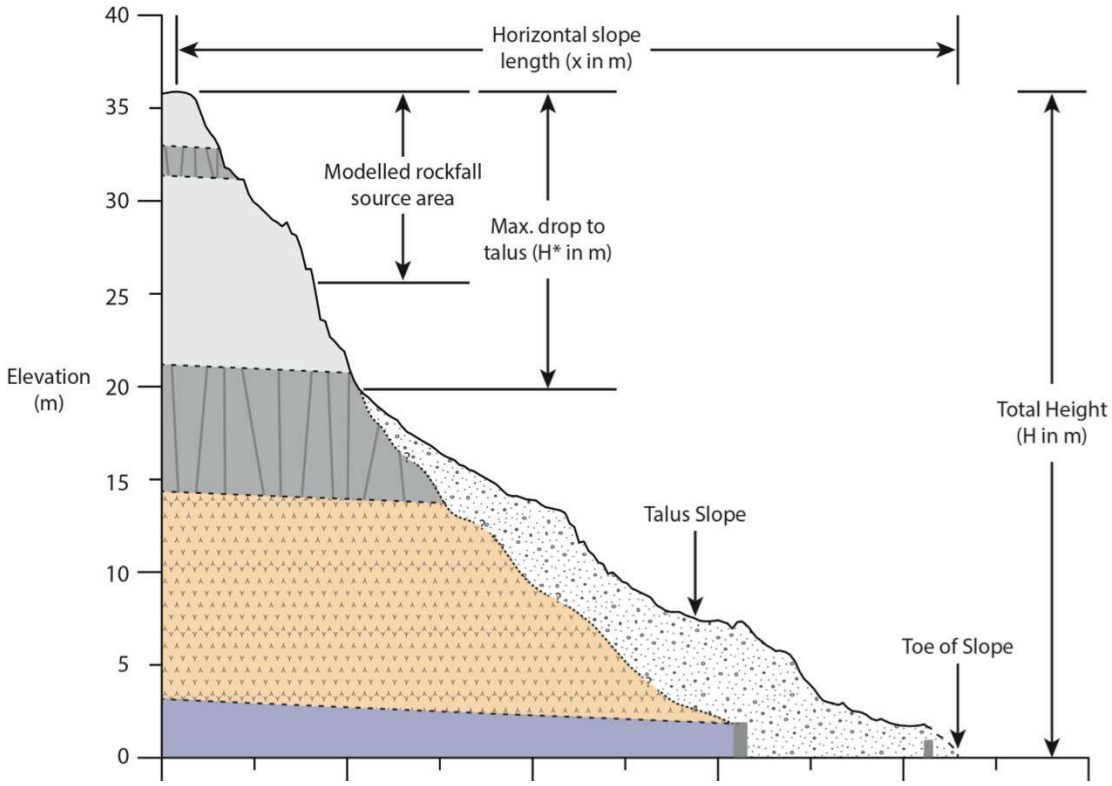

Figure 6.14: Schematic cross-sectional diagram indicating basic terminology used in this section.

Table 6-14: Summary of selected parameter values used in analysis of rockfall modelling for all sections. Note marked variation for Section Line D (shaded blue).

Section Line	Total Height, H (m)	Max. Drop Height to Talus, H* (m)	Horizontal Slope Length, x (m)	H/x	H*/x	% Passing toe of slope	Max. Bounce Height at toe of slope (m)
A	36.0	16.0	41.8	0.86	0.38	1.0	1.0
B	43.0	18.5	43.5	0.99	0.43	0.0	0.0
C	54.0	38.0	52.0	1.04	0.73	23	1.0
D	66.0	54.0	47.0	1.40	1.15	85	8.0
E	71.0	39.0	66.5	1.07	0.59	5.0	0.5

The ratio between "Maximum Drop Height to Talus" and "Horizontal Distance" was identified as a key parameter to explain the modelled runout characteristics when compared to field observations. As shown by Section Lines A, B, and E, where the H*/x ratio is low (<0.60 in each case), both the percentage of rocks passing the toe of the slope and the maximum bounce height at the toe compare closely with field observations. In contrast to this, as the H*/x ratio increases above 0.60, so too do the values for the percentage of rocks passing the toe and the maximum bounce height at the same point. A critical point or threshold value appears to occur above H*/x =0.6, and implies that the height of drop from the source area is a fundamental control on runout when modelled in 2D by RocFall™. It is recognised that not all boulders will be sourced from the upper part of the cliff face, but there is a clear implication that future rockfalls form this source area would run out well beyond the existing talus apron base on some section lines.

Relationships between these parameters and their influence on rockfall modelling are discussed in the following sections (6.7.2, 6.7.3, and 6.7.4).

6.7.2 Runout versus Height of Drop

Figure 6.15 shows a scatter plot of the relationship between drop height to talus, H*, and the horizontal slope length of each section line. From this plot, a linear trendline has been fitted to the data, showing a roughly positive correlation between drop height to talus and horizontal slope length distance. The R^2 value of 0.2 is low, however, and the graph is clearly influenced by the section D result (circled on Figure 6.15). If the value for Section D is ignored, the correlation coefficient for H*/x becomes R^2= 0.75 (Figure 6.16).

It is well known that the H/x parameter (often termed H/L) is an appropriate criterion to define landslide mobility or runout travel (Hutchinson 1970; Houghton & Hegan 1980; Bell et al. 2003; Massey, McSaveney, & Heron 2012). A plot of this parameter for the five section lines is given in Figure 6.17, from which the same linear trend is observed with an R^2 value of 0.62. In this latter case (Figure 6.17) Section D has not been excluded, and a maximum value for H/x

of 1.40 has been established (Table 6-14). The H/x ratio for the five modelled sections ranged between 0.86 and 1.4 (Figure 6.17), and the "x" dimension in all cases also represents the observed runout. Considered on the basis of this plot only, (i.e. total cliff height to runout distance (Figure 6.17), this plot implies greater runout as the talus apron flattens. This is counter-intuitive, and it is in fact the H*/x ratio that controls the runout when defined as the drop height to horizontal distance.

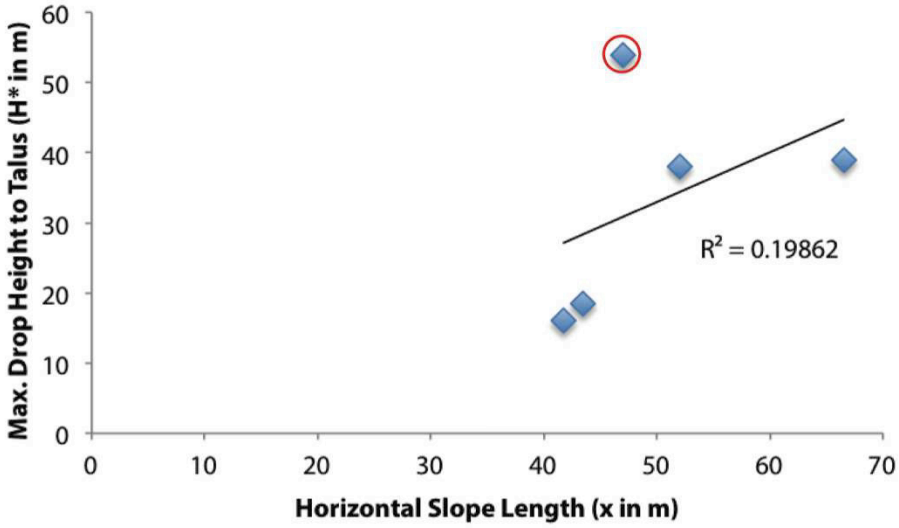

Figure 6.15: Scatter plot showing relationship between maximum vertical drop height to talus (H* in m), and the horizontal slope distance (x in m). Section D data point circled.

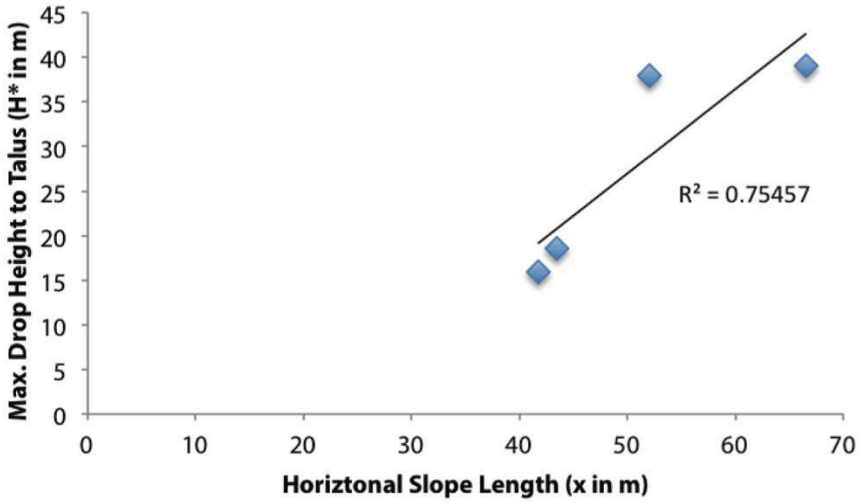

Figure 6.16: Scatter plot showing relationship between maximum vertical drop height to talus (H* in m) and the horizontal slope distance (x in m) with the value for Section Line D having been excluded. Note the increased R^2 value for this plot compared to Figure 6.15.

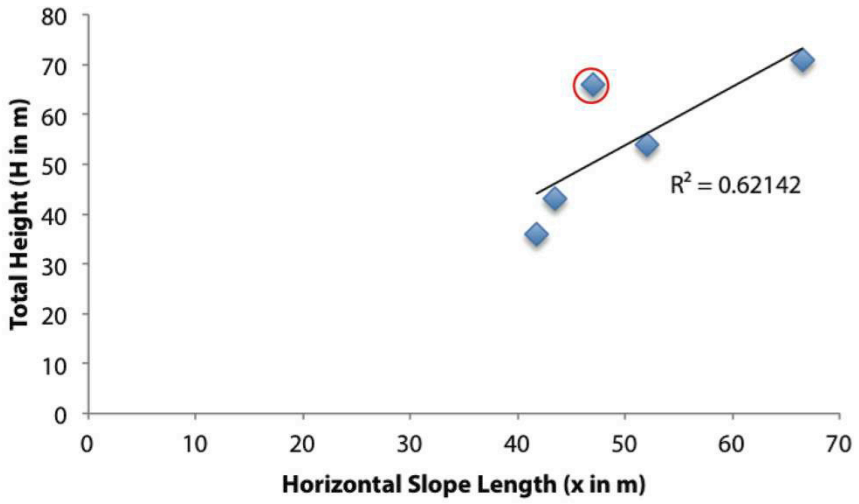

Figure 6.17: Scatter plot showing relationship between total cliff height (H in m) and horizontal slope distance (x in m).

Modelling using RocFall™ could be adjusted to match observed runout with the programme output in all cases except for Section D (Table 6-14). In this latter case, the implication is that further regression of the cliff face could theoretically be anticipated, but all five profiles relate to the same basaltic ignimbrite unit. The data obtained therefore suggests that H/x will be a maximum of 1.4H:1V (~35°) for the slopes at Redcliffs, and that future issues could be anticipated where H*/x exceeds about 0.6. Figure 6.18 plots the maximum and minimum runout trajectories, and also shows the 2H:1V line (26.5°).

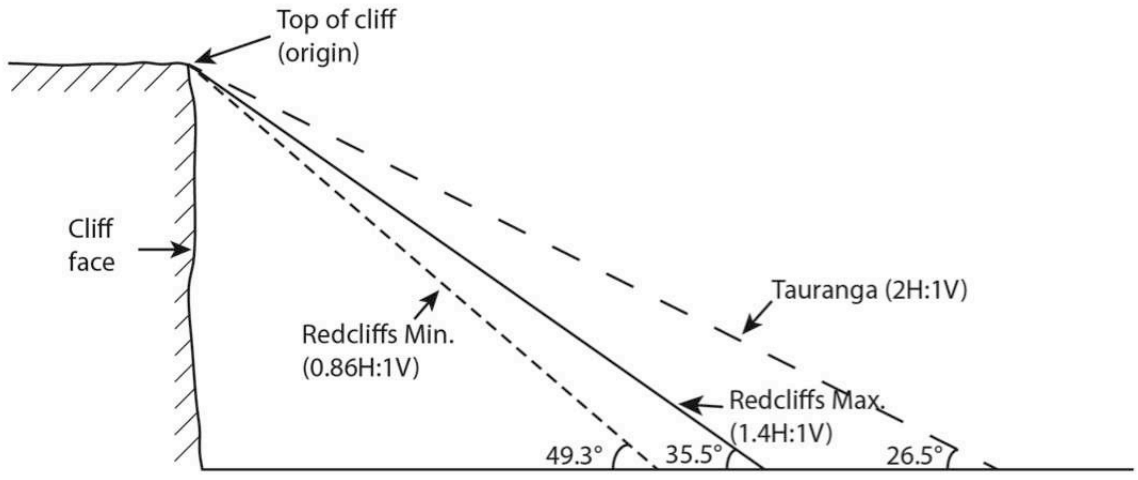

Figure 6.18: Schematic diagram illustrating the ratio between horizontal distance and vertical height (H:V), showing estimated rockfall runout envelopes for different horizontal to vertical ratio conditions.

The 2H:1V line from Figure 6.18 is used in Tauranga City to assess cliff collapse and potential runout as well as for geotechnical investigation purposes (Bell et al. 2003). Although the geology is different at that location, being volcanic-derived units often with soil-like characteristics, the approach has been shown to be valid and useful for planning purposes. At Redcliffs the inference is that for seismically-generated cliff collapse in the ignimbrite material, a maximum runout angle of ~35° (1.4H:1.0V) is realistic, with any added safety margin for fly-rock. Further section line analysis would be required, but a realistically conservative ratio for Redcliffs could be1.5H:1V (33.7°) for future planning purposes with any additional protection. This is also in spite of the fact that RocFall™ more accurately models the slopes with a higher H/x ratio.

6.7.3 Percentage passing toe of modelled slope

Figures 6.19 - 6.21present scatter plots of relationships of H*, H*/x, and H/x, against the percentage of rocks passing the toe of the slope respectively for each of the five Sections modelled at Redcliffs. All plots show a high correlation with the percentage of rocks passing the toe of the slope ($R^2 \geq 0.70$), with Figure 6.20 showing the highest correlation between H*/x against percentage of rocks passing the slope toe ($R^2 = 0.94$).

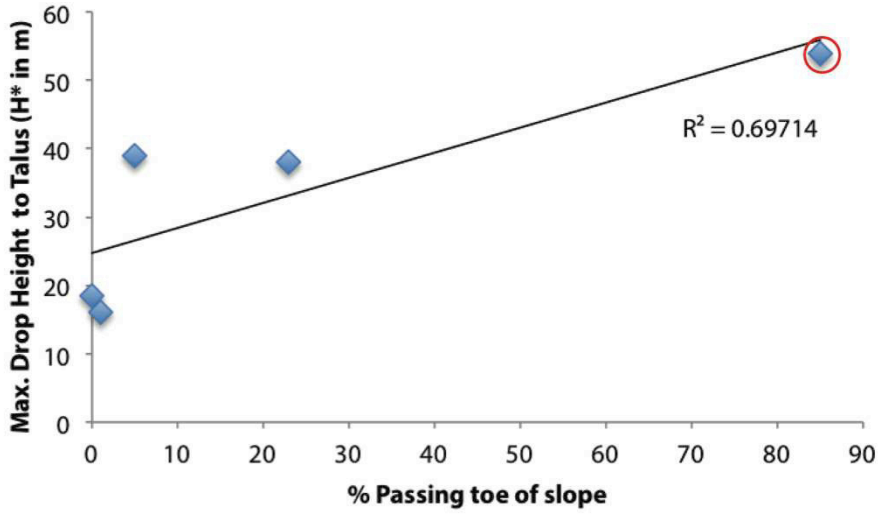

Figure 6.19: Scatter plot showing relationship between maximum vertical drop height to talus (H* in m), and percentage of rocks passing the modelled toe of the slope.

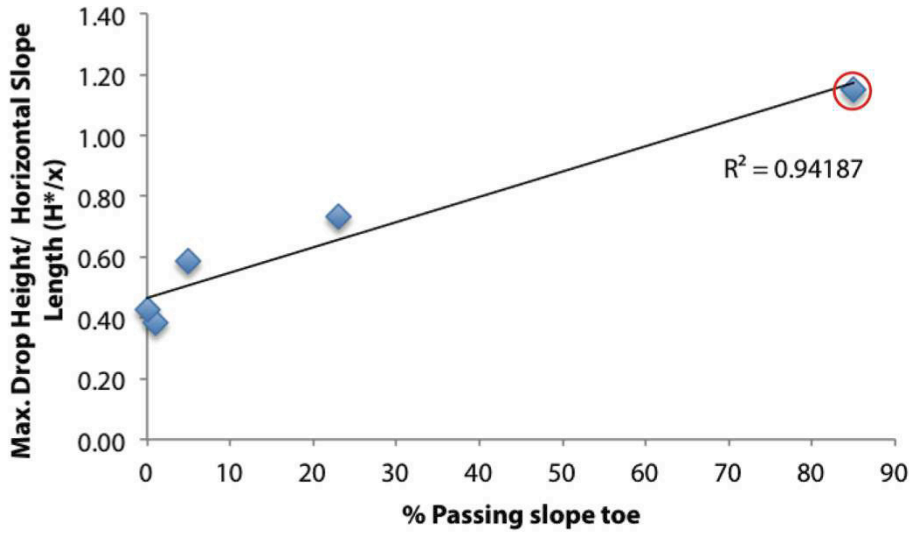

Figure 6.20: Scatter plot showing relationship between ratio of drop height and horizontal slope length, H*/x, versus percentage of rocks passing the modelled toe of the slope.

The RocFall™ modelling programme provides useful data when constrained by the known extent of runout. Figures 6.19 and 6.20 imply that the percentage of rocks passing the slope (= talus apron) toe will increase linearly with the maximum drop height. This is similar to the outcome predicted by the maximum drop height versus runout distance (H* vs. x) plots (Figures 6.15 and 6.16), and is an artifact of the programme in that source area height is the principal control. The roughness of the talus apron slope is indirectly modelled by the number of segments used to create the profile (Section 5), and is therefore not a primary determinant of predicted runout.

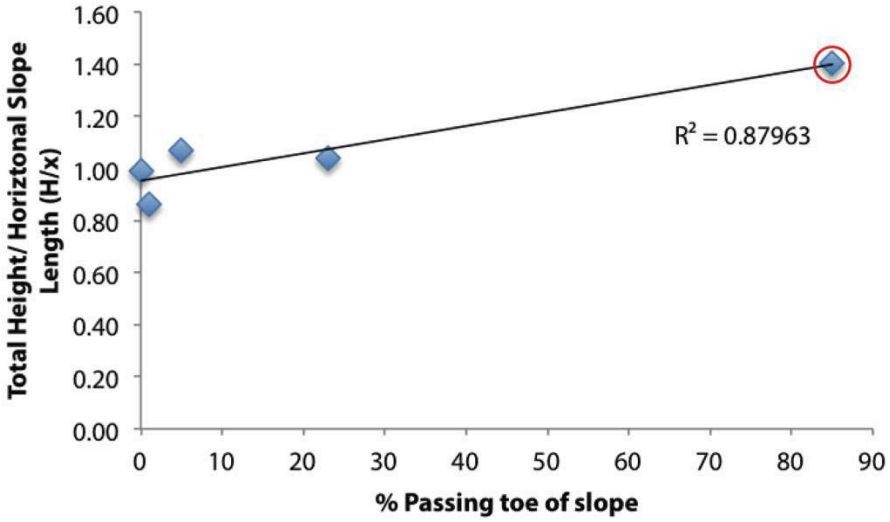

Figure 6.21: Scatter plot showing relationship between ratio of total height and horizontal slope length, H/x, versus percentage of rocks passing the modelled toe of the slope.

Figure 6.21 plots the cliff height to runout distance parameter (H/x) against the percentage of rocks passing the slope toe. As discussed in Section 6.7.2, this is in effect the actual runout distance at which debris (other than fly-rock) stopped. The talus apron profiles allow consideration of surface or slope roughness, and there is a similarly high correlation with the percent passing the slope toe (R^2=0.88). This is a useful design parameter for protection measures, such as bunding, but the actual performance of the talus "ramp" in future earthquake events is still only modelled approximately.

6.7.4 Bounce Height at toe of modelled slope

Table 6-15 summarises maximum bounce height envelope data at 10m increments along the length of the five modelled sections at Redcliffs. Individual bounce height envelopes were presented for each section line in Sections 6.3-6.6 and in Section 5.8 for Section Line E. From the data presented in Table 6-15, it is observed that for three of the sections modelled bounce heights are identified as being >5m above the slope surface for at least three consecutive horizontal increments, with Section D recording three consecutive maximum bounce heights ≥14m. These are considered artifacts of the RocFall™ programme given the profile steepness and the arbitrary location of the sampling points.

Table 6-15: Summary table showing incremental bounce height along the length of the slope, for each modelled section at Redcliffs.

Profile	Bounce Height Envelope (horizontal distance, x in m)[1]						
	10	20	30	40	50	60	70
A	6.3	1.8	0.8	0.2	0.0	0.0	0.0
B	1.8	5.0	1.7	0.0	0.0	0.0	0.0
C	6.5	10.0	10.0	2.5	1.5	0.0	0.0
D	7.0	16.0	21.5	14.0	7.0	1.0	0.0
E	5.0	19.0	13.0	5.2	5.1	3.0	0.5

[1]with respect to zero datum

This data, when viewed in conjunction with the maximum bounce height data presented for each section line, gives the appearance of repeated, extraordinarily high bounce heights. In reality, these high maximum bounce height envelope values are distorted by the steep topographical profiles being modelled, where rocks pass over high near-vertical sections. At these locations, falling rocks are in fact many metres above the slope surface, but rather than bouncing, are merely free-falling over ledges and drops. It is therefore important to interpret bounce height envelope data with care. It is for this reason, and for the benefit of assessing protection requirements, that maximum bounce height data are presented at the toe of the slope, as this is where bounce height is of greatest relevance.

Figures 6.22-6.24 show the relationship between H*, H*/x, and H/x against maximum bounce height at the toe of the slope for all five sections modelled at Redcliffs. All three plots show an acceptably high correlation coefficient, with R^2 values ≥0.56.

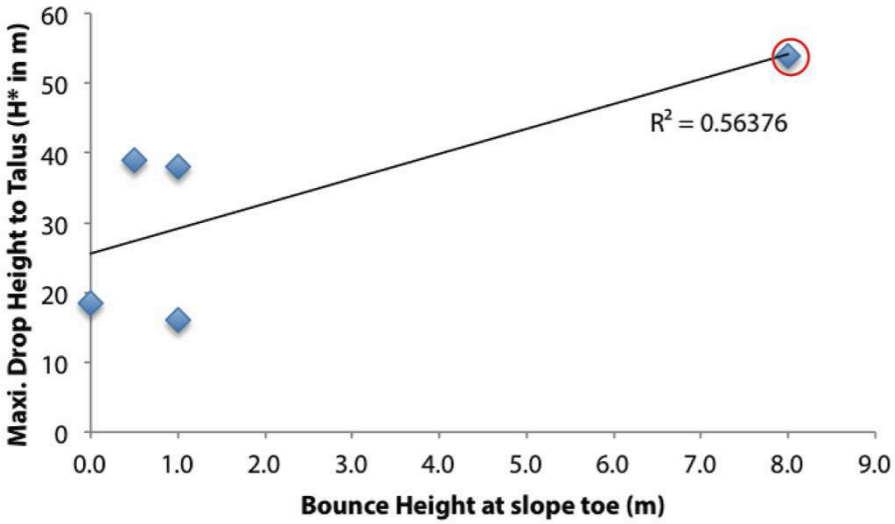

Figure 6.22: Scatter plot showing relationship between maximum drop height and maximum rock bounce height at the toe of the slope.

Plots of maximum drop height (H*), and H*/x versus bounce height (Figures 6.22 and 6.23), show a linear relationship between increasing drop height and bounce height at the toe of the slope, although the linearity is in part due to the one data point from Section D. This is

similar to the maximum drop height versus runout distance (H* vs. x) plots (Figures 6.16 and 6.17), and the H* and H*/x versus the percentage of rocks passing the toe of the slope (Figures 6.19 and 6.20). As discussed in Section 6.7.2, source area height provides the key control over bounce height, as opposed to slope surface roughness, which is an artifact of the modelling programme using RocFall™.

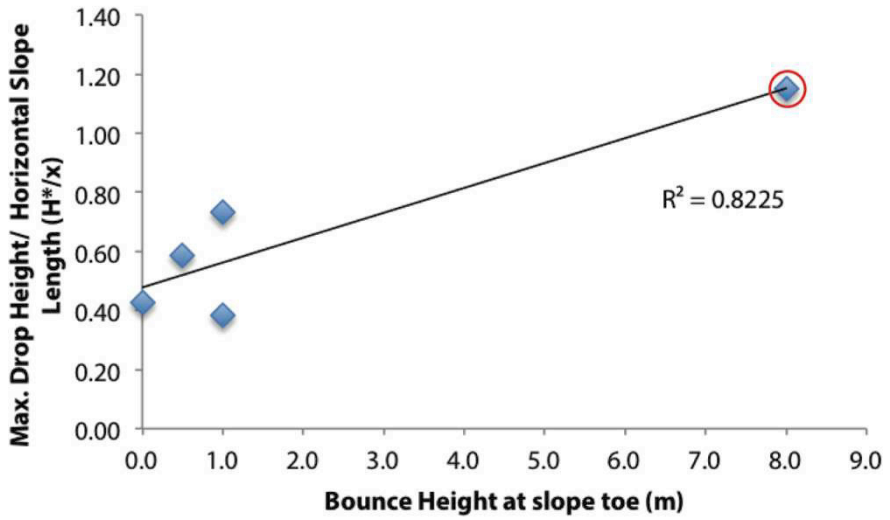

Figure 6.23: Scatter plot showing relationship between ratio of maximum drop height and horizontal distance, H*/x, versus maximum rock bounce height at the toe of the slope.

As discussed in Section 6.7.2, the H/x parameter is essentially a measure of runout, so with a higher runout parameter, maximum bounce height at the toe of the slope is also expected to increase. This relationship is shown in Figure 6.24, and the high R^2 value of 0.81 represents a strong correlation between these two variables. As with the relationship between H/x and percentage of rock passing the toe of the slope (Figure 6.21), the correlation between H/x and bounce height at the toe of the slope is also an important parameter for consideration in design of protection measures.

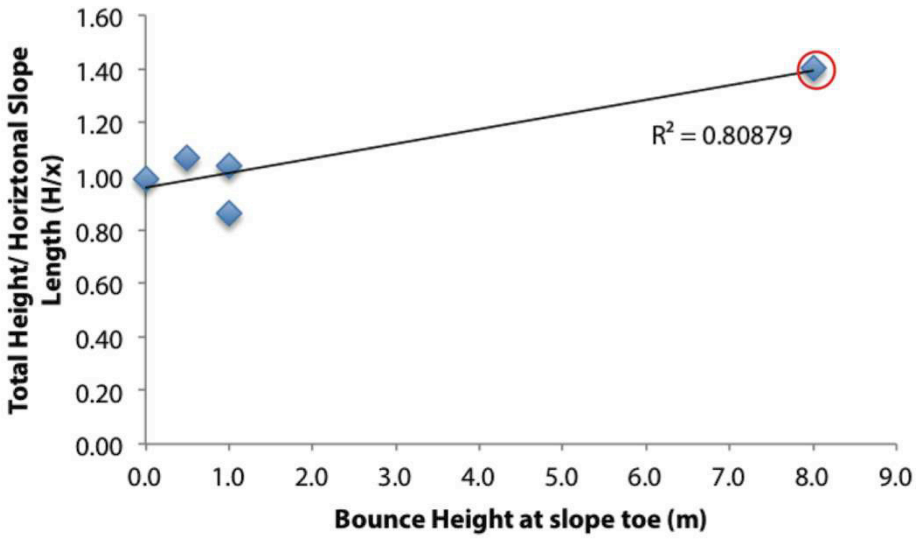

Figure 6.24: Scatter plot showing relationship between ratio of total height and horizontal slope length, H/x, versus maximum rock bounce height (in m) at the toe of the slope.

6.7.5 Protection Implications

Implications for protection measures based on rockfall modelling at Redcliffs are primarily related to the influence that source area height has on the behaviour of rocks at the toe of the slope. Through the detailed analysis undertaken (Sections 6.7.1-6.7.3), the two key parameters to consider when designing protection measures at Redcliffs are:

- Total cliff height over horizontal slope distance (H/x)
- Maximum drop height to talus over horizontal slope distance (H*/x)

For the H*/x parameter, two threshold values have been identified to estimate the ratio of maximum drop height to talus (H*) to horizontal slope distance (x) at which the percentage of rocks passing the toe of the slope, and the maximum bounce height at the toe of the slope become markedly different from observed limits. The following statements define this:

- If H*/x ≥0.6, modelling suggests that the percentage of rocks passing the current toe of the talus slope will exceed 5%; and

- If H*/x ≥0.75, modelling suggests that this could be an indication of significantly greater bounce height, as shown by the maximum bounce height at the toe of the slope of 8.0m for Section D, but ≤1.0m for all four other modelled sections, but this requires more data and analysis

For the H/x parameter, a threshold value has been identified for the percentage of rocks passing the toe of the slope. The following statement defines this value:

- If H/x ≥1.04, modelling suggests that the percentage of rocks passing the toe of the talus slope will be ≥5%.

A threshold value pertaining to maximum bounce height at the toe of the slope has not been identified. This suggests that the H*/x parameter is the primary control of this variable.

Kinetic energy has not been considered in the detailed analysis in Section 6.7 as this parameter is controlled by the mass of the falling boulder, a component that does not alter the trajectory of modelled rocks in RocFall™. This variable has been estimated in analysis of each modelled section line (Sections 6.3-6.6 and 5.8) however, and reference to these sections should be made prior to considering protection measures in any detail.

Selection and design of protection measures is not within the scope of this thesis. However, considering the large quantity of rocks modelled as exceeding the base of the talus slope, and the high bounce heights and kinetic energy values produced at the toe of the slope, a reinforced, earthen bund seems to be an appropriate device to contain or stop debris at the base of the talus apron. If required, a rockfall fence could be constructed at the top of the bund to increase the height of the protection structure. It should be noted that RocFall™ does not allow consideration of fly-rock trajectory, as fragmentation is not considered in the programme. The addition of a rockfall fence with appropriately spaced linkages and anchors could provide extra protection from fly-rock.

Analysis of further section lines would be necessary to better define the likely runout extent for boulders impacting the present talus apron as part of any design programme. It is

suggested that the computed runout distance should be initially derived from the RocFall™ programme, and that protection measures be designed for placement at this location. A more detailed hazard analysis should therefore precede a full design recommendation for a bunding system at this site, including further evaluation of long-term cliff stability. Evaluation of the suitability to use fallen rock in the construction of the bunding system would also be beneficial.

6.8 Synthesis

- Modelling of Section Lines A-D proved that the RocFall™ model developed through calibration at Section E was generally accurate when applied to other areas of the cliff at Redcliffs.
- Section Line D produced significantly higher results for maximum runout distance, percentage of rocks passing the modelled toe of the slope, and maximum bounce height at the toe of the modelled slope.
- Rockfall source area elevation with respect to the top of the talus apron was known to be the primary control on rockfall runout behavior as identified through testing of Section E. Further analysis of a selection of cliff parameters (total cliff height, H; maximum drop height to talus, H*; horizontal slope distance, x; H/x; and H*/x), led to the identification of a number of key parameters:
    - A maximum horizontal distance to cliff height (H:V) ratio of 1.4H:1V was identified. This provides a maximum runout envelope giving an angle from the top of the cliff to the toe of the talus slope of 35°.
    - The "maximum drop height to talus" over "horizontal slope distance" parameter (H*/x) exhibits the greatest control in modelled sections over the percentage of rocks passing the existing toe of the slope, and the maximum bounce height at the base of the slope.
    - A threshold value of H*/x ≥0.6 suggests that the percentage of rockfall runout passing the existing toe of the slope will exceed 5%

- A threshold value of H*/x ≥0.75 suggests that this could be an indication of significantly greater bounce heigh at the toe of the slope, as shown by the maximum bounce height of 8.0m for Section D, but ≤1.0m for all four other modelled sections, however this value requires more data and analysis to be of greater application

- The 1.4H:1V ratio can be applied (with additional consideration for fly-rock) to future land-use planning decisions, as is commonly used in other cities throughout New Zealand for similar mass-movement failures
- H*/x threshold values can be used in conjunction with the 1.4H:1V ratio in the design of rockfall protection measures at Redcliffs.

7. Summary and Conclusions

7.1 Thesis Objectives and Scope

The focus of this study is an area of Redcliffs which is dominated by a basaltic ignimbrite unit not previously recognised in the Banks Peninsula volcanic record. The basaltic ignimbrite unit is up to ~55m in exposed thickness in parts, and because of this the ignimbrite unit is considered the primary rockfall source area. Both welded and non-welded ignimbrite has been recognised and mapped remotely.

A difficulty that had to be overcome at the Redcliffs field area was the limited access to the base of the talus slopes because of the danger associated with such a potentially unstable area, and the potential for further aftershocks producing high ground accelerations. Face mapping relied on high-resolution photographs and observations often made from >100m away from the cliff face, and were supplemented with closer observations where possible. Aerial photographs were also used in mapping the runout following the two cliff collapse events of 22 February 2011 and 13 June 2011.

Because of the limitations placed on site access and time constraints, the scope of this thesis does not extend to kinematic analysis of failure mechanisms or any analysis of cliff top recession. For the same reasons, restitution coefficients used in rockfall modelling have been initially based on values suggested in the literature, rather than through field or laboratory analysis to calculate specific values for the site. This study is not intended to be sufficiently detailed to permit design of effective rockfall protection measures, but does provide the basis for further decision-making.

7.2 RocFall™ Modelling of Cliff Sections

Five section lines were modelled by RocFall™ 4.0 using TLS-derived slope profiles determined in March 2011 by GNS Science (Section Lines A-E). RocFall™ is a two-dimensional, hybrid, probabilistic rockfall trajectory model that is simple to use and widely available. Topographical profile data is entered into the programme, as well as rock starting locations (seeders), and a range of input variables. RocFall™ uses restitution coefficients to represent the energy transformation as rocks contact the slope surface, however determination of these parameters was reliant on suggested values from the literature rather than laboratory or field testing.

Rocks are modelled as infinitely small circles, so simulated rocks travel independently of others. The mass of the rocks is not considered in calculating rock paths, rather it is only included in calculating kinetic energy values. Because the mass of a rock in RocFall™ is constant throughout a simulation, there is no consideration for fragmentation of rocks during downslope transport, which is a potentially limiting attribute of the model. By limiting the model in this way, the programme can remain simplistic in operation, however consideration must then be given to the possibility of fly-rock travelling beyond the runout limits and bounce heights presented by the model.

Section lines were located to allow representative coverage of the failed section of the cliff, with a focus on proximity and orientation to buildings or other residential dwellings to increase the application of results to future land use. For two of the sections, the lower ~10m of the section lines were obscured from the TLS survey, so the base of the talus slopes was estimated from aerial photograph interpretation and field observations. Section lines were oriented perpendicular to the cliff face to allow the worst-case runout scenario to be modelled for each section line.

The School Hall Section (Section E) has been used as the primary case study to test the sensitivity of the RocFall™ model, and to calibrate the result with field observations. The location of the section line was chosen because the cliff height was the highest in the field

area (~70m AGL), the talus apron reached its highest point along this section line, and it was in close proximity to two major building structures.

Initial modelling of the School Hall Section (E) proved that the TLS-derived slope data contained too many data points for the slope roughness parameter in RocFall™ to have any effect. This was because any slope vertex variation by the model to increase the roughness was offset by variation of neighbouring vertices, resulting in no net change in slope surface roughness. This was a limitation of the RocFall™ model that was unknown to this author prior to the study. In order to achieve variation in rock runout through variation in the slope roughness parameter, the slope profile was reduced from ~280 slope vertices to 20. The results from this simplified slope profile did not calibrate with field observations as well as the TLS-derived slope profile model did. Therefore, it was decided that more accurate modelling results would be obtained by using the measured roughness provided by the TLS-derived slope profile.

7.3 Evaluation of Future Rockfall Runout

Input variables were methodically tested using the School Hall Section (E), and the optimal values were then applied to the other four Sections (A-D) to confirm the accuracy of the model (Table 7.1). The results of this testing proved the model to be accurate for four of the five sections, with analysis of the high values observed in Section D summarised in the following section. The percentage of rocks passing the toe of the slope were within acceptable ranges based on field observations for Sections A, B, and E (≤5%), with Sections C and D producing more rocks exceeding the toe of the modelled slope than observed in the field. All sections except for Section D produced modelled maximum bounce heights ≤1m at the toe of the slope. Kinetic energy at the toe of the slope was also considerably higher for Section D compared to the other four modelled sections, which as with bounce height, is considered to be a reflection of the greater drop height to talus (H*) for Section D, so the rocks are in free-fall for a longer period of time than the rocks from other modelled sections.

Table 7-1: Summary table showing results of RocFall™ modelling for all section lines at Redcliffs.

Section Line	Max. Predicted Runout Distance (m)	% Passing toe of slope	Max. Kinetic Energy at toe of slope (J)[1]	Max. Bounce Height at toe of slope (m)
A	50.3	1.0	690 000	1.0
B	43.7	0.0	50 200	0.0
C	62.0	23.0	2 100 000	1.0
D	69.0	85.0	8 500 000	8.0
E	75.0	5.0	4 300 000	0.5

[1] Maximum Kinetic Energy calculated for a rock with mass of 20 000kg.

7.4 Rockfall Modelling Parameters

Modelling of all five section lines using the parameters selected from the School Hall Section provided useful data for understanding the key cliff parameters that have significant control over rock runout when using RocFall™ version 4.0. When modelled with the selected parameters, Section D showed 85% of modelled rocks exceeding the toe of the existing talus slope, and a maximum bounce height at the toe of the slope of 8.0m. Both of these output values are markedly higher than field observations, amd are either incorrect or the modelling has identified potential for further large falls.

Through analysing the ratio of the total cliff height (H) against the horizontal slope distance (x), and similarly the maximum drop height from the top of the cliff to the talus slope (H*) against the horizontal slope distance (x), two fundamental relationships were identified. Firstly, through analysis of the total cliff height over horizontal slope distance parameter (H/x), a value of 1.4H:1V was observed for Section D, which represents the maximum ratio from all five modelled sections at Redcliffs. Conversely, the minimum value for the same ratio was

0.86H:1V. This relationship is counterintuitive because a steeper angle from the toe of the talus slope to the top of the cliff was expected to result in greater runout.

The 1.4H:1V ratio identified from modelled slopes at Redcliffs can be applied to other parts of Redcliffs to estimate maximum envelopes for future runout distances based on the cliff height and the horizontal runout distance. This is useful as both H and x values are simple to obtain from field or survey data, and it provides a quick and easy tool that could be used to inform future land use planning decisions. The parameter has been used in New Zealand for around 20 years as a way of estimating potential slope stability limits, and at the least as a way of identifying relic landslips in need of further geotechnical assessment. Both of these situations are applicable at Redcliffs, and it is acknowledged that further work is required to create a more robust model.

The ratio between the maximum drop height to the top of the talus (H*) and the horizontal slope distance (x) is also a useful parameter in the estimation of future rockfall runout and bounce height limits, and this parameter (H*/x) was found to have a profound impact on both outputs. Through analysis of the five modelled section lines at Redcliffs, two threshold values were identified to influence the percentage of rocks exceeding the modelled toe of the slope, and the maximum bounce height at the base of the slope, respectively. These thresholds are:

- If H*/x ≥0.6, modelling suggests that the percentage of rocks passing the current toe of the slope will exceed 5%; and
- If H*/x ≥0.75, the maximum bounce height at the toe of the slope was modelled to be almost a factor of ten greater.

In 2D rockfall modelling at Redcliffs, the H*/x parameter proved a more robust tool for estimating future rockfall limits than the H/x parameter. As with the H/x parameter, the relationship between H*/x can be used to estimate runout limits, and additionally to provide some indication of bounce heights at the base of the slope. In using either parameter for estimation purposes, it should be noted that the source area for the simulations was set to release from the upper 10m of each slope, regardless of geology, so as to reflect the worst-

case scenario for each slope. In addition, through the design of the RocFall™ programme, there is no consideration for fragmentation of rock during fall, so additional factors of safety would be required to accommodate this for possible fly-rock.

7.5 Further Research

The scope of this thesis has restricted analysis to the behaviour of modelled rocks on the slope and at the base of the debris apron. The primary purpose of this study has been to assess the controls on runout using the RocFall™ modelling programme. Further research is recommended to develop a more comprehensive understanding of the cliff face performance, both under gravity in combination with weathering, and in the event of further high PGA earthquakes. Research is recommended into the following aspects of the cliff slopes at Redcliffs within the study area:

- Investigation, monitoring and modelling of the cliff top section to establish the distance behind the present face where instability could or is presently developing.
- Establishment of remote monitoring points (e.g. by using geo-referenced TLS equipment) around the face itself to identify areas undergoing continuing deformation.
- Collection and testing of basaltic ignimbrite samples to establish normal and tangential coefficients of restitution for more reliable modelling of runout on the talus apron.
- Further analysis of the geotechnical reasons for apparently excessive runout on Sections C and D, both of which suggested much longer block travel distances because of the greater height of drop to the talus (H*).
- Using the above research data, development of robust criteria for any future occupation of the land beyond the base of the current talus apron.

8. References

Altaye, E. (1989). *The Geology and Geochemistry of the North-Eastern Sector of Lyttelton Volcano, Banks Peninsula, New Zealand*. Unpublished MSc Thesis. University of Canterbury, Christchurch, New Zealand.

Angular Velocity. (2012). *Encyclopaedia Brittanica*. Retrieved from http://www.britannica.com/EBchecked/topic/25354/angular-velocity

ASTM. (2004). ASTM Standard D4543: Standard Practices for Preparing Rock Core Specimens and Determining Dimensional and Shape Tolerances, 691–695.

Azzoni, A., La Barbera, G., & Zaninetti, A. (1995). Analysis and Prediction of Rockfalls Using a Mathematical Model. *International Journal of Rock Mechanics, Mining Science & Geomechanics Abstracts*, *32*(7), 709–724.

Bell, D. (2010). *Proposed Parking Areas A, B and C - 124 Main Road - Redcliffs*. Consultant Report. Christchurch.

Bell, D., & Crampton, N. (1986). Engineering Geological Evaluation of Tunneling Conditions, Lyttelton-Woolston LPG Project, Christchurch, New Zealand. *Proceedings of the Fifth IAEG Congress, Buenos Aires* (pp. 2485–2501). Buenos Aires.

Bell, D., Richards, L., & Thomson, R. (2003). Relic Slip Verification Study - Tauranga District. *Geotechnics on the Volcanic Edge - New Zealand Geotechnical Society Symposium - Proceedings of Technical Groups Vol. 30* (pp. 281–289). Tauranga.

Berrill, J., Avery, H., Dewe, M., Chanerley, A., Alexander, N., Colin, D., Holden, C., et al. (2011). The Canterbury Accelerograph Network (CanNet) and some results from the September 2010, M 7.1 Darfield earthquake. *Proceedings of the Ninth Pacific Conference on Earthquake*

Engineering Building an Earthquake-Resilient Society (pp. 1–8). Auckland. Retrieved from http://db.nzsee.org.nz/2011/181.pdf

Bieniawski, Z. (1968). The effect of specimen size on compressive strength of coal. *International Journal of Rock Mechanics and Mining Sciences*, *5*(ii), 325–335.

Bieniawski, Z. (1989). *Engineering rock mass classifications*. New York: Wiley.

Bourrier, F., & Hungr, O. (2011). Rockfall Dynamics: A Critical Review of Collision and Rebound Models. In S. Lambert & F. Nicot (Eds.), *Rockfall Engineering* (1st ed., pp. 175–203). London: ISTE Ltd.

Bradley, B., & Cubrinovski, M. (2011). Near-source strong ground motions observed in the 22 February 2011 Christchurch earthquake. *Bulletin of the New Zealand Society for Earthquake Engineering*, *44*(4), 181–194. Retrieved from http://srl.geoscienceworld.org/content/82/6/853.short

Brown, L., & Weeber, J. (1992). *Geology of the Christchurch Urban Area. Scale 1:25 000. Institute of Geological and Nuclear Sciences geological map 1.* (M. Reay, Ed.) (p. 1 sheet + 104p.). Lower Hutt, New Zealand: Institute of Geological and Nuclear Sciences Limited.

Buckley, S., Enge, H., Carlsson, C., & Howell, J. (2010). Terrestrial laser scanning for use in virtual outcrop geology. *The Photogrammetric Record*, *25*(131 (September)), 225–239. Retrieved from http://onlinelibrary.wiley.com/doi/10.1111/j.1477-9730.2010.00585.x/full

Caulfield, J., Cronin, S., Turner, S., & Cooper, L. (2011). Mafic Plinian volcanism and ignimbrite emplacement at Tofua volcano, Tonga. *Bulletin of Volcanology*, *73*(9), 1259–1277. doi:10.1007/s00445-011-0477-9

Christchurch Post-Earthquake Aerial Photos (24 Feb 2011). (2011). www.koordinates.com. Accessed on 4 April 2012.

Crampton, N. (1985). *Engineering geological aspects of the Lyttelton to Woolston LPG Pipeline*. Unpublished MSc Thesis. University of Canterbury, Christhchurch, New Zealand.

Cubrinovski, M. (2010). Geotechnical Aspects of the 2010 Darfield (Canterbury) Earthquake. Retrieved from http://ir.canterbury.ac.nz/handle/10092/5366

Cubrinovski, M., Green, R. A., Wotherspoon, L., Allen, J., Bradley, B., Bradshaw, A., Bray, J., et al. (2011). *GEOTECHNICAL RECONNAISSANCE OF THE 2011 CHRISTCHURCH , NEW ZEALAND EARTHQUAKE* (Vol. 2011). Retrieved from http://www.geerassociation.org/GEER_Post EQ Reports/Christchurch_2011/Cover_Christchurch_2011.html

Dorren, L. K. A. (2012). Rockyfor3D (v4.1) revealed – Transparent description of the complete 3D rockfall model. *ecorisQ paper (www.ecorisq.org)*, 1–30. Retrieved from www.ecorisq.org

Dorren, L. K. A., Berger, F., & Putters, U. S. (2006). Real-size experiments and 3-D simulation of rockfall on forested and non-forested slopes. *Natural Hazards and Earth System Sciences*, *6*, 145–153.

Eberhart-Phillips, D., & Bannister, S. (2002). Three-dimensional crustal structure in the Southern Alps region of New Zealand from inversion of local earthquake and active source data. *Journal of Geophysical Research*, *107*(B10), 1–18.

Evans, S., & Hungr, O. (1993). The assessment of rockfall hazard at the base of talus slopes. *Canadian Geotechnical Journal*, *30*, 620–636.

Forsyth, P., Jongens, R., & Barrell, D. (2008). *Geology of the Christchurch area* (p. 1 sheet + 67 p.). Lower Hutt: GNS Science. Retrieved from http://vm-aklh01.gns.cri.nz/index.php/content/download/3508/19652/file/Chri_text_lowres.pdf

Freundt, A., Wilson, C., & Carey, S. (2000). Ignimbrites and Block-And-Ash Flow Deposits. In H. Sigurdsson, B. Houghton, S. McNutt, H. Rymer, & J. Stix (Eds.), *Encyclopedia of Volcanoes* (pp. 581–599). San Diego: Academic Press.

Geociel. (2012). RocPro3D - Information leaflet. Retrieved October 26, 2012, from http://www.geociel.fr/src/index.php#

Geonet 2011. www.geonet.org.nz. Accessed 4 April 2012.

Gledhill, K., Ristau, J., Reyners, M., Fry, B., & Holden, C. (2011). The Darfield (Canterbury, New Zealand) Mw 7.1 Earthquake of September 2010: A Preliminary Seismological Report. *Seismological Research Letters*, *82*(3), 378–386. doi:10.1785/gssrl.82.3.378

Guzzetti, F., Crosta, G., Detti, R., & Agliardi, F. (2002). STONE : a computer program for the three-dimensional simulation of rock-falls. *Computers & Geosciences*, *28*, 1079–1093.

Haggerty, S., & Baker, I. (1967). The Alteration of Olivine in Basaltic and Associated Lavas. Part I: High Temperature Alteration. *Contributions to Mineralogy and Petrology*, *16*(3), 233–257.

Hampton, S. (2010). *Growth, Structure and Evolution the Lyttelton Volcanic Complex, Banks Peninsula, New Zealand*. *Unpublished PhD Thesis*. Unpublished PhD Thesis. University of Canterbury, Christchurch, New Zealand. Retrieved from http://ir.canterbury.ac.nz/handle/10092/4117

Hampton, S., & Cole, J. (2009). Lyttelton Volcano, Banks Peninsula, New Zealand: Primary volcanic landforms and eruptive centre identification. *Geomorphology*, *104*(3-4), 284–298. doi:10.1016/j.geomorph.2008.09.005

Harris, D. (2002). *Geotechnical Properties of Coal and Mine Pillar Design in the Greymouth and Reefton Coalfields, West Coast, South Island.* Unpublished MSc Thesis. University of Canterbury, Christchurch, New Zealand.

Hoek, E., & Brown, E. (1997). Practical estimates of rock mass strength. *International Journal of Rock Mechanics and Mining Sciences*, *34*(8), 1165–1186. doi:10.1016/S0969-4765(04)00066-9

Houghton, B., & Hegan, B. (1980). *Preliminary Assessment of Geological Factors influencing Slope Stability and Landslipping in and around Tauranga City*.

Hutchinson, J. (1970). Field and Laboratory Studies of a Fall in the Upper Chalk Cliffs at Joss Bay, Isle of Thanet. *Proceedings of the Roscoe Memorial Symposium, Cambridge*.

ISRM. (1979). Suggested Methods for Determining the Uniaxial Compressive Strength and Deformability of Rock Materials. *International Society for Rock Mechanics Commission on Testing Methods*, 151–156.

Kaiser, a, Holden, C., Beavan, J., Beetham, D., Benites, R., Celentano, a, Collett, D., et al. (2012). The M w 6.2 Christchurch earthquake of February 2011: preliminary report. *New Zealand Journal of Geology and Geophysics*, *55*(1), 67–90. doi:10.1080/00288306.2011.641182

Kanari, M. (2008). *Evaluation of Rockfall Hazard to Qiryat Shemona - Possible Correlation to Earthquakes*. Tel Aviv University.

Lan, H., Martin, C., & Lim, C. (2007). RockFall analyst: A GIS extension for three-dimensional and spatially distributed rockfall hazard modeling. *Computers & Geosciences*, *33*(2), 262–279. doi:10.1016/j.cageo.2006.05.013

Lemmens, M. (2011). Terrestrial Laser Scanning. *Geo-information* (pp. 101–121). Dordrecht: Springer Netherlands. doi:10.1007/978-94-007-1667-4

Lucchitta, B. K. (1979). Landslides in Valles Marineris, Mars. *Journal of Geophysical Research*, *84*(B14), 8097. doi:10.1029/JB084iB14p08097

Luckman, B. (2007). Talus Slopes. In S. Elias (Ed.), *Encyclopedia of Quaternary Science* (pp. 2242–2249). Elsevier.

Lundy, P. (1995). *Engineering Geological Evaluation of Rockfall Hazards on Banks Peninsula, Canterbury*. Unpublished MSc Thesis. University of Canterbury, Christchurch, New Zealand.

Massey, C. (2012). GNS Science public presentation on Cliff Collapse on the Port Hills, Christchurch during the Canterbury Earthquake Sequence. http://www.youtube.com/watch?v=YyTLM2Y6rQ8&feature=youtu.be

Massey, C., McSaveney, M., Heron, D., & Lukovic, B. (2012). *Canterbury Earthquakes 2010/11 Port-Hills Slope Stability: Pilot study for assessing life-safety risk from rockfalls (boulder rolls)*. *GNS Science Consultancy Report*. Retrieved from http://scholar.google.com/scholar?hl=en&btnG=Search&q=intitle:Canterbury+Earthquakes+2010+/+11+Port+Hills+Slope+Stability+:+Pilot+study+for+assessing+life-safety+risk+from+rockfalls+(+boulder+rolls+)#0

Massey, C., McSaveney, M. J., & Heron, D. (2012). *Canterbury earthquakes 2010/11 Slope Stability: Life-safety risk from cliff collapse in the Port Hills* (p. 35 p + Appendices).

McDowell, B. (1989). *Site Investigations for Residential Development on the Port Hills, Christchurch*. Unpublished MSc Thesis. University of Canterbury, Christchurch, New Zealand.

McSaveney, E. (1971). *The surficial texture of rockfall talus*. Unpublished MSc Thesis. Ohio State University, Columbus, United States of America.

Norris, R., & Cooper, A. (1995). Origin of small-scale segmentation and transpressional thrusting along the Alpine fault, New Zealand. *Geological Society of America Bulletin*, *107*(2), 231–240.

Norris, R., & Cooper, A. (2001). Late Quaternary slip rates and slip partitioning on the Alpine Fault, New Zealand. *Journal of Structural Geology*, *23*(2-3), 507–516.

NZGS. (2005). *Field Description of Soil And Rock - Guideline for the field classification and description of soil and rock for engineering purposes*. (D. Burns, G. Farquar, M. Mills, & A. Williams, Eds.) (pp. 1–39). New Zealand Geotechnical Society Inc.

Peng, B. (2000). *Rockfall Trajectory Analysis - Parameter Determination and Application*. Unpublished MSc Thesis, University of Canterbury, Christchurch, New Zealand.

Perez, F. L. (1989). Talus fabric and particle morphology on Lassen Peak, California. *Geografiska Annaler*, *71*(1), 43–57.

Pfeiffer, T., & Bowen, T. (1989). Computer Simulation of Rockfalls. *Bulletin of the Association of Engineering Geologists*, *XXVI*(1), 135–146.

Quigley, M., Van Dissen, R., Villamor, P., Litchfield, N., Barrell, D., Furlong, K., Stahl, T., et al. (2010). SURFACE RUPTURE OF THE GREENDALE FAULT DURING THE DARFIELD (CANTERBURY) EARTHQUAKE, NEW ZEALAND: INITIAL FINDINGS. *Bulletin of the New Zealand Society for Earthquake Engineering*, *43*(4), 1–7. Retrieved from http://www.nzsee.org.nz/db/SpecialIssue/43(4)0236.pdf

Richards, L., Peng, B., & Bell, D. (2001). Laboratory and Field Evaluation of the Normal Coefficient of Restitution for Rocks. In P. Sarka & A. Eloranta (Eds.), *Proceedings of the ISRM Regional Symposium Eurock* (pp. 149–155). Espoo, Finland: Balkema, AA.

Ring, U., & Hampton, S. (2012). Faulting in Banks Peninsula: tectonic setting and structural controls for late Miocene intraplate volcanism, New Zealand. *Journal of the Geological Society*, *169*(2-3), 773–785. doi:10.1144/jgs2011-167.Faulting

Ritchie, A. (1963). The evaluation of rockfall and its control. *Highway Research Record*, *17*, 13–28.

RocScience. (2003). Determining Input Parameters for a RocFall Analysis.

Sewell, R. (1985). *The Volcanic Geology and Geochemistry of Central Banks Peninsula and Relationships to Lyttelton and Akaroa Volcanoes*. Unpublished PhD Thesis. University of Canterbury, Christchurch, New Zealand.

Sewell, R. (1988). Late Miocene Volcanic Stratigraphy of Central Banks Peninsula, Canterbury, New Zealand. *New Zealand Journal of Geology and Geophysics*, *31*, 41–64.

Sewell, R., Weaver, S., & Reay, M. (1992). *Geology of Banks Peninsula. Scale 1:100,000.* (p. Map 3). Lower Hutt, New Zealand: Institute of Geological and Nuclear Sciences Limited.

Stevens, W. (1998). *A Tool for Probabilistic Analysis, Design of Remedial Measures and Prediction of Rockfalls*. Unpublished MSc Thesis. University of Toronto, Toronto, Canada.

Sutherland, R., Berryman, K., & Norris, R. (2006). Quaternary slip rate and geomorphology of the Alpine fault: Implications for kinematics and seismic hazard in southwest New Zealand. *Geological Society of America Bulletin*, *118*(3/4), 464–474.

Tagliavini, F., Reichenbach, P., Maragna, D., Guzzetti, F., & Pasuto, a. (2008). Comparison of 2-D and 3-D computer models for the M. Salta rock fall, Vajont Valley, northern Italy. *GeoInformatica*, *13*(3), 323–337. doi:10.1007/s10707-008-0071-2

Van Dissen, R., Barrell, D., Litchfield, N., Villamor, P., Quigley, M., & King, A. (2011). Surface rupture displacement on the Greendale Fault during the M w 7 . 1 Darfield (Canterbury) earthquake , New Zealand , and its impact on man-made structures, (186), 1–8.

Watkins, S., Giordano, G., Cas, R., & Rita, D. De. (2002). Emplacement processes of the mafic Villa Senni Eruption Unit (VSEU) ignimbrite succession, Colli Albani volcano, Italy. *Journal of Volcanology and Geothermal Research*, *118*, 173–203. Retrieved from http://www.sciencedirect.com/science/article/pii/S0377027302002561

Weaver, S., & Sewell, R. (1986). *Cenozoic Volcanic Geology of Banks Peninsula*. (B. Houghton & S. Weaver, Eds.) (p. 92). Wellington: New Zealand Geological Survey.

Weaver, S., Sewell, R., & Doorsey, C. (1985). *Extinct Volcanoes: A Guide to the geology of Banks Peninsula. Guidebook No.7*. Lower Hutt, New Zealand: Geologica Society of New Zealand.

Webb, T., Bannister, S., Beavan, J., Berryman, K., Cousins, J., Fry, B., Gerstenberger, M., et al. (2011). The Canterbury earthquake sequence and implications for seismic design levels. *GNS Science Consultancy …*, 1–21. Retrieved from http://scholar.google.com/scholar?hl=en&btnG=Search&q=intitle:The+Canterbury+Earthquake+sequence+and+implications+for+Seismic+Design+Levels#0

Wood, C., Cox, B., Wotherspoon, L., & Green, R. (2011). Dynamic Site Characterization of Christchurch Strong Motion Stations. *Bulletin of the New Zealand Society for Earthquake Engineering*, *44*(4), 195–204. Retrieved from http://canterbury.royalcommission.govt.nz/documents-by-key/20120724.4812/$file/BUI.MAD249.0543.pdf

APPENDIX 1: SUMMARY STRATIGRAPHY OF MIOCENE VOLCANICS OF BANKS PENINSULA

(Weaver & Sewell 1986)

Group	Formation	K/Ar Age Range (Ma)	Lithology	Main Localities
STODDART VOLCANICS	Stoddart Point Olivine-Basalts	7.0 – 5.8	Fresh, columnar jointed, olivine ± clinopyroxene phyric basanites, olivine-basalts and olivine-hawaiites – rare olivine-basalt dykes	Taitapu – Ahuriri, Kaituna Valley, Port Levy, Diamond Harbour, Quail Island
	Kaioruru Olivine Hawaiites	6.9 – 6.8	Commonly weathered, vesicular, pale pink, olivine + clinopyroxene – phyric and aphyric olivine-hawaiites	Diamond Harbour, Quail Island
CHURCH VOLCANICS	Church Bay Olivine-Basalts	7.8 – 7.3	Fresh, columnar-jointed, olivine ± clinopyroxene – phyric olivine-basalts	Diamond Harbour, Quail Island, Taitapu – Ahuriri
	Darra Basanitoids	8.1 – 7.7	Fresh, columnar-jointed olivine ± clinopyroxene – phyric basanitoids – rare basanitoid dykes	Diamond Harbour, Quail Island, Taitapu – Ahuriri
AKAROA VOLCANICS		9.0 – 8.0	Fresh, medium to fine grained, olivine-clinopyroxene-plagioclase -phyric and grey, aphyric hawaiites – rare trachyte domes and dykes	South side of Kaituna Valley – Port Levy
MT HERBERT VOLCANICS	Mt Herbert Hawaiites	8.5 – 8.0	Grey, columnar-jointed, aphyric and rarely olivine-phyric olivine-hawaiites	Mt Herbert – Mt Bradley
	Chateau Intrusives	8.0	Grey, columnar-to knobbly-jointed aphyric hawaiites	Charteris Bay – Bradley Park
	Port Levy	8.9 – 8.5	Grey-black, columnar-	Port Levy – Western

	Formation		jointed, aphyric hawaiites – rare porphyritic basalts and mugearites	Valley
	Orton-Bradley Formation	9.5 – 8.6	Black, fresh aphyric, olivine-hawaiites & olivine + clinopyroxene-plagioclase-phyric olivine-hawaiites	Mt Herbert – Mt Bradley
	Kaituna Olivine-Hawaiittes	9.7 – 9.5	Columnar-jointed, dark grey-black, fresh, olivine + clinopyroxene- phyric olivine-hawaiites	Kaituna – McQueens Valleys
LYTTELTON VOLCANICS		11 – 10	Moderately weathered, plagioclase ± clinopyroxene – phyric-hawaiites – trachyte lava flows and domes – numerous trachytic and basaltic dykes	North side of Kaituna Valley – Mt Herbert
GOVERNORS BAY VOLCANICS		?12 – 11	Altered plagioclase + clinopyroxene ± olivine ± orthopyroxene – phyric andesite flows and quartz-alkali feldspar – phyric rhyolite domes	Governors Bay – Charteris Bay, Quail Island, Gebbies Pass

APPENDIX 2: CHRONOLOGICAL HISTORY OF RECORDED ROCLFALL EVENTS, BANKS PENINSULA

(Lundy 1995)

Date	Location	Details	Reference
17/08/1886	Annandale, Pigeon Bay	Large debris slide destroying homestead.	Ogilivie (1990)
23/12/1907	Sumner Cliffs	Tramway blocked, metals, wire and water mains damaged. Covered 1.5 chains. Some rocks up to 100 tons.	Press 10/04/1907
5/10/1909	Andrews Quarry, Sumner Road	Josiah Millar (36) killed when a rockface collapsed.	Press 6/10/1909
8/10/1912	Sumner Cliffs	Large rockfall on tramline as a result of blasting.	Cant. Times Illus. 9/10/1912. pp 42-43
5/10/1914	Sumner Cliffs between Shag Rock and Gollins Point.	Result from blasting.	Press 6/10/1914, 13/10/1914, 13/11/1914
12/8/1916	Sumner, several rockfalls. Langdales residence, (slide). Falls foot of Lyttelton Road.	Langdales residence 2t of material. Followed heavy weather June, July, August. 28 Jul rainfall 1.67" & snow. 5 Aug, snow, eclipse of sun and a minor earthquake.	Press 12/8/1916
25/7/1918	Shag Rock, one heavy boulder breaking principle water main and numerous other landslides.	Followed heavy rain and snow from 10-16 Jul 1918.	Press 26/7/1918
12/3/21	Shag Rock	Recent heavy fall of hard rock from the top altering its appearance.	Press 12/3/1921
26/3/21	Hillside residences.	Induced by persons unknown.	Press 26/3/1921
19/7/23	Scarborough Rockfall, Bells Path. Road impassable. Talylors Mistake Road also blocked by a landslide halfway down.	Followed heavy rain and flooding of Sumner & Redcliffs.	Press 20/7/1923. Photo Sumner Museum.
11/8/25	Shag Rock, Sumner Road.	Numerous landslides and rockfalls. Sumner Road blocked by 3 heavy 'slips' following heavy rain.	Press 11/8/1925
20/4/26	Shag Rock	Blasting induced.	Press 20/4/1926
31/8/26	Black Rock, Taylors Mistake	Dingy and Boatshed destroyed. Huge masses some ~ton moved downhill	Press 31/8/1926

		quarter mile from a height of 700ft. Occurred during construction of road from Evans Pass to lighthouse.	
8/1/27	Shag Rock	Several minor falls on road. (Blasting).	Press 8/1/1927
25/6/27	Shag Rock	Blasting	Press 25/6/1927
3/12/27	Shag Rock	Blasting	Press 3/12/1927
23/6/28	Scarborough Road	Fall of rock (no size description) in same location as previous large fall.	Press 23/6/1928
13/9/29	Sumner Cliffs, proposed baths site	Largest boulders 4ft. Source 30ft uphill. Reference to heavy rain and a recent earthquake and a much larger fall in the same place 15 years prior. (Previous rockfalls in this locality all documented as the result of blasting).	The Sun 13/9/1929 plus photos
9/8/30	Shag Rock, Redcliffs, Clifton Spur	Numerous 'slips' of rock and clay following heavy rain.	Press 9/8/1930
30/6/32	Sumner	General article on the danger of falling rock. Also reference to a rock crashing into a car on the Lyttelton side of the Sumner-Christchurch Highway.	Press 30/6/32
13/9/32	Shag Rock	Council proposal to shift road and widen it to avoid rockfalls.	Press 13/9/32
28/7/33	Clifton	Council work to remove loose and dangerous rocks.	Press 27/7/33
1/3/36	Clifton (halfway between Shag Rock and Sumner)	2 or 3 hundred weight mass swept onto roadway. Largest pieces ~2lbs. Source high up in an outcrop of softish 'laterite'. Same location as 1929 fall. Occurred after heavy easterly weather.	Press 2/3/36
2/3/35	Scarborough Road (near tearooms)	Blasting to obtain fill for roading, 30-40 tons.	Press 2/3/36
16/3/36	Evans Pass Road	Rock/debris fall following storm event.	Press 16/3/36
5/9/66	Shag Rock	Blasting, -70 cubic yards of rock removed from the cliff face as part of a program to minimise the danger of falling rock.	Press 6/9/66
1986	Edwin Mouldey	Rockfall damaged the pumping	?

	Track (Scarborough)	station. Triggered by fretting and spalling in particular rubbly lava and agglomerate.	
1986	Govenors Bay	Rock dislodged from 200m upslope passed through the rear wall of a house and continued out the front	?
7/6/92	Raekura Place, Redcliffs	Rockfall triggered by progressive weakening and fretting of a 0.5m thick ash unit immediately underlying lava blocks. Also storm event over previous weekend and recent Marlborough earthquake contributing factors.	D. Bell

APPENDIX 3: PEAK GROUND ACCELERATION (PGA) MAPS

Sourced from Geonet (www.geonet.org.nz)

-4 September 2010 M_w 7.1 Darfield Earthquake

-22 February 2011 M_w 6.3 Christchurch Earthquake

-13 June 2011 M_w 5.6 Earthquake

-13 June 2011 M_w 6.3 Earthquake

-23 December 2011 M_w 5.8 Earthquake

-23 December 2011 M_w 6.0 Earthquake

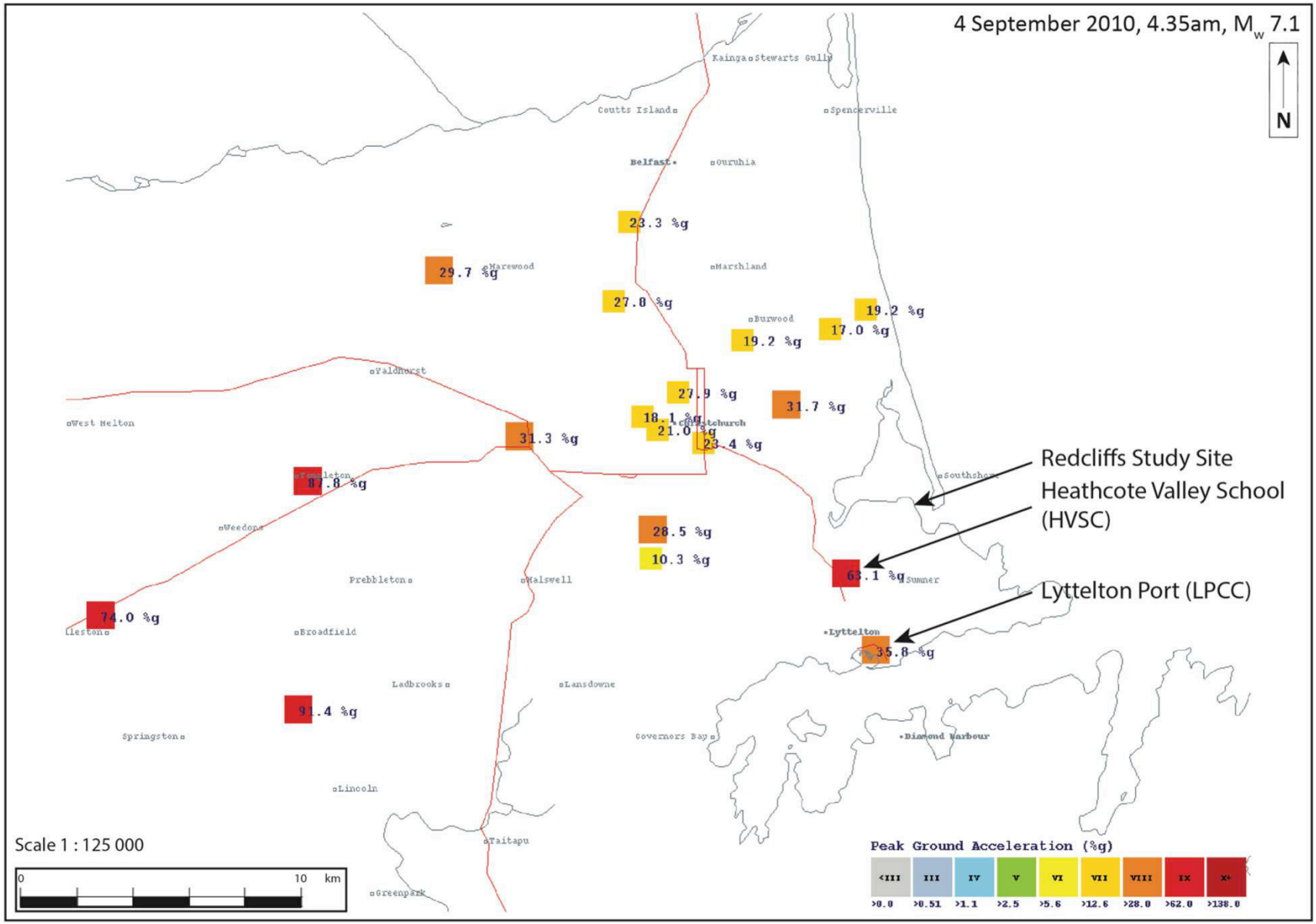
4 September 2010, 4.35am, M_w 7.1
N
Redcliffs Study Site
Heathcote Valley School (HVSC)
Lyttelton Port (LPCC)
Kainga
Stewarts Gully
Coutts Island
Spencerville
Belfast
Ouruhia
Marshland
Burwood
Waldronst
West Melton
Weedons
Prebbleton
Halswell
Broadfield
Ladbrooks
Lansdowne
Springston
Lincoln
Taitapu
Greenpark
Governors Bay
Diamond Harbour
Lyttelton
Sumner
Southshore
29.7 %g
23.3 %g
27.8 %g
19.2 %g
17.0 %g
19.2 %g
27.9 %g
18.1 %g
21.0 %g
23.4 %g
31.7 %g
31.3 %g
87.8 %g
28.5 %g
10.3 %g
63.1 %g
74.0 %g
35.8 %g
91.4 %g
Scale 1 : 125 000
0
10 km
Peak Ground Acceleration (%g)
<III
III
IV
V
VI
VII
VIII
IX
X+
>0.0
>0.51
>1.1
>2.5
>5.6
>12.6
>28.0
>62.0
>138.0

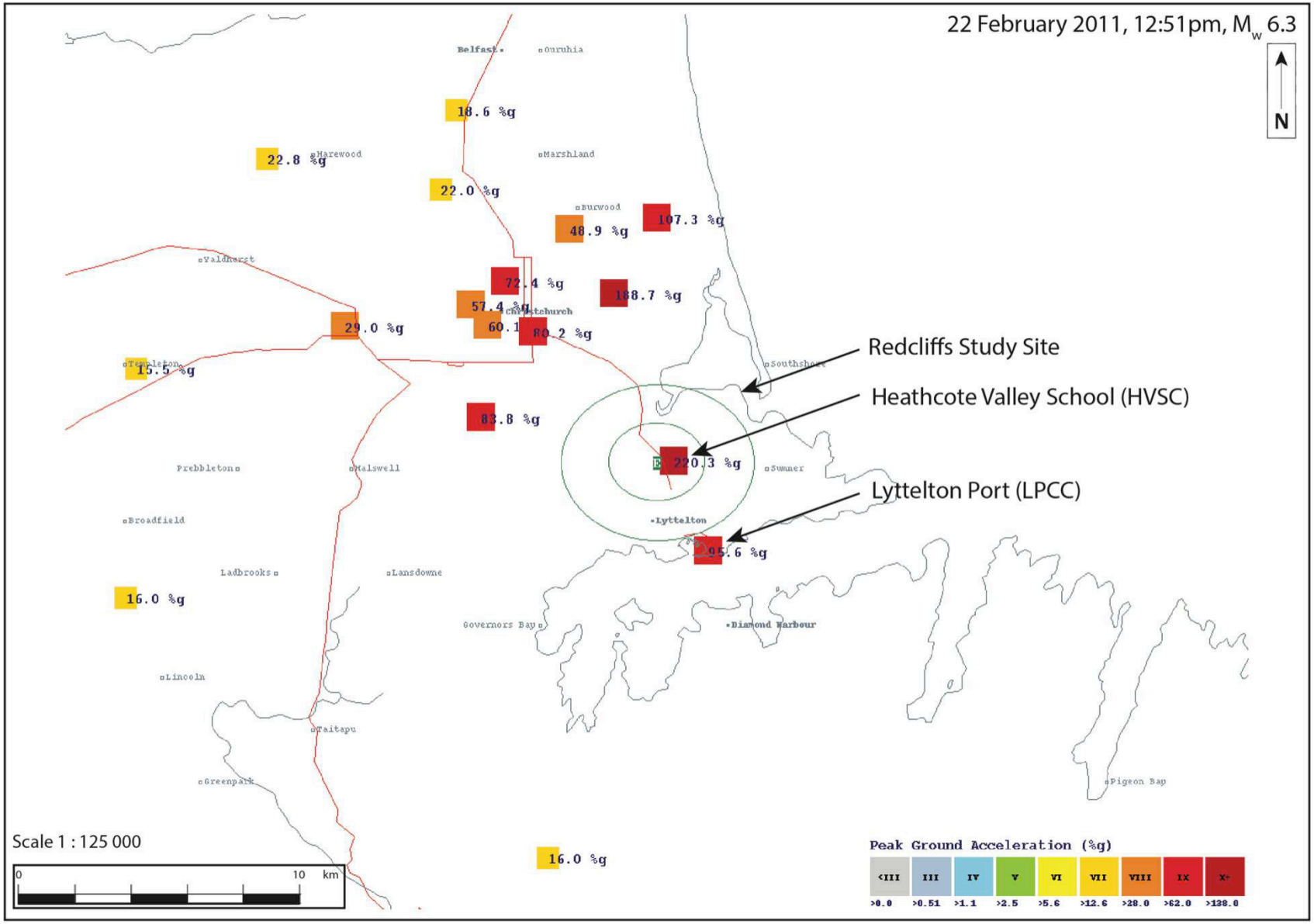
22 February 2011, 12:51pm, M_w 6.3
N
Redcliffs Study Site
Heathcote Valley School (HVSC)
Lyttelton Port (LPCC)
Belfast
Ouruhia
Harewood
Marshland
Burwood
Valdwarst
Templeton
Prebbleton
Halswell
Broadfield
Ladbrooks
Lansdowne
Lincoln
Taitapu
Greenpark
Governors Bay
Lyttelton
Sumner
Southshore
Diamond Harbour
Pigeon Bay
18.6 %g
22.8 %g
22.0 %g
48.9 %g
197.3 %g
72.4 %g
57.4 %g
60.1
188.7 %g
29.0 %g
83.8 %g
220.3 %g
95.6 %g
16.0 %g
16.0 %g
Scale 1 : 125 000
0
10 km
Peak Ground Acceleration (%g)
<III
III
IV
V
VI
VII
VIII
IX
X+
>0.0
>0.51
>1.1
>2.5
>5.6
>12.6
>28.0
>62.0
>138.0

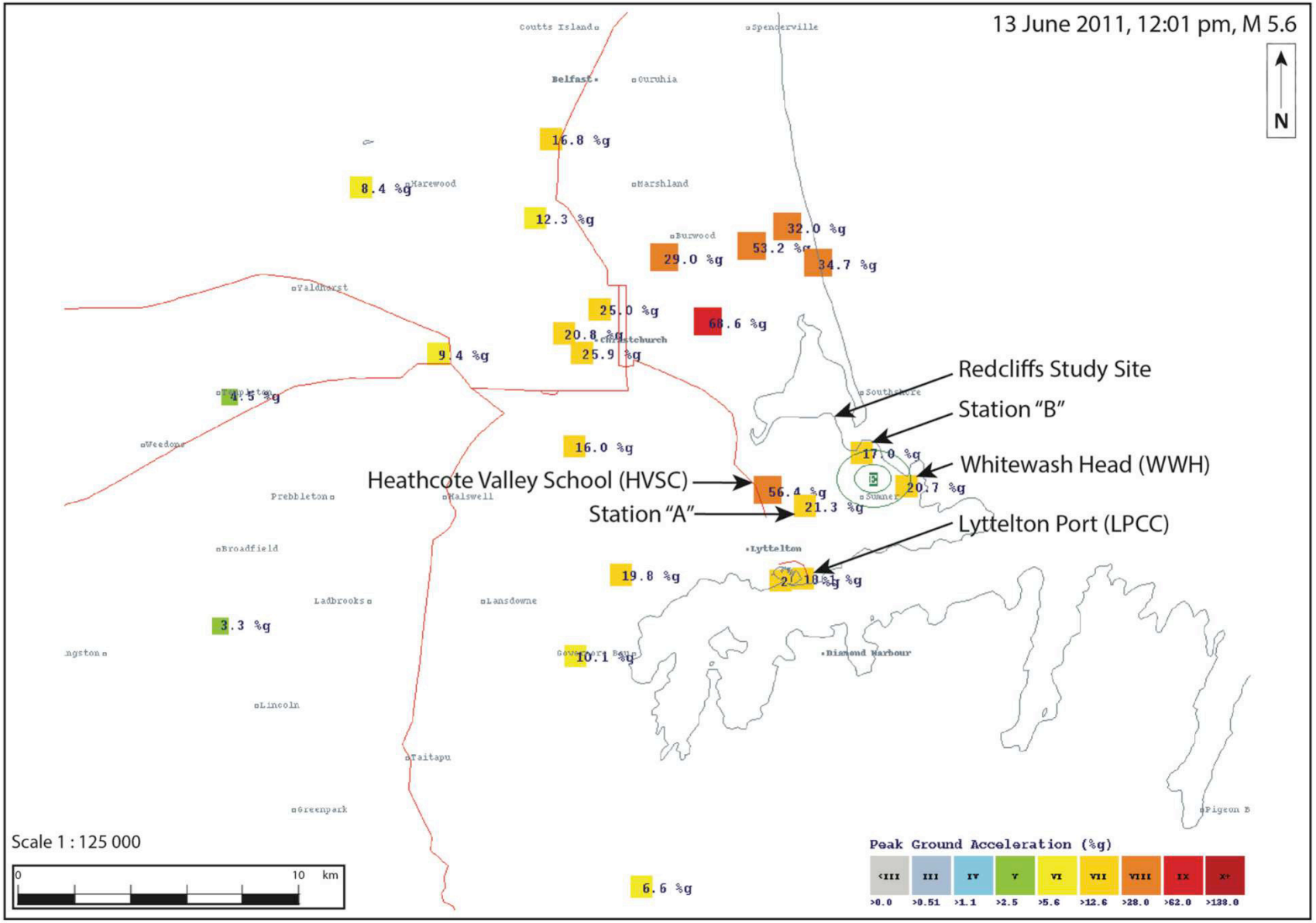
13 June 2011, 12:01 pm, M 5.6
N
Redcliffs Study Site
Station "B"
Whitewash Head (WWH)
Heathcote Valley School (HVSC)
Station "A"
Lyttelton Port (LPCC)
16.8 %g
8.4 %g
12.3 %g
32.0 %g
53.2 %g
29.0 %g
34.7 %g
25.0 %g
68.6 %g
20.8 %g
25.9 %g
9.4 %g
4.5 %g
16.0 %g
17.0 %g
56.4 %g
20.7 %g
21.3 %g
19.8 %g
3.3 %g
10.1 %g
6.6 %g
Scale 1 : 125 000
0
10 km
Peak Ground Acceleration (%g)
<III
III
IV
V
VI
VII
VIII
IX
X+
>0.0
>0.51
>1.1
>2.5
>5.6
>12.6
>28.0
>62.0
>138.0

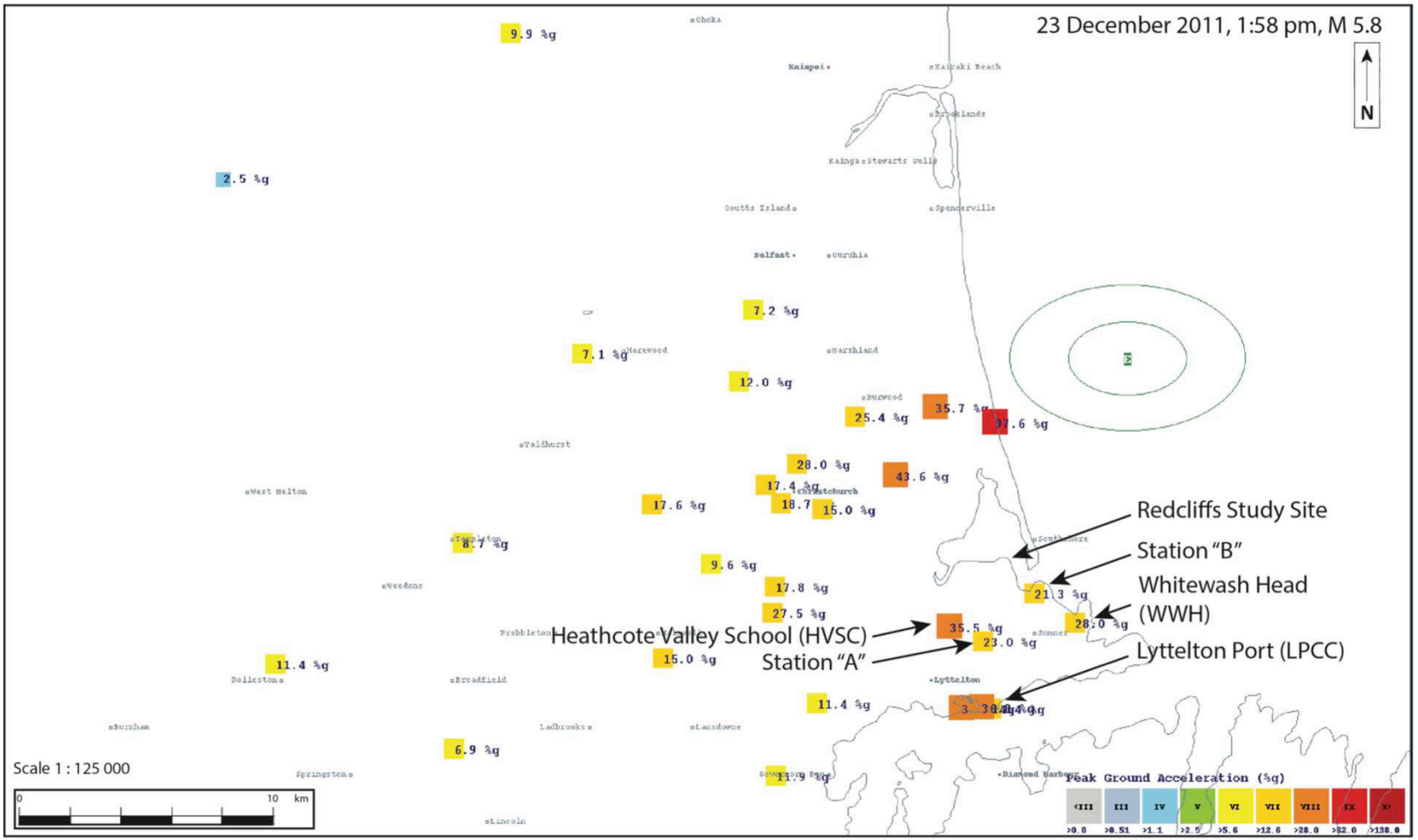
23 December 2011, 1:58 pm, M 5.8
N
9.9 %g
2.5 %g
7.2 %g
7.1 %g
12.0 %g
25.4 %g
35.7 %g
37.6 %g
28.0 %g
17.4 %g
43.6 %g
17.6 %g
18.7
15.0 %g
8.7 %g
9.6 %g
17.8 %g
27.5 %g
21.3 %g
28.0 %g
35.5 %g
23.0 %g
15.0 %g
11.4 %g
11.4 %g
6.9 %g
11.9 %g
Redcliffs Study Site
Station "B"
Whitewash Head
(WWH)
Heathcote Valley School (HVSC)
Station "A"
Lyttelton Port (LPCC)
Scale 1 : 125 000
0
10 km
Peak Ground Acceleration (%g)
<III
III
IV
V
VI
VII
VIII
IX
X+
>0.0
>0.51
>1.1
>2.5
>5.6
>12.6
>28.0
>62.0
>138.0

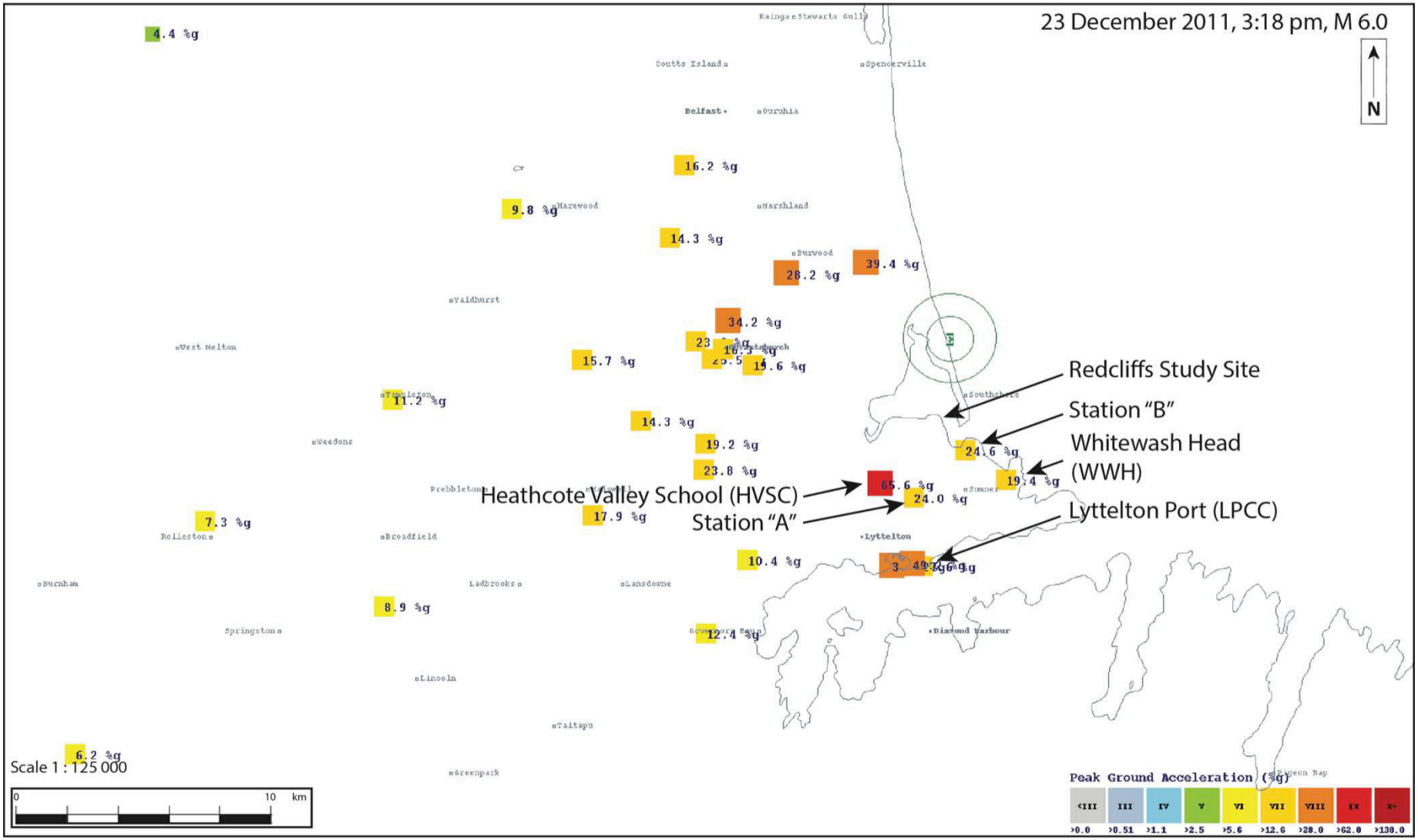
23 December 2011, 3:18 pm, M 6.0
N
4.4 %g
16.2 %g
9.8 %g
14.3 %g
39.4 %g
28.2 %g
34.2 %g
15.7 %g
14.6 %g
11.2 %g
14.3 %g
19.2 %g
23.8 %g
24.6 %g
19.4 %g
65.6 %g
24.0 %g
17.9 %g
7.3 %g
10.4 %g
8.9 %g
12.4 %g
6.2 %g
Redcliffs Study Site
Station "B"
Whitewash Head
(WWH)
Heathcote Valley School (HVSC)
Station "A"
Lyttelton Port (LPCC)
Kaingas Stewarts Gully
Coutts Islands
Spencerville
Belfast
Ouruhia
Marewood
Marshland
Burwood
Waldhurst
West Melton
Templeton
Weedons
Prebbleton
Rolleston
Broadfield
Lyttelton
Burnham
Ladbrooks
Lansdowne
Springston
Diamond Harbour
Lincoln
Taitapu
Greenpark
Scale 1 : 125 000
0
10 km
Peak Ground Acceleration (%g)
<III
III
IV
V
VI
VII
VIII
IX
X+
>0.0
>0.51
>1.1
>2.5
>5.6
>12.6
>28.0
>62.0
>130.0

APPENDIX 4: BULK GEOCHEMICAL PLOTS

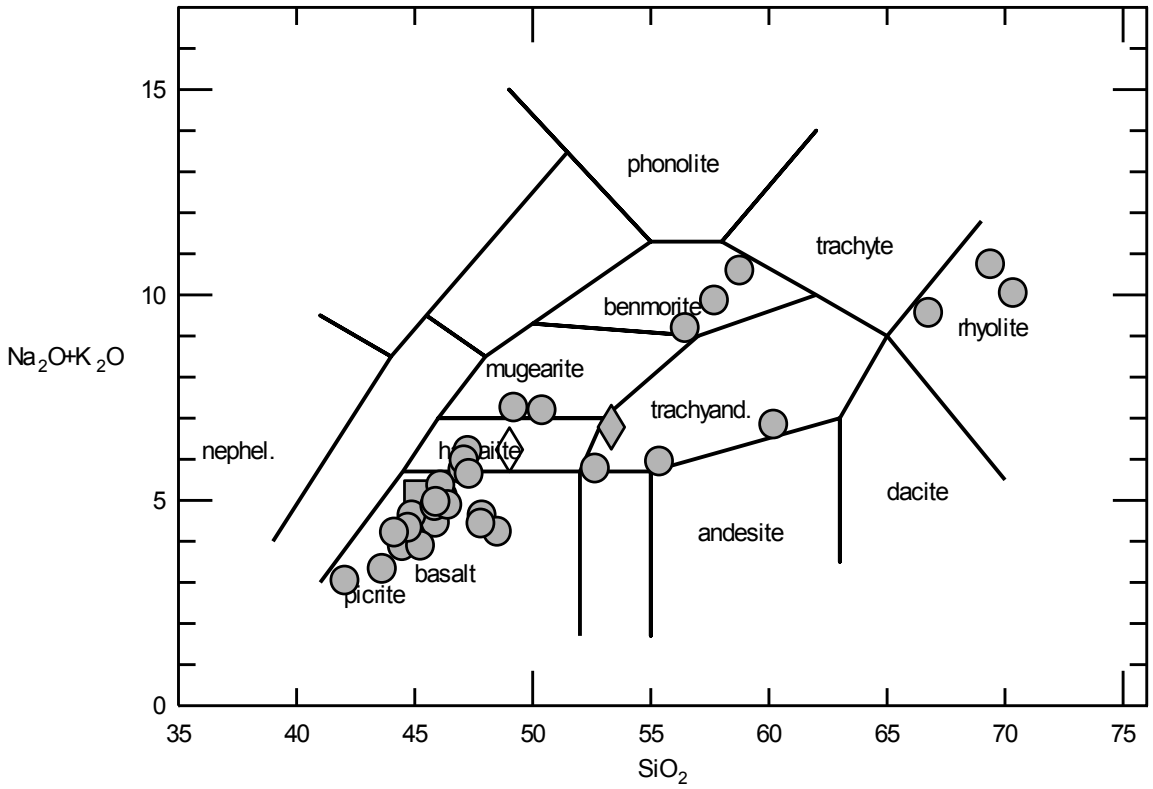

APPENDIX 4.1: Alkalis-Silica Plot (Cox, Bell, and Pankhurst, 1979). Grey Square=Welded columnar jointed unit; Open Diamond=Brecciated unit; Closed Diamond=Orange tuff unit; Closed Circles=Lyttelton Suite.

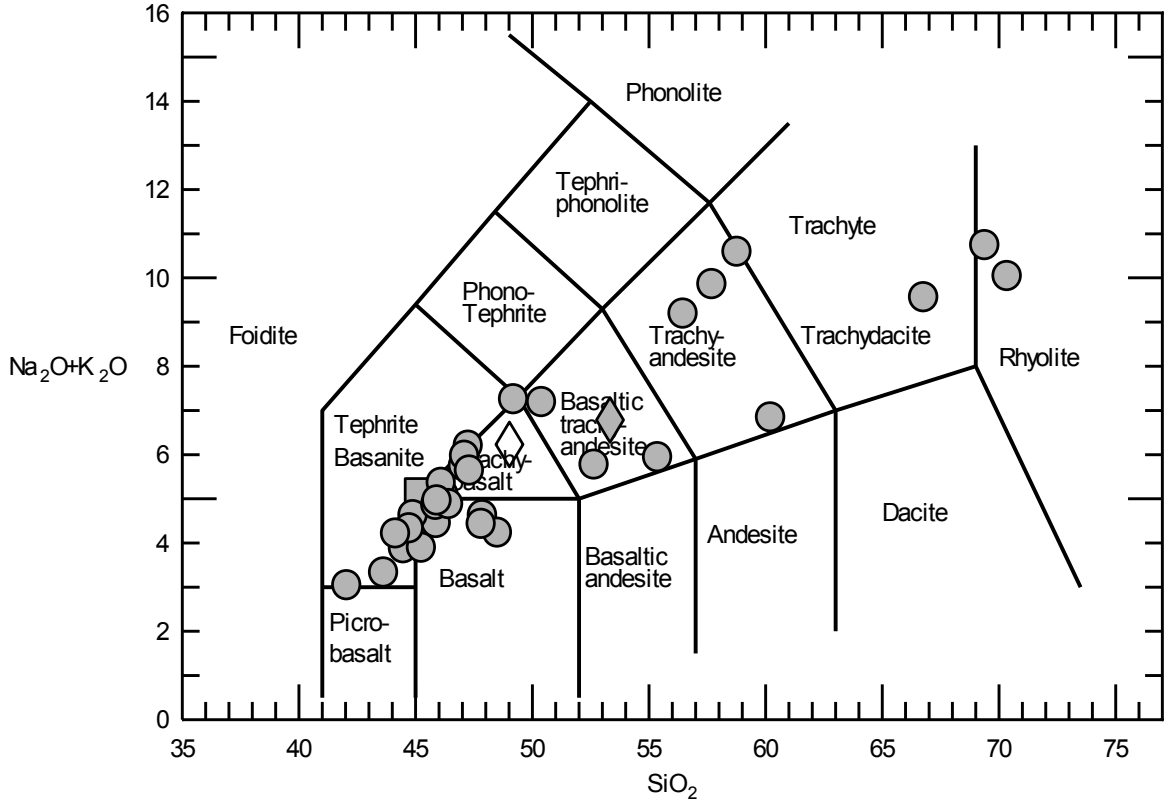

APPENDIX 4.2: TAS Alkali Silica (LeBas et al 1996). Grey Square=Welded columnar jointed unit; Open Diamond=Brecciated unit; Closed Diamond=Orange tuff unit; Closed Circles=Lyttelton Suite.

APPENDIX 5: ROCK STRENGTH TERMS

(NZGS 2005)

Term	Field Identification of Specimen	Unconfined uniaxial compressive strength q_u (MPa)	Point load strength $I_{s(50)}$ (MPa)
Extremely strong	Can only be chipped with geological hammer	> 250	>10
Very strong	Requires many blows of geological hammer to break it	100 – 250	5 – 10
Strong	Requires more than one blow of geological hammer to fracture it	50 – 100	2 – 5
Moderately strong	Cannot be scraped or peeled with a pocket knife. Can be fractured with single firm blow of geological hammer	20 – 50	1 – 2
Weak	Can be peeled by a pocket knife with difficulty. Shallow indentations made by firm blow with point of geological hammer	5 – 20	<1
Very weak	Crumbles under firm blows with point of geological hammer. Can be peeled by a pocket knife	1 – 5	
Extremely weak (also needs additional description in soil terminology)	Indented by thumb nail or other lesser strength terms used for soils	<1	

Note: No correlation is implied between q_u and $I_{s(50)}$